X-ray *in-situ* study of copper electrodeposition on UHV prepared GaAs(001) surfaces

vorgelegt von
Diplom-Physikerin
Yvonne Gründer
aus Berlin

von der Fakultät II-Mathematik und Naturwissenschaften
der Technischen Universität Berlin
zu Erlangung des akademischen Grades
Doktorin der Naturwissenschaften
-Dr. rer. nat-

genehmigte Dissertation

Promotionsausschuss:
Vorsitzender: Prof. Thomas Moeller
Gutachter: Prof. Christian Thomsen
Gutachter: Priv.-Doz. Jörg Zegenhagen

Tag der wissenschaftlichen Aussprache: 2. Juni 2008

Berlin 2008

D 83

Abstract

The physics and chemistry of semiconductor/electrolyte interfaces are of major interest for technological applications and for the understanding of the charge transfer process in fundamental research. For the metalization process in semiconductor industry electrochemical deposition is an attractive alternative beside the classical (and expensive) method of vacuum deposition. Often a better control of the deposition process is possible.
Surface X-Ray diffraction (SXRD) is ideal for the investigation of electrochemical metal deposition on the atomic scale, as also buried interfaces are accessible. X-ray in-situ studies can give detailed structural information of the surface and the region close to it.

For this work a unique setup for in-situ electrochemical studies was employed and improved. This setup permits UHV preparation of the GaAs(001) surface with a defined surface termination (arsenic-rich or gallium-rich) and its characterization by SXRD in UHV, under ambient pressure in inert gas and in electrolyte under potential control without passing through air.
The GaAs(001) surfaces were prepared by MBE and capped by amorphous arsenic at the University of Trondheim by the group of B.O. Fimland. This permitted to ship them through ambient air. Afterwards smooth well defined GaAs(001) surfaces could be recovered by thermal annealing in UHV.
A first investigation of the arsenic capped sample was done by atomic force microscopy (AFM) and Surface X-Ray Diffraction (SXRD). The non bulk like termination of the arsenic buried GaAs(001) surface was revealed. For the electrochemical metal deposition, arsenic terminated (2×4) reconstructed and gallium terminated (4×2) reconstructed GaAs(001) surfaces were employed. These surfaces were characterized by STM, LEED and a first time by SXRD. The surfaces are smooth, however, a higher degree of disorder than for MBE prepared reconstructed GaAs(001) is found. After exposure of the sample to nitrogen, the surfaces were then again studied by SXRD. These two steps characterizing the bare GaAs(001) surfaces permitted us to get a better knowledge of the starting surface and its influence on the later electrodeposited copper. At ambient pressure both reconstructions are lifted, but the surface is not bulk-like terminated as can be deduced from the crystal truncation rods.

Epitaxial copper clusters grow upon electrodeposition on the UHV prepared GaAs(001) surface. The copper lattice is rotated and inclined with respect to the GaAs substrate lattice, leading to eight symmetry equivalent domains. The influence of the surface termination as well as the nucleation potential on the structure of the electrodeposited copper were investigated. The tilt and rotation angles do not depend on the deposition potential but a small influence of the surface termination (Ga-rich or As-rich) could be found. The quality dependence of the copper epitaxy depends on the nucleation potential and on the surface termination was investigated. The variation of the copper lattice constant and the out-of-plane mosaicity of the copper were found to depend on the nucleation potential. Further investigation of the Cu/GaAs interface revealed interdiffusion processes at the interface.
Comparative studies of copper deposited on chemical etched (resulting rough) surfaces by SXRD revealed a less well defined epitaxy. In addition the surfaces obtained by potential controlled stripping from an arsenic capped wafer was investigated by AFM. The copper deposition on a such obtained surface was studied ex-situ by AFM.

Kurzfassung

Die physikalischen und chemischen Eigenschaften von Halbleiter/Elektrolyt Grenzflächen sind für technische Anwendungen und für das fundamentale Verständnis des Ladungsaustauschs an Grenzflächen von großem Interesse. Für die industrielle Metallbeschichtung ist die elektrochemische Abscheidung eine attraktive Alternative zur klassischen Metallbeschichtung im UHV. Oft ist eine bessere Kontrolle des Abscheideprozesses möglich.
Oberflächenröntgenbeugung (SXRD) ist ideal für die Untersuchung der elektrochemischen Metallabscheidung auf atomarer Ebene, da verdeckte Grenzflächen erreichbar sind.

Für diese Arbeit wurde ein besonderer Versuchsaufbau zur in-situ Untersuchung elektrochemischer Grenzflächen benutzt und verbessert. Dieser Aufbau erlaubt die UHV-Präparation verschiedener Terminierungen (Arsen- oder Gallium-reich) der GaAs(001) Oberfläche und deren anschließende Charakterisierung mit SXRD im UHV, in Inertgas bei Luftdruck und in Elektrolyt unter Potentialkontrolle, ohne zwischendurch Luft ausgesetzt zu sein.
Die GaAs(001)-Oberflächen wurden in der Gruppe von B.O. Fimland an der Universität von Trondheim mit MBE präpariert und anschließend mit amorphem Arsen bedeckt. Dies verhindert die Oxidation der reinen GaAs(001)-Oberfläche und ermöglicht die Verschickung der Proben in Luft. Glatte, geordnete GaAs(001) Oberflächen können anschließend durch das Abdampfen der Arsenschicht im UHV erhalten werden. Eine erste Untersuchung der As-beschichteten GaAs(001)-Oberfläche mit AFM und SXRD wurde durchgeführt. Die verdeckte Galliumarsenidoberfläche ist nicht bulk-terminiert wie die gemessenen CTR's enthüllen.
Für die elektrochemische Metallabscheidung wurden (2×4) und (4×2) rekonstruierte GaAs(001) Oberflächen präpariert. Diese Oberflächen wurden im UHV mit STM, LEED und mit SXRD untersucht. Die Oberflächen sind glatt, weisen jedoch eine höhere Unordnung als MBE präparierte rekonstruierte GaAs(001)-Oberflächen auf. Die anschließende Untersuchung dieser Oberflächen in Stickstoff bei Luftdruck offenbart die Aufhebung der Rekonstruktion. Jedoch sind die Oberflächen nicht bulk-terminiert wie aus den CTR's gefolgert werden kann.
Diese schrittweise Charakterisierung der Oberflächen im UHV und in Stickstoff ermöglicht eine bessere Kenntniss der Ausgangsoberfläche und deren Einfluss auf die Eigenschaften des elektrochemisch abgeschiedenen Kupfers.
Kupfer wächst epitaktisch und ist bezüglich des GaAs-Gitters gedreht und verkippt. Insgesamt konnten acht symmetrisch identische Domänen identifiziert werden. Kupfer wächst in Inseln und ist durch $\{111\}$-Facetten begrenzt.
Die Rotations- und Verkippungswinkel des Kupfergitters bezüglich des GaAs-Gitters hängen von der Terminierung der Ausgangsoberfläche jedoch nicht vom Abscheidepotential ab. Die Abhängigkeit der Qualität der Kupferepitaxie vom Abcheidepotential und von der Oberflächenterminierung wurde untersucht. Die Mosaizität des Verkippungswinkels und die Änderung der Kupfergitterkonstanten hängen vom Nukleationspotential ab. Weitere Untersuchungen der Cu/GaAs-Grenzfläche weisen auf Diffusionsprozesse an der Grenzfläche hin.
SXRD-Messungen der elektrochemischen Abscheidung von Kupfer auf chemisch geätzte GaAs-Oberflächen wurde zum Vergleich durchgeführt. Zusätzlich wurden GaAs Oberflächen, die durch die potentialkontrollierte Auflösung der amorphen Arsenschicht von As/GaAs Wafern erhalten wurden, mit AFM untersucht. Auch eine anschließende ex-situ Studie des elektrochemisch auf solche Oberflächen abgeschiedenen Kupfers wurde untersucht.

Contents

Introduction

Interfaces of solids in contact with (aqueous) electrolyte solutions are of major interest for both, fundamental and practical incentives. Up to now studies were mainly focused on metal electrodes, which can be fairly well understood with classical tools like cyclic voltammetry [1] and STM [2]. Semiconductor electrodes are of particular importance for the metalization process in semiconductor industry, since, beside the classical (and expensive) method of vacuum deposition electrochemical deposition is an attractive alternative. One of the most commonly used materials in electrodeposition is copper, which has become of major importance in electronics industry. Cu electrodeposition is used for the defect-free filling of trenches on ultra large scale integrated (ULSI) microchips. In addition, solar cells can be protected from corrosion and their efficiency can be increased by deposition of metal monolayers.
Although the metal electrodeposition on semiconductors is a technologically interesting process, not many studies of this topic were carried out [3, 4, 5, 6, 7]. The semiconductor/electrolyte interface was earlier investigated by classical electrochemical methods [3, 5, 8, 9]. For metal electrodes these studies permit the description of the thermodynamical properties on a macroscopic scale and can reveal important information about the atomic structure; but the application and understanding of the results of traditional electrochemical methods like cyclic voltammetry and in-situ STM are difficult for semiconductor/electrolyte interfaces because of the energy band gap and band-bending in the semiconductor. However, experiments able to give information on the atomic scale are pivotal for the understanding and improvement of the deposition process.

Another inconvenience in semiconductor-electrochemistry is the difficulty to obtain smooth and clean semiconductor surfaces. For the study of the metal-electrolyte interface, noble metals (e.g. gold) are commonly used for which a convenient procedure (e.g. flame annealing) for the surface preparation can often be utilized [10]. Smooth and clean semiconductor surfaces can be prepared by UHV methods, however, the transfer to an electrochemical cell for an adequate electrochemical characterization often results in a change (e.g. oxidation, adsorption, creation of defect) of the surface. Another way of preparing semiconductor surfaces is chemical etching. The thus obtained surfaces are clean but often rough. Especially in the case of the GaAs(001) surface the roughness leads to an additional complication as both gallium and arsenic sites are present and can e.g. both act as nucleation sites for metal deposition.
For the realization of electronic devices, GaAs has superior properties, relative to silicon, such as a direct band gap which is important for opto-electronic devices (but also introduces photocorrosion) and a smaller effective mass (of the electrons and holes) permitting a faster response of GaAs-based electronic devices and a better performance for high-frequency signal-processing applications. However, silicon is chemically and electrochemically much more sta-

ble. Corrosion is not a serious problem for silicon but can be severe for III-V compound semiconductors, limiting their applications. GaAs is an ideal model for studying the corrosion on a binary compound semiconductor. The anodic oxidation of GaAs has been studied by Heinz Gerischer [11] already in 1965 and is still investigated [12]. In strong acid solution GaAs is decomposed resulting in a rough surface exposing surface states. Worthy of note, GaAs wafers are commonly cleaned in acidic solutions.
The Cu electrodeposition was up to now investigated on chemically etched GaAs(001) surfaces. Several studies were carried out by scanning probe techniques, X-ray diffraction, X-ray absorption fine structure measurements (XAFS) and electrochemical methods as impedance spectroscopy and current transient studies. It was found that the copper grows in islands. The initial number and size of the copper clusters was found to depend on the deposition potential and the concentration of Cu^{2+}. In addition, the study of the copper epitaxy by SXRD [13, 14] revealed the epitaxial copper growth with the Cu[100]-direction aligned with the GaAs[100] direction. The copper lattice was found to be tilted by an angle of 6° with respect to the GaAs lattice. No azimuths of the planes seemed to be preferred, resulting in an isotropic inclination of the $\{001\}$ planes of the epitaxial Cu islands with the GaAs(001) planes. The starting surface for copper deposition was rough with steps of several GaAs bi-layers present on the surface. The nucleation mechanisms and the reason for the unusual epitaxy could not be resolved.
Surface X-Ray scattering (SXS) is ideal for investigating electrochemical metal deposition on atomic scale. X-rays have a weak interaction with matter and buried interfaces are therefore accessible. However, the weak interaction of the X-rays with materials is also a problem for surface X-ray diffraction due to the relatively small number of atoms contained within a surface. Since the advent of synchrotron X-ray facilities, intense X-rays are obtainable. They are convenient for the in-situ study of the surface/electrolyte interface as detailed information on the structure, roughness and morphology of the surface and the region close to it are accessible.

For this work a unique setup for in-situ electrochemical studies was employed and improved. This setup permits UHV preparation of the GaAs(001) surface with a defined surface termination (arsenic-rich or gallium-rich) and its characterization by SXS in UHV, under ambient pressure in inert gas and in electrolyte under potential control without passing through air. With this setup the epitaxy of the copper electrodeposited on GaAs(001) was studied.
The GaAs(001) surfaces were prepared by MBE and capped by amorphous arsenic. This permitted to ship them through ambient air. Afterwards smooth well defined GaAs(001) surfaces could be recovered by thermal annealing in UHV. A first investigation of the arsenic capped sample was done by atomic force microscopy (AFM) and Surface X-Ray Diffraction (SXRD). The non bulk like termination of the arsenic buried GaAs(001) surface was revealed. For the electrochemical metal deposition, arsenic terminated (2×4) reconstructed and gallium terminated (4×2) reconstructed GaAs(001) surfaces were employed. These surfaces were characterized by STM, LEED and a first time by SXRD. The surfaces are smooth, however, a higher degree of disorder than for MBE prepared reconstructed GaAs(001) is found. After exposure of the sample to nitrogen, the surfaces were then again studied by SXRD. These two steps characterizing the bare GaAs(001) surfaces permitted us to get a better knowledge of the starting surface and its influence on the later electrodeposited copper. At ambient pressure both reconstructions are lifted, but the surface is not bulk-like terminated as can be deduced from the crystal truncation rods.

The influence of the surface termination as well as the nucleation potential on the structure of the deposited copper were investigated. Epitaxial copper clusters grow upon electrodeposition on the UHV prepared GaAs(001) surface. The copper lattice is rotated and inclined with respect to the GaAs substrate lattice, leading to eight symmetry equivalent domains. The tilt and rotation angles do not depend on the deposition potential but a small influence of the surface termination (Ga-rich or As-rich) could be found. In addition, the quality of the epitaxy depends on the nucleation potential and on the surface termination. Further investigation of the Cu/GaAs interface revealed interdiffusion processes at the interface.

The thesis is organized in the following way. In Chapter 1 and Chapter 2 the basics concerning the electrochemistry of semiconductors and SXRD are briefly revisited. An overview of the GaAs(001)-reconstructed surfaces and the copper deposition on GaAs(001) is given in Chapter 3. The experimental methods are discussed in Chapter 4. After a short description of the chemical cleaning of GaAs(001)-surfaces and the presentation of the in-situ thin layer cell used for X-ray diffraction measurements on such prepared surfaces as well as of the AFM technique for ex-situ study, a short introduction to the UHV-preparation and -characterization is given. Finally the ID32 beamline and its setup for diffraction experiments are presented, followed by a description of the portable UHV-electrochemistry chamber and electrochemical droplet cell used for in-situ diffraction experiments of electrochemical reactions.
In the second part of this work the experimental results are presented, starting with the characterization of the arsenic capped GaAs(001) surface by AFM and SXRD in Chapter 5. The characterization of the bare reconstructed GaAs(001) surfaces in UHV and under ambient nitrogen pressure are presented in Chapter 6.
The results obtained for copper deposited on differently prepared GaAs(001) surfaces are presented in Chapter 7. Furthermore, the characterization by AFM of the GaAs(001) surfaces obtained by the potential controlled stripping of the arsenic cap in electrolyte are presented. AFM was used as well to study the copper deposited on a such obtained surface. Afterwards, an in-situ SXRD study of the copper electrodeposition on a chemical cleaned GaAs(001) surface is shown.
The major part of this chapter contains the results obtained by SXRD for copper electrodeposited on UHV prepared GaAs(001) surfaces. The epitaxy of the copper as well as the morphology of the deposited copper clusters were investigated. This chapter ends with a discussion of the copper electrodeposition on GaAs(001). Finally, a conclusion and outlook is given in the last chapter (Chapter 8).

Chapter 1

Electrochemistry

Electrochemistry deals with the charge transfer reactions across the interface of a solid (conductor or semiconductor) and an ionic conductor (the electrolyte), which is influenced by the electrical double layer due to potential differences between electrode and electrolyte. The electrical and chemical potentials of the electrode control the charge distribution close to the interface. A brief review of the basics of electrochemical processes will be given in this chapter. The energy band model for semiconductors and ions in solution will be introduced in Section 1.2. An overview of the solid/electrolyte interface is given in Section 1.3. The basics of metal deposition are explained in Section 1.4. Finally an important tool for electrochemical studies, the cyclic voltammetry, is introduced in Section 1.5. A more general introduction to electrochemistry is given in Reference [15]. More detailed information about semiconductor electrochemistry and electrodeposition can be found in References [16, 17, 18, 19, 20].

1.1 Electrochemical reactions

If charge transfer between the electrode and the ions in solution occurs, accompanied by a faradaic current, an electrochemical reaction is taking place. The process of an atom or a molecule losing electrons is called oxidation, the inverse process of an atom or molecule gaining electrons is called reduction. Reduction and oxidation reactions can be described by the oxidation number, which is zero for a neutral atom. By gaining an electron through a reduction process the oxidation number decreases by one,

$$\text{reduced state} \rightleftharpoons \text{oxidized state} + \text{n } e^{-}. \tag{1.1}$$

The possibility of the spatial separation of the reduction and oxidation process by using two half-cells is important for studying electrochemical processes. These cells build up the galvanic couple and are electrically contacted. Each cell contains an electrode and a solution of the respective metal salt. The two half-cells connected to each other by a salt-bridge. Electrochemical reactions take place at both electrodes, which serve as donor and acceptor of electrons respectively. The combination of the two half-cells leads to the redox-reaction

$$\begin{array}{rcl} M_1^{n+} + n\,e^- & \rightleftharpoons & M_1(s) \\ M_2(s) & \rightleftharpoons & M_2^{n+} + n\,e^- \\ \hline M_1^{n+} + M_2(s) & \rightleftharpoons & M_1(s) + M_2^{n+}. \end{array}$$

The driving force determining the direction of the reaction and the processes taking place on the electrode surfaces is the chemical potential of the free particles such as the electrons in the electrode or the ions in the solution. At equilibrium the chemical potential has the same value everywhere. For charged particles an additional influence, called the inner potential or the Galvani potential ϕ_i, due to the electrical potential at the site of the particle, has to be taken in account. As only potential differences can be measured, ϕ_i is a priori unknown.
The electrochemical potential $\tilde{\mu}_i$ can be written as the sum of the chemical potential and an additional term which is related to the Galvani potential, giving the electrical energy

$$\tilde{\mu}_i = \mu_i + z_i\, F\, \phi_i, \tag{1.2}$$

where z_i is the charge of the particle and F is the Faraday constant. The chemical potential of each particle depends on the activity a_i of the species (normally the electrolyte)

$$\tilde{\mu}_i = \tilde{\mu}_i^0 + R\, T\, \ln a_i. \tag{1.3}$$

In this equation $\tilde{\mu}_i^0$ is the standard electrochemical potential defined for $a_i = 1$. R is the gas constant and T the temperature. Two different phases (I and II) in contact are at equilibrium when the eletrochemical potentials of each phase in the system are equal. From the condition

$$\tilde{\mu}_i(I) = \tilde{\mu}_i(II) \tag{1.4}$$

for the redox-reaction

$$M \rightleftharpoons M^{n+} + n\, e^- \tag{1.5}$$

the Galvani potential difference $\Delta\phi$ can be derived,

$$\Delta\phi = \Delta\phi_0 + \left(\frac{R\, T}{n\, F}\right) \ln a_{M^{n+}}, \tag{1.6}$$

with $\Delta\phi_0$ the standard Galvani potential difference, which is the difference of the inner potential of the electrode and of the inner potential of the solution for $a_{M^{n+}} = 1$.

This equation considers only the reaction on one half-cell with the liquid to be the reference. The potential of the liquid can not be determined experimentally since only potential differences can be measured. Therefore another reference in form of an electrode will be introduced as part of the second half-cell. Ideally, this electrode is in the same electrolyte to avoid additional potential drops through the liquid/liquid interface. The potential difference ΔE between both electrodes, the working electrode at potential $\Delta\phi(1)$ and the newly introduced reference electrode at potential $\Delta\phi(2)$, can then be written as

$$\Delta E = \Delta\phi(1) - \Delta\phi(2) = E^0 + \left(\frac{R\, T}{n\, F}\right) \ln \frac{a_{M^{n+}}}{a_{M(s)}}. \tag{1.7}$$

This is the so called Nernst equation for a metal electrode in contact with an electrolyte solution of its ions M^{n+}. The activity a_{Me} can be set equal one. The potential E^0 can in principle be chosen arbitrarily. It can be identified with the Fermi level in the electrolyte. The convention in electrochemistry is to use the Standard Hydrogen Electrode (SHE) as a reference. Such an

electrode is constructed by a platinum electrode in aqueous electrolyte with hydrogen activity $a_{H_3O^+} = 1$ by hydrogen purging at 1 bar pressure. The reaction catalyzed by the platinum is

$$2\,H_3O^+ + 2\,e^- \rightleftharpoons H_2 + H_2O \tag{1.8}$$

with the equilibrium potential

$$\Delta E = E^0 + \frac{R\,T}{F} \ln \frac{a_{H_3O^+}}{\sqrt{p_{H_2}}}. \tag{1.9}$$

Hydrogen's standard electrode potential E^0 is declared to be zero at all temperatures. Potentials of any other electrodes are compared with that of the SHE at the same temperature.

1.2 Energy Levels

The electronic properties of semiconductors are normally described by the band structure. To illustrate the processes of a semiconductor in contact with an electrolyte it is convenient to also describe the active ions in solution using an energy level diagram.

1.2.1 Energy Levels in a semiconductor

Energy bands

The energy bands describing the outer electrons in a semiconductor consist of a lower lying valence band, fully occupied by electrons, and a vacant conduction band at higher energy levels. These energy bands are separated by the band gap. In the case of GaAs the valence band maximum and the conduction band minimum occur at the same electron wave vector. GaAs thus has a direct band gap.

The band gaps in semiconductors are relatively narrow and therefore a few section of the valence electrons can be thermally excited to the conduction band, leaving "holes " in the valence band. The concentration n_i of thermally excited electron-hole pairs is given by the Boltzmann function

$$n_i = n_0 \cdot \exp \frac{-\varepsilon_g}{2\,k\,T}, \tag{1.10}$$

where k is the Boltzmann constant and n_0 is the concentration of electrons at the upper edge of the valence band. For a band-gap of ε_g=1.4 eV (corresponding to the band gap of GaAs), only a small concentration of electron-hole pairs is excited at room temperature ($n_i = n_0 \cdot 1.44 \cdot 10^{-12}$). A possibility to increase the conductivity of semiconductors is doping, which creates allowed energy levels localized at impurity atoms in the band gap.
Impurities delivering additional electrons are called donors and semiconductors doped with donors are n-type. In n-type materials donor levels ε_D are created near the top of the band gap ($\varepsilon_C - \varepsilon_D \approx 0.05$ eV), from which electrons can be more easily excited into the conduction band. Impurities producing electron vacancies are called acceptors, creating unoccupied electron energy levels (ε_A) in the band gap close to the valence band maximum ($\varepsilon_A - \varepsilon_V \approx 0.05$ eV). Through thermal excitation electrons from the valence band can reach the acceptor levels. The

created vacancies in the valence band contribute to the conductivity.
For intrinsic semiconductors (non-doped) the Fermi-level is located midway in the band gap

$$\varepsilon_F = \frac{1}{2} \cdot (\varepsilon_C + \varepsilon_V) + \frac{1}{2}\, k\, T \ln \frac{N_V}{N_C}, \tag{1.11}$$

as N_V (the effective state density at the upper edge of the valence band) and N_C (the effective state density at the lower edge of the conduction band) are equal. For a n-doped semiconductor the Fermi level is shifted towards the conduction band

$$\varepsilon_F = \frac{1}{2}(\varepsilon_C + \varepsilon_D) - \frac{1}{2} k\, T\ \ln \frac{2\, N_C}{N_D}, \tag{1.12}$$

where N_D is the concentration of ionized donors described by the Boltzmann function

$$N_D = \frac{C_D}{2} \cdot \exp \frac{\varepsilon_D - \varepsilon_F}{k\, T} \tag{1.13}$$

and C_D is the concentration of donors. For p-doped semiconductors the Fermi level is shifted towards the valence band:

$$\varepsilon_F = \frac{1}{2}(\varepsilon_V + \varepsilon_A) + \frac{1}{2} k\, T\ \ln \frac{2\, N_V}{N_A}. \tag{1.14}$$

with N_A the concentration of ionized acceptors described by the Boltzmann function:

$$N_A = \frac{C_A}{2} \cdot \exp \frac{\varepsilon_F - \varepsilon_A}{k\, T}. \tag{1.15}$$

C_A is the concentration of acceptors.

Surface states

In addition to the energy bands and impurity levels discussed previously, at the semiconductor surface localized electronic states exist. These are two dimensional energy levels in the band gap

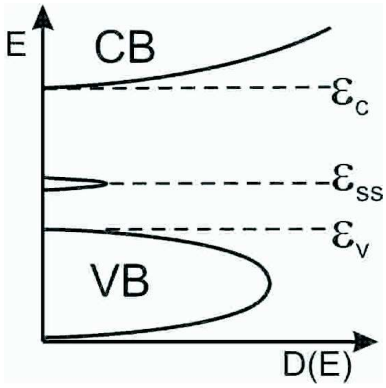

Fig. 1.1: *The density of states of a semiconductor with a surface state at an energy of ε_{SS}.*

which are localized at the semiconductor surface. The density of states of a semiconductor with

a so called surface state or interfacial state at an energy ε_{SS} is shown in Figure 1.1. Such states can influence the chemical and physical properties at the liquid/solid interface. The bonding of an adsorbate to the surface is determined to a great extent by surface states. Surface state energy levels can act in electrochemical reactions as intermediate states for the electron transfer between the energy band of the semiconductor and the ions in solution. Two surface states can be distinguished,

Shockley states The Shockley states or surface dangling-bond states are caused by unsaturated orbitals of surface atoms of a covalent semiconductor. These dangling bonds can act as either an acceptor surface state (electrons being captured to pair with the electron in the dangling bond) or a donor surface state (the electrons of the dangling bond being excited to the conduction band, leaving locally a positively charged surface).

Tamm states The Tamm-state or ionic-induced state is caused by the surface lattice potential different from the internal lattice potential. A surface lattice ion is surrounded by less than its normal charge complement. Surface anions have higher energy on the surface because of lower electrostatic attraction from the neighbouring cations. They are normally donor states located in the gap region above the valence band. An unoccupied energy level associated with a surface cation is an acceptor state located below the conduction band.

Tamm and Shockley surface states are intrinsic surface states which are characteristic for semiconductors. Additionally, extrinsic surface states produced by adsorbates and surface films can exist. They depend on the environment to which the surface is exposed. In electrochemistry, adsorption-induced surface states are important. Especially surface defects such as steps and kinks or heterogenicity (different crystal planes) on the surface can introduce surface states, as they disrupt the surface periodicity and therefore the ordered chemical environment of the surface atoms. The concentration of surface states is in the range of $1 \cdot 10^{10}$ to $1 \cdot 10^{14}$ cm^{-2}, which is around 1/10 to 1/100000 of the concentration of surface atoms. The concentration of surface states is greater on a rough surface.

1.2.2 Energy levels of ions in solution

Analogous to the solid state, the electrolyte can be described by the energy band model. Oxidized and reduced species have different charges and therefore different interactions with the ions of the solution. The so called solvation energy shifts the energy levels of the ions due to the interaction with hydronium and hydroxide ions. Accordingly two energy levels, one for the reduced species E_{red} and one for the oxidized species E_{ox}, exist. The energy levels of these species are not sharply defined but fluctuate due to the thermal (rotational and vibrational) motions of the surrounding polar molecules. These energy levels can be described by their probability distribution $D(E)$ to be found at a certain energy. It is described by a Gaussian distribution, e.g. for the oxidized species M^{n+} of a metal M, as

$$D(E) = \frac{c_{M^{n+}}}{\sqrt{4\,\pi\,\lambda\,k\,T}} \cdot exp\left(-\frac{(E_{ox}-E)^2}{4\,\lambda\,k\,T}\right), \tag{1.16}$$

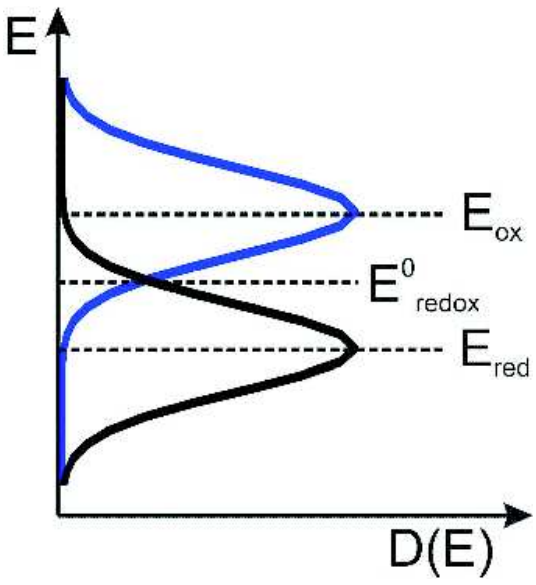

Fig. 1.2: *The energy levels for a redox system. Two levels exist due to the different solvation energy of the reduced and the oxidized species. These energy levels are not sharply defined but fluctuate (are broadened) due to the thermal motion of the coordinated polar molecules.*

where λ is the reorganization energy (with typically $\lambda = 0.4$ to 1.2 eV) and $c_{M^{n+}}$ the concentration of the oxidized species in the electrolyte. In Figure 1.2 the energy levels for a redox system with equal concentrations of the reduced and oxidized species are shown. The energy levels of the oxidized and reduced species can act as acceptor and donor states, respectively. The time fluctuating energy levels can be interpreted as bands of energy (similar to solid state physics). However, these "bands" arise from polarization fluctuations of the ions and have properties different from the fixed bands of a solid, e.g. no optically induced transitions between occupied and unoccupied levels (the reduced and oxidized states) exist, as the levels of the two species do not overlap in real space. However, for describing the electrochemistry at a metal/electrolyte interface and especially at a semiconductor/electrolyte interface this model is convenient.
In electrochemistry the redox-potential of the SHE is used as zero of the potential range (Section 1.1). By contrast, in solid state physics the Fermi-level and therewith the energy of an electron at infinity is used. To compare both energy scales, an energy of -4.5eV for the SHE on the vacuum energy scale is assumed,

$$E_{vac} = -4.5eV - e \cdot E_{redox}. \tag{1.17}$$

With increasing potential the energy of an electron decreases. This is equivalent to the fact that electrons tend to move from more negative to more positive potentials.

1.3 The Solid/Liquid Interface structure

The electrolyte is a solution of ions. Charge transfer on the surface and the potential drop through the electrolyte/electrode interface are influencing the charge distribution close to the

interface.

1.3.1 The Metal/Electrolyte Interface

At the metal/solution interface of an electrode immersed in the aqueous solution of its salt exchanges of metal ions between the two phases take place. Depending on the preferred reaction (oxidation or reduction) the electrode can be positively or negatively charged. For a preferred reduction of the metal, the electrode is charged positively. This charge will be concentrated on the electrode surface (due to the good conductivity of metals no charge will be accumulated in the bulk) and attract anions from the solution. Therefore, a space charge layer is formed, causing the electrode and the electrolyte to be at different potentials. The space charge layer has two origins: the ion redistribution and the reorientation of water dipoles in the solution.
By applying a voltage between the metal electrode and a counter electrode immersed in the solution, the potential can be changed and the charging of the space charge layer can be influenced. Electrochemical processes accompanied by a cathodic or anodic current can be inducted. Several models describing the double layer were developed by Helmholtz, Gouy-Chapman and Stern.

Helmholtz compact double-layer model

The Helmholtz compact double-layer [21] is the simplest model of the structure of the metal-solution interface. All excess charge is lined up at a fixed distance from the electrode, the so called Helmholtz-plane. The distance is determined by the hydration sphere of the ions and the Helmholtz-plane is defined by the centers of the hydrated ions. The double layer is equivalent to a parallel plate capacitor, as it consists of two equally but opposite charged layers, the metal and the solution. This model predicts a potential independent capacitance

$$C = \frac{\varepsilon}{4\,\pi\,d} \tag{1.18}$$

only depending on the distance of the Helmholtz-plane from the electrode surface d, in agreement with experiment for high ionic concentrations.

Gouy-Chapman diffuse-charge model

Gouy [22] and Chapman [23] independently proposed another model allowing a potential-dependent, statistical distribution of the ions in the double layer of the solution. This is based on the assumption that the ions are not adsorbed on the surface but are concentrated close to the surface in a diffuse layer. Assuming Boltzmann distribution and point charges for this diffuse layer, the number of positive ions per unit volume at a distance x from the electrode is (assuming two types of ions of equal and opposite charge),

$$n^{+}(x) = n^{+}(b) \cdot \exp\left(\frac{-z\,e\,\phi(x)}{k\,T}\right), \tag{1.19}$$

where $n(b)$ is the number of corresponding ions per volume in the bulk of the solution, $\phi(x)$ is the potential at distance x from the electrode surface. The number of negative ions per unit

volume is correspondingly:

$$n^-(x) = n^-(b) \cdot \exp\left(\frac{z\,e\,\phi(x)}{k\,T}\right). \tag{1.20}$$

The net charge per unit volume at position x in the double layer region is then:

$$q(x) = z\,e\left(n^-(x) - n^+(x)\right). \tag{1.21}$$

The potential dependence of C

$$C \propto \sqrt{n(b)}\cosh\left(\frac{e\phi(x=0)}{k\,T}\right) \tag{1.22}$$

is the basic improvement of the model. However in concentrated solutions and for larger distances the theory is in disagreement with experiment.

Stern model

The Stern model is a combination of the Helmholtz model and the Gouy-Chapman model, dividing the double layer in a compact (Helmholtz) and a diffuse (Gouy-Chapman) double layer. From the electrode to a plane of fixed charge (the Helmholtz-plane) a compact double layer is assumed and the diffuse layer extends from this plane to the bulk of the solution. According to this model the ions can not go closer to the electrode than the Helmholtz plane (therefore also called plane of closest approach). It therefore eliminates the point-charge approach from the Gouy-Chapman model.
The total capacitance C behaves like two capacitances (the Helmholtz and the Gouy-Chapman capacitance) in series:

$$\frac{1}{C} = \frac{1}{C_H} + \frac{1}{C_{GC}}. \tag{1.23}$$

A close agreement between the experimental and calculated double-layer capacitances is found.

1.3.2 The Semiconductor/Electrolyte Interface

Similar to metals, space charge regions are created at the semiconductor/electrolyte interfaces during the charge transfer through the solid/electrolyte interface. At a metal/electrolyte interface the space charge region is created in the electrolyte close to the interface. At a semiconductor/electrolyte interface this space charge region extends into the semiconductor and induces a bending of the energy bands close to the interface.

In a semiconductor this space charge can have the form of immobile charged impurities or trapped carriers near the surface, but it can also be created by the mobile charge carriers (electrons or holes) in the valence or conduction band.
Semiconductors with a concentration of charge carriers $< 10^{20} cm^{-3}$ have a space charge region extending into the bulk similar to the diffuse double layer in electrolyte. The potential distribution at a semiconductor/electrolyte interface is therefore more complicate than that at a

metal/electrolyte interface. In equilibrium without an applied potential the Fermi levels of the solution and the semiconductor are equal.
The amount of charge in the space charge region of the semiconductor depends on several processes. A semiconductor contacted by an electrolyte may develop a space charge region because:

- the surface states interact with the electrolyte and their charge is therefore changing,
- ions in the electrolyte inject or extract electrons to or from the energy levels of the semiconductor or
- a potential is applied between the semiconductor and a second electrode and charges up the interface.

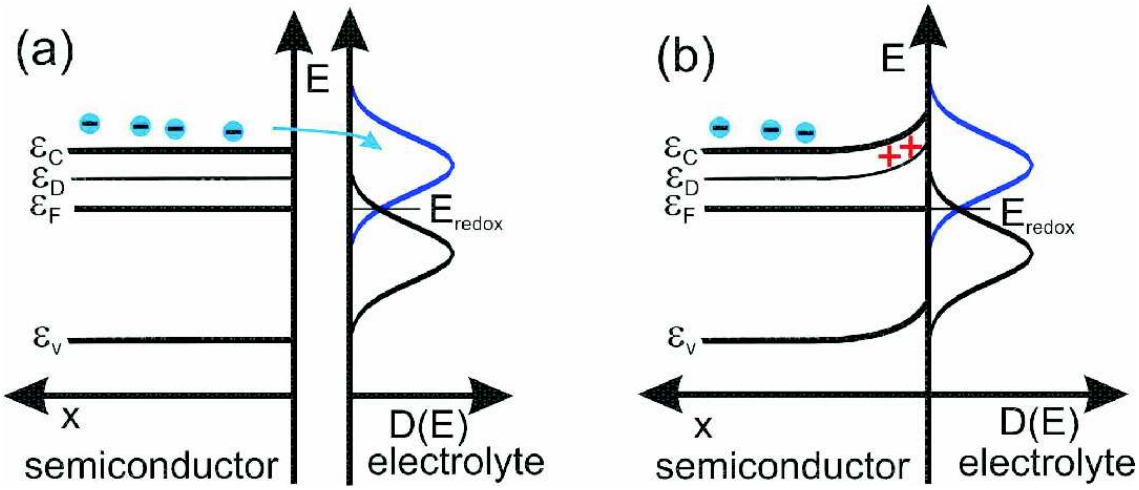

Fig. 1.3: *The formation of a space charge layer at the semiconductor/electrolyte interface due to electrons being extracted to the solution. The situation before contacting (a) and after contacting (b) of the semiconductor with electrolyte is shown. When contacting the semiconductor with electrolyte, the Fermi level of the semiconductor and the redox-potential of the electrolyte are equalized.*

The case for the ions extracting electrons from the conduction band of an n-doped semiconductor is shown in Figure 1.3. After the contact, the Fermi level of the semiconductor and the redox-potential of the electrolyte are aligned. Electrons can then be transferred from the conduction band to the metal ions in the electrolyte. A space charge layer is thus formed and the energy bands in the semiconductor are bent.
Four types of space charge layers can form in a semiconductor, as shown in Figure 1.4 for a n-doped semiconductor. The band bending as well as the concentration of the charge carriers are shown for each case. An accumulation layer is formed when the majority carriers (electrons for a n-doped semiconductor) are injected into the semiconductor from the surface forming a space charge layer. A depletion layer (or exhaustion layer) is formed if the majority carriers are extracted from the semiconductor in moderate amount. The inversion layer results also from the extraction of the majority carriers, but the majority carrier band (the conduction band for

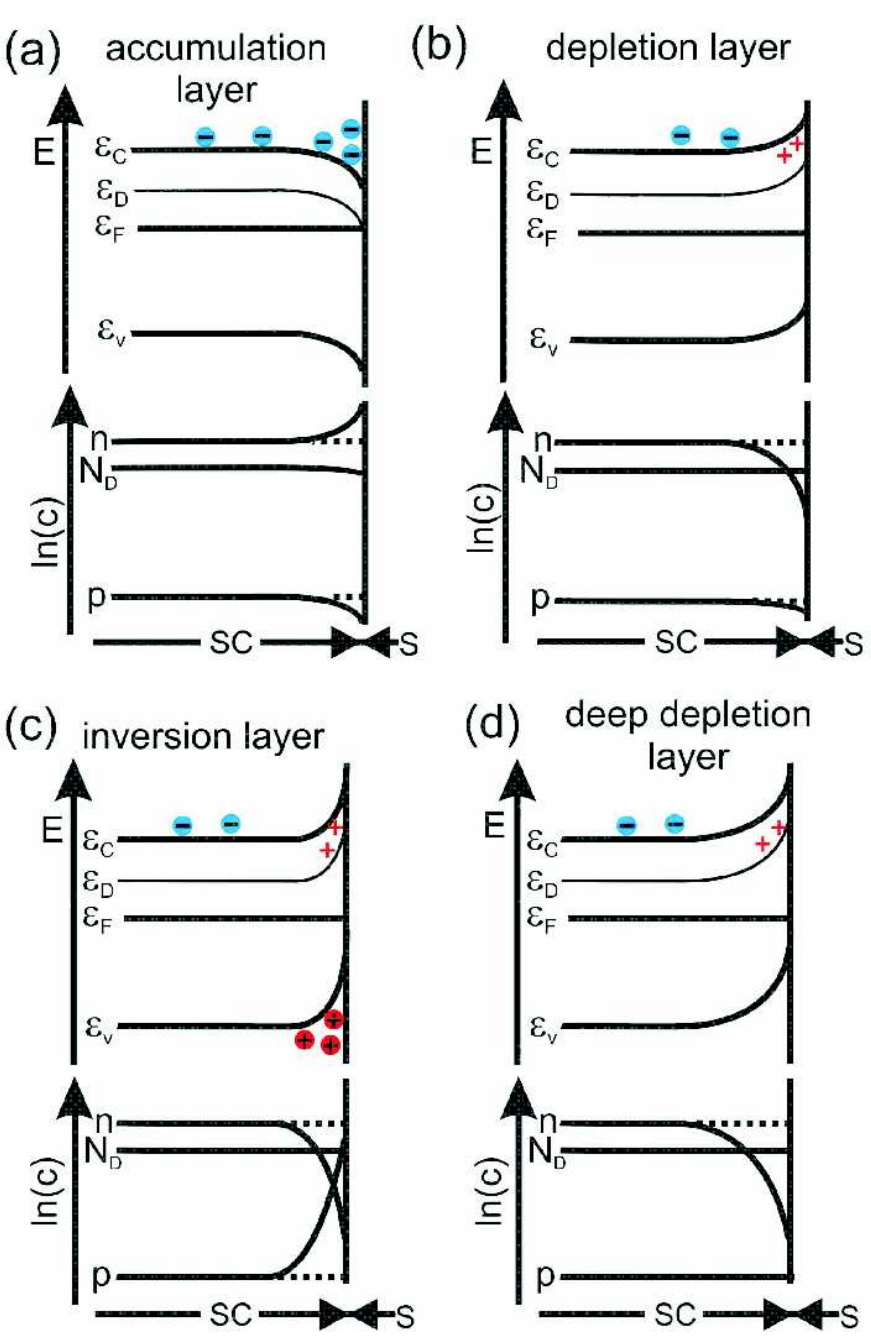

Fig. 1.4: *Four forms of space charge layers can be formed depending on the charge carrier concentration at the interface: the accumulation layer (a), the depletion layer (b), the inversion layer (c) and the deep depletion layer (d). The band structure close to the interface as well as the carrier concentration are shown for each case for a n-doped semiconductor. (SC=semiconductor, S=solution, n=concentration of electrons in the conduction band, p= concentration of holes in the valence band, N_D=concentration of ionized donors)*

a n-doped semiconductor) can not supply all the charge without excessive band bending. The carriers have to come from the minority band (the valence band in the case of n-doping). The semiconductor changes in the surface region from n-doped to p-doped (or inverse). A deep depletion layer is formed when the minority charge carriers are prevented from accumulating and thus an inversion layer can not be formed. The depletion layer is extended.
Any of these space charge layers can also be produced by applying a potential to the semiconductor electrode. For a negative potential $-\phi$ applied to the semiconductor, the Fermi level of the semiconductor is shifted by ϕ to higher energies with respect to the Fermi level of the electrolyte. The semiconductor is charged negatively and the energy bands will bend downward at the interface, resulting in an accumulation layer. Similarly, for a positive potential ϕ applied to the semiconductor, the semiconductor will be charged positively and the energy bands near the semiconductor/electrolyte bend upward, leading to an inversion (large ϕ) or depletion layer (small ϕ). The potential at which the space charge of the semiconductor is zero (all space charge is accumulated in the electrolyte) is called the flatband potential.

1.4 Electrodeposition

1.4.1 Charge transfer at a semiconductor/electrolyte interface

Three mechanisms are known for metal deposition at a semiconductor electrode [7], they are shown in Figure 1.5.

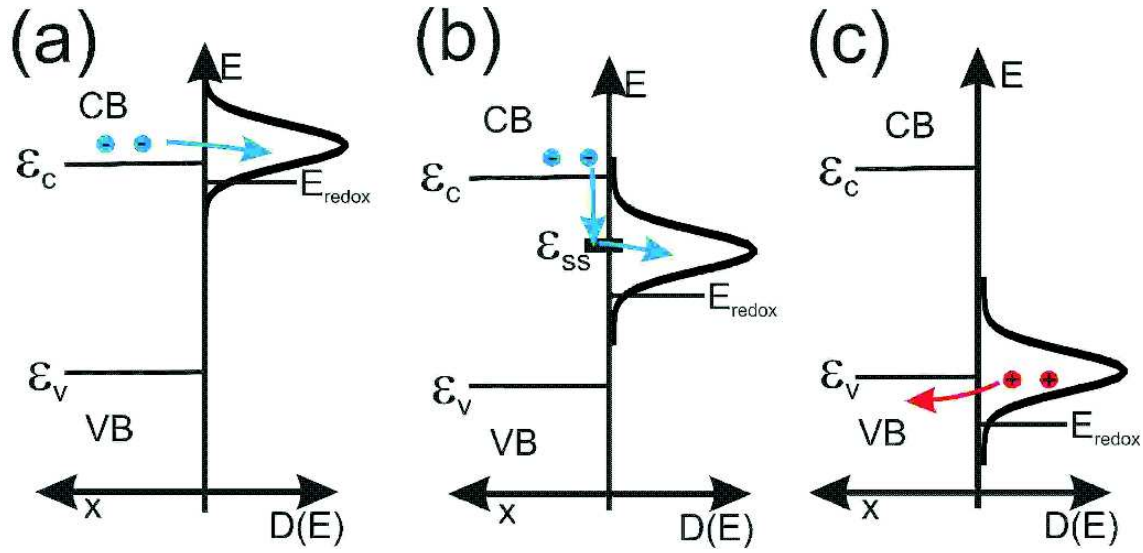

Fig. 1.5: *The three mechanisms for electrochemical metal deposition on a semiconductor electrode. A reduction of the metal ion involving surface states is possible (b). The metal ion can be reduced via the conduction(a) or the valence band(c).*

In Figure 1.5 (a) the reduction of the metal ions over the conduction band is shown. This mechanism takes place when the redox-potential of the metal is negative enough to overlap with the conduction band of the semiconductor. The second case [shown in Figure 1.5 (b)] is the transfer of the electrons via surface states. If the surface states are filled they can interact

as nucleation sites for the metal deposition. For surface states above the Fermi level electrons can be captured from the conduction band and then be transferred to the solution. The exact mechanism depends on the positions of the surface states and the applied potential (influencing the position of the conduction and valence bands at the surface via band bending). The third case, shown in Figure 1.5 (c), is the reduction of the metal ions via the valence band.

1.4.2 Nucleation and growth

The mode of growth for the deposition of a metal on a substrate depends on the interaction between the adsorbed metal atom and the substrate. Also the difference in interatomic spacing of the bulk metal phase and the substrate is influencing the growth mode. Three different modes of growth exist:

- layer-by-layer (Frank-van der Merwe growth)
- three-dimensional island formation (Volmer-Weber growth)
- two dimensional layer deposition followed by growth of 3D islands (Stranski-Krastanov growth)

Due to the weak interaction energy between an adsorbed metal atom and the semiconductor, deposition of metals on semiconductors normally proceeds in the three-dimensional island growth. The rate of the island growth during electrochemical deposition depends on the mechanism of nucleation and growth. It is assumed that nucleation for the deposition on a foreign substrate occurs at specific nucleation sites. If the rate of nucleation is fast compared to the rate of growth, nuclei are formed almost immediately at all possible growth sites and the nucleation is continuous. Otherwise, if the nucleation is slow, it will continue while other clusters are growing. Such a nucleation process is called progressive.

1.5 Cyclic voltammetry

An important electrochemical method relies on the current-potential measurements, the so-called voltammetry. The resulting current is measured while the potential of the working electrode with respect to the reference electrode is swept at a constant rate. Starting at an initial holding potential, the potential is increased in a linear manner up to a predefined limiting value. In the case of reversible systems, the sweeping direction can be reversed in both the upper and lower (not necessarily the starting) potential values, leading to a of triangular waveform of potential, thus this method is called cyclic voltammetry. This method is a fast and simple initial characterization of the redox-active system, including the space charge double layer, and can give information regarding the potential at which electrochemical processes occur. The shape of a cyclic voltammogram is determined by external parameters like the cycling speed and the concentration and mobility of species involved. Faradaic currents are the result of specific processes like adsorption, desorption, dissolution or redox reactions at the interface.

Chapter 2

Theory of X-Ray Scattering

X-ray diffraction (XRD) is nowadays the dominant technique for structure determination of crystals. However, due to the small scattering volume, the scattered intensity of a surface is about a million times less than the one scattered from a bulk crystal. This and the low scattering cross section leads to the need of synchrotron radiation sources. In most cases the kinematical scattering theory can be used to describe XRD. The large penetration depth of the X-rays, which is a result from the low scattering cross section, allows to study buried interfaces. XRD can be used in non-vacuum environments, which makes it possible to characterize solid/liquid or solid/gas interfaces, to which UHV surface techniques can not be applied. A brief review of X-ray scattering from crystalline structures and surfaces is given in this chapter. A more general introduction to X-ray diffraction of three dimensional samples and powders can be found in most solid state textbooks [24, 25, 26]. Some review articles are also available for an introduction and a general overview about surface X-ray diffraction (SXRD) [27, 28, 29] and its theoretical description.

2.1 X-Ray Diffraction from single crystals

X-ray diffraction can be described by the kinematical scattering theory (which is not the case for the scattering of electrons). This approach assumes that the incident beam is only diffracted once, without changing its energy and without interfering with the scattered beam. Inelastic scattering like Compton scattering only contributes to the background. For perfect, infinitely large single crystals this approach is not strictly valid close to the Bragg reflections (e.g. semiconductor single crystals at large incident and diffracted angles). However, for non-perfect crystals and grazing incidence the approach is valid. The crystal is described by its unit cell, spanned by the vectors $\vec{a}$, $\vec{b}$ and $\vec{c}$. The reciprocal space is then defined by the reciprocal lattice vectors:

$$\vec{u} = 2\,\pi\frac{\vec{b}\times\vec{c}}{V},\ \ \vec{v} = 2\,\pi\frac{\vec{c}\times\vec{a}}{V}\ \text{ and }\ \vec{w} = 2\,\pi\frac{\vec{a}\times\vec{b}}{V} \tag{2.1}$$

where V is the volume of the unit cell $V = \vec{a}\cdot(\vec{b}\times\vec{c})$. Similar to the lattice units (l.u.) used in real space ($|\vec{a}|$, $|\vec{b}|$ and $|\vec{c}|$) corresponding to the norm of the base vectors defining the real space, reciprocal lattice units (r.l.u.) are used in reciprocal space ($|\vec{u}|$, $|\vec{v}|$ and $|\vec{w}|$). In the case of GaAs(001) surfaces $\vec{w}$ and $\vec{c}$ are describing the out-of-plane lattice constant in reciprocal

and real space, respectively. This vectors are in this case parallel to the surface normal (z-direction). The incident monochromatic beam can be described by a wave with a wavelength λ and the wave vector $\vec{k}_i$ (with $|\vec{k}_i| = 2\pi/\lambda$). The diffracted beam has the wave vector $\vec{k}_f$ (with $|\vec{k}_f| = 2\pi/\lambda$). The difference between the two wave vectors $\vec{Q} = \vec{k}_f - \vec{k}_i$ defines the momentum transfer. Starting with the Thomson formula for the scattering from one single electron one can deduce the scattered intensity at each point in reciprocal space as the square of the structure factor

$$I(\vec{Q}) \propto |F(\vec{Q})|^2. \tag{2.2}$$

The structure factor is the Fourier transform of the electron density $\rho(\vec{r})$ in the crystal

$$F(\vec{Q}) = \int_V \rho(\vec{r}) \cdot \exp(i\,\vec{Q}\cdot\vec{r}) dV. \tag{2.3}$$

The electron density of a crystal is determined by the atomic distribution. Therefore the best way to calculate the structure factor is to replace the integral by a sum over all atoms and to integrate over each atom,

$$\rho(\vec{r}) = \sum_{j=1}^{N} \rho_j(\vec{r} - \vec{r}_j), \tag{2.4}$$

where $\rho_j(\vec{r} - \vec{r}_j)$ describes the electron density from the j-th atom. $\vec{r}_j$ is the vector pointing to the center of the j-th atom in the crystal and can be expressed in terms of the basic vectors of the unit cell

$$\vec{r}_j = x_j \cdot \vec{a} + y_j \cdot \vec{b} + z_j \cdot \vec{c} \tag{2.5}$$

The resulting structure factor is

$$I(\vec{Q}) \propto |\sum_{j=1}^{N} f_j(\vec{Q}) e^{(i\cdot\vec{Q}\cdot\vec{r}_j)}|^2 = |\sum_{j=1}^{N} f_j(\vec{Q}) e^{(i\cdot\vec{Q}\cdot(x_j\cdot\vec{a}+y_j\cdot\vec{b}+z_j\cdot\vec{c}))}|^2, \tag{2.6}$$

with

$$f_j(\vec{Q}) = \int_V \rho_j(\vec{R}) \exp(i\vec{Q}\cdot\vec{R}) dV \tag{2.7}$$

where $\vec{R} = \vec{r} - \vec{r}_j$ and $f_j(\vec{Q})$ is the Fourier transform of the electron density of one atom, the so called atomic form factor. By replacing the sum over all atoms in the crystal in Equation 2.6 by the sum over all atoms in the cell and the sum over all unit cells (assuming the crystal having the shape of a parallelepiped with N_1, N_2 and N_3 unit cells in the respective directions), the intensity factor can be expressed as

$$I(\vec{Q}) \propto \left| \sum_{n_1=0}^{N_1-1} \sum_{n_2=0}^{N_2-1} \sum_{n_3=0}^{N_3-1} \sum_{j=1}^{N} f_j(\vec{Q}) e^{i\cdot\vec{Q}\cdot(\vec{r}_j+n_1\cdot\vec{a}+n_2\cdot\vec{b}+n_3\cdot\vec{c})} \right|^2 \tag{2.8}$$

$$= \left| \sum_{n_1=0}^{N_1-1} \sum_{n_2=0}^{N_2-1} \sum_{n_3=0}^{N_3-1} e^{i\vec{Q}(n_1\cdot\vec{a}+n_2\cdot\vec{b}+n_3\cdot\vec{c})} \right|^2 \times \left| \sum_{j=1}^{N} f_j(\vec{Q}) e^{(i\cdot\vec{Q}\vec{r}_j)} \right|^2 \tag{2.9}$$

$$= \left| \frac{\sin(\frac{1}{2}\,N_1\vec{Q}\vec{a})}{\sin(\frac{1}{2}\,\vec{Q}\vec{a})} \cdot \frac{\sin(\frac{1}{2}\,N_2\vec{Q}\vec{b})}{\sin(\frac{1}{2}\,\vec{Q}\vec{b})} \cdot \frac{\sin(\frac{1}{2}\,N_3\vec{Q}\vec{c})}{\sin(\frac{1}{2}\,\vec{Q}\vec{c})} \right|^2 \times \left| F_{unitcell}(\vec{Q}) \right|^2 \tag{2.10}$$

$$= \left| G(\vec{Q}) \right|^2 \times \left| F_{unitcell}(\vec{Q}) \right|^2, \tag{2.11}$$

where $\left|G(\vec{Q})\right|^2$ is the interference function. In Equation 2.10 we applied the geometric progression $\sum_{n=0}^{N-1} a^n = \frac{1-a^N}{1-q}$ and the relation $e^{i\cdot\theta} = \cos\theta + i\cdot\sin\theta$. In Figure 2.1 we calculated

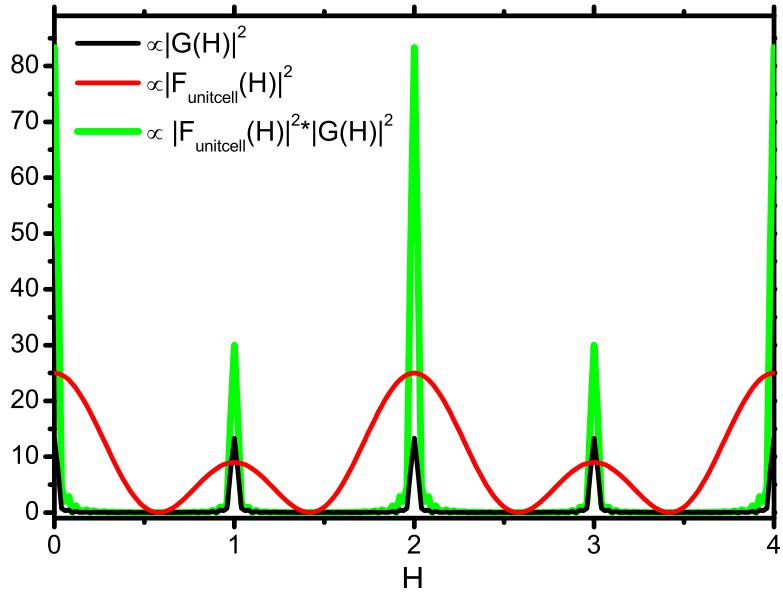

Fig. 2.1: *The interference function of a small crystal (black line) and the square of the structure factor of the crystal (red line) with two different atoms in one unit cell are shown. The measured intensity correspond to the product of both, which is drawn as green line.*

$|G(\vec{Q})|^2$, $\left|F_{unitcell}(\vec{Q})\right|^2$ and their product for a one-dimensional unit cell of two atoms at x=0 and at x=1/2 l.u.. The interference function $|G(\vec{Q})|^2$, reflecting the periodic distribution of the atoms in the crystal, gives rise to the diffraction pattern with discrete intensity spots in reciprocal space, the Bragg reflections. The positions of these spots, which are a function of $\vec{Q}$, can be described equivalently with integer H, K and L by the Laue equations

$$\vec{Q}\cdot\vec{a} = 2\,\pi\,H,\;\; \vec{Q}\cdot\vec{b} = 2\,\pi\,K \text{ and } \vec{Q}\cdot\vec{c} = 2\,\pi\,L, \tag{2.12}$$

the Ewald construction

$$\vec{Q} = H\cdot\vec{u} + K\cdot\vec{v} + L\cdot\vec{w} \tag{2.13}$$

and the Bragg condition

$$2d_{hkl}\sin\Theta = n\cdot\lambda \tag{2.14}$$

where Θ is half of the angle beween the vectors $\vec{k}_i$ and $\vec{k}_f$ and the parameter n is a positive integer number. The Bragg reflections are indexed in reciprocal space by the integer numbers H, K and L, the so-called Miller indices. Each Bragg reflection can be interpreted as the diffraction from the corresponding lattice planes in real space (perpendicular to the vector $\vec{Q}$ in reciprocal space) with the lattice spacing (assuming an orthorhombic unit cell)

$$d_{hkl} = \frac{1}{\sqrt{\left(\frac{H}{a}\right)^2 + \left(\frac{K}{b}\right)^2 + \left(\frac{L}{c}\right)^2}}, \tag{2.15}$$

where a, b and c are the norms of the vectors $\vec{a}$, $\vec{b}$ and $\vec{c}$ defining the unit cell in real space respectively. The relative intensities of the Bragg peaks are determined by the structure factors of the unit cell and therefore reflect the atomic distribution in one unit cell.

2.1.1 Crystal size effects

The interference function is derived as the sum over all unit cells. Its shape depends on the crystal size in each direction. The square of the interference function in the H-direction for

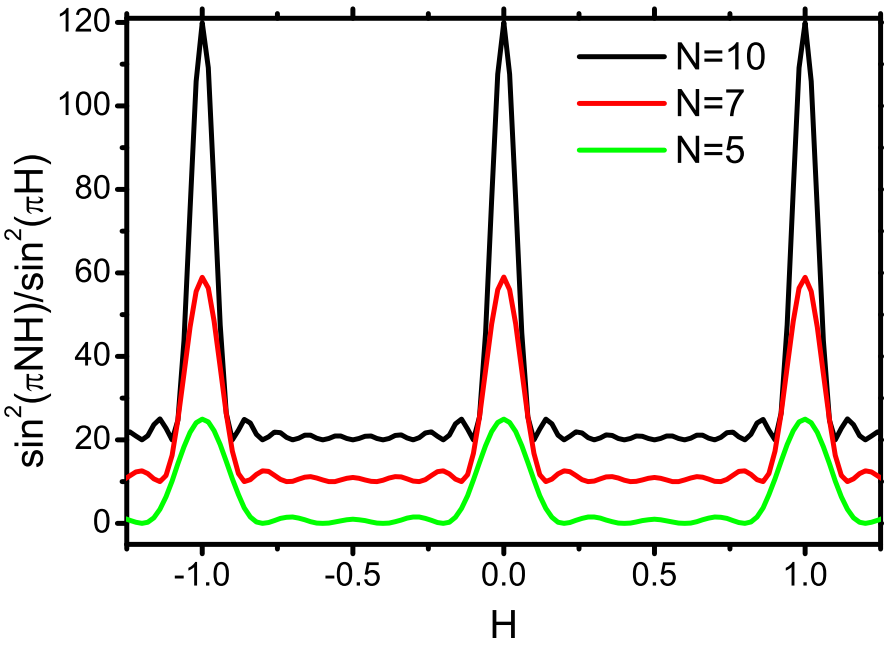

Fig. 2.2: *The square of the interference function determining the peak-width in the H-direction is shown for different crystal sizes (N=5, N=7 and N=10).*

different crystal sizes is shown in Figure 2.2. The Bragg peaks are broadened due to the finite size of the crystal. The peak height is proportional to the volume square of the crystal and the peak width is inversely proportional to the crystal width in real space in the respective direction. If ΔH is the peak width measured in reciprocal space, the corresponding crystal size ΔX in real space along the $\vec{a}$-axis is

$$\Delta X = \frac{a}{\Delta H}. \tag{2.16}$$

A detailed line-shape analysis of the Bragg reflections can therefore give information about the dimensions of the diffracting crystal, which is especially of interest when studying crystal growth. Furthermore strain and defects as well as mosaicity can affect the peak widths. In addition the instrumental broadening has to be taken into account when analyzing the width of Bragg peaks. In Equation 2.11, the relative integrated peak intensities of the Bragg reflections are proportional to the square of the structure factor of the unit cell and do not depend on $\left|G(\vec{Q})\right|^2$.

2.1.2 Debye-Waller factor

The thermal vibration as well as static disorder averaged over the diffracting part of the crystal are taken into account by the so-called temperature, Debye-Waller or atomic displacement factor. The last expression is the recommended one, as it points out that not only thermal vibrations but also static displacements are considered. The atomic motion and static disorder lead to a larger decrease of the peak intensity with increasing $|\vec{Q}|$. Accordingly the atomic displacement factor for an atom j can be written as $e^{-1/(4\pi)^2 \cdot B_j \cdot \vec{Q}^2}$, where $B_j = 8 \cdot \pi^2 \langle (x_j - \bar{x}_j)^2 \rangle$. In a first approximation an isotropic atomic displacement factor can be chosen (B_j is a scalar). For further refinements especially for surface atoms, an anisotropic atomic displacement factor has to be considered, $e^{-1/(4\cdot\pi)^2 \cdot \vec{Q}^T B_j \cdot \vec{Q}}$ (where B_j is a tensor). The structure of the unit cell takes then the form

$$F_{unitcell}(\vec{Q}) = \sum_{j=1}^{N} f_j(\vec{Q}) e^{-\frac{1}{(4\cdot\pi)^2} \cdot \vec{Q}^T B_j \cdot \vec{Q}} e^{(i \cdot \vec{Q} \vec{r}_j)}. \tag{2.17}$$

2.2 X-Ray diffraction from surfaces

A diffracting surface gives rise to crystal truncation rods (CTR's) in addition to the bulk Bragg reflections. These rods have their origin in the truncation of crystal at the surface. Due to the broken translational symmetry in the z-direction the intensity between the Bragg reflections is not fully extincted. Assuming a perfectly flat bulk terminated surface the intensity distribution perpendicular to the surface can be calculated as

$$I_\perp(Q) \propto \left| \sum_{n=-\infty}^{0} e^{i \cdot n \cdot \vec{Q} \cdot \vec{c}} e^{-n\nu} \right|^2 \times \left| F_{unitcell}(\vec{Q}_\perp) \right|^2 \tag{2.18}$$

$$= \left| \frac{F_{unitcell}(\vec{Q})}{1 - e^{-\nu} e^{i\vec{Q}\cdot\vec{c}}} \right|^2 = \frac{|F_{unitcell}|^2}{(1-e^{-\nu})^2 + 4e^{-\nu} \sin^2(\frac{\vec{Q}\vec{c}}{2})}, \tag{2.19}$$

where the limit of the geometric progression $\sum_{n=0}^{N} q^n = (q^{N+1} - 1)/(q-1) \overset{N\to\infty}{\longrightarrow} 1/(1-q)$ is used. In addition, an attenuation factor ν is introduced to take into account the absorption of the X-ray beam by the crystal and to permit the sum to converge at the Bragg reflections. This attenuation can be calculated as a function of the crystal material and the incident angle and is of the order of $\nu \approx 10^{-4}$. Absorption has only an effect near the Bragg peaks (having a contribution from the bulk) and can be neglected for regions where the diffracted intensity purely arises from the surface

$$I_\perp(\vec{Q}) \propto \frac{\left| F_{unitcell}(\vec{Q}) \right|^2}{4 \cdot \sin^2(\frac{\vec{Q}\vec{c}}{2})}. \tag{2.20}$$

The intensity distribution perpendicular to the surface is shown in Figure 2.3 (black line) at the position of an in-plane Bragg reflection (H and K integer). The other two intensity distributions (red and green lines) in this figure will be discussed later in this section.
For integer L (at the position of the Bragg reflections) the intensity is large. Between two Bragg reflections at L=n+0.5 (n integer) the intensity has its minimum. These are the so-called anti-Bragg positions. In Figure 2.3 only the contribution from the surface truncation is shown. In

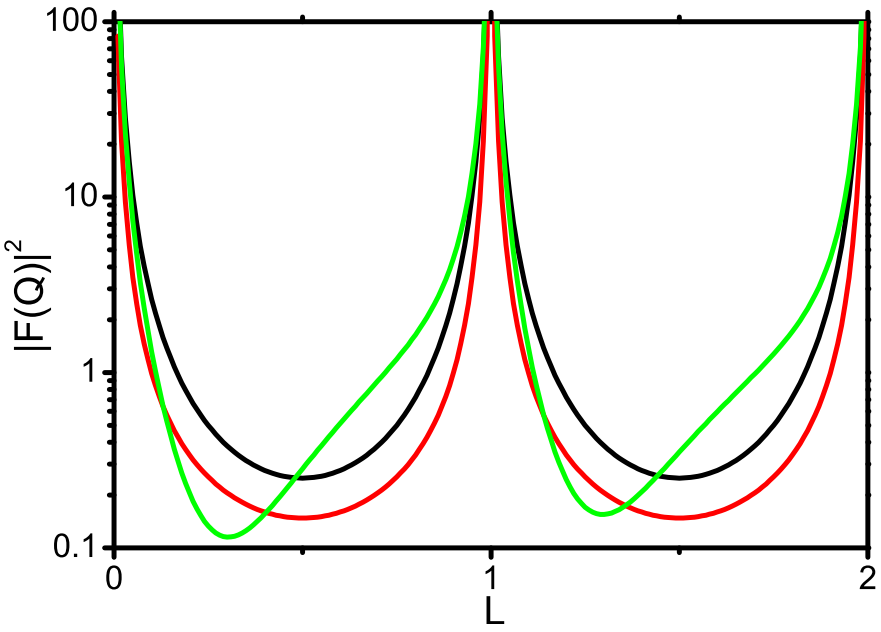

Fig. 2.3: *The CTR of a smooth terminated crystal is drawn as black line. In comparison the CTR's for a rough surface (red line) and a relaxed surface (green line) are drawn.*

addition, the structure factor from the crystal unit cell can affect the intensity distribution, e.g. by extinction rules. In general, a crystal is not terminated by a perfectly flat surface but relaxation and reconstruction (see Section 3.1) can affect the surface structure. Often the rougheness of the surface has to be also taken into account. The structure factor of the whole crystal is then the sum of the surface structure factor and the bulk structure factor

$$F_{crystal}(\vec{Q}) = F_{bulk}(\vec{Q}) + F_{surface}(\vec{Q}), \tag{2.21}$$

where

$$F_{bulk}(\vec{Q}) == \frac{|F_{bulk\_unitcell}|^2}{(1-e^{-\nu})^2 + 4e^{-\nu}\sin^2(\frac{\vec{Q}\vec{c}}{2})} \tag{2.22}$$

and

$$F_{surface}(\vec{Q}) = \frac{F_{surface\_super\_structure\_cell}(\vec{Q})}{A_{surface\_super\_structure\_cell}}. \tag{2.23}$$

$A_{surface\_super\_structure\_cell}$ is the area of the super structure unit cell. The intensity in reciprocal space is proportional to the square of $|F_{crystal}(\vec{Q})|^2$,

$$I(\vec{Q}) \propto |F_{crystal}(\vec{Q})|^2 = |F_{bulk}(\vec{Q}) + F_{surface}(\vec{Q})|^2. \tag{2.24}$$

For a relaxed surface the position of the Bragg peaks does not change. However the intensity distribution of the rod depends on the detailed surface structure, e.g. the amount of relaxation. The change of a CTR due to a relaxation of the first atomic layer is shown in Figure 2.3.
For a reconstructed surface, the surface unit cell is a multiple of the bulk-unit cell. Superstructure rods at non integer H and K (depending on the nature of the reconstruction) occur in

reciprocal space due to the larger surface periodicity, e.g, a (2×1) reconstructed surface will give rise to superstructure rods at H=n+1/2 (with n integer). The crystal truncation rods at integer H and K can still be observed, but they are modified with respect to those for the bulk terminated surface due to the reconstructed surface layer. The super structure rods contain no bulk contribution but only information of the surface structure. The variation of the intensity along the fractional order rods depends on the thickness of the reconstructed surface layer.
The roughness of a surface is caused by missing atoms in the first atomic layers. To take into account this effect, an occupancy θ_j per atom/layer is introduced. The surface structure factor is then written as

$$F_{surface}(\vec{Q}) = \sum_j f_j \ \theta_j e^{-\vec{Q}^T B_j \cdot \vec{Q}} e^{i\vec{Q}\cdot\vec{r}_j}. \tag{2.25}$$

Different roughness models exist for different height variations of θ_j. Assuming an exponential roughness model with an occupancy of the first layer equal β, the second layer β^2 etc., the total structure factor for a cubic lattice is found to be [30]

$$F_{rough}(\vec{Q}) = \frac{1-\beta}{\sqrt{1+\beta^2-2\beta\cdot\cos(2\cdot\pi\cdot c\cdot L)}} \cdot F_{crystal}(\vec{Q}). \tag{2.26}$$

The CTR of a rough surface (β=0.3) is drawn in Figure 2.3 as a red line. The roughness leads to a decrease in intensity between the Bragg reflections.
A so-called specular CTR has no in-plane component (H=0, K=0) and depends only on the atomic positions in the surface normal direction. A non-specular CTR has an additional dependence on the integer values of H and K (satisfying the Laue diffraction conditions). These CTR's are sensitive also to the in-plane atomic positions.

It is convenient to express surface roughness as a root-mean-square elevation of the surface contour, σ_{rms}. The β values can be converted into σ_{rms}

$$\sigma_{rms} = \frac{\sqrt{\beta}}{(1-\beta)} \cdot d_\perp, \tag{2.27}$$

where $d_\perp$ is the lattice spacing perpendicular to the surface.

2.2.1 Patterson function

A method for direct imaging of the interatomic distances is the so called Patterson map [31, 32], which is defined as the autocorrelation function of the electron density

$$P(\vec{r}) = \int_V \rho(\vec{r}') \cdot \rho(\vec{r}+\vec{r}') d^3\vec{r}' \tag{2.28}$$

Replacing the electron density by its Fourier series

$$\rho(\vec{r}) \propto \sum_{H,K,L} F_{HKL} e^{-2\pi\ i(H\cdot x+K\cdot y+L\cdot z)}, \tag{2.29}$$

one obtains for the Patterson function

$$P(\vec{r}) = \sum_{H,K,L} |F_{HKL}|^2 cos[2\pi(H\cdot x+K\cdot y+L\cdot z)]. \tag{2.30}$$

When only in-plane structure factors are available, often a two-dimensional Patterson map, the projection of the Patterson map along the z-axis onto the surface, is used in surface X-ray diffraction

$$P(x,y) \propto \sum_{H,K} |F_{HK}(L=0)|^2 \cos[2\pi(H\cdot x + K\cdot y)]. \tag{2.31}$$

This map can be directly calculated from the measured in-plane structure factors. As the Patterson map is the autocorrelation function of the electron density, each vector pointing from the origin to one of the maxima of the Patterson function corresponds to an interatomic vector of the structure. To avoid the domination of the bulk structure (which is often known and of less interest) and to obtain information about the surface structure, only the fractional order peaks are included in the calculation.

2.3 Scans in reciprocal space

In order to characterize the epitaxy and morphology of a crystalline sample, four explicit scans along special directions in reciprocal space are often used:

Radial scan The radial scan is directed parallel or nearly parallel to the scattering vector $\vec{Q}$ of a particular reciprocal-lattice point. An in-plane radial scan is directed parallel to the in-plane component $\vec{Q}_{\|}$ of the scattering vector $\vec{Q}$.

Specular scan A particular case of a radial scan is the specular scan, which is directed parallel to the surface normal. This scan corresponds to a scan along the [00L]-axis in reciprocal space.

Rod scan A rod scan is directed parallel to the surface normal with the in-plane compound of the scattering vector $\vec{Q}_{\|}$ non zero.

Rocking scan The angular or rocking scan rotates the sample at a constant $\vec{Q}$. In this work, rocking scans are (limited by the diffractometer geometry) in-plane rocking scan with the sample being rotated about the surface normal.

Chapter 3

GaAs(001) surfaces

In this chapter a first overview about the relaxation and reconstruction of metal and semiconductor surfaces and interfaces is given. Then the GaAs compound semiconductor and its (001) surface are presented. A short overview of the c(4×4), the (2×4)/c(2×8) and the (4×2)/c(8×2) surface structures observed on GaAs(001) is given. The surface passivation technique of the GaAs(001) surface by amorphous arsenic is introduced. Finally, former studies of copper deposited on GaAs surfaces are shortly reviewed.

3.1 Relaxation and reconstruction of surfaces

On a surface or interface the interactions of the atoms in the topmost and the adjacent layers are modified compared to the bulk atoms. The reduced number of neighbouring atoms introduces a new equilibrium configuration, which minimizes the surface free energy and results in rearrangement and displacement of the atoms close to the surface. This can be achieved by two processes, relaxation or reconstruction. Both processes may occur on clean surfaces in UHV, but also the adsorption of atoms may introduce a rearrangement of the atomic positions in the first atomic layers.

3.1.1 Relaxation

The atomic rearrangements can be a compression or expansion of the first atomic layer as a whole in the surface normal direction, the so called surface relaxation. No in-plane changes introducing a different layer periodicity parallel to the surface occur. In UHV, single crystal metal surfaces are often found to relax with the first atomic layer contracted towards the second atomic layer, whereas at metal/electrolyte interfaces the first atomic layer is often retracted from the sub-layers. STM is not sensitive to surface relaxations. However, they can be studied with surface X-ray diffraction by recording the crystal truncation rods, especially the specular rod is sensitive to atomic displacements in the direction of the surface normal.

3.1.2 Reconstruction

The rearrangements of the atoms in the first atomic layers can result in an atomic displacement in the surface plane, changing the surface periodicity, and a simultaneous relaxation. This

process is called surface reconstruction. The symmetry parallel to the surface is lower than the symmetry of the bulk structure. Accordingly, surface reconstructions can be observed by STM, as well as by LEED and surface X-ray diffraction. On semiconductor surfaces, reconstructions arise as the direct chemical bonds normally holding together the bulk atoms are broken on the surface, creating dangling bonds. The surface atoms of a semiconductor are repositioning themselves to saturate these bonds under the following conditions [33, 34, 35]:

- The new surface structure has the lowest free-energy kinetically accessible under the given conditions.
- No net charge accumulates on the surface (autocompensation).
- The atomic rearrangement is determined by the lowering of the surface state bands via either surface bonds or filled anion dangling bonds.

The autocompensation is also called the electron counting model.

3.1.3 The electron counting model

The electron counting model is especially important for polar surfaces of semiconductor compounds. Only structures are formed introducing filled dangling-bond valence states and empty dangling-bonds conduction states. The thus resulting ideal surface is non-metallic with a band gap at the surface. To determine in practice an allowed surface reconstruction the electrons of one unit cell must be counted. If the number of electrons needed to fill all the bonds is equal to the total number of available electrons from the atoms forming the reconstruction, the structure is allowed. A concrete example is given in Ref. [36]. For GaAs(001) surfaces [and also InP(001) surfaces] this model works well, however other compound semiconductors (like antimony and nitrogen based semiconductors) are known to violate the electron counting model.

3.2 The GaAs(001) surface

GaAs is a semiconductor with a zinc-blende structure, with a lattice constant of 5.65 Å. The zinc-blende structure consists of two face-centered cubic lattices (one of arsenic, one of gallium), displaced by (1/4, 1/4, 1/4) of one unit cell one against another (Figure 3.1).
As can be seen from Figure 3.1, in the [001]-direction the atomic planes are alternately occupied by gallium and arsenic. A monolayer on GaAs(001) corresponds to a 2.82 Å thick bi-layer. The (001)-surface is a polar surface terminated either by arsenic or by gallium that forms a 3.98 Å square 1×1 lattice when unreconstructed. Therefore, it is more convenient to describe the GaAs(001) surface by surface coordinates. These are rotated by 45° about the z-axis compared to the bulk coordinates. The bulk GaAs cell a=b=c=5.64 Å ($\alpha=\beta=\gamma=90°$), is leading to a GaAs(001) surface cell with a=b=3.98 Å and c=5.64 Å ($\alpha=\beta=\gamma=90°$). In Figure 3.2 the bulk terminated GaAs(001) surface is shown. The basic vectors in the surface plane are shown for a bulk unit cell ($\mathbf{a}_b$ and $\mathbf{b}_b$) as well as for a surface unit cell ($\mathbf{a}_s$ and $\mathbf{b}_s$). The transformation matrix from surface to bulk coordinates in real space is :

$$\begin{pmatrix} X \\ Y \end{pmatrix}_{(bulk)} = \begin{pmatrix} 1 & 1 \\ -1 & 1 \end{pmatrix} \cdot \begin{pmatrix} X \\ Y \end{pmatrix}_{(surface)} \tag{3.1}$$

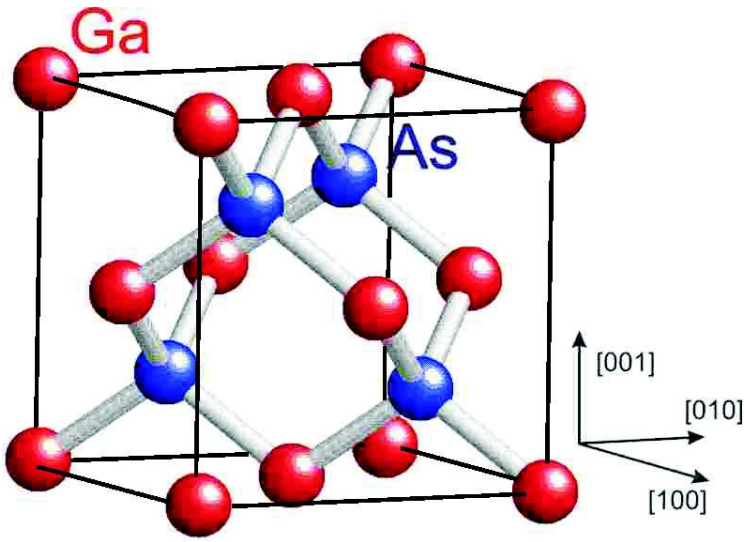

Fig. 3.1: *A GaAs bulk unit cell (zinc-blende) with the gallium atoms drawn as red balls and the arsenic atoms as blue balls. The basic vectors of the bulk unit cell are indicated.*

The inverse transformation matrix is:

$$\begin{pmatrix} X \\ Y \end{pmatrix}_{(surface)} = \begin{pmatrix} \frac{1}{2} & -\frac{1}{2} \\ \frac{1}{2} & \frac{1}{2} \end{pmatrix} \cdot \begin{pmatrix} X \\ Y \end{pmatrix}_{(bulk)} \tag{3.2}$$

If not stated otherwise, surface coordinates are used in this work.

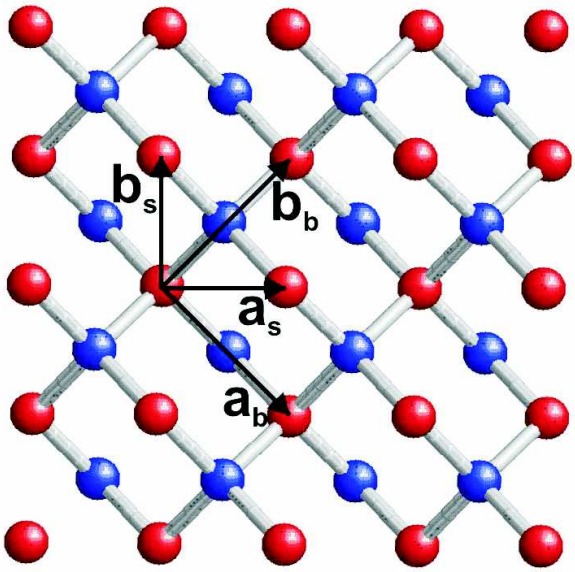

Fig. 3.2: *The GaAs(001) surface is shown with the basic vectors for a bulk unit cell ($\boldsymbol{a}_b$ and $\boldsymbol{b}_b$) and the basic vectors for a surface unit cell ($\boldsymbol{a}_s$ and $\boldsymbol{b}_s$).*

3.2.1 GaAs(001) reconstructed surfaces

The polar nature of the GaAs(001) surface gives rise to a wide range of reconstructions depending on the arsenic/gallium ratio on the surface. These reconstructions can be formed by MBE varying the As-flux on the surface and the temperature of the substrate. A higher arsenic flux tends to the formation of a more arsenic rich surface whereas a higher substrate temperature forms a more gallium rich surface. The structure changes from the most As-rich c(4×4) phase over (2×4)/c(2×8) to the gallium-rich phases (3×1), (4×2)/c(8×2) to several (n×6) phases.

GaAs(001)-c(4×4)

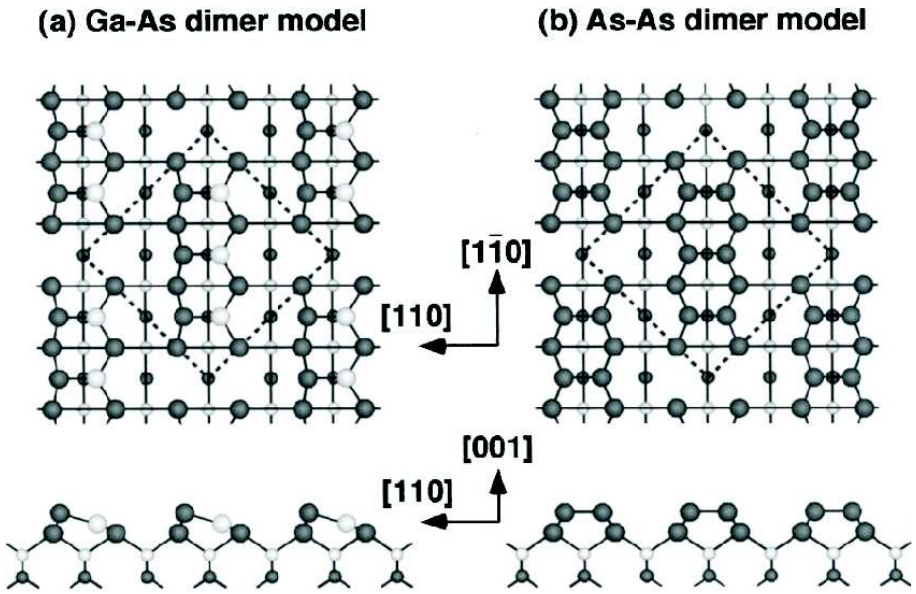

Fig. 3.3: *The top and side views of the α (Ga-As dimer) and β (As-As dimer) phases of the As-rich GaAs(001)-c(4×4) surface. Grey circles are As-atoms, white circles are Ga-atoms [37].*

Two c(4×4) phases exist as shown in Figure 3.3 [37]. One structure is stabilized at temperatures below 400°C (under arsenic flux), the c(4×4)β surface [Figure 3.3 (b)] consisting of three As-As dimers. The structure was analyzed by LEED structural analysis [38, 39]. The other phase, the c(4×4)α [Figure 3.3 (a)], is observed in a temperature range of 400-700°C under arsenic flux. It was resolved by element specific surface X-ray diffraction [40] and LEED structural analysis [39]. It consists of three arsenic-gallium heterodimers on the surface. A diverse combination of As-As dimers and Ga-As heterodimers are present in the transition region of the two phases.

GaAs(001)-(2×4)/c(2×8)

The GaAs(001)-(2×4)/c(2×8) surface is technologically the most important one as it is used for growing high quality epi-layers for opto-electronic devices. Four different models, which

are consistent with the electron counting model, were proposed and are shown in Figure 3.4.

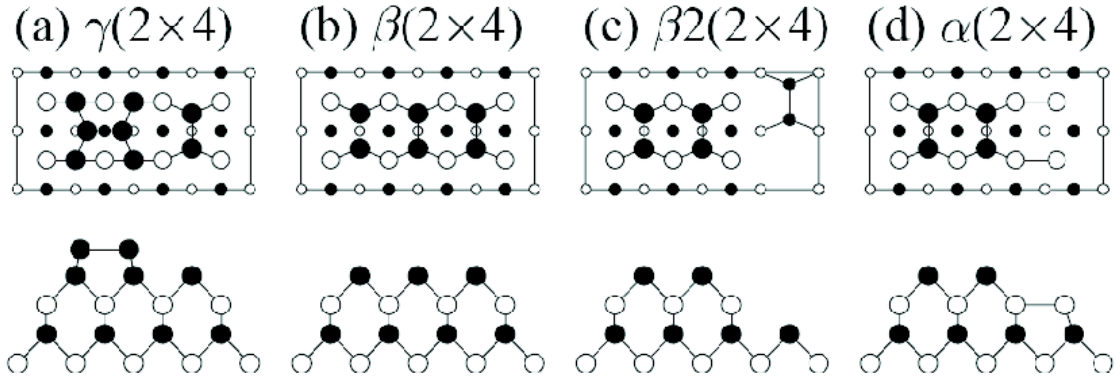

Fig. 3.4: *The four models proposed for the (2×4) reconstructed GaAs(001) surface. From the γ phase over the β and $\beta 2$ phases to the α phase the arsenic concentration on the surface is decreasing slightly. [41]*

They differ slightly in the arsenic concentration on the surface. The structure of the (2×4) surface reconstruction was studied by combinations of RHEED [42, 43], STM [41, 42, 43, 44], LEED [44] and surface diffraction [45, 46, 47], the surface structure was also investigated theoretically by first principles calculations [41, 48] and density-functional theory [44]. An overview about the investigation of the (2×4)/c(2×8) surface structure is given by LaBella et al. [36]. The well-ordered GaAs(001)-(2×4) is best described by the $\beta 2$ model. However, spontaneous island formation or roughening seems to introduce α (more explicitly $\alpha 2$ [45]) phase like structures on the surface [45, 46]. In contrast, the γ(2×4) phase seems to be a mixture of the c(4×4) and the $\beta 2$(2×4) structure [46, 49]. Especially surface kinks and defects, like arsenic ad-atoms or missing arsenic atoms, are introducing disorder on the surface, leading to a non perfect (2×4) structure with as a mixture of the α and $\beta 2$ phases and/or a mixture of the γ and $\beta 2$ phases. Also the displacement of the (2×4) unit cells in the [010]-directions is leading to a non perfect ordered surface with defects. The amount of defects and kinks on the surface can be controlled by the preparation conditions.
The coexistence of the (2×4) and c(2×8) structure is due to the displacement of the (2×4) unit cell in the [100]-direction by half the reconstruction unit cell. This displacement does not introduce any disorder as the dimer rows are running smoothly in the [100]-direction, but is leading to a diffuse broadening of the half order reconstruction peaks in the 2×- (H-) direction. These peaks are getting too broad to be observed by LEED, RHEED or surface diffraction, which leads to an additional constraint in the surface structure determination by diffraction methods.

GaAs(001)-(4×2)/c(8×2)

Several models for the (4×2)/c(8×2) structure were proposed [50, 51, 52]. Finally, a model explaining the (4×2) reconstructions on metal-rich III-V semiconductor (001)-surfaces was developed from surface X-ray diffraction [53, 54], also explaining the GaAs(001)-(4×2)/c(8×2) surface structure [54]. The proposed surface model is shown in Figure 3.5. It is based on sub-

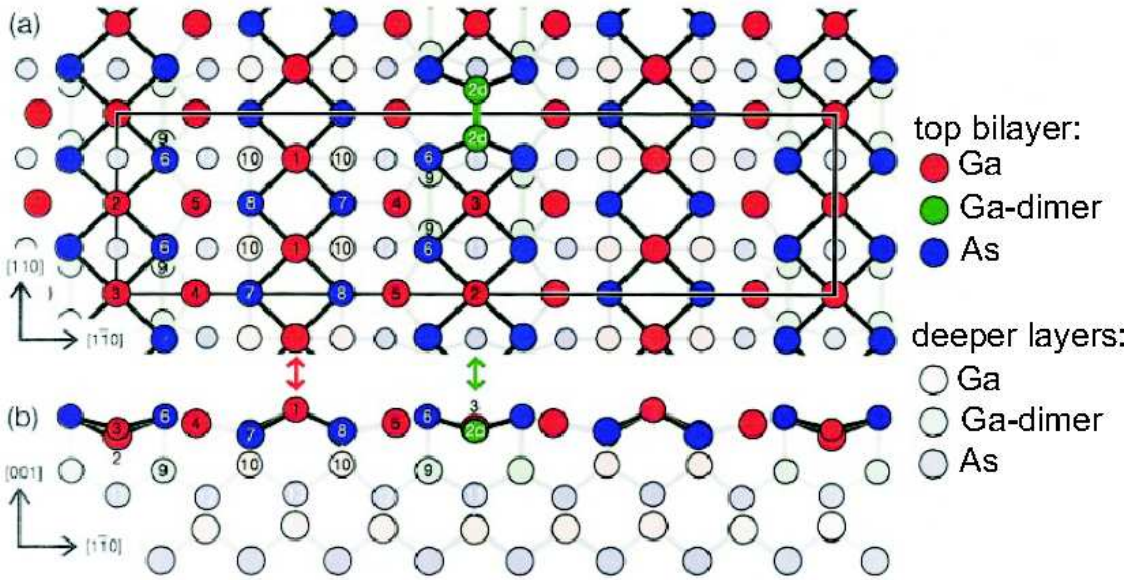

Fig. 3.5: *The surface model for the (4×2)/c(8×2) reconstructed (001) surfaces of III-V semiconductors. The Atoms 2d (the subsurface dimers) in the Figure have an occupancy of 63%, the atom labeled 1 has an occupancy of 19% for a GaAs surface. The Sites 2 and 3 are not occupied for GaAs.[53]*

surface dimerization of group III atoms (Atom 2d in Figure 3.5) with an occupancy of 63% on the GaAs surface, in the second bilayer. The surface layer consists of linear chains of atoms on non-bulk like sites along the [100]-direction. Site 1 has an occupancy of 19% on the GaAs(001) surface. The Sites 2 and 3 in Figure 3.5 are not occupied for GaAs. The subsurface dimerization explains the difficulties to resolve this structure by STM.

3.2.2 Surface passivation of GaAs(001) by amorphous As

GaAs-surfaces are sensitive to oxygen [55]. In order to be able to transfer the GaAs wafer through air without contamination or oxidation, the As passivation technique was developed [56]. An amorphous arsenic (α-As) layer is immediately deposited on top of the MBE grown GaAs, in order to prepare the arsenic cap. The arsenic cap is deposited by cooling down the samples in an As-flux from an As_2 cracker cell for two hours. An arsenic cap layer preparation with As_4 is possible but results in a rougher GaAs(001) surface.
This cap is protecting the GaAs(001) surface from oxidation during transfer through air. After several month of storage in atmosphere, arsenic caps show As_2O_3 crystallites on their top [56]. These crystallites are desorbed by thermal annealing up to 160°C. The arsenic cap desorbes at about 350°C. The different reconstructions observed on GaAs(001) by MBE preparation can also be obtained by thermal annealing of an α-As/GaAs wafer in UHV [57]. The surface structure depends on the temperature the wafer is heated to. This preparation is not reversible as it consists in dissolving the arsenic from the surface. Also the disorder on the surface is often higher [especially for the As-rich (2×4) reconstruction] than for MBE prepared surfaces as the temperatures are lower and therefore the surface atoms are less mobile. However, high

ordered reconstructed surfaces can be obtained, but need the exact knowledge of the preparation conditions.
The GaAs samples used to prepare the surfaces for this work were as prepared GaAs/As. The samples were prepared at the University of Trondheim in the group of B.O. Fimland.

3.3 Cu on GaAs(001)

Previous studies of the Cu electrodeposition on (n- and p-type) GaAs(001)-surfaces were carried out by scanning probe techniques [58, 59], X-ray diffraction [13, 14] as well as X-ray absorption fine structure measurements (XAFS) [60, 61] and electrochemical methods, such as impedance spectroscopy [62] and current transient studies [63]. All these studies were carried out on chemically cleaned GaAs(001) surfaces. AFM as well as current transient studies reveal the island growth. The initial number and size of the copper clusters depends on the deposition potential and the concentration of Cu^{2+}. A higher number of Cu clusters is observed for more negative potentials. The initial deposits of Cu on the surface act as effective nucleation center. The number of clusters is constant during the deposition process as the copper growth takes preferentially place at the former deposited copper. The islands growth for coverages larger than 0.25 ML was confirmed by XAFS [60, 61] with the copper lattice totally relaxed. For a lower coverage, copper nanoclusters with a shorter Cu-Cu distance were observed, which could be explained by the formation of dimers, trimers and/or tetramers. By in-situ AFM $\{111\}$-oriented Cu planes were observed on the GaAs(001)-surface [58].
A closer investigation of the copper epitaxy was carried out by SXRD [13, 14] also confirming the three dimensional cluster growth. The Cu[100]-direction was found to be aligned with the GaAs[100]-direction. The copper is growing epitaxially, it is found to be unstrained with the GaAs(001) surface. The in-plane mosaic spread is about 4.5°, which is a significant derivation from perfect alignment. The clusters were about 30 nm broad and 10 nm high. A tilted geometry of the copper lattice with a tilt angle of 6° was found. No azimuths of the planes seem to be preferred, resulting in an isotropic inclination of the $\langle 001 \rangle$-planes of the epitaxial Cu islands with the GaAs(001) planes.
Additionally, submonolayer amounts of copper electrodeposited on GaAs(001) were investigated by X-ray Standing Waves in combination with X-ray fluorescence spectroscopy [64, 65, 66]. Cu is diffusing several nm into the GaAs near surface region, predominantly occupying Ga lattice sites. This interdiffusion is more pronounced in n-type than in p-type GaAs.
The barrier height of n-GaAs/Cu contacts electrodeposited from copper containing sulfuric acid was determined by current-potential and capacitance-potential measurements [62]. The barrier height is about 0.9 eV. An increase of the barrier height is observed with time. After a period of 10 to 20 days the barrier height increases by 0.035 to 0.01 eV, depending on the deposition potential. Such an effect could be explained by the formation of an interfacial oxide layer, as well as the diffusion of the Cu into the GaAs, creating a p-type layer upon n-GaAs. The copper electrodepositon on GaAs(001) is not yet understood on atomic scale.

Chapter 4

Experimental Setups

Up to now studies of Cu-electrodeposition on GaAs(001) have been carried out on chemically etched and therefore often rough surfaces. Consequently, the X-Ray diffraction measurements were done without knowledge about the initial surface. As GaAs is a binary compound, the termination after such cleaning procedure is a priori unknown. It has been observed that metal deposits on semiconductors grow predominantly on step edges. For a better understanding of the Cu growth process on GaAs, well defined starting surfaces are required. One way to achieve a well defined surface is by UHV preparation. The transfer to the electrochemical setup has to be done without exposure to ambient air, which would result in a structural change and oxidation of the surface.

In this work a careful characterization of the surface during all steps from UHV to electrochemical control has been carried out.The samples were first characterized in UHV by LEED, STM and surface diffraction. Then the surface changes during exposure to inert gas at atmospheric pressure and under potential control in electrolyte could be monitored. To accomplish this study a special setup, which will be presented in Section 4.7, has been used. Additionally some studies of copper deposition on chemically etched GaAs(001) surfaces have been done.
In this chapter the sample preparation by chemical etching as well as in UHV is described. The UHV tools as well as the ID32 beamline with the six-circle diffractometer used to measure the X-ray diffraction data are presented. Two different set-ups for in-situ characterization of the surfaces under potential control are presented. The in-situ electrochemical thin layer cell was used for the chemically etched samples. The other one is a combined UHV-electrochemistry setup for X-ray diffraction, comprising a portable UHV-electrochemistry chamber and a droplet cell.

4.1 Chemical cleaning of the GaAs(001) surface

To study the copper deposition on chemically cleaned GaAs(001) surfaces, α-As/GaAs samples were first "decapped" on a heating plate and then contacted on the backside with an In/Zn-alloy. During these procedures the GaAs-surface oxidizes. This oxide layer can be removed in three steps by chemical etching:

- In a first step neutral and acid oxides are removed by dipping the surface for 2 minutes in

7M ammonia solution (conc. NH_3/H_20=1:1)

- To remove neutral and basic oxides the surface is dipped in 2.5M hydrochloric acid solution (conc. HCl/H_20=1:3)

- In the last step the surface is smoothened by etching with a solution of ammoniacal hydrogen peroxide (NH_3:H_20_2:H_20=3/1/15)

After each step the surface is rinsed with ultra pure water for 30 seconds, the whole procedure is repeated once. Fresh solutions were prepared for each electrode. The mixing ratios are given in volumes.

4.2 Potentiostat

For electrochemical measurements a three electrode setup with a reference electrode (RE), a working electrode (WE) and a counter electrode (CE) is used. The electrochemical experiment is then carried out with the help of a potentiostat. It controls the potential applied between working electrode and reference electrode in such a way that the potential drop between the two electrodes is equal to a desired voltage. The reference electrode is connect with a high input impedance and is ideally current free. The current in the electrochemical cell is passing through a working electrode and the counter electrode. A schematic a of a potentiostat is shown in Figure 4.1. We used a VersastatII (Princeton Applied Research) potentiostat, which was placed

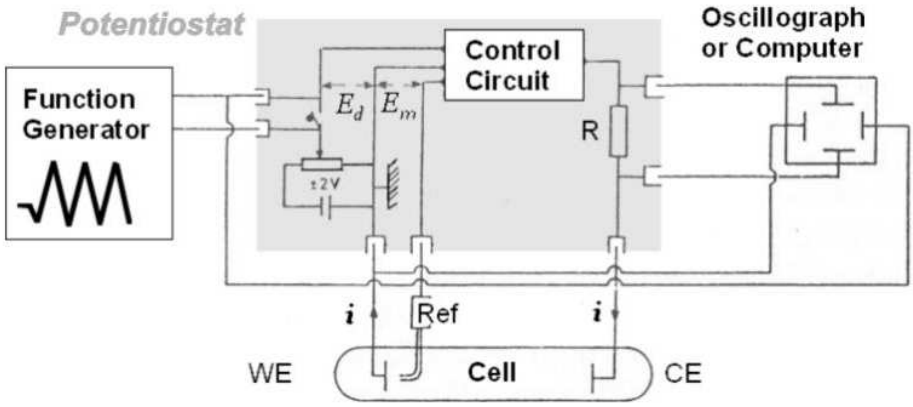

Fig. 4.1: *Schematic of a potentiostat, which controls the potential difference between a reference and the working electrode.*

in the experimental hutch for the in-situ X-ray measurements. The potentiostat was controlled by a computer in the control room by the commands given in Appendix B.1.

4.3 The in-situ electrochemical thin layer cell

The copper deposition on chemical etched GaAs(001) surface was studied in-situ by X-ray diffraction using the thin layer cell. Such a cell is shown in Figure 4.2. The sample is fixed by

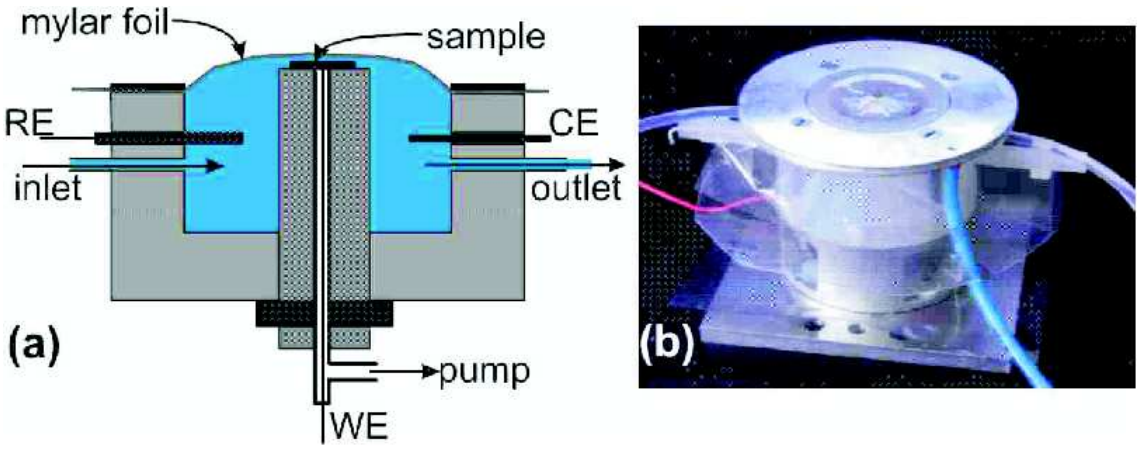

Fig. 4.2: *Schematic (a) and photo (b) of the electrochemical thin-layer cell.*

pumping with a roughening pump (used together with a liquid trap to protect the pump in case of leaking) on the sample holder. For this issue the sample holder has a hole to which the tube is connected to the pump. The electrical contact for the working electrode is passed through the same hole and connected to the backside of the sample. It is separated from the pumping tube by a T-connector. The sample holder is screwed by a nut and a sealing ring to the main body of the cell. Due to this construction, the height of the sample can be adjusted with respect to the main body of the cell, permitting to use differently shaped samples. The main body has four through-holes with a 1/4”-28 threads used to insert the Pt counter electrode and the Ag/AgCl micro reference electrode. The other two remaining through-holes are connected to the electrolyte inlet and outlet tubing. The cell is sealed with a polyethylene film (mylar). The thickness of the electrolyte layer above the sample can be controlled by the amount of electrolyte in the cell. The polyethylene film can be inflated (to perform electrochemical measurements or processes) and lowered (for X-ray measurements) depending on the pressure of the electrolyte on the inlet tube. All parts are made of PCTFE or Teflon to permit their cleaning with strong oxidative acid.

The thin-layer X-ray cell can be used with a X-ray beam with beam energies in the range of 10 keV or higher. During X-ray measurement, only a small volume of electrolyte is sustained, therefore this set-up is not ideal for electrochemical deposition processes.

4.4 Atomic Force Microscopy (AFM)

Atomic force microscope is one type of Scanning Probe Microscopes (Scannin Probe Microscope), which are a family of instruments for studying surface properties like surface conductivity, local friction, morphology, elastic modulus or static charge distribution, by direct imaging. In such instruments a tip moves in a certain range over the surface. The interactions between

the surface and tip depend on the type of SPM used and determine the properties imaged. The advantage of AFM over Scanning Tunneling Microscopy (STM), which will be presented in Section 4.5.2) is that it can also be used to image the topography of insulators or insulating films. The AFM can be used in two different modes, the contact mode and the non-contact tapping mode. The AFM images presented in this work were taken with an in-air atomic force

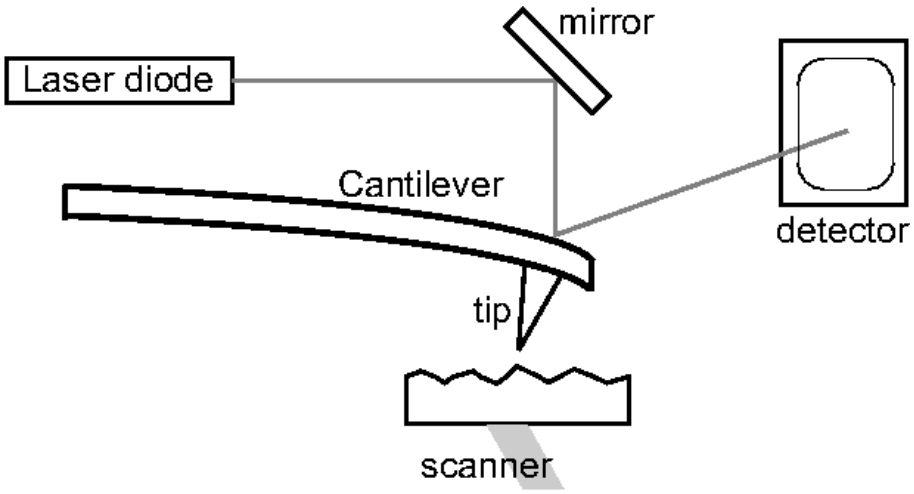

Fig. 4.3: *Scheme of an AFM-setup. The AFM-tip is mounted on a cantilever. The bending of this cantilever depends on the interaction between surface and tip and can be observed by the laser spot reflected on the backside of the cantilever.*

microscope (Molecular Imaging (MI) Dimensions 3100) in non-contact tapping mode. The set-up for an AFM is shown in Figure 4.3. The surface of a sample is probed with a sharp tip (several micrometer long and less then 10 nm wide), located at the free end of a cantilever.
In the non-contact mode the AFM cantilever vibrates close to its resonant frequency with an amplitude about ten Ångstroms. The distance between the tip and the sample is on the order of tens to hundreds of Ångstroms. The resonant frequency of the cantilever varies as the square root of its spring constant, which depends on the force gradient experienced by the cantilever. Changes in the resonant frequency or vibration amplitude due to the change of the distance between the averaged tip position and the surface are detected by a laser, which is deflected by the cantilever. The frequency is kept constant by a feedback system moving the scanner up and down, while the movement in the z-direction is monitored.

4.5 UHV preparation and characterization

The so called R2P2 UHV chamber in the surface characterization laboratory was used for sample preparation and characterization. The chamber has a base pressure in the range of 10^{-10} mbar. It is a multi-component UHV (Omicron) system, composed of a main chamber to which several smaller chambers with preparation, storage and characterization tools e.g. molecular beam epitaxy, LEED, STM, AUGER, ion gun and heater (e-beam and filament heater) are connected as shown in Figure 4.4.

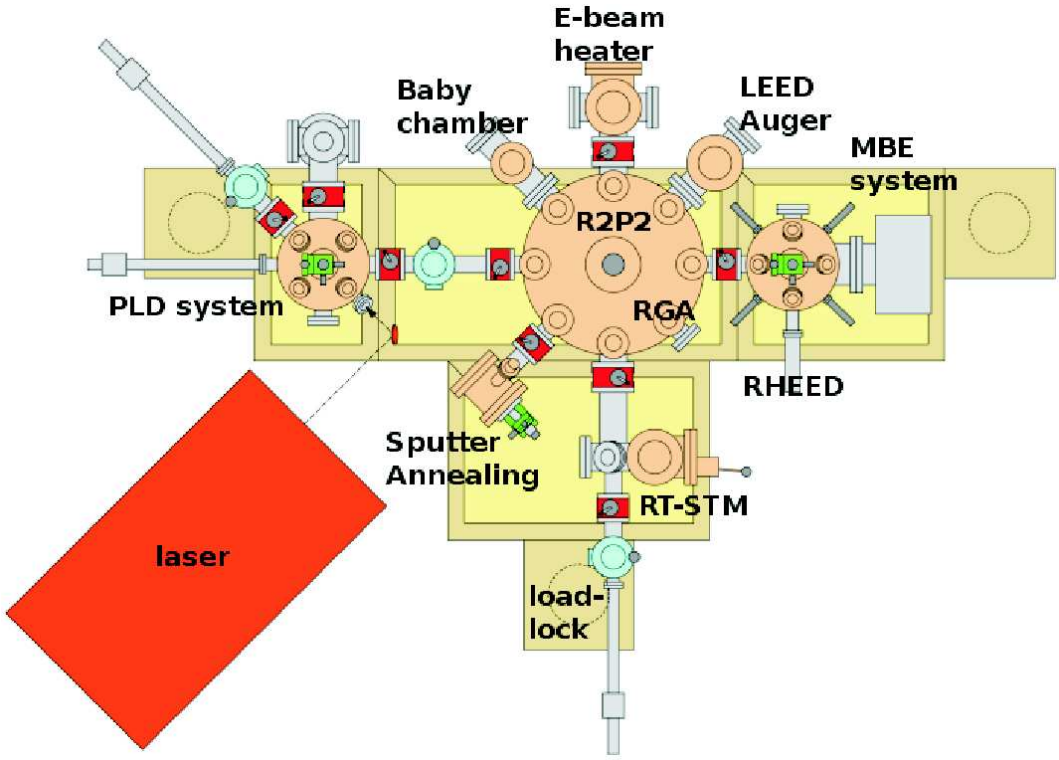

Fig. 4.4: *A schematic of the R2P2 UHV chamber used for sample preparation and characterization .*

4.5.1 Low Energy Electron Diffraction (LEED)

One of the most commonly used methods for studying a surface structure is Low Energy Electron Diffraction (LEED). In such an experiment electrons accelerated by an applied electrical potential difference U have a momentum $p = \sqrt{2\, m_e\, e\, U}$ and a thus resulting de-Broglie wavelength $\lambda = h/p = 12.285/\sqrt{U[V]}$Å. The wavelength for electrons accelerated by 40 eV is about 2 Å and therefore suitable for diffraction from atomic structures.

Low energy electrons have a small penetration depth and are only diffracted by a few atomic layers when hitting a crystalline surface. The surface bombarded with monochromatic low energy electrons gives rise to rods in the reciprocal space. The intersection of each rod with the Ewald sphere for the given beam energy is observed as an intensity spot. The projection of these spots can be observed on a fluorescent screen.

A schematic view of a LEED system with the rods from the surface, the Ewald sphere and the incident and diffracted wave vectors are shown in Figure 4.5. The relative positions of the spots reveal the surface symmetry. The intensity and sharpness of the spots reveal the ordering of the surface. In this work LEED was used to check the surface structure during and after UHV preparation.

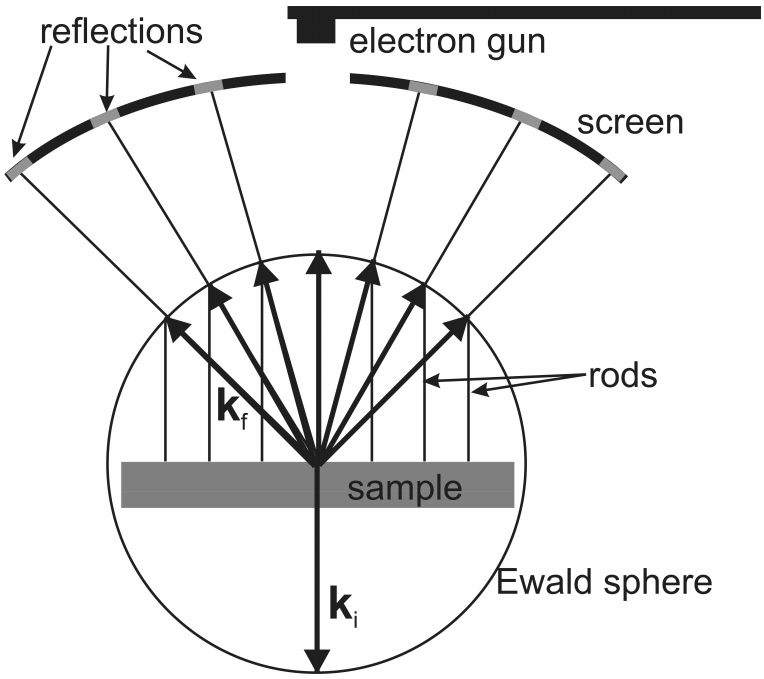

Fig. 4.5: *A schematic of a LEED set-up and the obtained diffraction pattern. By diffraction of low energy electrons, rods in reciprocal space occur, the projection of their intersection with the Ewald sphere can be observed on a fluorescent screen.*

4.5.2 Scanning Tunneling Microscopy (STM)

Scanning Tunneling Microscopy (STM) provides real-space atomic-resolution images of the surface topography. An atomically sharp tip is scanned over the sample surface while a voltage between the sample and tip is applied. Depending on this voltage, electrons might be able to pass the vacuum barrier between sample and tip, due to the exponential decay of the electron wave function into the classically forbidden region. A tunneling current I is measured which is described by the following equation

$$I \propto U \cdot \exp\left(-A \cdot \sqrt{\phi} \cdot d\right).$$

U is the applied voltage between sample and tip, d their distance, A is a constant and ϕ is the barrier height depending on the electronic structures of the tip and the sample. The barrier height can be determined from current-distance measurements. The tunneling current decays exponentially with the barrier width, which introduces a good resolution in the z-direction and gives rise to atomically resolved images in tunneling microscopy.
The principle set-up of a STM is shown in Figure 4.6. A voltage is applied between the sample and the tip. The tip can then be approached to the surface by measuring the tunneling current. Once the desired current is obtained, the tip is scanned over the surface. In the constant current mode, the tunneling current is kept constant and the tip-sample distance is adjusted by the piezo on which the tip is mounted and the movement of the tip perpendicular to the surface is monitored. For the images presented in this work a conventional Omicron single tube scanner (microSTM) was used.

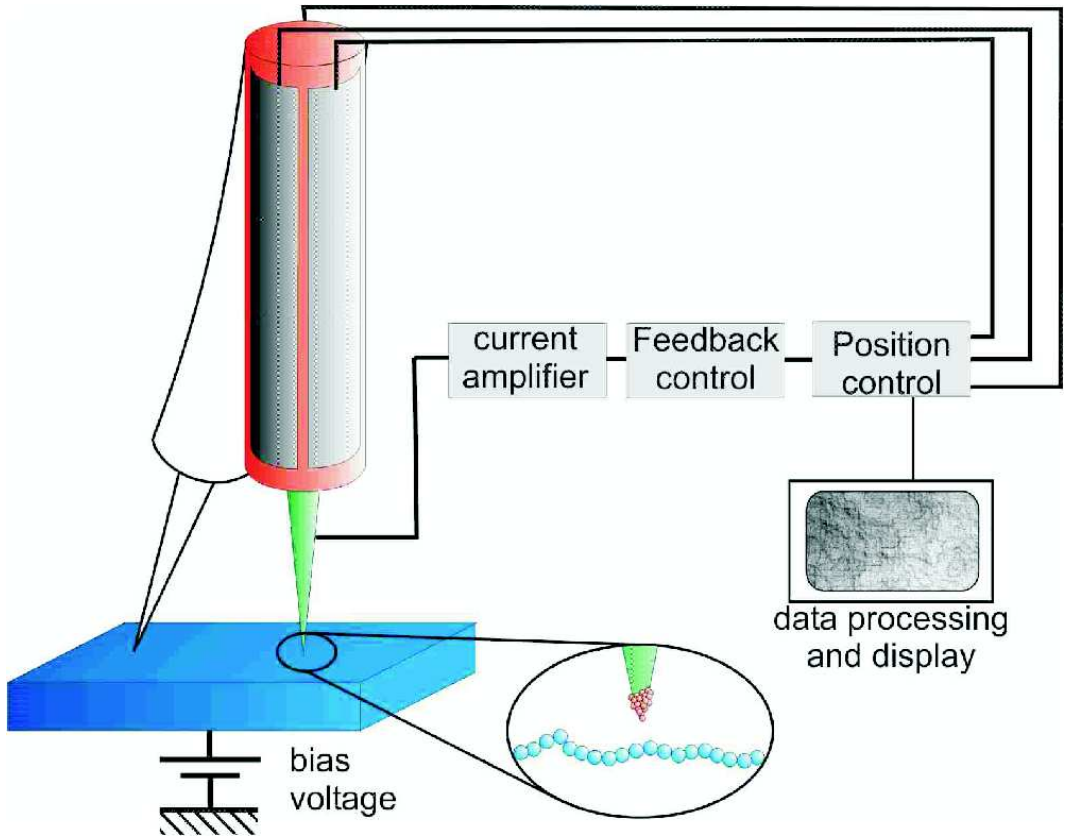

Fig. 4.6: *Set-up of a STM. The tip is scanned over the surface controlled by a feed-back system. The tunneling current can be monitored at constant height or it can be kept constant and the changes in the sample-tip distance is monitored.*

The tunneling current depends on the transition probability of an electron tunneling from the sample to the tip (or inverse, depending on the applied voltage). This probability depends crucially on the local electronic states into or out of which electrons can tunnel. Therefore, a STM image is not really displaying the surface topology but rather the local density of states (LDOS). This is especially important for STM, as the polarity of the applied bias determines if filled or empty states are imaged. E.g. in the case of the GaAs(001) surface the polarity of the applied bias determines if arsenic or gallium atoms are imaged.

4.5.3 Sample preparation

The GaAs(001) surfaces which were used for electrochemical deposition experiments were prepared in UHV from arsenic capped GaAs wafers. The wafers were cut into 7 mm $\times$ 7 mm pieces, which were glued on a hat shaped sample plate. In-Zn-alloy was used as glue and created at the same time the ohmic contact. The sample plate was heated on a heating plate to 120°C. A small piece of the In-Zn alloy was deposited on it. When the alloy started melting the sample was pressed on the sample-plate and immediately removed from the heating plate. The sample was then introduced into the UHV system to prevent the arsenic cap from oxidizing.

After degassing the sample at 200°C the arsenic cap was removed by gently increasing the temperature to 350°C, keeping the pressure lower than $2 \cdot 10^{-9}$ mbar. For this first step the heater in the sputter chamber was used, which had the advantage that this chamber can be separated by a valve from the big chamber and then pumped separately by a turbo molecular pump. Once the sample was "decapped" it was transfered into the LEED chamber to verify the c(4×4) reconstruction.

During this work an additional heater was installed just in front of the LEED. The further preparation of the surface could therefore be done in front of the LEED. The temperatures were read by a thermocouple fixed close to the sample. The (2×4) reconstruction of the GaAs(001) surface is obtained by heating the sample to a temperature between 380°C and 420°C. During the transition from the c(4×4) to the (2×4) reconstruction a slight increase of the pressure can be observed. The (4×2) surface was prepared by heating to temperatures in the range between 470°C and 600°C.

4.6 Beamline and Diffractometer

A schematic view of the optics setup used for diffraction experiments on the insertion device beamline ID32 at the ESRF is shown in Figure 4.7. The undulator radiation is monochromatized by a pair of Si(111) crystals. To avoid the damage by the high power-density from the undulators, both crystals are cooled by liquid nitrogen. When the energy is changed by rotating the two crystals around a common axis, the output beam height is kept constant by changing the gap between the two crystals. The monochromatic beam can be focused by up to 15 2-dimensional Be compound refractive lenses (CRL). The number of focusing lenses used depends on the energy of the X-ray beam. An X-ray mirror coated with three stripes (SiO_2, Ni and Pd) is used with an instant angle of 0.1° for rejecting higher order harmonics generated by the undulators. For the X-ray beam energies used for this work between 17 keV and 23 keV, the Pd coating of the mirror was used. Behind the mirror an X-Ray Beam Positioning Monitor (XBPM) is installed. It monitors the beam position, which can then be stabilized by a feedback system connected to the monochromator.

The final beam size is defined by the entrance slits about 70 cm before the sample. The vertical slit size was optimized to illuminate only the sample surface, in order to decrease the scattering (leading to a higher background) from the electrolyte. For an incident angle of 0.2° with the surface and a sample of 7 mm × 7 mm size the optimal vertical beam size is about 20 μm. An ionization chamber, measuring the incident beam intensity, is installed right after the slits. Using this signal the measured intensity of the diffracted beam can be normalized to the intensity of the incident beam.
A fast shutter, placed behind the ionization chamber and the slits blocks the incident beam when no data is taken. Its purpose is to reduce beam damage due to photoelectrons created on the surface or interface of the sample by the X-ray beam. To measure the diffracted intensity from the sample a point detector (Cyberstar) was used, placed about 1 m away from the sample. In the front of the flight tube before the detector, a fixed aperture of 1(H) × 5(V) mm^2 is used to define the sample surface area contributing to the diffracted intensity. This aperture is placed

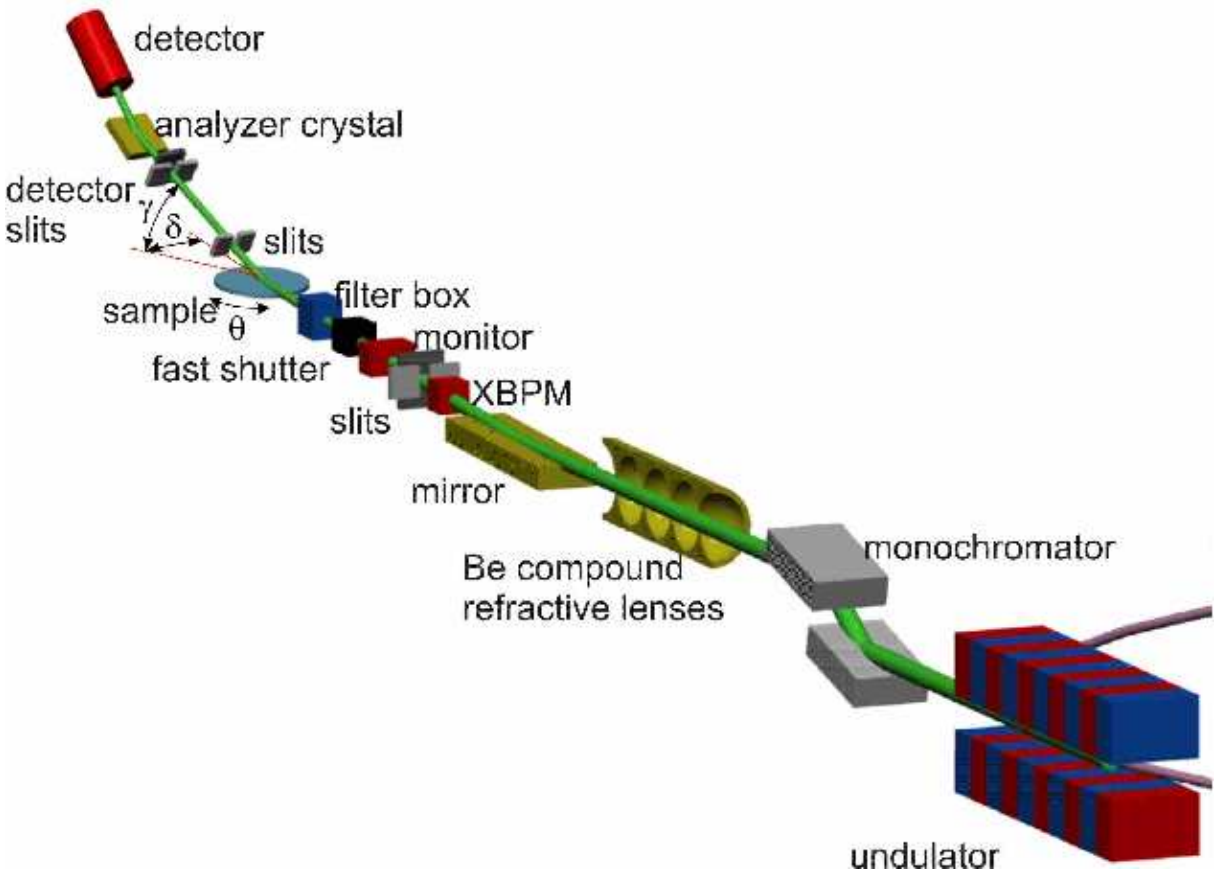

Fig. 4.7: *Schematic of the beamline in the configuration used for surface X-ray diffraction*

about 10 cm away from the sample. A second aperture is placed about 1 m after the sample defining the in-plane and out-of-plane resolution in reciprocal space. The size of these slits can be chosen individually to improve the intensity to background ratio, which depends e.g. on the the sample properties and the experimental setup. Aperture sizes of 0.5 mm, 1 mm, 3 mm and 5 mm are available in horizontal and in vertical directions. An analyzer crystal (graphite) is placed before the detector to block the Ga K- and As K-fluorescence X-rays emitted from the samples .

Surface X-ray experiments at ID32 are done with a computer controlled HUBER six-circle diffractometer. The diffractometer can be operated with a ”HUBER tower” on the theta circle with a sample-weight capacity of 50 kg. The two angles, ”chi” and ”phi”, of the tower were used for sample alignment and frozen afterwards. Also the incident angle (”tabtlt”) of the beam with the sample surface was fixed during the measurement of one sample (values between 0.13° and 0.2° were used). The three motors that were not fixed were the motor (”theta”) rotating the sample in the plane about its surface normal and the two motors driving the detector to the desired in-plane (”delta”) and out-of-plane (”gamma”) angles of the diffracted beam. The correction factors for the ID32 diffractometer geometry are given in Appendix A.2.

4.7 The combined UHV- electrochemistry setup for X-ray diffraction

4.7.1 The portable UHV-electrochemistry chamber

Light weight metals like beryllium and aluminum have small absorption and are used as X-ray windows. A chamber with a beryllium dome has already been used on the ID32 diffractometer to study surfaces prepared and characterized in the large UHV chamber in the sample characterization laboratory (SCL) of ID32. Based on this "baby-chamber", a new setup, shown in Figure 4.8, convenient for electrochemistry, has been developed at ID32 and has been tested and improved during this work.
It allows to study the sample successively in UHV, under atmospheric pressure in inert gas and in contact with electrolyte without exposure to ambient air [67].
The bottom part is a cross shaped body piece with five CF38 ports and a CF63 top flange. A Be

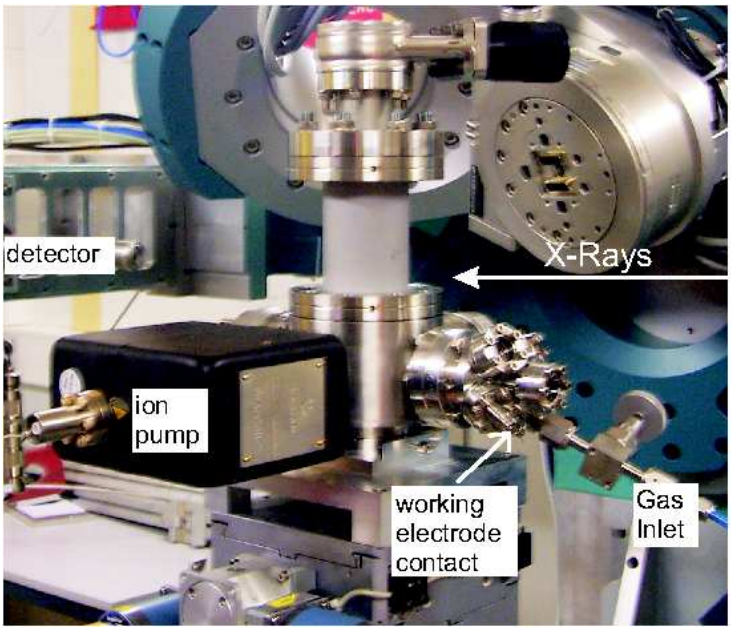

Fig. 4.8: *The portable UHV chamber mounted on the ID32 diffractometer. The direction of the incident X-ray beam is indicated as well as the detector defining the direction of the exit beam. An ion pump permits to keep the chamber under UHV during the whole measurement. An electrical feedthrough connected to the sample plate permits to ground the sample during UHV measurements and to apply a potential under electrochemical control. The chamber can be vented to inert gas through a gas inlet to permit a clean transition between UHV and electrochemical control.*

cylinder with two welded CF63 flanges is used as X-ray window and mounted on the bottom part. During measurements the sample is mounted with the surface normal along the cylinder axis. The chamber allows, mounted on the ID32 diffractometer, an incident or exit angle up to 40°, which is determined by the top flange of the beryllium cylinder blocking the X-ray beam at higher angles.

The top part of the cylinder is terminated with a CF63/38 adapter and a CF38 UHV valve, through which the electrochemical droplet cell can be inserted. The four ports on each side of the cross shaped bottom part are used for sample transfer, a vacuum gauge, an ion pump (to maintain the chamber at better than $1x10^{-9}$ mbar during UHV measurements), an electrical feedthrough for the working electrode, a gas inlet and a view-port. The sample holder is fixed on the CF36 bottom part (Figure 4.9). It is mounted on a flexible UHV bellow, which allows to lower the sample holder from the measurement position inside the beryllium cylinder to the transfer position inside the base chamber. A metal rod running along the inside of the flexible bellow is fixed to the sample holder situated on the top of the bellow. At the measurement position this rod is locked to the chamber by three screws. The sample holder is made of ceramics

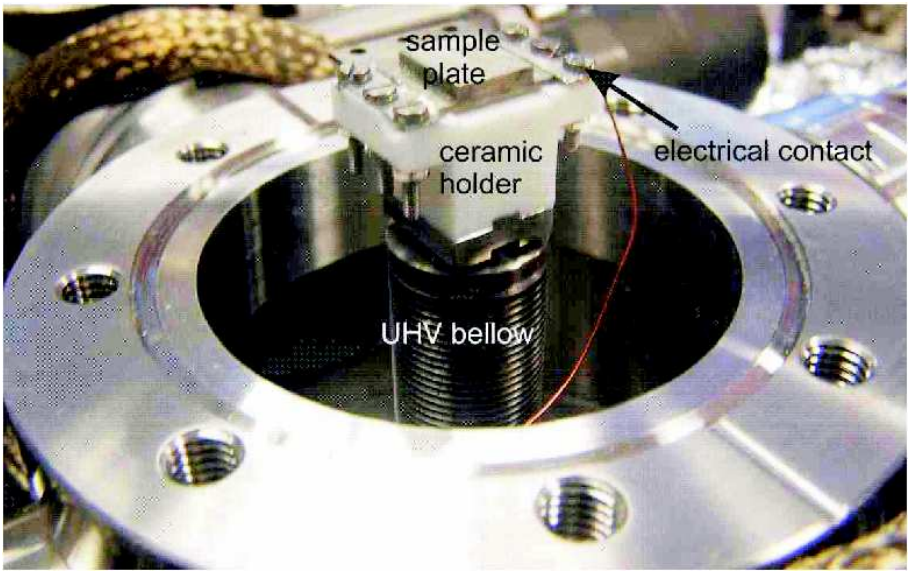

Fig. 4.9: *The bottom part of the portable UHV chamber with the sample holder in the upper position used for X-ray measurements. The sample holder is made of ceramics to insulate the sample from the ground which is essential for electrochemical control. An additional electrical contact is made between the sample plate and a feedthrough to permit potential control when the sample is in contact with the electrolyte.*

to isolate the sample plate from the chamber. The metal clips fixing the sample plate on the sample holder are connected to the UHV feedthrough for the working electrode. During UHV measurements the sample should be grounded via this feedthrough to the chamber to prevent sample charging due to the photoelectrons created by the X-ray beam. For the experiments on GaAs wafers hat shaped sample plates were used as shown in Figure 4.9, to avoid that the screw fixing the metal clips are blocking the beam in grazing incidence geometry.
The portable UHV chamber can be connected to the docking port of the UHV preparation chamber in the surface characterization laboratory. A turbo-molecular pump on the T-connector allows individual pumping and baking of the portable UHV chamber and the docking port before opening the valve to the large UHV system in order to transfer the sample. The sample can be inserted into the portable chamber by the transfer arm of the large UHV system when the sample holder is lowered.

Two chambers of this type were assembled at ID32, while one is pumped and baked, measurements can be performed with the second chamber.

4.7.2 The electrochemical droplet cell

The electrochemical droplet cell used in combination with the portable UHV chamber is shown in Figure 4.10. It is composed of a ≈ 20 cm long glass rod (with inner diameter: 2 mm and

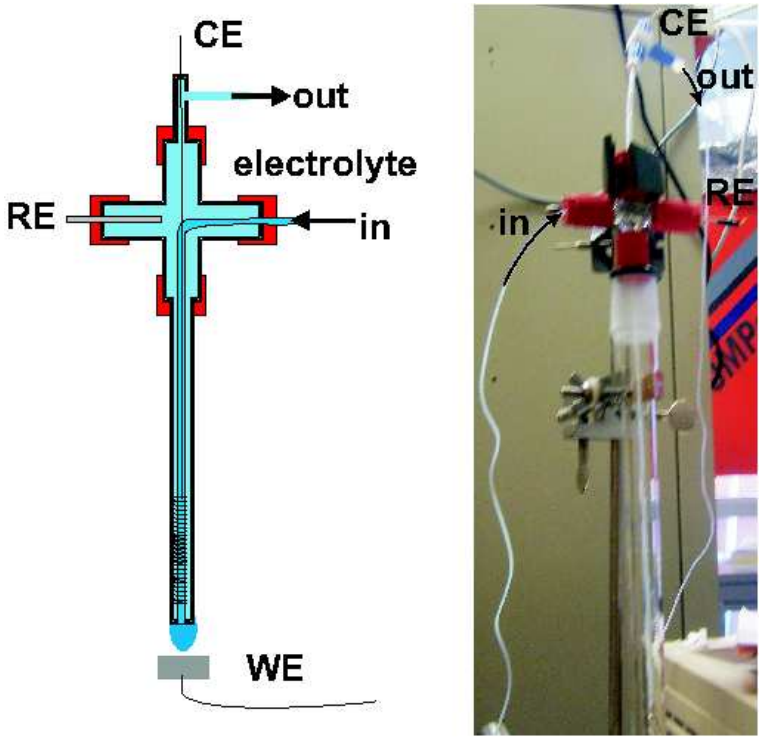

Fig. 4.10: *The electrochemical droplet cell with the in- and outlet for electrolyte and the connections for the counter and reference electrode. The glass tube has an outer diameter of 4 mm and an inner diameter of 2 mm. The inlet tube for the electrolyte is going down to the bottom of the glass tube permitting an exchange of the droplet with fresh electrolyte.*

outer diameter: 4 mm) connected to a cross shaped glass piece. Inlet and outlet tubes (PFA-PTFE) with a diameter of 1.6 mm are used for the electrolyte. The tube for the electrolyte inlet is going through one of the side openings of the glass cross down to the end of the long glass tube to allow complete exchange of the electrolyte droplet hanging on the tip of the glass tube. The electrolyte outlet is connected to the top opening of the glass cross which is convenient to fill the cell and to remove any gas bubbles. The counter electrode (0.1 mm Pt wire) is introduced through the electrolyte outlet tube by a T-connector and is wound around the electrolyte inlet down to the tip of the glass tube.

All parts touching the electrolyte are made of PCTFE or Teflon (PTFE) (so that cleaning with strong oxidative acid is possible) and are commercially available. The reference electrode (a commercial micro-electrode) is introduced through one of the side openings of the glass cross.
In- and outlet tubes for the electrolyte are connected to a computer controlled pumping system

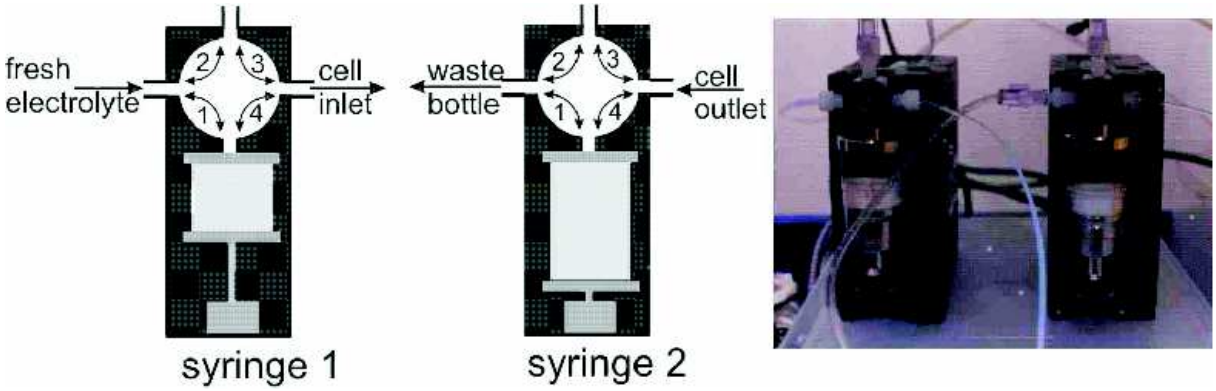

Fig. 4.11: *(a) Schematic view of the pumps with the possible positions of the valve and the assignment of its connections. The pumps are connected to a four-way valve which itself is connected in one position to the fresh electrolyte or waste bottle and in the other position to the in- or outlet of the cell. (b) The computer controlled pumps to regulate the droplet inside the beryllium cylinder.*

(PSD3 syringe pumps, Hamilton Company) shown in Figure 4.11. A detailed description of the commands for using the pumps with *spec* is given in Appendix B.2. The syringes are connected to a four-way-valve with four possible positions. The syringes are moved by stepper motors with 15000 steps for a volume of 12.5 ml, which allows to adjust the size of the electrolyte droplet when the sample is contacted.
During the experiment the droplet can be monitored by an endoscope as shown in Figure 4.12. One of the pumps is connected by one of the side connectors of the valve to the bottle of fresh electrolyte (position 1) and the other (position 4) to the electrolyte inlet of the cell. The second syringe is connected with the side connectors of the valve to the electrolyte outlet of the cell (position 4) and to the waste bottle (position 1). The top connectors of the first valve can be connected instead of the waste bottle to the second syringe in order to rinse the tubes (both pumps in position 2) through a syringe connected to the top position of the second pump. Then the second pump can be filled with fresh electrolyte (position 1) and the droplet cell can easily be filled with electrolyte.
The cell and the endoscope as well as a torch lamp illuminating the inner part of the beryllium cylinder are mounted on the top of the beryllium cylinder via an adjustable bellow shown in Figure 4.13. During the mounting the top valve can be kept closed. The bellow is terminated by a plexi-glass window with through-holes for the cell, the endoscope and an gas inlet to purge the volume of the bellow before opening the top valve of the beryllium cylinder. The cell and the endoscope can be adjusted separately.
The fine positioning of the glass tube above the sample is done by the adjustment screws holding the bellow [see Figure 4.13 (a)] and can be verified by X-rays (x-, y- and z-scan of the sample stage) as shown in Figure 4.13 (b) and 4.13 (c). The beryllium cylinder allows an exit angle of

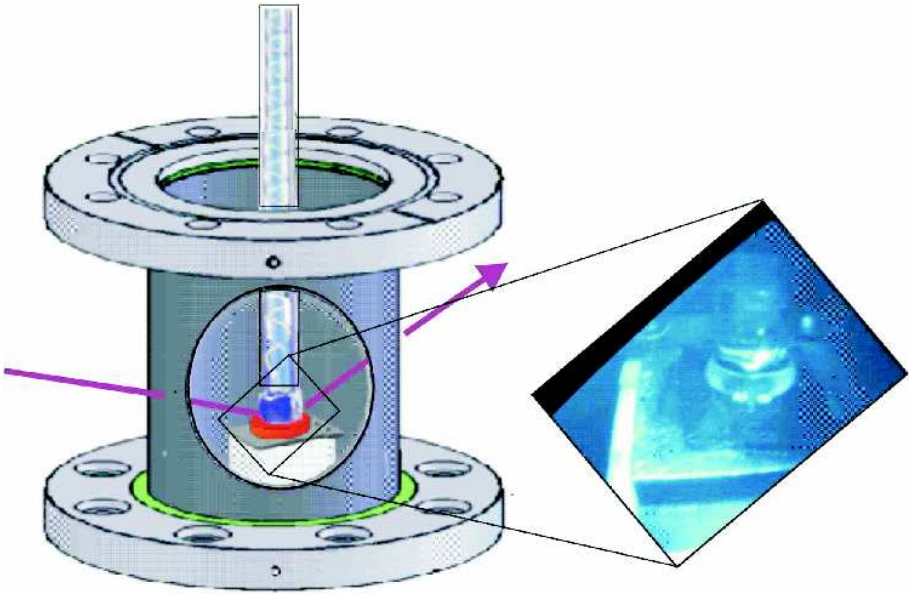

Fig. 4.12: *Schematic view of the sample contacted with electrolyte inside the chamber and the droplet as it is seen during experiment with the endoscope.*

40°, so that the glass tube (which has an outer diameter of 4 mm) can be lowered down to 1.3 mm above the sample without blocking the beam at this angle. The distance between sample and glass tube should be kept small to get a better stability of the droplet.

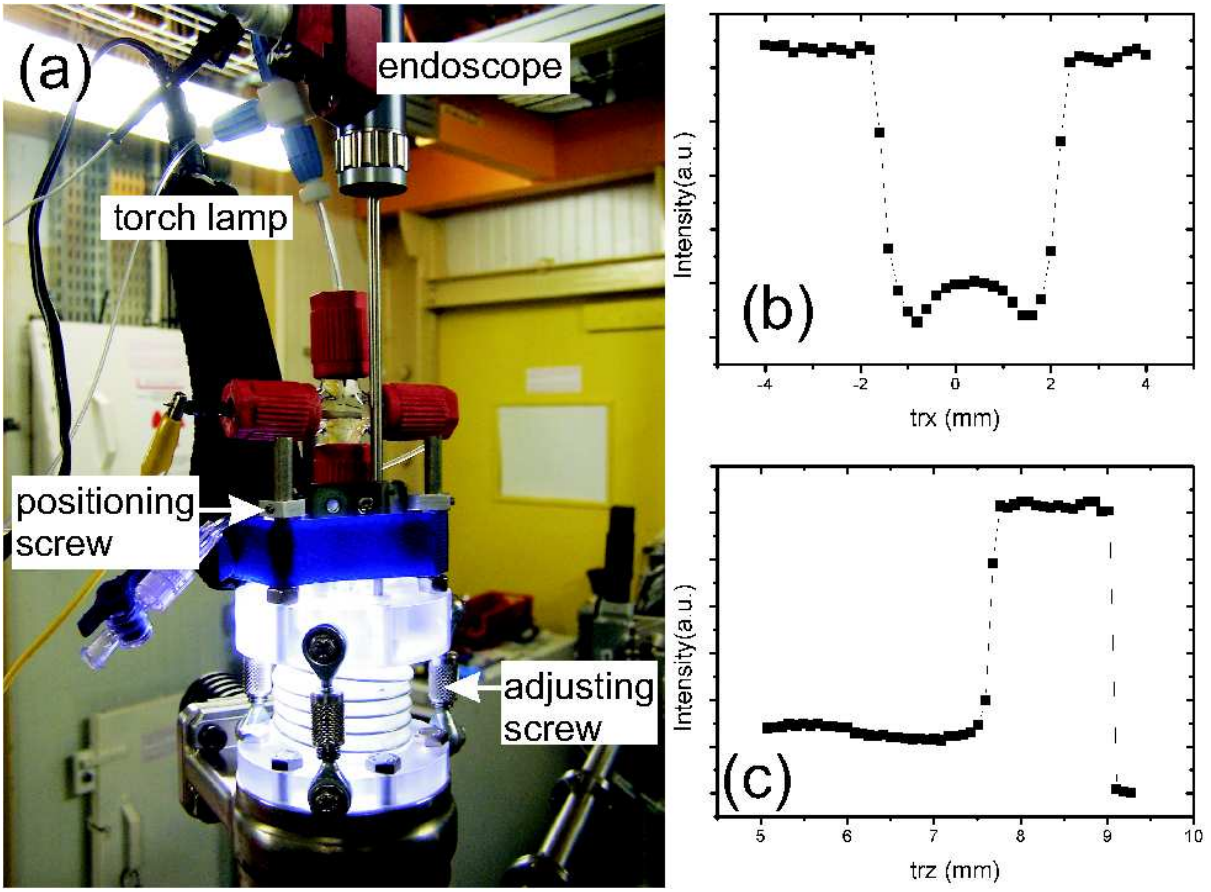

Fig. 4.13: *(a): The bellow to mount the droplet cell, the endoscope and the torch lamp to illuminate the droplet on top of the beryllium cylinder. The position of the cell can roughly be adjusted by the positioning screws holding the cell. A fine adjustment can then be done by three adjusting screws permitting to tilt the cell with respect to the chamber and hence moving the end of the glass tube in horizontal direction above the sample. (b) and (c): Scans performed in the x- and z-direction to verify the position of the glass tube with the direct beam.*

Experimental Results

Chapter 5

The arsenic capped GaAs(001) surface

The samples used for this work were GaAs(001) samples with different surface reconstructions obtained from arsenic capped GaAs wafers. The arsenic capped samples were characterized by AFM in air. An additional characterization of the arsenic cap and especially the α-As/GaAs interface was carried out with X-rays. The samples used were stored in UHV to avoid oxidation of the arsenic cap and consequently the oxidation of the GaAs surface. However, the samples were shipped in air and the surface of the cap was partially oxidized.

5.1 AFM studies

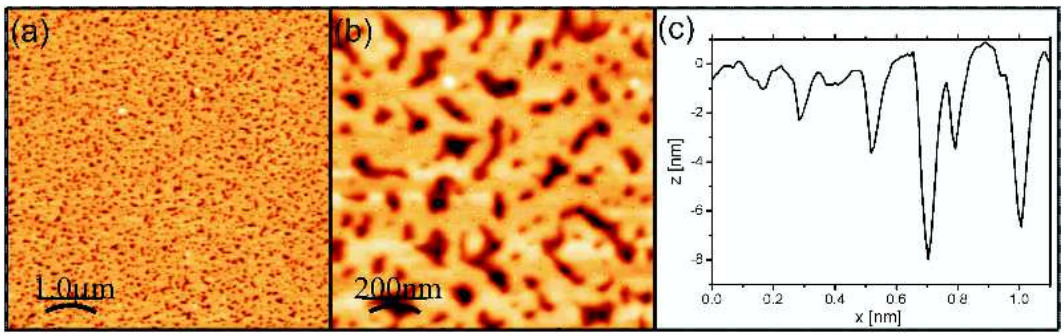

Fig. 5.1: *AFM-images of an arsenic capped sample. Images of 5 µm × 5 µm (a) and 1 µm × 1 µm (b) were recorded. Also a height profile of the arsenic cap is shown (c). Holes of about 8 depth are present on the surface, probably indicating an oxide layer on the top of the arsenic cap.*

The results obtained by AFM on arsenic capped GaAs(001) wafers are shown in Figure 5.1. These samples were shipped from Norway in air and stored under UHV for four years. The cap is smooth, however holes up to 10 nm depth can be observed. Earlier studies of the arsenic cap by X-ray reflectivity revealed an oxygen layer of about 8 nm thickness [68]. This thickness corresponds approximately to the depth of the holes observed on the surface, which indicates an oxidation layer on top of the surface. The root mean square roughness is about $\approx$ 2.2 nm which is larger than the one obtained earlier from X-ray reflectivity ($\approx$0.2 nm).

5.2 Characterization by X-ray diffraction

The samples characterized by X-rays were glued to a hat shaped sample plate with an indium-zinc alloy, which permits ohmic contact to GaAs, and transfered into the UHV chamber of the SCL. The samples were degassed at 200° C in the sputter chamber and afterwards transfered into a separate UHV chamber with a beryllium dome. This chamber was mounted on the ID32 diffractometer and the samples, still under UHV, could be characterized with X-rays. The evaporation temperature of arsenic oxide is about 160°C, the degassing process therefore removes the oxide layer on top of the arsenic cap. Only a diffraction pattern from the arsenic cap and not from the arsenic oxide is expected. An arsenic capped sample measured previously in air reveals its oxidation by the beam, consequently powder rings corresponding to arsenic oxide could be observed. The sample presented here was measured with a X-ray beam with an energy of 19.7 keV and an incident angle of 0.2° with the sample surface. In Figure 5.2, a radial in-

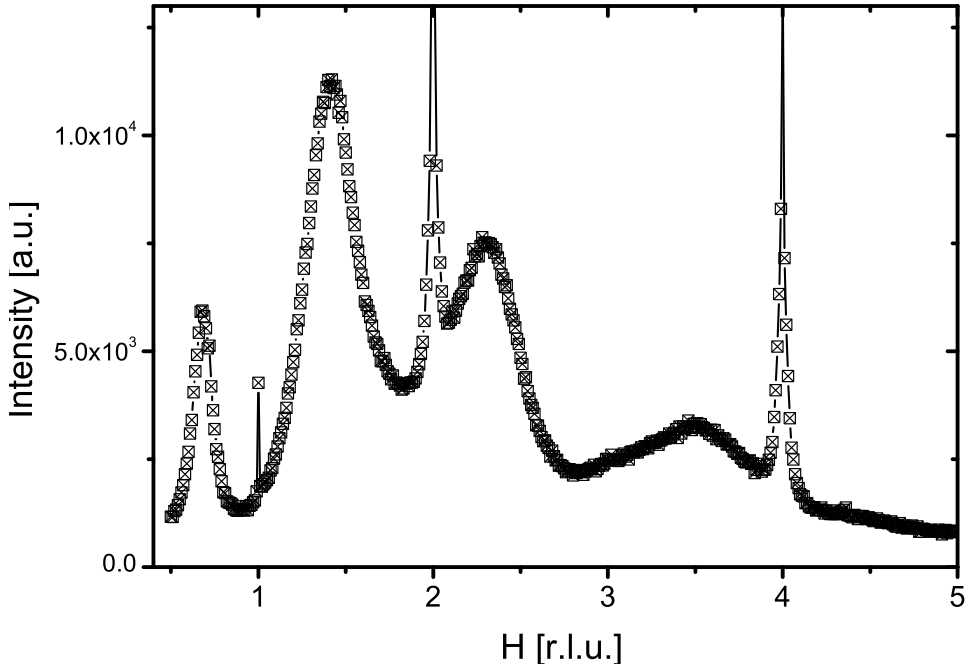

Fig. 5.2: *A radial in-plane (L=0.06 r.l.u.) scan of a arsenic capped GaAs(001) surface. The GaAs(200)- and GaAs(400)-reflections can be identified. Additional broad peaks can be observed at H=0.6, 1.4, 2.3, 3.5 r.l.u. coming from the amorphous scattering of the arsenic cap.*

plane scan along the H-direction is shown. The GaAs(200) and (400) Bragg peaks are observed at H=2 r.l.u. and at H=4 r.l.u. respectively. At H=1 r.l.u. an additional peak from the GaAs(1,0) crystal truncation rod is showing up. No reconstruction of the GaAs(001)-surface under the arsenic cap seems to exist. As the surface is arsenic capped, an arsenic-rich reconstruction like c(4×4) or (2×4)/c(2×8) might be expected. In both cases additional half order reconstruction peaks would exist. However, additional maxima of intensity are obtained at H=0.6, 1.4, 2.3, 3.3 r.l.u.. Rocking scans at this positions show no peak but constant intensity. These intensity maxima are therefore coming from the scattering from the amorphous cap.

Scattering from amorphous materials

The intensity distribution obtained by scattering from an amorphous material is reflecting the interatomic distances of the material. The radial electron density distribution can directly be deduced from the intensity pattern.
Assuming a continuous distribution of atoms around any reference atom, the intensity distribution from a monoatomic amorphous material can be written as [24]

$$I = N \cdot f^2 \left[1 + \int_0^\infty 4\pi r^2 \rho(r) \frac{\sin(k \cdot r)}{k \cdot r} dr \right], \tag{5.1}$$

where f is the structure factor of one atom and $\rho(r)$ is the radial electron distribution in the material. N is the number of atoms contributing to the scattering.
The variation of the radial electron distribution, $\rho(r)$, from the average one, ρ_a, can than be written as

$$2\pi r^2[\rho(r) - \rho_a] = \frac{2r}{\pi} \cdot \int_0^\infty \frac{I/N - f^2}{f^2} \frac{\sin(k \cdot r)}{k \cdot r} dr. \tag{5.2}$$

The structure factor of arsenic is known [69], its absolute value decreases with increasing $|\vec{Q}|$. At large $|\vec{Q}|$ the scattered intensity per atom I/N oscillates about f^2. This fact is used to fit (for large $|\vec{Q}|$) the corrected intensity I to $N \cdot f^2$ to determine N (and the value of the term $\frac{I/N - f^2}{f^2}$). Finally the integral in Equation 5.2 can be calculated numerically.

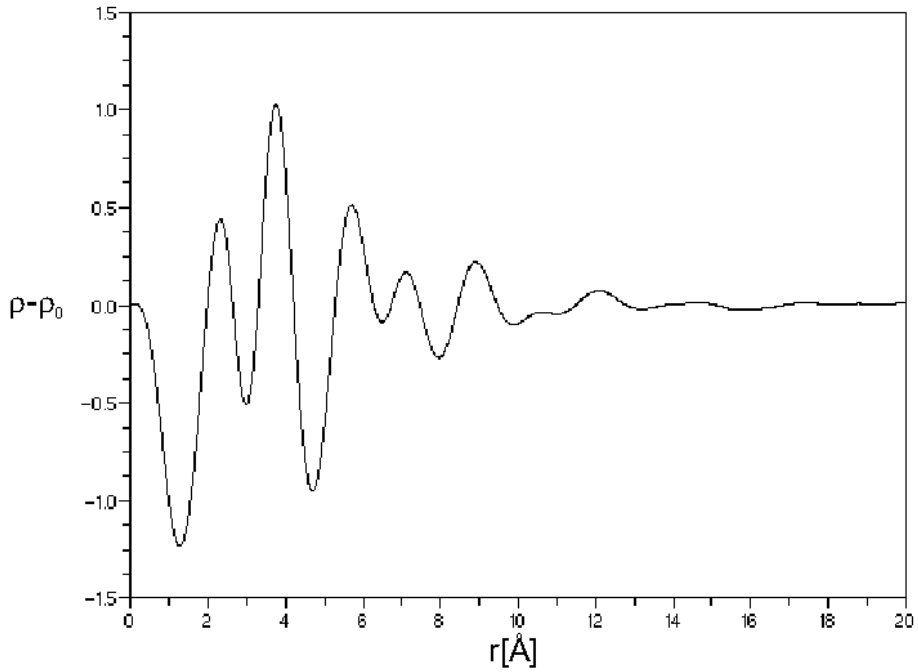

Fig. 5.3: *The radial electron density could be deduced from the intensity distribution due to the scattering from the amorphous arsenic. The nearest neighbour distance is about 2.4 Å.*

For the data analysis, the Bragg reflections were not taken into account to consider only the

intensity distribution arising from the amorphous arsenic cap. The value deduced for N by fitting $N \cdot f^2$ is not to accurate for large $|\vec{Q}|$, since data was only taken at low momentum transfer. However, this only changes the shape of the obtained radial electron density but not the positions of the maxima and minima giving the atomic positions of the nearest neighbours. The obtained values for the electron density is arbitrary due to the uncertainty in N.

The radial electron density distribution for the amorphous arsenic cap obtained in this way is shown in Figure 5.3. The first nearest neighbour distance can accordingly be determined to ≈ 2.4 Å and the distance to the second nearest neighbour is ≈ 3.8 Å. The bondlength of As-As is 2.49 Å, which agrees with the nearest neighbour distance obtained from the scattering profile. Compared to the radial electron density obtained from the scattering on water [70, 71] the distances for the nearest neigbours are smaller and the features in the electron density distribution coming from the short range order can be followed up to a larger radial distance (up to 10 Å for the amorphous arsenic compared to 7 Å for water). The solid arsenic has less thermal vibration and motion compared to liquid and therefore the short range order is sustained further.

Crystal truncation rods

Four non-equivalent CTR's were recorded from the arsenic buried GaAs(001) surface. In a first

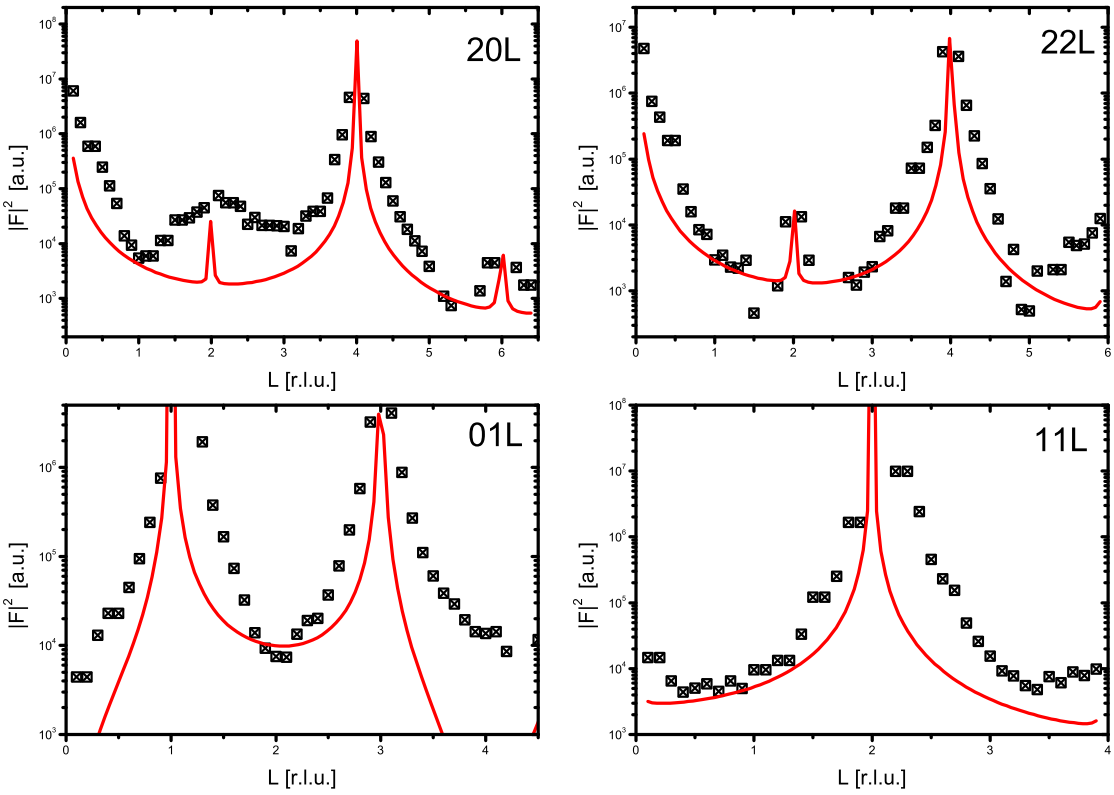

Fig. 5.4: *The square of the structure factor deduced from the integrated intensities measured on the arsenic capped GaAs(001) surface are plotted as black squares. The corresponding CTR's for a bulk terminated GaAs(001) are plotted as a red curve.*

approach these rods are compared with the ones which would arise from a bulk-like termination of the surface. The measured rods are plotted together with the corresponding calculated curve in Figure 5.4.
The only free parameter is the scalefactor for the shown comparison. The introduction of additional free parameters, like statistical displacement or roughness, does not lead to a better shape matching between the calculated and measured CTR's. An additional crystalline layer of arsenic or a variation of the z-positions of the first atomic layers does not reproduce all the features of the measured rods. Especially the measured intensities at the anti-Bragg positions are not reproduced.

During the MBE growth of the arsenic overlayer the surface is exposed to an overpressure of arsenic. A reason for the non-bulk-like shape of the measured CTR's could therefore be a buried reconstruction of the GaAs surface. This reconstruction would probably be arsenic rich and therefore lead to a c(4×4) or (2×4)/c(2×8) surface structure. During the growth of the arsenic cap the surface is monitored by RHEED and the last observed reconstruction before the growth is a GaAs(001)-c(4×4) structure [72]. The measured CTR's and the corresponding cal-

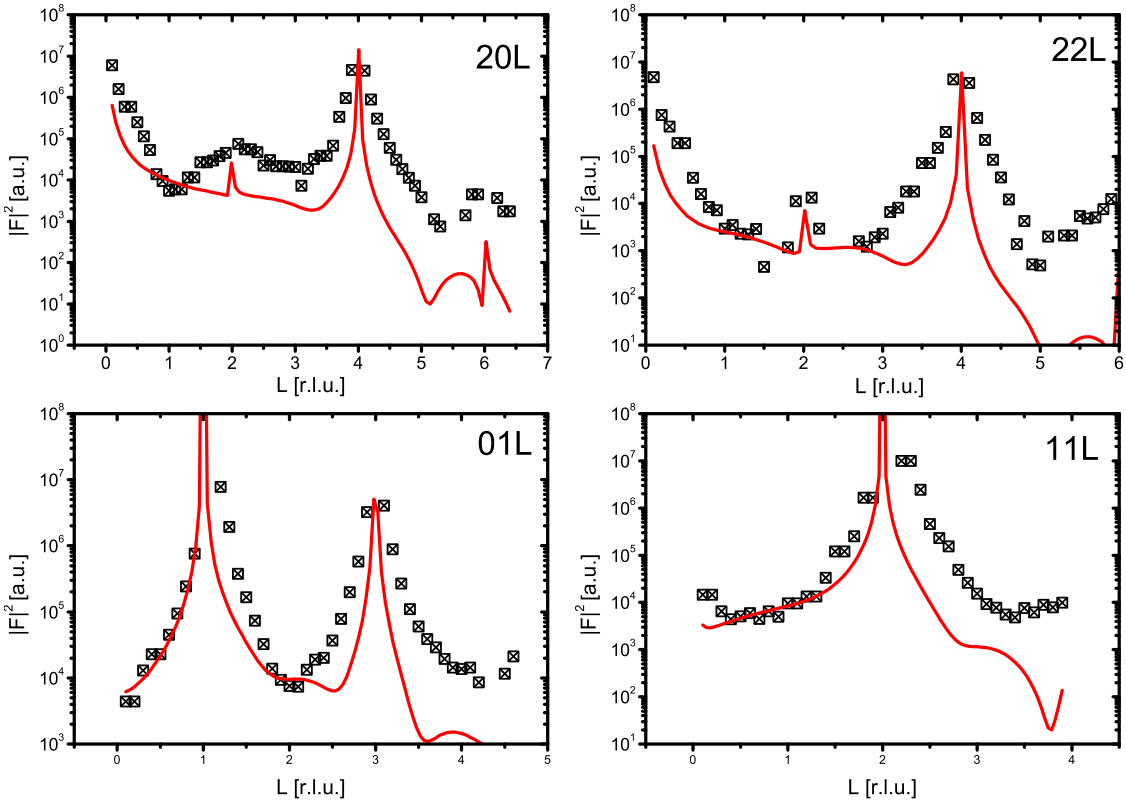

Fig. 5.5: *The square of the structure factor obtained from the integrated intensities measured on the arsenic capped GaAs(001) surface are plotted as black squares. The corresponding CTR's for a c(4×4) reconstructed GaAs(001) surface are plotted as a red curve.*

culation of a c(4×4) structure are shown in Figure 5.5. The black squares are representing the

square of the structure factor deduced from the measured data, the red line is the corresponding calculation. The atomic positions for the calculation of the CTR's are taken from A. Nagashima et al. [39]. The c(4×4)β structure is assumed as it is the most arsenic-rich one. Only the scale factor and the Debye-Waller factor (assuming one Debye-Waller factor for all surface atoms in a first approach) were varied during the fit. The Debye-Waller factor was obtained to be ≈ 8 Å^2, which is quite large compared to the bulk values of the Debye-Waller factor (DW_{As}=0.87 Å and DW_{Ga}=1.43 Å) . The shape of the CTR's calculated for the c(4×4) surface structure agrees better with the measured CTR's than the CTR's calculated for a bulk like terminated surface, however the agreement is still not satisfying.

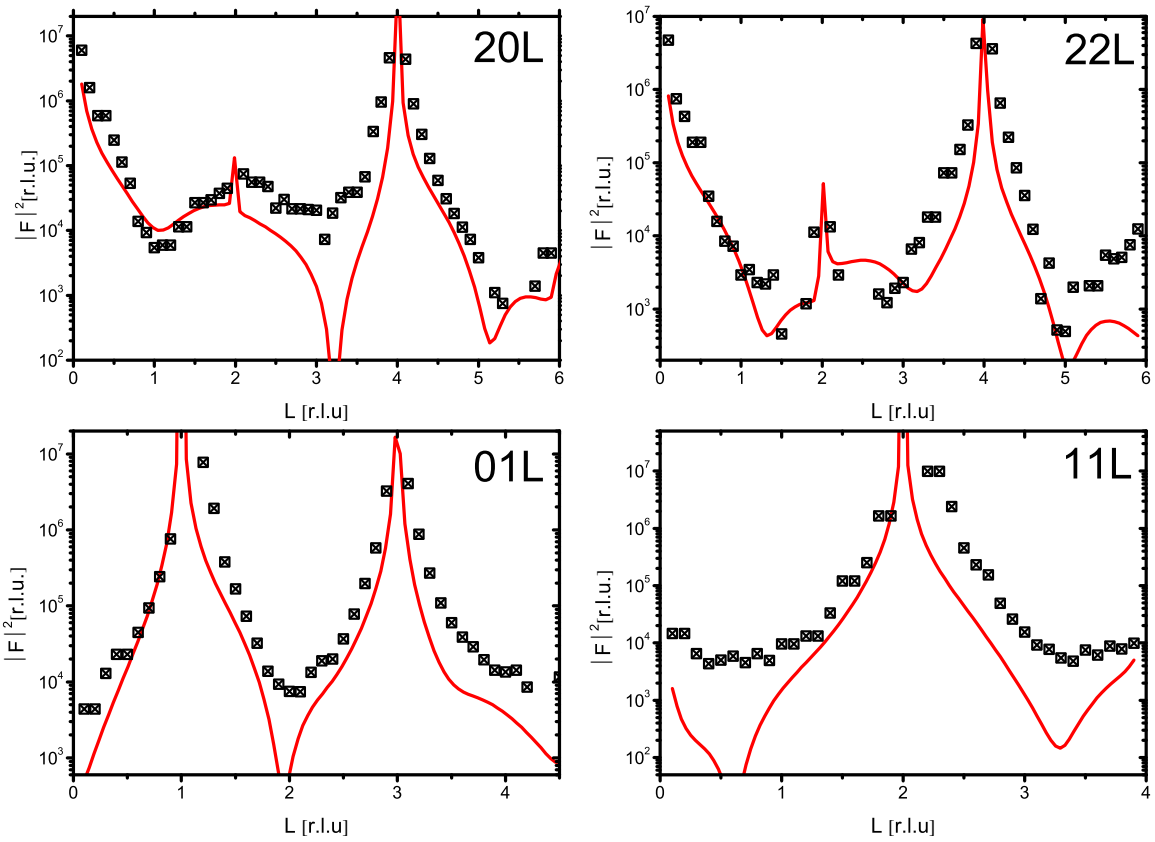

Fig. 5.6: *The square of the structure factor obtained from the integrated intensities measured on the arsenic capped GaAs(001) surface are plotted as black squares. The corresponding CTR's for a (2×4) reconstructed GaAs(001) surface are plotted as a red curve.*

An additional fit of the measured CTR's was carried out assuming a GaAs(001)-β2(2×4) surface structure. The thus obtained CTR's are plotted as red curves in Figure 5.6. The measured CTR's are plotted as black squares. The scale factor as well as the Debye-Waller factor (assuming one Debye-Waller factor for all atoms) were varied. The Debye-Waller factor was obtained to ≈ 4 Å^2. The thus obtained fit agrees better with the measured data. However, the sharp features expected for a pure GaAs(001)-(2×4) reconstruction are not reproduced by the data.

5.3 Summary and Conclusion

The arsenic capped GaAs(001) surface was investigated by AFM and SXRD studies. The arsenic cap oxidizes in air, leading to a not continuous oxygen layer of about 7 nm thickness. This layer is dissolved at 160°C, whereas the underlying arsenic cap remains. The amorphous arsenic gives rise to a typical intensity distribution from which the interatomic distances of the amorphous arsenic can be deduced. The nearest neighbour distance is about 2.4 Å.

No reconstruction peaks can be observed with SXRD. However, CTR's were recorded and reveal a non-bulk like termination of the arsenic covered GaAs. The shapes of the CTR's are the best reproduced by assuming the arsenic rich (2×4)-structure. The buried reconstruction has probably high disorder and/or small domains leading to broad diffuse reconstruction peaks as no sign of a reconstructed interface could be found in the in-plane scans taken from this sample. These effects, especially the disorder could lead to less sharp features in the shape of the rods. Also the presence of minor domains of other arsenic rich reconstruction could increase the disorder and affect the structure at the interface.

The amount of data taken did not allow a more reliable fit using more parameters. The atomic positions of the reconstructed surfaces were fixed, but a deviation of the atomic positions is probable. Accordingly, the atomic displacement factors are tending to high values to compensate the impact of these atoms. The arsenic cap is probably introducing a displacement of the atoms in the first layers compared to a (2×4) reconstruction in UHV. Especially a difference in the z-position of the atoms in the first atomic layers is expected.
The interface is not bulk terminated, but most likely composed of small (2×4)-reconstructed domains. The existence of minor c(4×4) reconstructed domains at the interface can not be excluded.

Chapter 6

The clean GaAs(001) surfaces

6.1 The GaAs(001)-(2×4) surface in UHV

6.1.1 Surface characterization by LEED and STM

The GaAs(001)-(2×4)/c(2×8) surfaces were prepared as described in Section 4.5.3. To obtain information about the starting surfaces used for the electrochemical copper deposition and to optimize the preparation conditions for forming the surface reconstructions, the surfaces were analyzed by LEED and STM. Figure 6.1 (a) shows a STM image taken from a clean GaAs(001)-

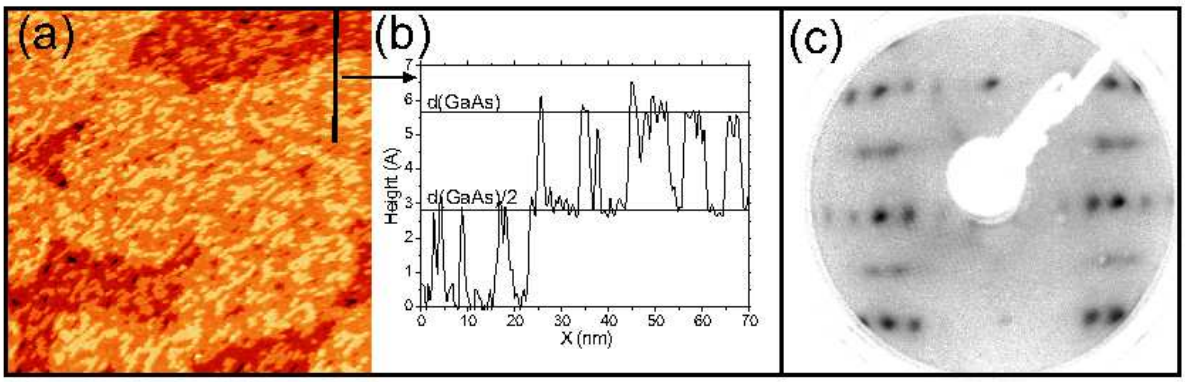

Fig. 6.1: *(a) STM-Image (200 nm × 200 nm) of the (2×4)/c(2×8) reconstructed GaAs(001). In (b) the height profile along the line in (a) is shown. The heights corresponding to half the GaAs lattice constant (first arsenic layer) and the GaAs lattice constant (second arsenic layer) are indicated. (c) LEED-image of a (2×4)/c(2×8)-reconstructed GaAs(001) surface taken at 43 eV .*

(2×4)/c(2×8) surface. The sample was biased negatively to typically -1.8 to -2.2 V so that the filled electronic states were imaged. The best images were achieved with a tunneling current of 0.06 to 0.1 nA. Dimer rows consisting of arsenic blocks of two As-As dimers and running in the [100]-direction are clearly visible. A typical surface exhibits three different height levels. The two lower ones can be identified as terraces with an average width of about 100 nm. The upper one is composed of islands of single dimer rows. The different levels are separated by

steps of 2.8 Å as revealed by Figure 6.1 (b), which corresponds to the thickness of one GaAs bilayer (half the lattice constant of the GaAs bulk unit cell).

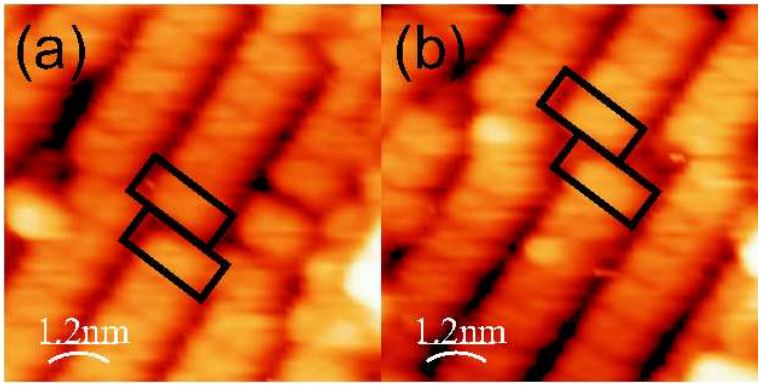

Fig. 6.2: *STM images (6 nm × 6nm) revealing phase boundaries in the [010]-direction. The (2×4) unit cells are highlighted. Displacement of the order of one GaAs unit cell (b) as well as of two GaAs unit cells (a) can be found.*

The dimer rows are not always running straight. Displacements in the [010]-directions of the order of one and two GaAs (1×1) unit cells can be observed as pointed out in Figure 6.2 (a) and (b), respectively. These dislocations are often accompanied by defects in the nearby dimer rows. Displacements of just one unit cell, as shown in Figure 6.2 (a), are more commonly observed.

Figure 6.1 (c) shows the LEED picture taken from a (2×4)-GaAs(001) surface. Due to the coexistence of small domains of the (2×4) and c(2×8) reconstructions no sharp peaks can be observed at a fractional H. The peaks for the c(2×8)-reconstruction are shifted by 0.125 r.l.u. in K for the half H order reflections in comparison to the (2×4) reconstruction. LEED shows an diffraction pattern of the average surface and therefore only diffuse streaks can be observed for the half H order reflections. The presence of the c(2×8)- and (2×4)-reconstructed areas can also be observed with STM, as shown in Figure 6.3. In Figure 6.3 (a) one c(2×8) and four (2×4) unit cells are highlighted. The c(2×8) reconstruction can be created from the (2×4) one by shifting every second dimer row by half a (2×4) unit cell in the [100]-direction, as indicated by the arrow in Figure 6.3 (b).

6.1.2 Surface characterization by X-ray diffraction

After the preparation of a GaAs(001)-(2×4) reconstruction and its verification by LEED, the samples were transferred (under UHV) to the portable UHV-electrochemistry chamber described in Section 4.7.1, which was then moved to the ID32 diffractometer. The pressure in the chamber was about $1 \cdot 10^{-9}$ mbar during the characterization of the reconstructed surface. The (2×4)-reconstruction was investigated using an X-ray beam of 22.5 keV with an incident angle of 0.1° with the sample surface.

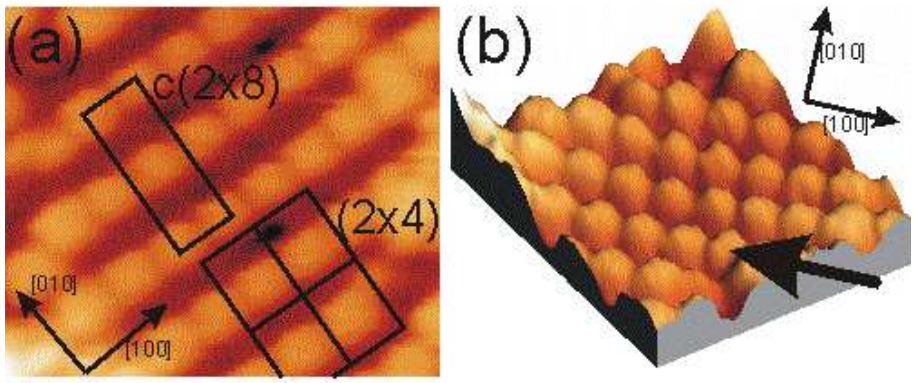

*Fig. 6.3: STM-Image (5.6 nm × 6.6 nm) showing the coexistence of the c(2×8) and the (2×4) reconstruction. In (a) the c(2×8) and the (2×4) unit cells are pointed out. (b) shows a 3D view of the surface. One of the dimer rows (pointed out by an arrow) is shifted by one unit cell in the [*100*]-direction and creates this way a c(2×8)-reconstruction.*

In-plane scans

Figure 6.4 shows an in-plane radial scan along the K-direction of a GaAs(001)-(2×4) reconstructed surface. In addition to the Bragg peaks from the bulk at K=2 r.l.u. and K=4 r.l.u., the 4th-order reconstruction peaks can be observed. Half-order reflections due to the 2× periodicity in the H-direction were too weak to be measured. This weakening is caused by the coexistence of small domains of the (2×4)- and c(2×8)-reconstructions, as described in Section 6.1.1. The presence of such small domains broadens the half H order reflections in the K-direction [73]. As a result these reflections can only be observed by LEED as diffuse streaks (Figure 6.1), which are not resolvable by X-ray diffraction. Similarly, the disorder due to the anti-phase boundaries in the [010]-direction affects the width in the H-direction of the fourth-order reconstruction peaks observed at integer H [47].

Line-shape analysis and modeling The terrace size can be deduced from the in-plane width of a crystal truncation rod where the bulk Bragg reflection is forbidden (H=0 r.l.u. and K=1 r.l.u. or K=3 r.l.u.). Based on the peak width of 0.004 r.l.u., the terrace size was determined to be about 100 nm, which agrees well with the results from STM (section 6.1.1). The width of an in-plane fractional order peak, on the other hand, corresponds to the domains size of the (2×4) or c(2×8) reconstruction and is significantly larger. In addition, due to the presence of the anti-phase boundaries, the half-K order reconstruction peaks are broader than the neighbouring fourth-K order ones, as shown in Figure 6.5.

In the following we discuss the effects of anti-phase boundaries on the peak widths of the fractional K order reflections. As considered in Reference [47], three faulted positions are possible, as illustrated in Figure 6.6. Define $\vec{a}$ and $\vec{b}$ to be the lattice vectors of the (2×4) unit cell in the [100]- and [010]-direction, respectively. Note that under such a coordinate system,

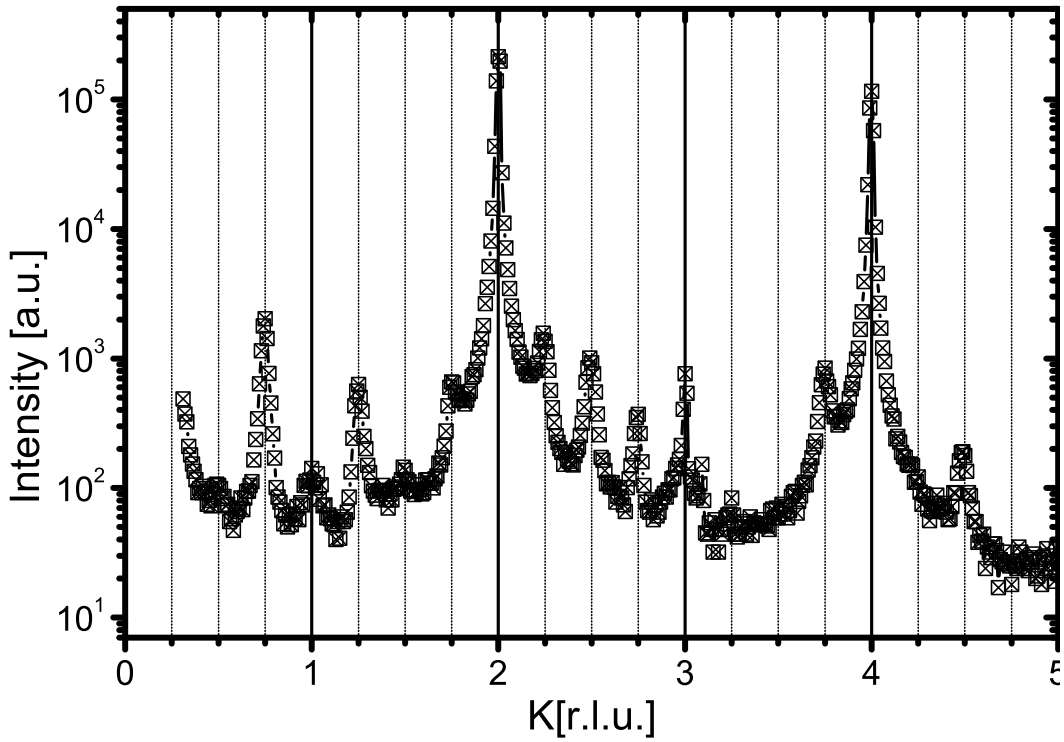

Fig. 6.4: *In-plane radial scan (H=0) along the K direction of (2×4)-reconstructed GaAs(001) surface. The GaAs bulk peaks are situated at K=2 r.l.u. and K=4 r.l.u.. The GaAs(010)- and GaAs(030)-reflections are forbidden, the intensity observed at K=1 r.l.u. and K=3 r.l.u. is due to the truncation of the crystal and their width is therefore reflecting the terrace size of the reconstruction.*

the fractional order reflections mentioned earlier, which appear at K=1/4, 1/2, 3/4,... will now occur at K=1,2,3,..., respectively. The position $\vec{R}$ of each (2×4) unit cell can then be given by the nearest unfaulted (2×4) unit cell at the position $j \cdot \vec{a} + q \cdot \vec{b}$, with q and j being integers, plus the displacement of the cell in the [010]-direction due to the faults, i.e. $\vec{R} = j \cdot \vec{a} + (q + n_j) \cdot \vec{b}$. This additional displacement is given by $n_j \cdot \vec{b}$ with n_j=0, 1/4, 1/2 or 3/4. For $n_j = 0$, $\vec{R}$ points at an unfaulted position (e.g. A in Figure 6.6). For $n_j = \frac{1}{4}$, $\frac{1}{2}$ and $\frac{3}{4}$, $\vec{R}$ points to a faulted unit cell such as B, C and D, respectively, in Figure 6.6. The structure factor F_{total} can then be written as

$$F_{total} = F_{unit\ cell} \sum_{j,q=-\infty}^{\infty} \sigma(j,q) \cdot e^{2\pi i(h \cdot j + k \cdot q)} \cdot e^{2\pi i k n_j}. \tag{6.1}$$

Here, $\sigma(j,q)$ is the shape function of the domain. For $j \cdot \vec{a} + q \cdot \vec{b}$ pointing to a unit cell within in the domain, $\sigma(j,q)$ is equal to one and otherwise σ is zero. $F_{unit\ cell}$ is the structure factor of one (2×4) unit cell. The summation is performed over all (2×4) unit cells on the surface.

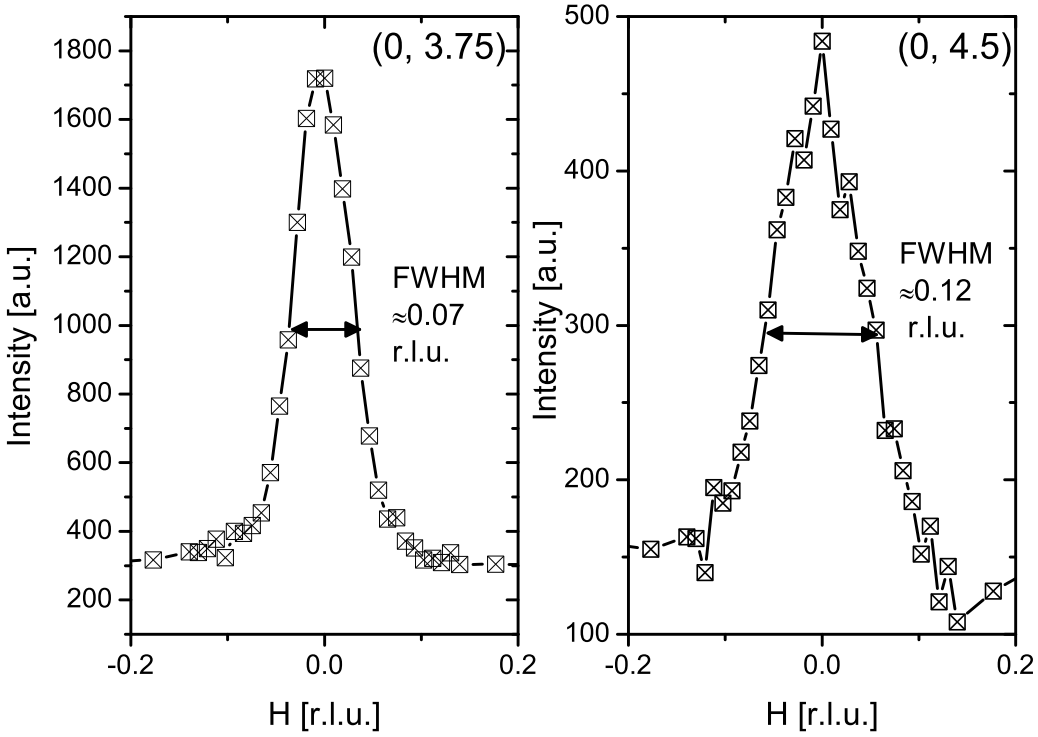

Fig. 6.5: *Rocking scans through two in-plane reconstruction peaks at (a) $\vec{Q}_{||}$=(0, 3.75) and (b) $\vec{Q}_{||}$=(0, 4.5). The rocking scans are plotted in dependence of H which is parallel to the direction of the rocking scans. The plot in H was chosen to show the difference in the peak width between half-order and fourth-order peaks. The peak at $\vec{Q}_{||}$=(0, 4.5) is slightly broader than the peak at $\vec{Q}_{||}$=(0, 3.75) due to phase boundaries along the ×4 direction*

The measured intensity can then be written as

$$\begin{aligned} I(h,k) &\propto |F_{total}|^2 \\ &= |F_{unit\ cell}|^2 \sum_{j,q,j',q'=-\infty}^{\infty} \sigma(j,q)\cdot\sigma(j',q')\cdot e^{2\pi ih(j-j')} e^{2\pi ik(q-q')}\cdot e^{2\pi ik(n_j-n_{j'})}. \end{aligned} \tag{6.2}$$

The broadening of the fractional order peaks is due to the relative displacements of the (2×4) unit cells. It is therefore more convenient to express the intensity in terms of the distance between two unit cells by introducing, $m = j - j'$ and $s = q - q'$. m and s are the distances in the [100]- and [010]-directions, respectively, of two (2×4) unit cells measured from the nearest unfaulted positions (i.e. m and s are both integers) in units of the (2×4) unit cell. $n_m = n_j - n_{j'}$ defines the relative displacement introduced by the faults in the [010]-direction between (2×4)

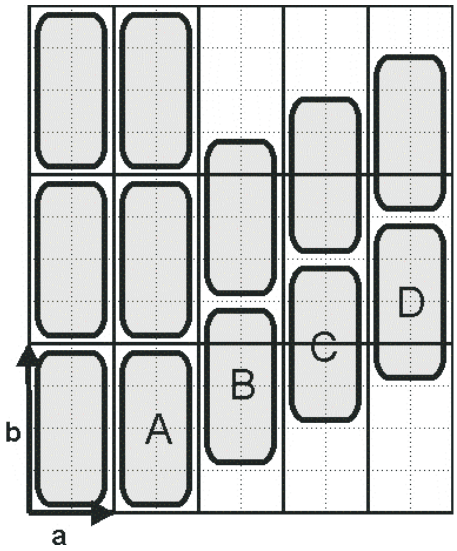

Fig. 6.6: *The three faulted positions possible by shifting the (2×4) unit cell by* $1/4\cdot\vec{b}$ *(B),* $1/2\cdot\vec{b}$ *(C) or* $3/4\cdot\vec{b}$ *(D) against the unfaulted unit cell A.* $\vec{a}$ *and* $\vec{b}$ *are the lattice vectors of the (2×4) unit cell in the [100]- and [010]-direction respectively.*

unit cells that are separated by $m\cdot\vec{a}$ in the [100]-direction. Equation 6.2 then becomes

$$\begin{aligned} I(h,k) &\propto |F_{unit\ cell}|^2 \sum_{m,s=-\infty}^{\infty} \left\{ \sum_{j',q'=-\infty}^{\infty} \sigma(j'+m,q'+s)\cdot\sigma(j',q')\cdot e^{2\pi i k n_m} \right\} e^{2\pi i h m} e^{2\pi i k s} \\ &= |F_{unit\ cell}|^2 \sum_{m,s=-\infty}^{\infty} \left\{ \sum_{j',q'=-\infty}^{\infty} \sigma(j'+m,q'+s)\cdot\sigma(j',q') \right\} \left\langle e^{2\pi i k n_m} \right\rangle_{(j',q')} e^{2\pi i h m} e^{2\pi i k s} \\ &= |F_{unit\ cell}|^2 \sum_{m,s=-\infty}^{\infty} \left\{ \{\sigma\otimes\sigma\}(m,s)\cdot\left\langle e^{2\pi i k n_m} \right\rangle \right\} e^{2\pi i h m} e^{2\pi i k s} \end{aligned} \tag{6.3}$$

Here $\left\langle e^{2\pi i k n_m} \right\rangle_{(j',q')}$ is the phase shift between two (2×4) unit cells separated by $m\cdot\vec{a}$ in the [100]-direction averaged over all possible j' and q'. It can be calculated once the distribution of n_m (=0, 1/4, 1/2, 3/4) as a function of m is assumed. In the second step of Equation 6.3, since $\sigma = 1$ within the domain, $e^{2\pi i k n_m}$ can be averaged and placed outside the summation of the shape function over all j' and q', which is then replaced in the third step by the convolution $\{\sigma\otimes\sigma\}$. Based on the convolution theory, Equation 6.3 can be reduced to

$$\begin{aligned} I(h,k) &\propto |F_{unit\ cell}|^2 \mathscr{F}(\sigma\otimes\sigma)\otimes\mathscr{F}\left(\left\langle e^{2\pi i k_0 n_m}\right\rangle\right) \\ &= |F_{unit\ cell}|^2 |\mathscr{F}(\sigma)|^2 \otimes \mathscr{F}\left(\left\langle e^{2\pi i k_0 n_m}\right\rangle\right). \end{aligned} \tag{6.4}$$

Here k has been replaced by k_0=1, 2 and 3, as the stacking faults only contribute to the peak-broadening in the H-direction. $\mathscr{F}(\sigma)$ and $\mathscr{F}\left(\left\langle e^{2\pi i k_0 n_m}\right\rangle\right)$ are the Fourier transforms of σ and $\left\langle e^{2\pi i k_0 n_m}\right\rangle$ respectively. The quantity $\left\langle e^{2\pi i k_0 n_m}\right\rangle$ is a constant of s and depends only on m, which corresponds to the separation in the [100]-direction between two (2×4) unit cells.

The averaging can be carried out for given probabilities of the relative displacements $n_m = 0$, 1/4, 1/2 and 3/4 of the unit cells in the [010]-direction for a fixed m,

$$\left\langle e^{2\pi i k_0 n_m} \right\rangle = P_{n=0}(m) \cdot e^{2\pi i k_0 \cdot 0} + P_{n=\frac{1}{4}}(m) \cdot e^{2\pi i k_0 \frac{1}{4}} + P_{n=\frac{1}{2}}(m) \cdot e^{2\pi i k_0 \frac{1}{2}} + P_{n=\frac{3}{4}}(m) \cdot e^{2\pi i k_0 \frac{3}{4}}. \tag{6.5}$$

$P_{n=0}(m)$, $P_{n=1/4}(m)$, $P_{n=1/2}(m)$ and $P_{n=3/4}(m)$ describe the probabilities for two unit cells separated by $m \cdot \vec{a}$ in the [100]-direction to have a relative shift in the [010]-direction of 0, $\vec{b}/4$, $\vec{b}/2$ and $\vec{b} \cdot 3/4$, respectively. As displacements of $\frac{1}{4} \cdot \vec{b}$ and $\frac{3}{4} \cdot \vec{b}$ are equiprobable, Equation 6.5 can be written as

$$\left\langle e^{2\pi i k_0 n_m} \right\rangle = P_{n=0}(m) + 2 \cdot P_{n=\frac{1}{4}}(m) \cos(\frac{\pi}{2} k_0) + P_{n=\frac{1}{2}}(m) e^{\pi i k_0} \tag{6.6}$$

For the integer order reflections ($k_0 = 0$) one obtains

$$\left\langle e^{2\pi i k_0 n_m} \right\rangle_{k_0=0} = P_0(m) + P_{1/2}(m) + 2 \cdot P_{1/4}(m) = C_0(m) = 1. \tag{6.7}$$

As the surface is completely covered with reconstructed unit cells (the domain size is taken into account by the shape function σ), the sum of the probabilities over all shifts of the (2×4) unit cells separated by a certain distance is equal to one. No diffuse broadening due to disorder can be observed for a CTR or a bulk Bragg reflection ($k_0 = 0$). For $k_0 = 1$, which corresponds to the reconstruction peak with $K = n \pm \frac{1}{4}$ (n integer), one obtains

$$\left\langle e^{2\pi i k_0 n_m} \right\rangle_{k_0=1} = P_0(m) - P_{1/2}(m) = C_1(m). \tag{6.8}$$

For $k_0 = 2$ corresponding to a reconstruction peak with $K = n + \frac{1}{2}$ (n integer),

$$\left\langle e^{2\pi i k_0 n_m} \right\rangle_{k_0=2} = P_0(m) - 2P_{1/4}(m) + P_{1/2}(m) = C_2(m). \tag{6.9}$$

Equation 6.4 can then be rewritten as

$$I(h,k) = |F_{unit\ cell}|^2 |\mathscr{F}(\sigma)|^2 \otimes \mathscr{C}_{k_0}(\vec{q}), \tag{6.10}$$

where $\mathscr{C}_{k_0}(\vec{q})$ is the Fourier transform of $C_{k_0}(m)$.
The line-shape of the fractional order peak is determined by the shape function σ, leading to peak broadening due to the domain size, and by a broadening of the peak due to the disorder in the ×4 direction expressed by $C_{k_0}(m)$. In Equation 6.10, $\mathscr{C}_{k_0}(\vec{q})$ depends on the k_0 value (k_0=0, 1, 2 or 3) of the measured peak.
The $P_n(m)$ can be related to $P_n(m-1)$ by the probabilities $p_n = P_n(1)$ for the nearest-neighbor unit cell to be displaced by $n \cdot \vec{b}$. Since the probability of having one neighbouring (2×4) unit cell in the [100]-direction is equal to one,

$$p_0 + 2 \cdot p_{1/4} + p_{1/2} = 1. \tag{6.11}$$

$P_n(m)$ can then be derived in terms of p_0, $p_{1/4}$ and $p_{1/2}$ because we know that $P_0(0) = 1$, $P_{1/4}(0) = 0$ and $P_{1/2}(0) = 0$,

$$\begin{aligned} P_0(m) &= \frac{1}{4}\left\{1 + 2\left[p_0 - p_{1/2}\right]^m + \left[p_0 - 2p_{1/4} + p_{1/2}\right]^m\right\} \\ P_{1/4}(m) &= \frac{1}{4}\left\{1 - 2\left[p_0 - 2p_{1/4} + p_{1/2}\right]^m\right\} \\ P_{1/2}(m) &= \frac{1}{4}\left\{1 - 2\left[p_0 - p_{1/2}\right]^m + \left[p_0 - 2p_{1/4} + p_{1/2}\right]^m\right\}. \end{aligned} \tag{6.12}$$

The $C_{k_0}(m)$ can than be expressed as

$$\begin{aligned} C_1(m) &= \left[p_0 - p_{1/2}\right]^m \qquad (6.13)\\ &= \left[p_0 - p_{1/2}\right]^{\frac{x}{|\vec{a}|}} \\ C_2(m) &= \left[p_0 - 2p_{1/4} + p_{1/2}\right]^m = \left[1 - 4p_{1/4}\right]^m \\ &= \left[1 - 4p_{1/4}\right]^{\frac{x}{|\vec{a}|}}. \qquad (6.14) \end{aligned}$$

The Fourier transform $\mathscr{C}_{k_0}(\vec{q})$ of the $C_{k_0}(m)$ are Lorentzian functions with a FWHM of

$$\begin{aligned} FWHM_{k_0=1} &= -\frac{2}{|\vec{a}|}\ln(p_0 - p_{1/2}) \qquad (6.15)\\ FWHM_{k_0=2} &= -\frac{2}{|\vec{a}|}\ln(1 - 4p_{1/4}). \qquad (6.16) \end{aligned}$$

The widths of the fractional order peaks in the H-direction depend on the k_0 value. Nevertheless the integrated intensity, which is proportional to $\int \mathscr{C}_{k_0}(\vec{q})d\vec{q} = C_{k_0}(m=0) = P_0(0) + 2P_{1/4}(0) + P_{1/2}(0) = 1$, is not affected by the presence of the anti-phase boundaries.

It was possible to measure the fractional order peak widths for four half order (k_0=2) and nine fourth order ($k_0 = 1$) in-plane peaks at H=0. After being corrected for the additional broadening of the peak width due to the slit size (Appendix A.2) and domain size (determined from the in-plane peak-widths of the CTR's) the average width of the in-plane fractional order peaks are

$$\begin{aligned} FWHM_{k_0=1} &= 0.111\ \text{Å}^{-1} \\ FWHM_{k_0=2} &= 0.176\ \text{Å}^{-1}. \qquad (6.17) \end{aligned}$$

Using Equations 6.11, 6.15 and 6.16, the disorder probabilities can be determined by

$$\begin{aligned} p_{1/4} &= \frac{1}{4}\left\{1 - e^{-\frac{FWHM_2 \cdot |\vec{a}|}{2}}\right\} = 7.4\% \\ p_{1/2} &= \frac{1}{2}\left\{1 - 2\cdot p_{1/4} - e^{-\frac{FWHM_1 \cdot |\vec{a}|}{2}}\right\} = 2.4\% \qquad (6.18)\\ p_0 &= 1 - 2\cdot p_{1/2} - p_{1/4} = 87.6\%. \end{aligned}$$

This result agrees with the STM images, showing a shift in the [010]-direction every ninth to tenth unit cell along the [100]-direction. Compared to the earlier results on a (2×4)-GaAs(001) surface prepared under arsenic flux ($p_0 = 99.4 \pm 0.4\%\%$, $p_{1/4} = 0.3 \pm 0.2\%$ and $p_{1/2} = \pm 0.1\%$) [47] our surface shows higher disorder but larger terrace sizes (100 nm compared to 57 nm from reference [47]), as observed earlier on GaAs(001) surfaces prepared by the desorption of an arsenic layer [57].

Analysis of the atomic structure

An in-plane data set was taken from a GaAs(001)-(2×4) surface with an X-ray beam energy of 22.5 keV and an incident angle of 0.1° with the sample surface. The half and fourth order

reflections (in K) were recorded at integer H and L=0.03 r.l.u.. The measured section of the reciprocal space covered 0 r.l.u $\leq H \leq$ 5 r.l.u. and 0.25 r.l.u $\leq K \leq$ 5.75 r.l.u.. This is up to now the largest in-plane data set taken on a GaAs(001)-(2×4)/c(2×8) surface. Compared to the present setup, the MBE diffraction chambers used to measure the GaAs(001)-(2×4) surfaces before [45, 47] allowed only limited access of the reciprocal space, which was restricted either by the beryllium windows for the diffracted beam or the maximum beam energy. In addition to the in-plane fractional order reflections, we recorded seven CTR's. The fractional order rods were too broad (as discussed in the previous section) to be measured at higher L.

The Patterson map calculated from the measured in-plane reflections is shown in Figure 6.7 (a). In comparison, the Patterson map calculated from the atomic structure predicted by the first-principles calculations [48] for the $\beta 2$ phase of the GaAs(001)-(2×4) surface is shown in Figure 6.7 (b). The Debye-Waller factors for the Patterson map of the theoretical positions were estimated by scaling the in-plane structure factors calculated from the atomic positions to the measured ones allowing only the Debye-Waller factors and a scale parameter to change. The

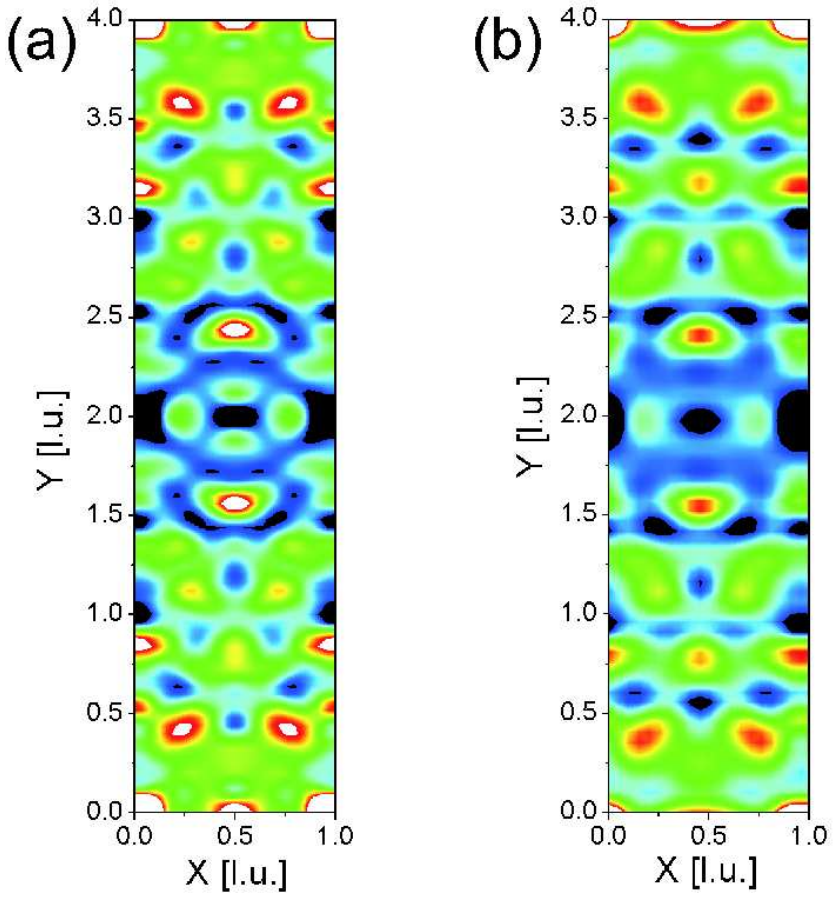

Fig. 6.7: *In-plane Patterson map of a (1×4) unit cell of the (2×4)-GaAs(001) surface. (a) The Patterson-map calculated from the measured in-plane data. (b) The Patterson map calculated from the atomic positions calculated by first-principle calculations [48]. The intensity range is going from black for low intensity over blue, green, yellow and red to white indicating high intensity.*

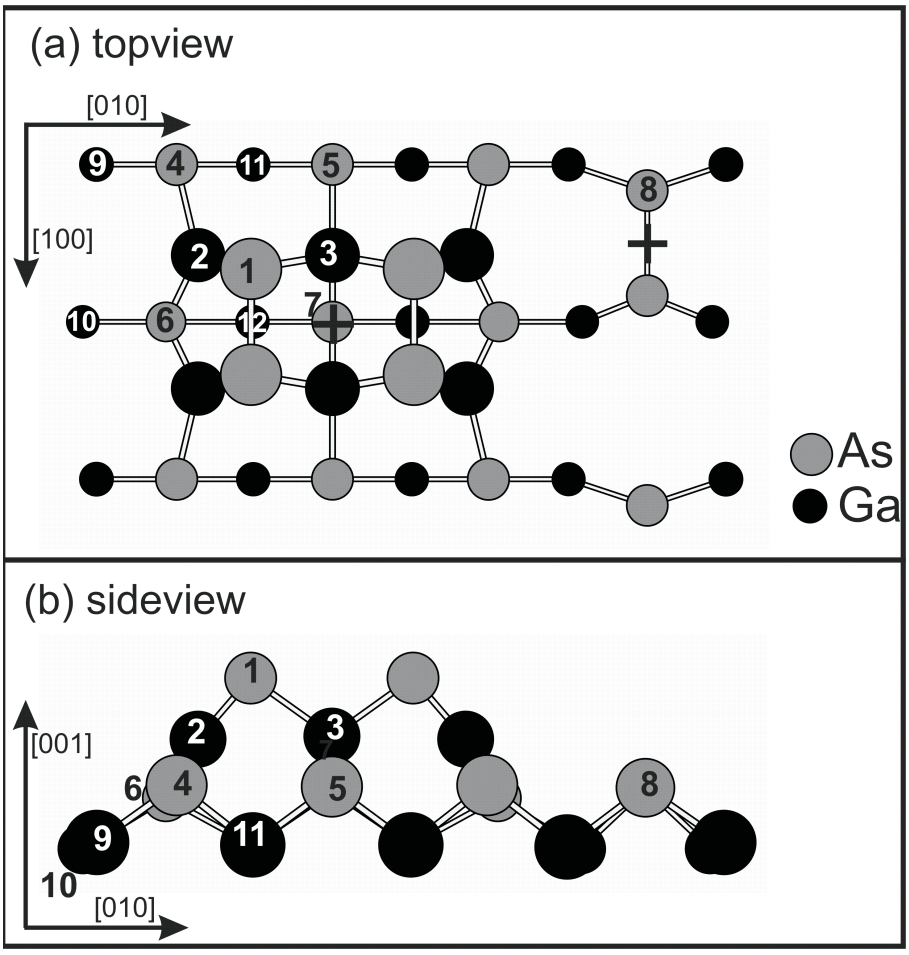

Fig. 6.8: *The (2×4) unit cell and the independent atoms introduced in the refinement procedure are presented. The base vectors of the GaAs (1×1) unit cell are indicated. (a) The top-view, looking in the* $[00\bar{1}]$ *direction. The positions of the two 2-mm symmetries are indicated by crosses. (b) The side-view in the* $[\bar{1}00]$*-direction of the first two atomic bilayers .*

thus obtained Debye-Waller mean square vibrational amplitudes have values between 0.3 and 18 Å^2. The high values of the Debye-Waller factor are probably due to unrelaxed atomic positions. As only reflections at integer H could be measured, the Patterson map represents a (1×4) unit cell.

Both the measured and calculated maps show similar features. However, there is some discrepancy at positions corresponding to large interatomic distances (at about Y = 1.7 l.u., X = 0 and Y = 1.9 l.u., X = 0.5 l.u.).
The structure refinement was performed by using the program *fit* written by Oliver Bunk. The atomic positions down to the second bilayer were adjusted by the refinement. Figure 6.8 shows the atoms included in the refinement assuming the $\beta 2$ model for the (2×4) reconstruction of

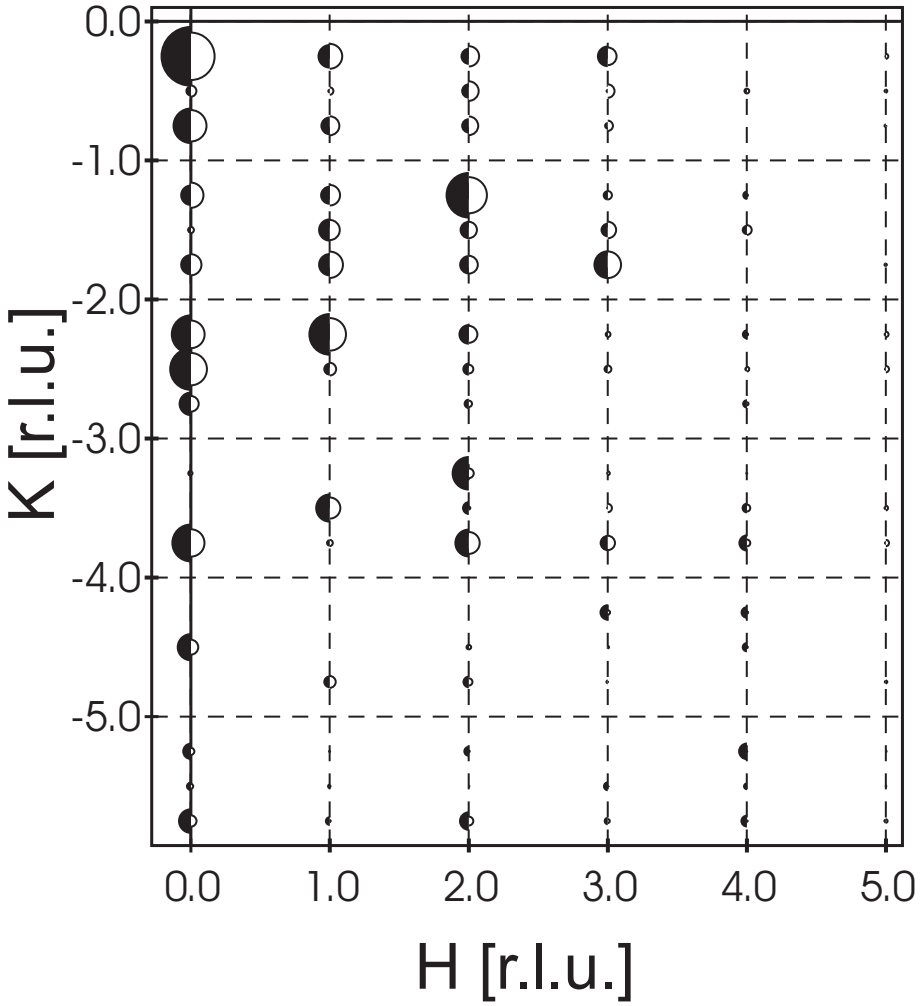

Fig. 6.9: *Comparison between measured (filled semicircles) and calculated (open semicircles) in-plane structure factors. H and K are given in units of the reciprocal lattice of the GaAs bulk 1×1 using surface coordinates.*

the GaAs(001) surface. The model consists of two arsenic dimers in the top-layer bonded to six gallium atoms in the second layer. One arsenic dimer in the third layer bonded to four gallium atoms in the fourth layer is assumed. The gallium and arsenic atoms in the third and fourth layer are close to bulk positions. The gallium and arsenic sites in the first and second layers above the arsenic dimer in the third layer are not occupied.

Two symmetry constraints, both 2-mm, were applied to the structure. The centers of the mirror planes are marked by the crosses in Figure 6.8 (a). One 2-mm symmetry is applied to the arsenic dimer (Atoms 8) in the second bilayer with the center of rotation and the two mirrors at the center of this dimer. The other 2-mm symmetry is applied to all the other atoms (Atoms 1-7 and 9-12), assuming the center of rotation and the mirror planes at the center of the two arsenic dimers in the toplayer (Atoms 1). With these symmetry constraints the structure of the unit cell contains twelve independent atoms. Only four of these atoms (Atoms 1, 2, 3 and 8) have no fixed x-coordinates and four of them (Atoms 3, 5, 7 and 8) have fixed y-coordinates due to the symmetry constraints.

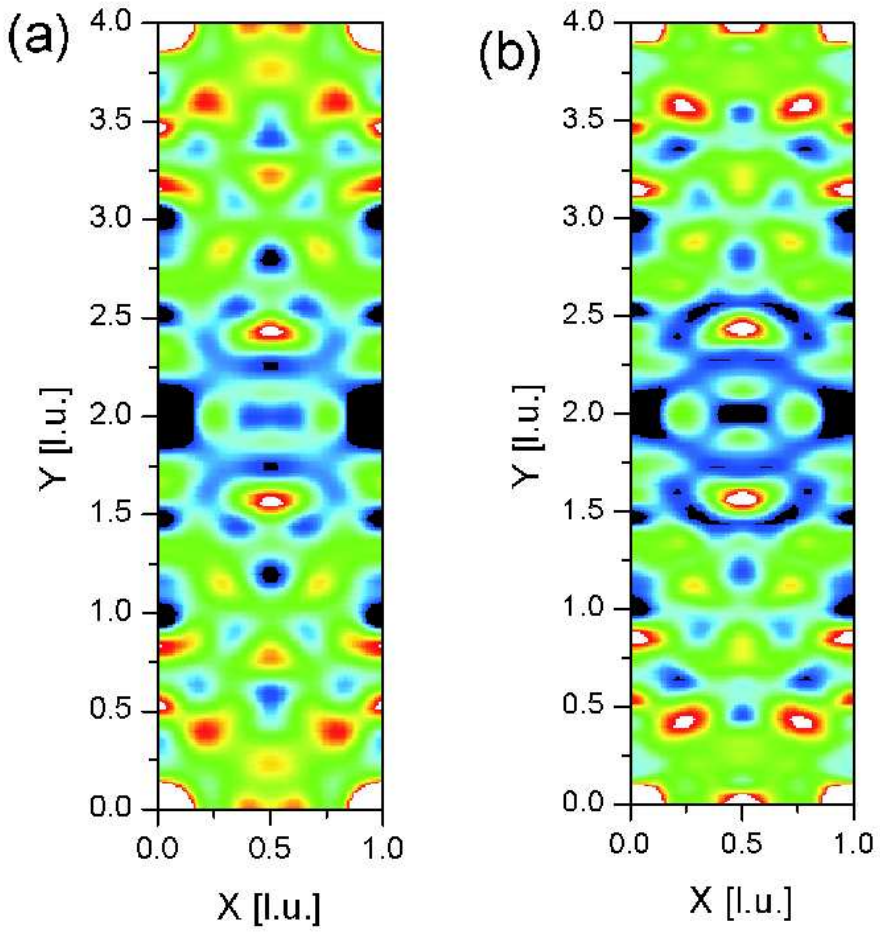

Fig. 6.10: *The Patterson map calculated for the positions obtained from the refinement (a) is shown together with the Patterson map (b). The intensity range is going from black for low intensity over blue, green, yellow and red to white, indicating high intensity.*

Twelve in-plane and twelve out-of-plane positional parameters were refined together with six Debye-Waller factors (two for the bulk and one for each layer) and one scale factor. In the first step only the in-plane data (L=0.03 r.l.u.) was fitted, allowing the variation of the Debye-Waller factors and the in-plane positions of the atoms. Finally, the CTR's were included, allowing also the change of the atomic positions in the z-direction. Figure 6.9 shows the comparison between the measured (filled semicircles) and fitted (open semicircles) in-plane structure factors. The radii of the semicircles are proportional to the amplitudes of the structure factors. The Patterson map calculated with the refined in-plane structure factors is shown in Figure 6.10 (a), in comparison with the one calculated from the measured data [Figure 6.10 (b)]. The region around Y=2 l.u. is reproduced better than in Figure 6.7, where the (2×4)-structure was taken from the first principle calculations.

The measured (black squares) and fitted (red line) CTR's are shown in Figure 6.11. The measured data are not very well reproduced at the anti-Bragg positions. The introduction of surface

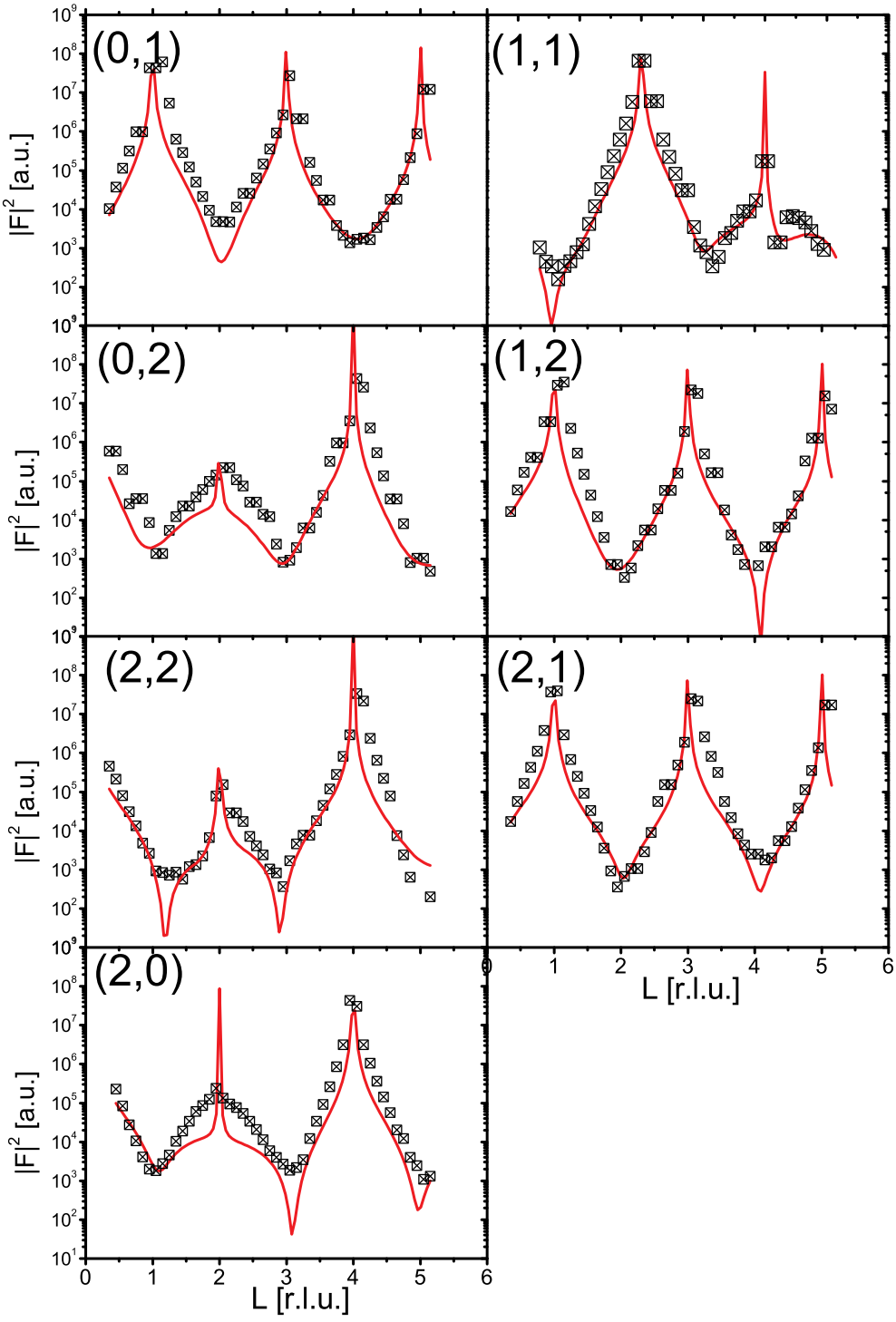

Fig. 6.11: *Comparison between measured (black squares) and calculated (red line) crystal truncation rods taken from the GaAs(001)-(2×4) surface.*

		fit				theory		
atom	element	Δx	Δy	Δz	DW	Δx	Δy	Δz
1	As	0.164	-0.018	0.013	8.79	0.183	0.015	0.012
2	Ga	0.076	0.146	-0.023	1.55	0.0275	0.1525	-0.055
3	Ga	0.076	fixed	0.004	1.55	0.0525	0.0125	-0.005
4	As	fixed	0.009	0.012	2.56	0	0.0	0.007
5	As	fixed	fixed	0.012	2.56	0	0.0075	0.028
6	As	fixed	-0.058	-0.032	2.56	-0.005	-0.03	-0.04
7	As	fixed	fixed	0.001	2.56	-0.005	0.0075	-0.046
8	As	0.166	fixed	0.015	2.56	0.180	0.0025	0.0212
9	Ga	fixed	0	0.012	2.49	0.025	0.04	0.007
10	Ga	fixed	0.087	-0.012	2.49	-0.0325	-0.06	-0.0177
11	Ga	fixed	-0.004	0.001	2.49	0	0.0125	0.0053
12	Ga	fixed	-0.009	0	2.49	-0.0025	-.005	-0.03

Tab. 6.1: *The atomic positions obtained from the refinement and the Debye-Waller factors for the first atomic layers introduced in the fitting procedure are given in the columns called "fit". For comparison the theoretical predicted positions are given in the column "theory". The numbering of the atoms corresponds to the one shown in Figure 6.8. The positions are given as a deviation from the bulk position (in Å) of each atom. Some positions are fixed to the bulk values due to symmetry constraints (Δx=0 and Δy=0).*

roughness as an additional fit parameter does not improve the fit. The refined Debye-Waller factor for the arsenic atoms in the bulk is $DW_{As} = 0.416$ Å^2 and the one for the gallium atoms is $DW_{Ga} = 1.486$ Å^2. The refined atomic positions and the Debye-Waller factors of the first four atomic layers are given in Table 6.1. As comparison the theoretically predicted positions are also given in this table [48]. The atoms are numbered according to Figure 6.8.

The refined displacements from the bulk positions of the arsenic atoms forming the dimers in the first and third layers are less than those obtained from the first principles calculations and those observed earlier [47]. The bond length obtained for the arsenic dimers in the first layer (Atom 1) is 2.688 Å (compared to 2.54 Å obtained from the first principles calculations [48]). The arsenic dimer in the third layer (Atom 8) has a bond length of 2.663 Å (compared to 2.56 Å obtained from the first principles calculations [48]). The z-value of the top arsenic dimers agrees with the z-shift calculated by the first principles calculations. This value was determined only by the fit of the CTR's as no fractional order rods were available. The y-shift of the arsenic dimers is of the same order of magnitude as the theoretical one. However, an increase of the distance between the two top arsenic dimers is observed, in contradiction to the theory.
The gallium atoms in the second layer (Atoms 2 and 3 in Figure 6.8) are found to shift uniformly in the x-direction by 0.3 Å. The theoretical calculations predict a non-uniform shift in the x-direction with a larger displacement expected for Gallium 3.

The observed discrepancies between the theoretical positions and the refined ones are in the

error range. The differences of the values is about 0.1 Å. However, *ab-initio* calculations of the influence of dimer kinks on the atomic structure of a GaAs(001)-(2×4) were carried out by Shiraishi and Ito [74]. The weakening of the arsenic dimers due to such defects is predicted. In these calculations only shifts of one (1×1) unit cell in the [010]-direction were investigated. Such a kink leads to the weakening of the nearby arsenic dimer in the second bilayer. This results in an elongation of 20% of this dimer. This elongated arsenic-arsenic bond-length corresponds to 3.07 Å. They also found that surface kinks on a GaAs(001)-c(2×8) surface does not affect the dimer bond length. However, the observed kinks resulting from shifts of the arsenic dimers by two (1×1) unit cells in the [010]-direction were not considered in these theoretical calculations.

The uniform shift of the gallium atoms in the second layer in the *x*-direction is probably due to the disorder in the [010]-direction. The interaction between two (2×4) unit cells in the *x*-direction is getting more uniform due to the shift in the [010]-direction leading to less differences in the position of atoms at the same *x*-position. An earlier, on formerly arsenic capped surfaces, observed mixture of the α and $\beta 2$ or the $\beta 2$ and γ structure [75] could exist. The positions determined by the refinement are average values fitting the best the assumed $\beta 2$ model of the reconstruction. Disorder as well as the coexistence of minor phases of other (2×4) reconstructions locally affect the structure of the (2×4) unit cell.

6.2 The GaAs(001)-(4×2) surface in UHV

The GaAs(001)-(4×2) surfaces were prepared as described in section 4.5.3. Afterwards these surfaces were characterized by LEED, STM and SXRD.

6.2.1 Surface characterization by LEED and STM

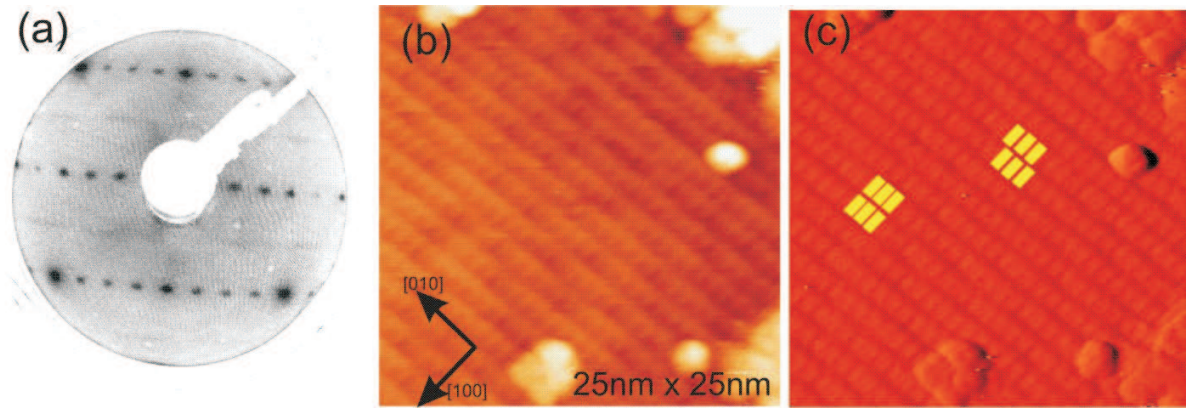

Fig. 6.12: *(a) A LEED-image of a (4×2)-reconstructed GaAs(001) surface taken at 40 eV. The fourth order reconstruction peaks are clearly visible. However, the half order reconstruction peaks can only be observed as a streaky line due to the presence of the (4×2) and c(8×2) reconstruction. (b) A STM image (25 nm × 25 nm) of the GaAs(001)-(4×2) surface taken at a bias voltage of -3 V and a tunnel current of 0.1 nA. Straight running rows can be observed in the [010]-direction. (b) The derivative of the STM-image is shown, enhancing the height contrast, the (4×2) unit cells can be identified. A coexistence of the (4×2) and c(8×2) structure can be observed.*

In Figure 6.12 (a) a LEED picture taken from a GaAs(001)-(4×2)/c(8×2) surface is shown. Only diffuse streaks can be observed for half-K order reflections due to the coexistence of small domains of the (4×2) and c(8×2) reconstructions. For the c(8×2)-reconstruction these peaks are shifted by 0.125 r.l.u. in H for half order K in comparison to the (4×2) reconstruction.
Figure 6.12 (b) shows a STM-image (25 nm × 25 nm, bias =-3 V, tunneling current =0.1 nA) taken from a GaAs(001)-(4×2)/c(8×2) reconstructed surface. Rows running in the [010]-direction can be identified. Compared to the GaAs(001)-(2×4)/c(2×8) surface studied in section 6.1.1, the rows are more straight and no kinks resulting from the displacements of the rows in the [100]-direction can be observed. However, by taking the derivative view [Figure 6.12 (c)] of Figure 6.12 (b), the contrast is enhanced and the individual (4×2) unit cells can be resolved. A shift of several rows in the [010]-direction by half a (4×2) unit cell can be observed [as highlighted by the yellow rectangles in Figure 6.12 (c)], indicating the coexistence of the (4×2) and c(8×2) structures. The islands present on the surface (Figure 6.12) are probably Ga-droplets, which often form during the preparation of gallium-rich GaAs(001)-surfaces by thermal annealing [57]. It was more difficult to establish stable tunneling conditions with the STM on the GaAs(001)-(4×2)/c(8×2) surface than on the (2×4)/c(2×8) one. This could be due

to the adsorption of Ga-atoms on the tip coming from the gallium islands present on the surface. Consequently, measuring larger STM images was not possible for the GaAs(001)-(4×2) surfaces.

6.2.2 Surface characterization by X-ray diffraction

After the preparation of the GaAs(001)-(4×2)/c(8×2) surface and its verification by LEED, the sample was transfered into the portable UHV-electrochemistry chamber, which was then mounted on the ID32 diffractometer. The (4×2)/c(8×2) structure was investigated using an X-ray beam of 23.5 keV and an incident angle of 0.106° with the sample surface.

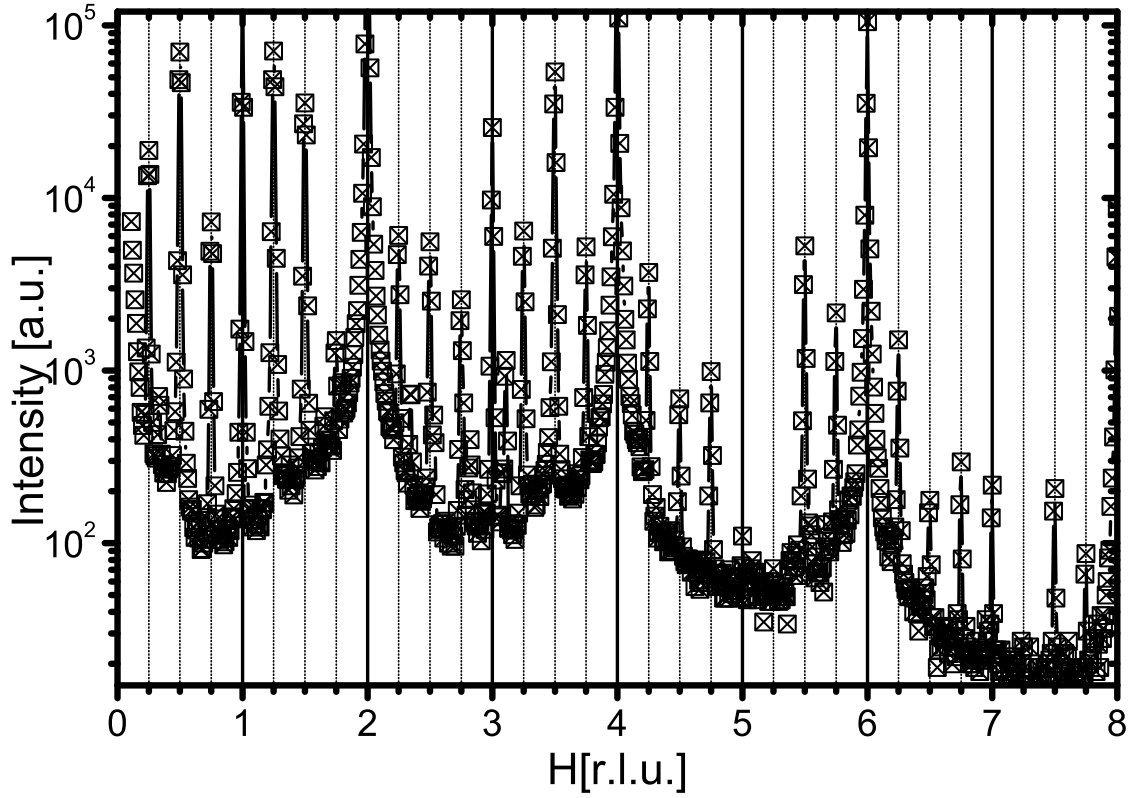

Fig. 6.13: *A radial in-plane scan (H=0) along the H direction of (4×2)-reconstructed GaAs(001) surface. The GaAs(020), (040) and (060) Bragg reflections can be identified together with fourth order reconstruction peaks (at H=0.25 r.l.u., 0.5 r.l.u, 0.75 r.l.u, 1.25 r.l.u.,...). Additional peaks not belonging to the (4×2) structure can be observed at H=2.3 r.l.u and 3.2 r.l.u. probably belonging to a more gallium rich structure (n×6) also present on the surface.*

A radial in-plane scan at K=0 r.l.u. and L=0.06 r.l.u. is shown in Figure 6.13. The GaAs Bragg reflections as well as the peaks coming from the crystal truncation rods of the GaAs(001) surface are observed at H equal to odd and even integer values, respectively. In addition, fourth order reconstruction peaks (H=0.25, 0.5., 0.75,...) are observed due to the (4×2)/c(8×2) structure of the surface. There are also peaks which can not be assigned to the (4×2)/c(8×2) structure, e.g. at H=2.3 and 3.2 r.l.u., and may belong to a more gallium-rich (n×6) surface structure.

An in-plane data set (L=0.06 r.l.u.) of the fractional order reflections at integer K was recorded. Two in-plane rocking scans through the reconstruction peaks at $\vec{Q}$=(1.25, 0, 0.06) and $\vec{Q}$=(2.75,

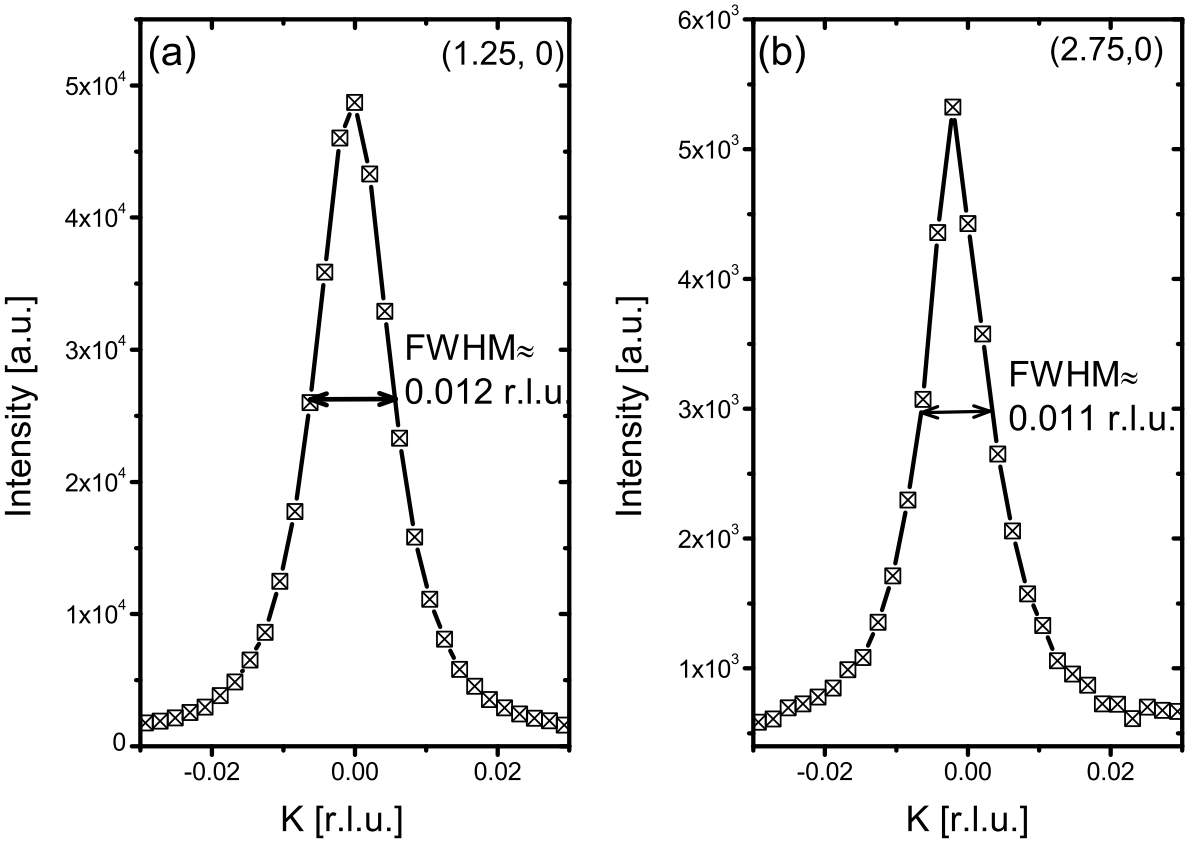

Fig. 6.14: *Two in-plane rocking scans through the reconstruction peaks at $\vec{Q}$=(1.25, 0, 0.06) (a) and $\vec{Q}$=(2.75, 0, 0.06) (b) are presented. The peaks are plotted in dependence of K, which is parallel to the direction of the rocking scan.*

0, 0.06) are presented in Figure 6.14 (a) and (b), respectively. The corrected peak-widths are about the same for all reconstruction peaks. This is consistent with the STM observation on the gallium-rich surface that reviews no kinks in the [100]-direction, which can contribute to the peak broadening if present.

The average corrected peak-width is about 0.0036 r.l.u.. The corresponding size of the terraces is about 111 nm, which is similar to the terrace size obtained for a GaAs(001)-(2×4) surface. The Patterson map calculated from the measured in-plane data set is shown in Figure 6.15 (a). In comparison, the Patterson map calculated with the atomic positions and Debye-Waller factors published by Kumpf *et al.* [53] based on the refinement of SXRD data is shown in Figure 6.15 (b). Both Patterson maps show similar features such as the strong peaks at (1.7, 0) and (2.3, 0) arising from the subsurface gallium dimers. However, some discrepancies between the two Patterson maps are present. These differences may be attributed to the coexistence of more gallium-rich (n×6) structures.
By measuring the in-plane fractional order reflections, especially for those of half-H order, the (n×6) structure may contribute to the peak intensities. The Patterson map calculated from the

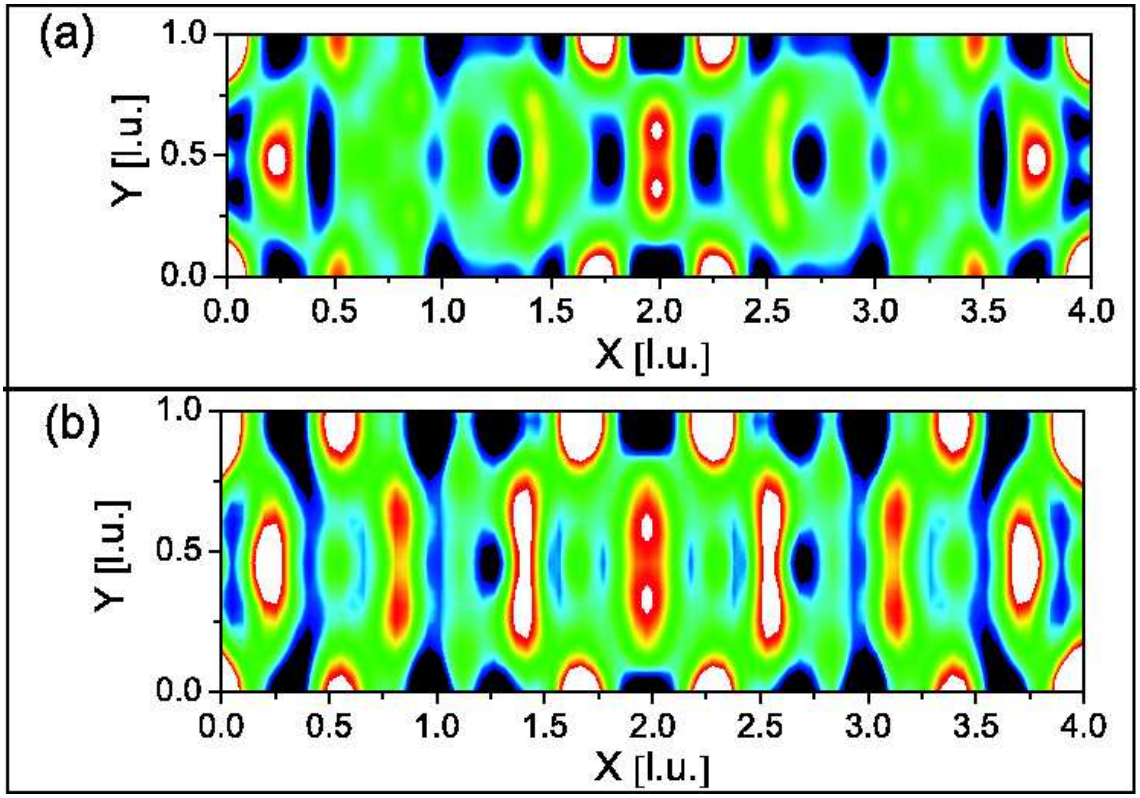

Fig. 6.15: *In-plane Patterson map of a (4×1) unit cell of the (4×2)-GaAs(001) surface. (a) The Patterson map calculated from the measured in-plane fractional order rods. (b) Patterson map calculated with the atomic positions and the Debye-Waller factors given by Kumpf et al. [53]. The intensity range is going from black for low intensity over blue, green, yellow and red to white indicating high intensity.*

measured data therefore does not represent a pure (4×2)/c(8×2) structure. Six crystal truncation rods of the GaAs(001)-(4×2)/c(8×2) surface were recorded. They are shown in Figure 6.16 (black squares) together with the calculated crystal truncation rods based on the (4×2)/c(8×2) structure published by Kumpf et al. [53] (red line in Figure 6.16). The only free parameter to fit the calculated rods to the measured ones was a scale factor. The calculated and the measured rods show the same features. However, some disagreement, especially close to the weak bulk Bragg reflections such as $\vec{Q}$=(0, 2, 2) and $\vec{Q}$=(2, 0, 2), can be observed. Introducing an additional roughness parameter, which tends to vanish in the refinement, does not improve the fit. The disagreement between the calculated and the fitted rods may be also due to the coexistence of some other gallium-rich reconstructions.

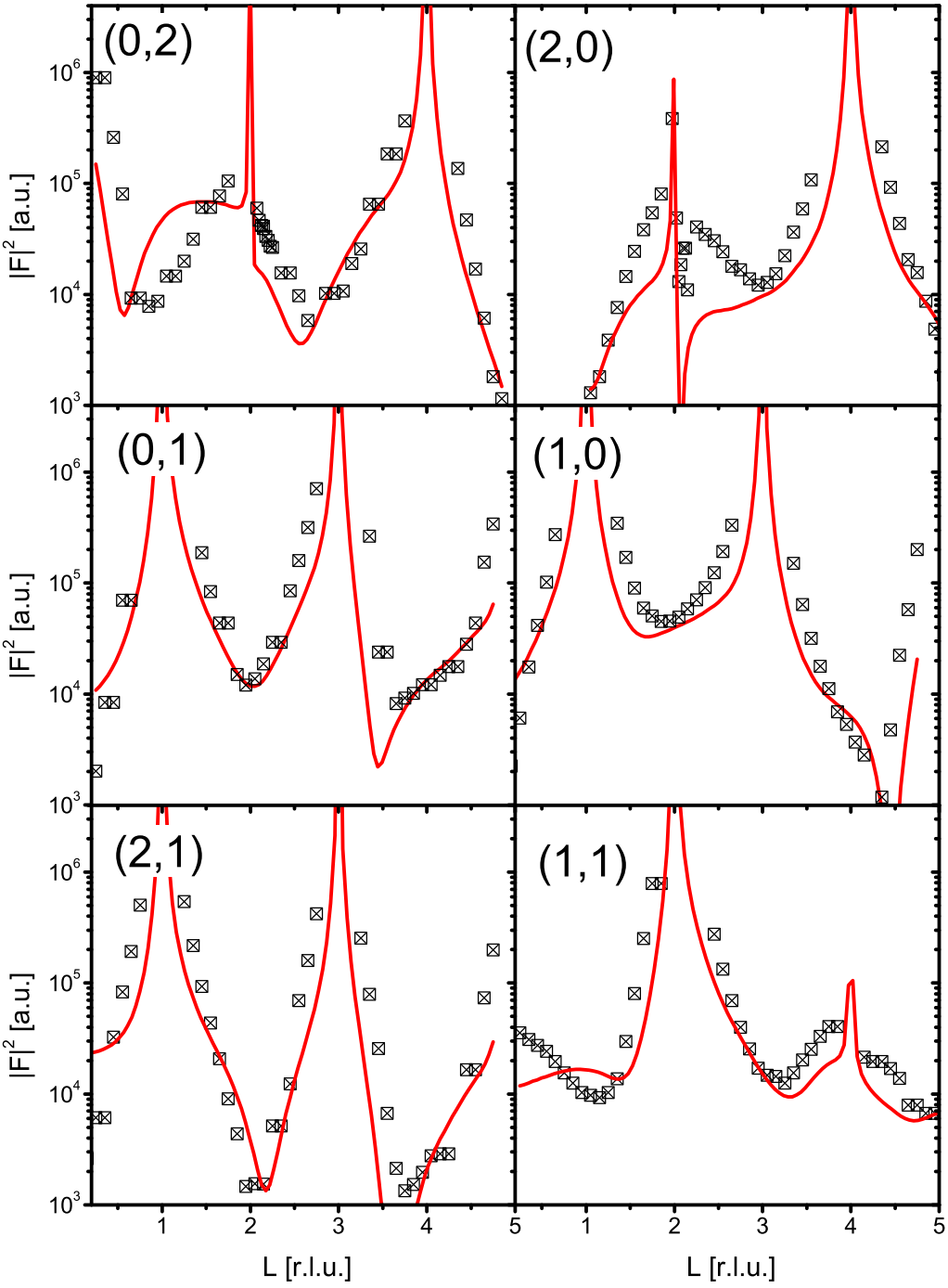

Fig. 6.16: *The crystal truncation rods taken from a GaAs(001)-(4×2)/c(8×2) surface (black squares) are shown together with the calculated crystal truncation rods based on atomic positions of the (4×2)/c(8×2) structure published by Kumpf et al. [53] (red line). The only free parameter to fit the rods calculated from the (4×2)/c(8×2) structure was the scale factor.*

6.3 The UHV prepared GaAs(001) surfaces under atmospheric pressure in inert gas

In order to perform electrochemical processes on the UHV prepared surfaces, the samples first have to be exposed to ambient pressure. After UHV characterization of the surfaces and before electrochemical measurements, the UHV-electrochemistry chamber was vented to nitrogen. To deduce more information about the starting surface prior to the electrodeposition, the samples were characterized by X-rays under nitrogen at ambient pressure. In this section the thus obtained results on a GaAs(001)-(2×4) and a GaAs(001)-(4×2) surface in nitrogen are presented.

6.3.1 The GaAs(001)-(2×4) surface under ambient nitrogen pressure

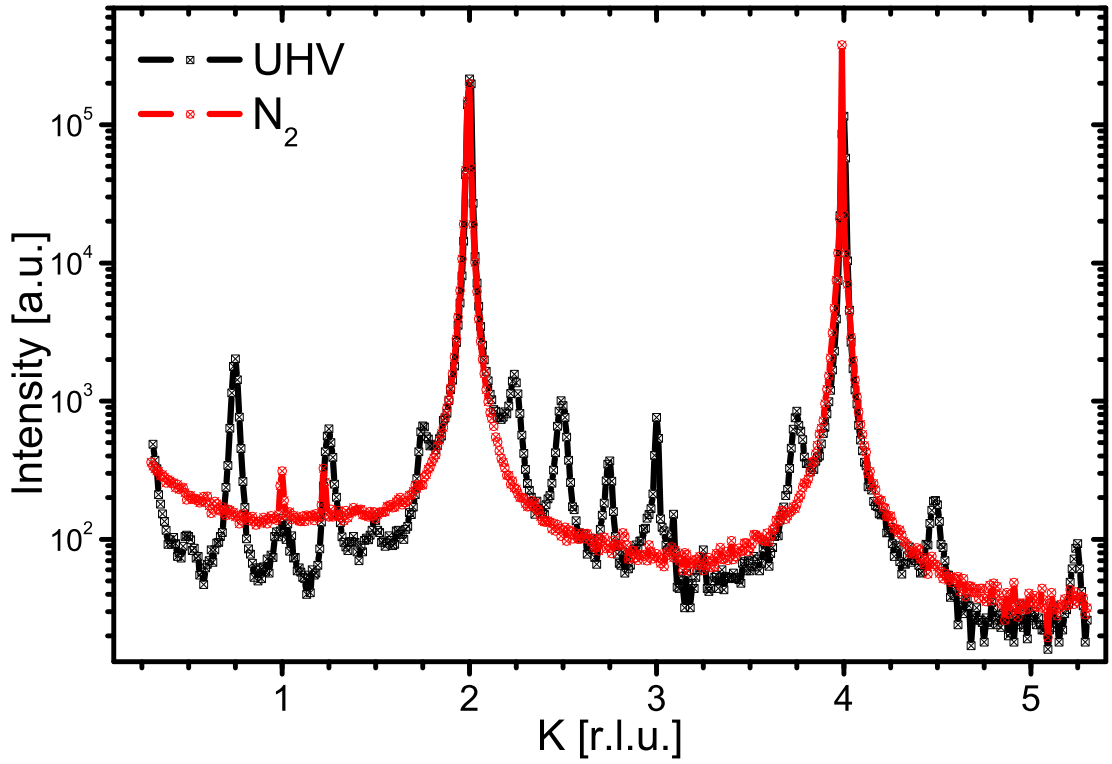

Fig. 6.17: *A radial in-plane scan (H=0 r.l.u., L=0.06 r.l.u.) taken on a GaAs(001)-(2×4) surface in UHV is presented (black squares) together with the radial in-plane scans on the same surface in nitrogen at ambient pressure (red circles)*

In Figure 6.17, radial in-plane scans (H=0 r.l.u., L=0.06 r.l.u.) of a GaAs(001)-(2×4) surface in UHV (black squares) and under atmospheric nitrogen pressure (red circles) are shown. The background is higher in nitrogen than in UHV especially for small $|\vec{Q}|$. In UHV the fractional order peaks due to the (2×4) reconstruction are visible. At ambient nitrogen pressure the reconstruction seems to be lifted as the reconstruction peaks disappear. Only the (020) and (040) Bragg reflections from the GaAs can be observed.

To get more information about the surface exposed to ambient pressure, a specular rod and six

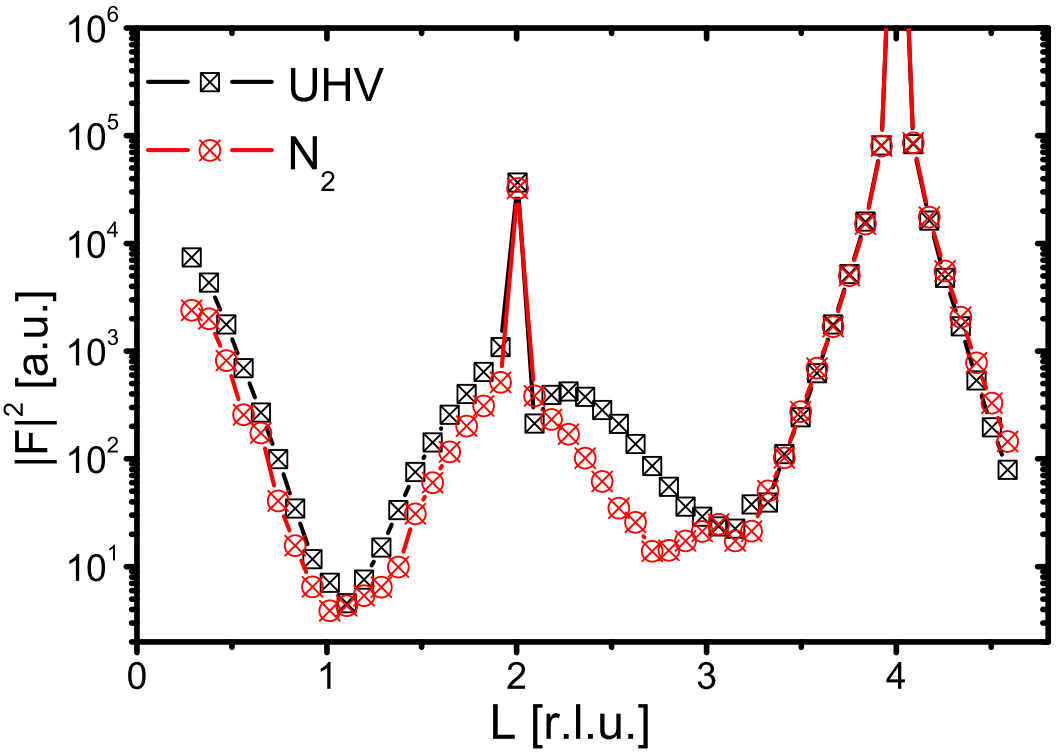

Fig. 6.18: *A specular rod taken on a GaAs(001)-(2×4) surface is presented (black squares) together with the specular rod taken on the same surface in nitrogen at ambient pressure (red circles)*

crystal truncation rods were recorded. The specular rods taken from a surface in UHV (black squares) and in nitrogen atmosphere (red circles) are shown in Figure 6.18. The GaAs(002) and (004) Bragg peaks are visible at L=2 r.l.u. and at L=4 r.l.u.. In UHV the shape of the specular rod is determined by the (2×4) reconstruction. The dip in the structure factor close to L=2 r.l.u. can be explained by the deviation of the atomic z-positions in the first atomic bilayer. This dip disappears under atmospheric nitrogen pressure, which indicates a relaxation and/or a rearrangement of the former reconstructed surface. The rod does not have the typical shape of a bulk terminated surface.

The crystal truncation rods taken in UHV on a (2×4) terminated GaAs(001) surface and the ones taken on the same surface under ambient nitrogen pressure are shown in Figure 6.19. Similar to the specular rods no significant differences between the CTR's taken of the surface in nitrogen and in UHV can be observed. Only sharp features are disappearing, in particular the dip in the structure factor in the (1,1)-rod close to L=4 r.l.u.. The intensity at the anti-Bragg positions is not changing, indicating still a smooth surface after exposure to nitrogen. After venting, the (1,2)- and the (2,1)-rod have the same shape and the same intensity at the anti-Bragg position.

The surface after exposure to nitrogen does not change into a bulk terminated surface. However, the reconstruction is most probably lifted. The first atomic layers of the surface seem to be relaxed and also the adsorption of nitrogen on the surface could be possible.

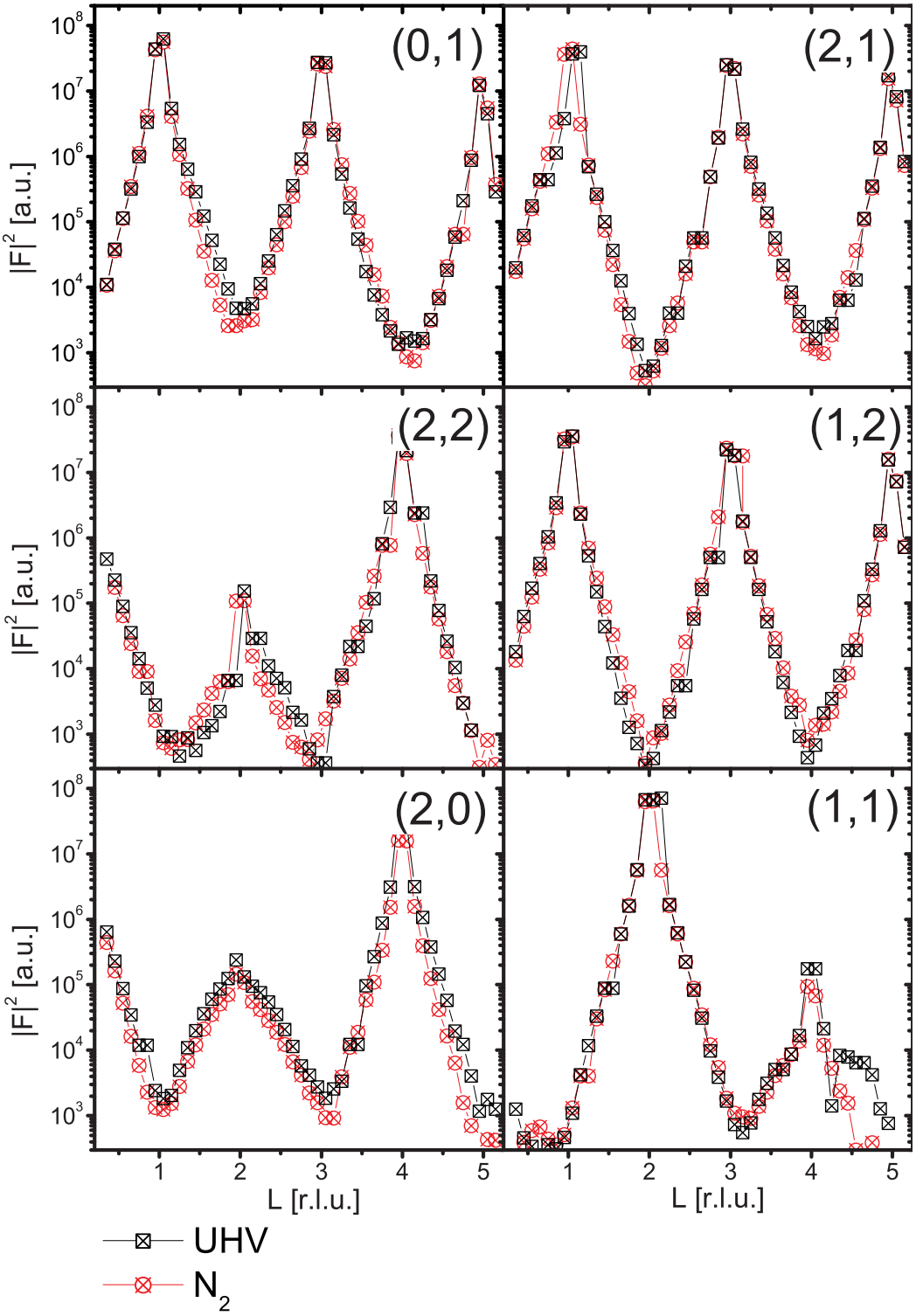

Fig. 6.19: *Crystal truncation rods taken on a GaAs(001)-(2×4) surface in UHV are shown (black squares) together with the crystal truncation rods taken on the same surface in nitrogen at ambient pressure (red circles).*

6.3.2 The GaAs(001)-(4×2) surface under ambient nitrogen pressure

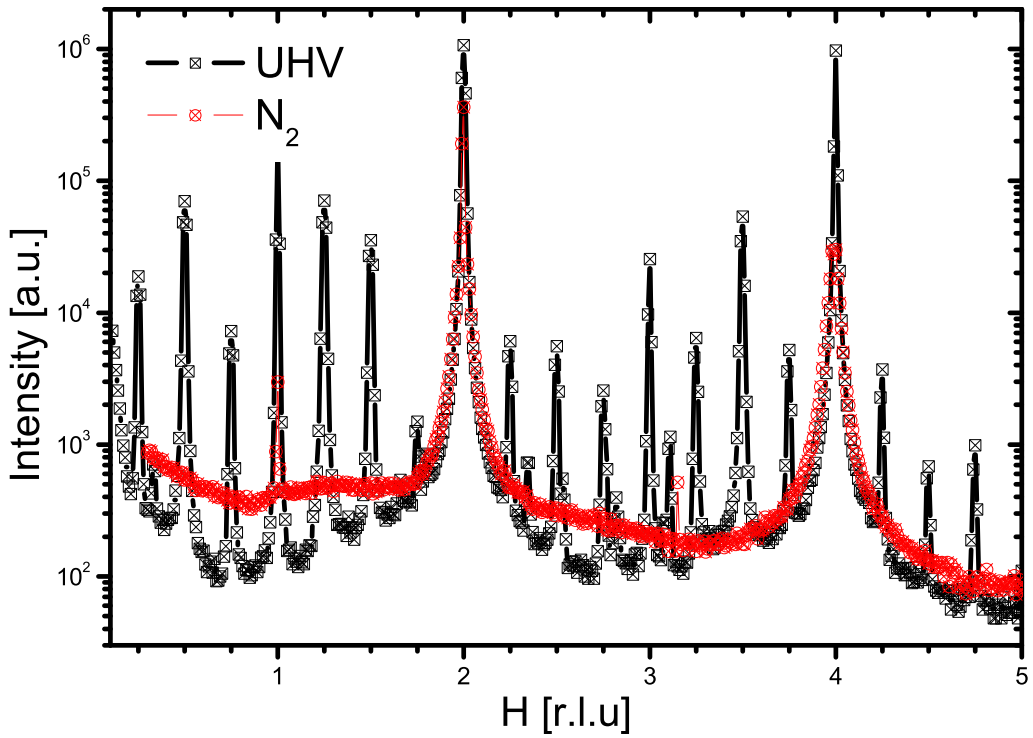

Fig. 6.20: *Radial in-plane scans (K=0 r.l.u., L=0.06 r.l.u.) taken on a GaAs(001)-(4×2) surface in UHV is presented (black squares) together with the radial in-plane scan on the same surface in nitrogen at ambient pressure (red circles)*

The radial in plane scans (K=0 r.l.u. and L=0.06 r.l.u.) of the GaAs(001)-(4×2)/c(8×2) surface in UHV (black squares) and after venting with nitrogen (red circles) are shown in Figure 6.20. Similar to the (2×4) surface, discussed in Section 6.3.1, the background increases after the venting the chamber to nitrogen. Except the GaAs(200) and (400) Bragg reflections and the peak at $\vec{Q}_{\|}$=(1,0) corresponding to the (1,0)-CTR of the GaAs(001)-surface, all the reconstruction peaks of the (4×2)/c(8×2) structure observed in UHV disappear in nitrogen under ambient pressure.

In addition to the radial in-plane scan, a specular rod and six crystal truncation rods were recorded. The specular rods taken in UHV (black squares) and under ambient nitrogen pressure (red circles) are shown in Figure 6.21. The GaAs(002) and (004) Bragg peaks are visible (at L=2 r.l.u. and at L=4 r.l.u.). In UHV the shape of the specular rod is mostly determined by the (4×2)/c(8×2) structure of the surface. The specular rod at ambient nitrogen pressure differs from the one taken in UHV close to the (002) Bragg peak, which is a weak reflection. The intensity modulations close to L=2 r.l.u. are determined from the rearranging of the first atomic layers due to the reconstruction. However, the shape of the specular rod taken on the GaAs(001)-(4×2)/c(8×2) surface exposed to nitrogen close to L=2 r.l.u. still differs from the shape expected for a bulk like surface termination.

The CTR's recorded from a (4×2) terminated GaAs(001) surface in UHV (black squares) as

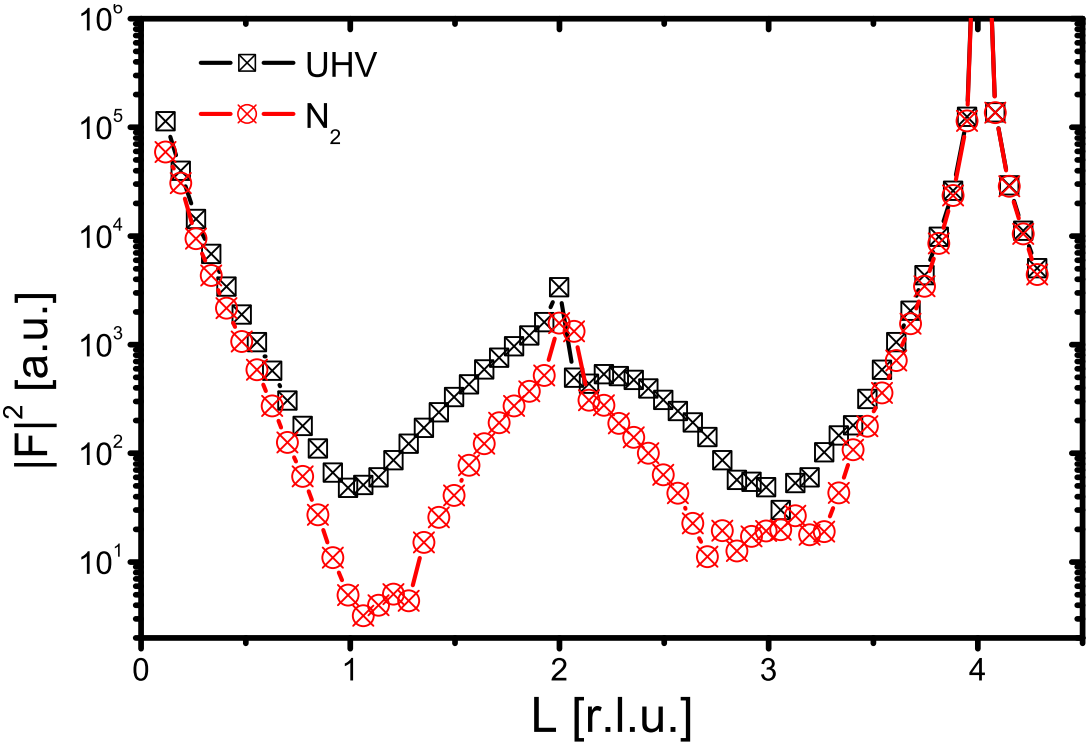

Fig. 6.21: *A specular rod taken on a GaAs(001)-(4×2) surface is presented (black squares) together with the specular rod taken on the same surface in nitrogen at ambient pressure (red circles)*

well as under ambient nitrogen pressure (red circles) are shown in Figure 6.22. The sharp intensity dip observed in UHV on the (2,0)-rod close to L=2 r.l.u., which arises from the interference of the diffracted X-rays from the reconstructed surface layer and the substrate, disappears at ambient pressure. Also the rod-asymmetries clearly visible along the (0,1)-, (1,0)-, (2,0)- and (0,2)-CTR's, on the UHV measured surface, are strongly reduced. The (2,0)- and (0,2)-rods as well as the (0,1)- and (1,0)-rods, which show different shapes in UHV, appear similar when measured in nitrogen. This indicates the lifting of the (4×2)/c(8×2) reconstruction to form a (1×1) surface. However, the rods measured in nitrogen still differ from the shape of the crystal truncation rods expected for a bulk terminated surface. These differences in shape suggest an additional relaxation of the surface and/or the adsorption of nitrogen.
The crystal truncation rods taken in nitrogen of a former (2×4)/c(2×8) reconstructed GaAs(001) surface look similar to the rods taken in nitrogen on a former (4×2)/c(8×2) reconstructed surface. However some differences in the shape can be observed close to the anti-Bragg positions.

In both cases the reconstruction seems to be lifted, but the surface is not bulk like. A relaxation as well as the adsorption of nitrogen could both be possible. The surface remains smooth after venting. The rods taken in ambient pressure on a former (2×4)/c(2×4) and a former (4×2)/c(8×2) still differ, indicating that different surface terminations remain also at ambient pressures.

6.4 Summary and Conclusion

In this chapter the clean GaAs(001) surfaces were characterized by STM, LEED and SXRD. Surfaces with two different terminations, the arsenic-rich GaAs(001)-(2×4)/c(2×8) structure and the gallium-rich GaAs(001)-(4×2)/c(8×2) structure were investigated. Both surfaces were obtained by thermal annealing of an arsenic capped GaAs(001) wafer.
The thus obtained GaAs(001)-(2×4)/c(2×8) surface has terraces of about 100 nm width. The surface is disordered in the [010]-direction, leading to a broadening of the fractional order peaks. From this broadening the probability of displacement of one reconstructed unit cell by one fourth or half of such a unit cell in the [010]-direction could be determined, 87.6% of the unit cells are not displaced, a dispacement of one fourth of a unit cell takes place with a probability of 7.4%. The less probable (2.4%) is the displacement by half a unit cell in the [010]-direction.

The structure refinement of the GaAS(001)-(2×4)/c(2×8) surface was performed by using the program *fit* written by Oliver Bunk. The $\beta 2$-model for the (2×4)-structure could be confirmed. The measured structure factors are reflecting the averaged surface. STM and the line-shape analysis of the fractional order peaks reveal that the surface has a high degree of disorder. This disorder is introduced by defects such as displacements of the (2×4) unit cell in the [010]-direction. The structure of the (2×4) unit cell close to these defects is probably affected and differs from a (2×4) unit cell embedded on a surface without defects. Also a coexistence of the $\alpha 2$ or γ-phase can not be excluded.

In addition, the GaAs(001)-(4×2)/c(8×2) surface was investigated by LEED, STM and SXRD. The terrace size is about 100 nm. No disorder in the [100]-direction is observed. However, gallium-islands on the surface as well as little domains of other gallium-rich structures coexist.

The sample analyzed by surface X-ray diffraction was essentially prepared for electrochemical copper deposition. The surface was not especially prepared to solve the GaAs(001)-(2×4) surface structure. The thus obtained results are reflecting the surface quality of a typically surface used for electrochemical copper deposition. A better surface quality could probably be obtained by a more careful adjustment of the parameters, like temperature and heating time.

Both surface terminations were investigated by SXRD after the exposure to ambient nitrogen pressure. As can be seen from the rods, the surfaces are still smooth (especially in comparison to the chemical cleaned GaAs(001) surfaces formerly used for electrochemical copper deposition). However, the exact surface structure in nitrogen is not known. It is likely that the surfaces are not anymore reconstructed, but a relaxation or nitrogen adsorption on the surface is probable. A slight difference in the CTR (specular and off-specular) of a former (2×4)/c(2×8) and (4×2)/c(8×2) reconstructed surface is indicating that the different surface terminations (As-rich and Ga-rich) are preserved.

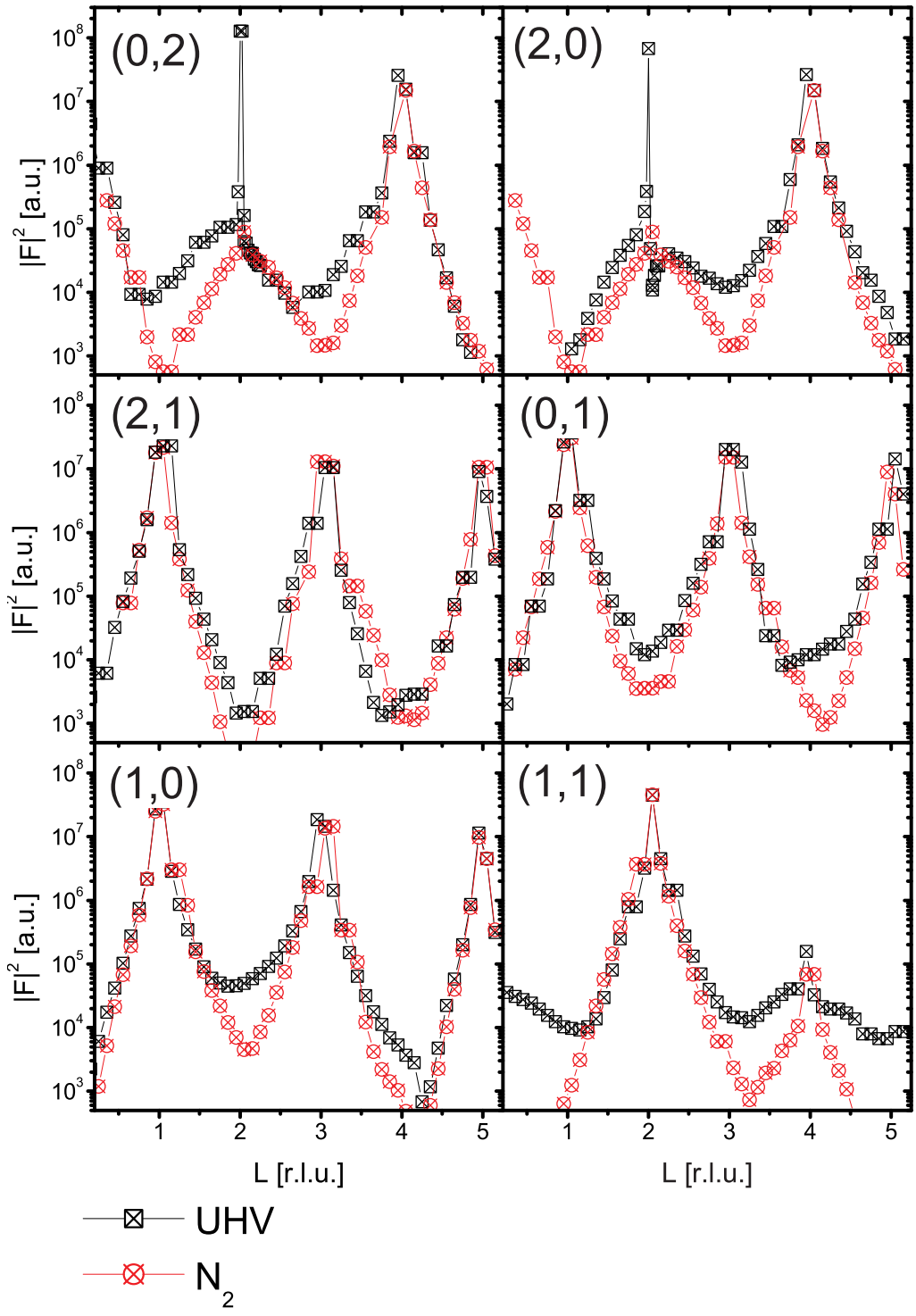

Fig. 6.22: *Crystal truncation rods taken on a GaAs(001)-(4×2) surface are shown (black squares) together with the crystal truncation rods taken on the same surface in nitrogen at ambient pressure (red circles).*

Chapter 7

Electrochemical Copper Deposition on GaAs(001)

In this chapter the results of the investigations of copper electrodeposition on GaAs(001) surfaces are presented. The copper containing electrolyte used for the deposition was in all cases 0.5 M H_2SO_4 containing 1 mM $CuSO_4$. In the first section of this chapter the potential controlled stripping of the arsenic cap layer and the copper deposition on the as obtained GaAs(001) surfaces was investigated by AFM and cyclic voltammetry. The potential controlled stripping of the arsenic cap layer is accompanied by AsH_3 and H_2 evolution, which makes the in-situ study difficult. Therefore the subsequent in-situ studies of the copper deposition concentrate on GaAs(001) surfaces prepared in UHV and by chemical etching.
The results obtained for copper deposition on chemically etched and UHV prepared GaAs(001) surfaces are presented in Section 7.2 and 7.3 respectively. In Section 7.3 the copper deposition on initially UHV prepared, reconstructed surfaces is investigated. The epitaxy of the deposited copper determined by surface X-ray diffraction is discussed. A detailed line-shape analysis of the copper peaks for several deposition conditions is given (Section 7.3.2). In Section 7.3.3 the analysis of the termination of the copper clusters by X-rays is presented. To investigate in more detail the copper epitaxy closer to the Cu/GaAs interface and to gain more information about the origin of the observed copper epitaxy, additional in-situ X-ray measurements monitoring the potential controlled copper stripping processes were carried out and are presented in Section 7.3.4. A final discussion of the results, including a comparison between the copper electrodeposition on chemically etched and UHV prepared GaAs(001) surfaces, is given together with the conclusion in Section 7.4. The potentials given in this chapter were all measured versus the Ag/AgCl reference electrode.

7.1 Potential controlled arsenic dissolution from α-As/GaAs wafers and subsequent copper electrodeposition

The amorphous arsenic layers of the capped GaAs wafers can be removed in UHV by thermal desorption. The arsenic cap can also be stripped away in electrolyte under potential control. At about -1.2 V in 0.5 molar sulfuric acid arsenic dissolves through an electrochemical reduction:

$$As + 3H^+ + 3e^- \rightarrow AsH_3 \nearrow \tag{7.1}$$

An almost linear increase in the current of the GaAs:As electrode due to the stripping is observed with time. After 2 hours of stripping the current increases more rapidly and reaches a constant after about 3 hours. Previously the intensity of the (200) surface reflection of the GaAs(001) surface was monitored during the stripping of the arsenic cap layer [76]. The (200) peak intensity increases linearly for the first two hours and stays almost constant afterwards. After three hours stripping the intensity of the GaAs(200) surface reflection started to decrease, indicating roughening of the GaAs surface.

In the next section AFM studies of the GaAs(001) surfaces after 2.5 hours and after 3 hours of arsenic dissolution are presented.

7.1.1 Characterization of electrochemically "decapped" GaAs(001) surfaces by AFM

In the first step the GaAs(001) surfaces obtained by potential controlled stripping of the arsenic caps were investigated by AFM in air. The surface obtained after 2 1/2 hours of dissolving of the arsenic layer at a potential of -1160 mV is shown in Figure 7.1. Two images with different resolutions (3 $\mu m \times$ 3 μm (a) and 500 nm $\times$ 500 nm (b)) were taken from this surface. The

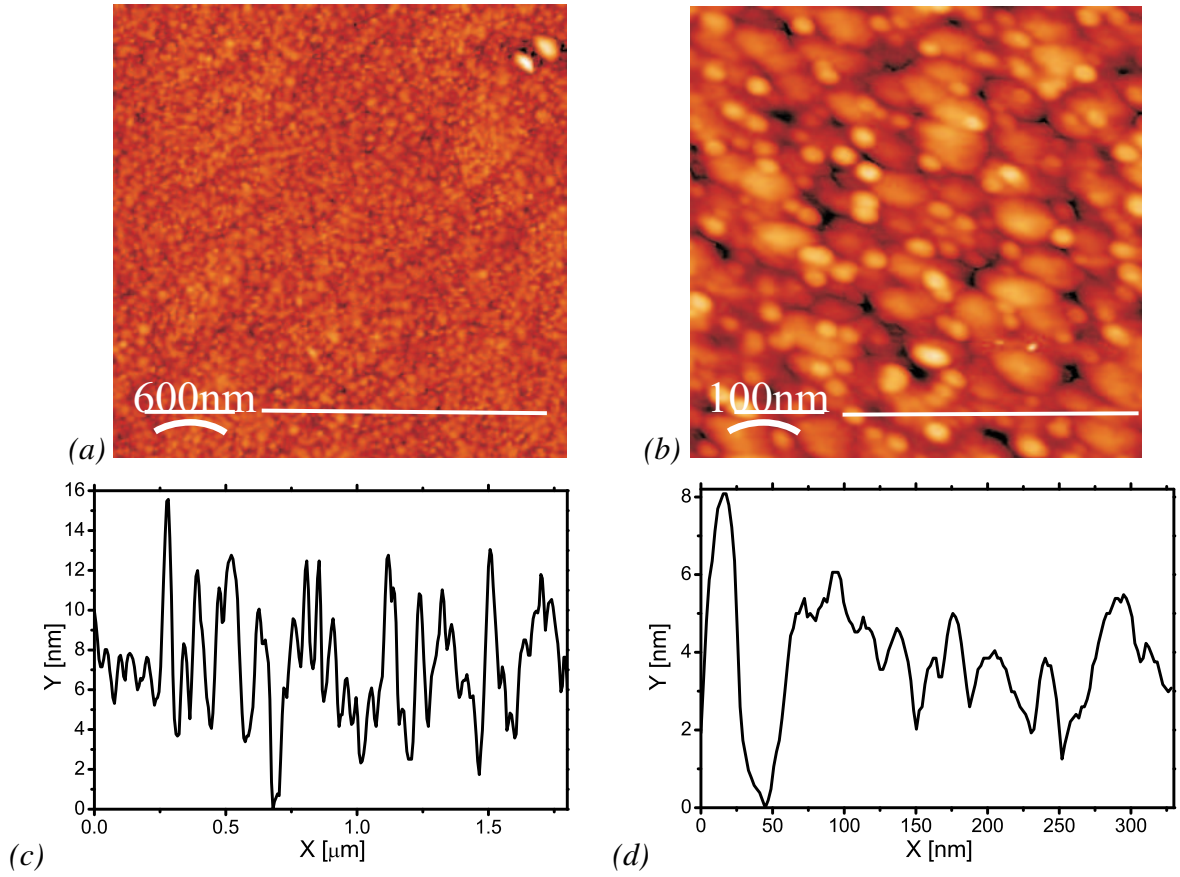

Fig. 7.1: *AFM image of a GaAs(001) surface obtained from an arsenic capped sample by electrochemical stripping of the arsenic cap for 2 1/2 hours.*

height profiles taken from the images (indicated by the white lines) are shown in figure 7.1 (c) and (d). The surface after two and an half hour of arsenic stripping is rough. The rms roughness σ_{rms} deduced from the STM images is about 2.7 nm. Small islands with a height of 8 nm and a width of about 15 nm can be found on the surface [Figure 7.1 (b)]. It is likely that some arsenic from the amorphous layer remains on the surface. In comparison AFM images obtained from

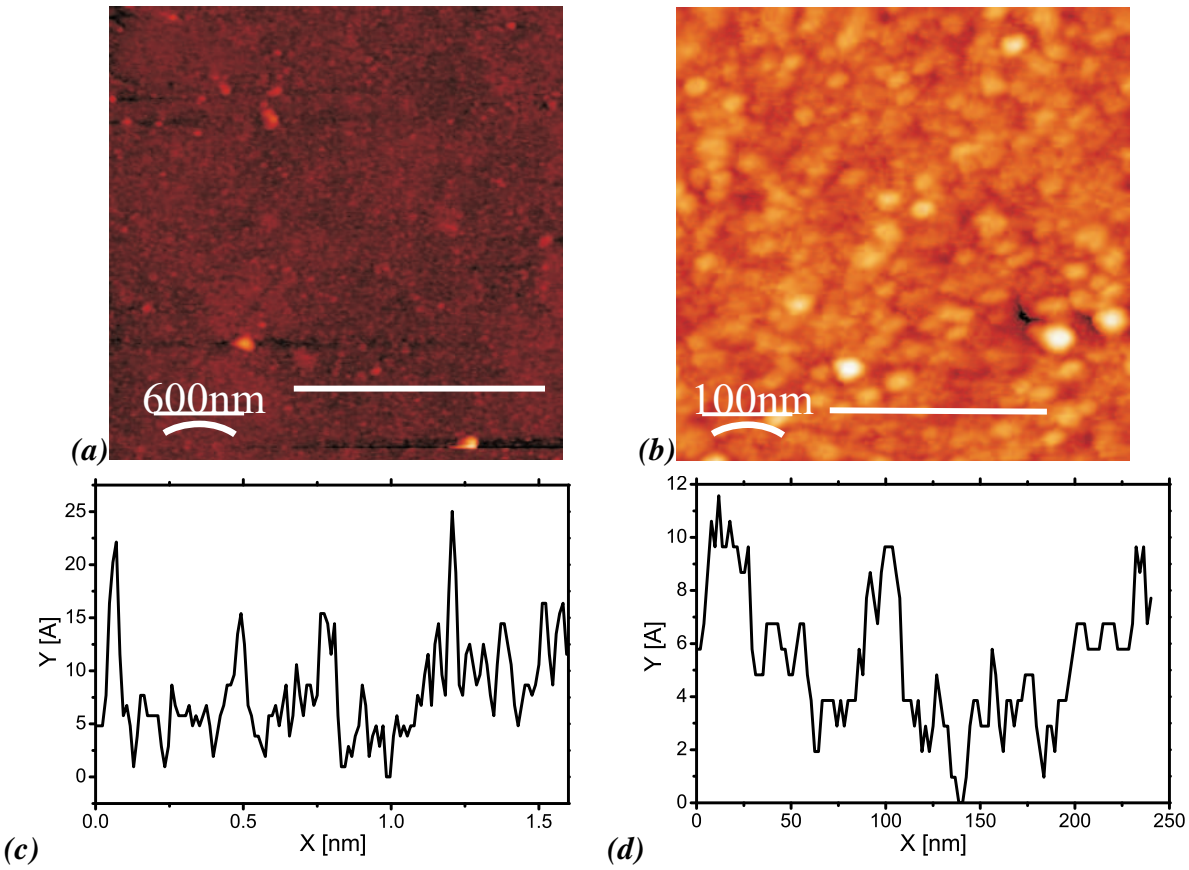

Fig. 7.2: *AFM image of a GaAs(001) surface obtained from an arsenic capped sample by elechtrochemical stripping of the arsenic cap for 3 hours.*

the GaAs(001) surface after the potential controlled stripping of the arsenic cap layer at a potential of -1160 mV for three hours are presented in Figure 7.2. Similar to Figure 7.1 two AFM images with different resolutions [3 μm × 3 μm (a) and 500 nm × 500 nm (b)] are presented together with the height profiles in figure 7.2 (c) and (d).

The height profile reveals a less rough surface. The rms roughness determined from the AFM images is about 7 Å, about four times less than the one of the surface obtained after half an hour less stripping of the arsenic cap. However, the surface is still covered by islands of about 10 Å high and 15 Å wide. These islands are likely to be the remaining arsenic from the cap layer. As the layer is dissolved under hydrogen evolution, the hydrogen bubbles may stick to the surface and stop locally the stripping process, resulting in a rough surface.
To remove the hydrogen bubbles, one sample was stripped in the X-ray thin layer cell with the sample surface held vertical and a continuous purging of the surface with nitrogen. By stripping

in this geometry more homogeneous dissolution of the arsenic cap and a less rough resulting surface is expected. A cyclic voltammogramm in copper containing electrolyte was taken from such a surface and will be discussed in the following section.

7.1.2 Copper electrodeposition on a GaAs(001) surface obtained by potential controlled stripping of the arsenic layer

In this section I will first present the cyclic voltammetry studies of the GaAs(001) surfaces in copper containing sulfuric acid. The surfaces were prepared by potential controlled dissolution of the arsenic caps. During this process the wafer samples were placed horizontally facing down in an electrochemical glass cell.
Once the arsenic caps were removed, $CuSO_4 \cdot 5\ H_2O$ was added to the electrolyte to obtain a concentration of 0.5 mM H_2SO_4 + 1mM $CuSO_4$ for the subsequent copper deposition. The morphology of the GaAs(001) surfaces after the deposition was characterized by AFM. For one of the studied samples the arsenic dissolution was done in the thin-layer X-ray cell with the sample surface oriented vertically to allow continuous nitrogen purging of the surface.

Cyclic voltammetry

The differences between the GaAs(001) surfaces after stripping of the arsenic cap for 2.5 hours and for 3 hours were discussed in the previous section. The cyclic voltammograms obtained in 1 mM $CuSO_4$ + 0.5 M H_2SO_4 for these two surfaces are shown in Figure 7.3. In both voltammograms the copper deposition peaks can be observed. In the voltammogram taken after 2.5 hours of stripping (black line in Figure 7.3) two copper deposition peaks appear, one at -180 mV and the other one at -400 mV. However,the increase of the deposition current while the potential was scanned towards more negative values occurs at about -100 mV. Also a copper dissolution peak can be observed at about 250 mV.

The voltammogram taken after three hours of stripping is shown as a gray line in Figure 7.3. An increase of the current when the potential moves towards negative values can be first observed at about -80 mV. Also in this case two copper deposition peaks are observed, one at about -180 mV and the other at about -300 mV . The peaks overlap with each other and the one at about -300 mV appears much stronger. The copper dissolution peak occurs at less positive potentials (160 mV) and has a small shoulder at about 200 mV which could be interpreted as a second dissolution peak.

In addition, a voltammogram was taken in 1 mM $CuSO_4$ + 0.5 M H_2SO_4 on a GaAs(001) surface which was continuously purged with nitrogen during a three hours stripping. The aim of the purging was to remove the hydrogen bubbles sticking to the surface during the arsenic dissolution in order to obtain a more homogeneously stripped surface. In Figure 7.4 the gray line shows the voltammogram measured from this surface compared to the previously discussed one (gray line). The two copper deposition peaks (at -200 mV and at -300 mV) of the surface with continuous N_2 purging are obtained at the same potentials. However, they are sharper and reach about the same current values. For the sample prepared without nitrogen purging the reduction peak at -300 mV shows a much higher current than the one at -200 mV.

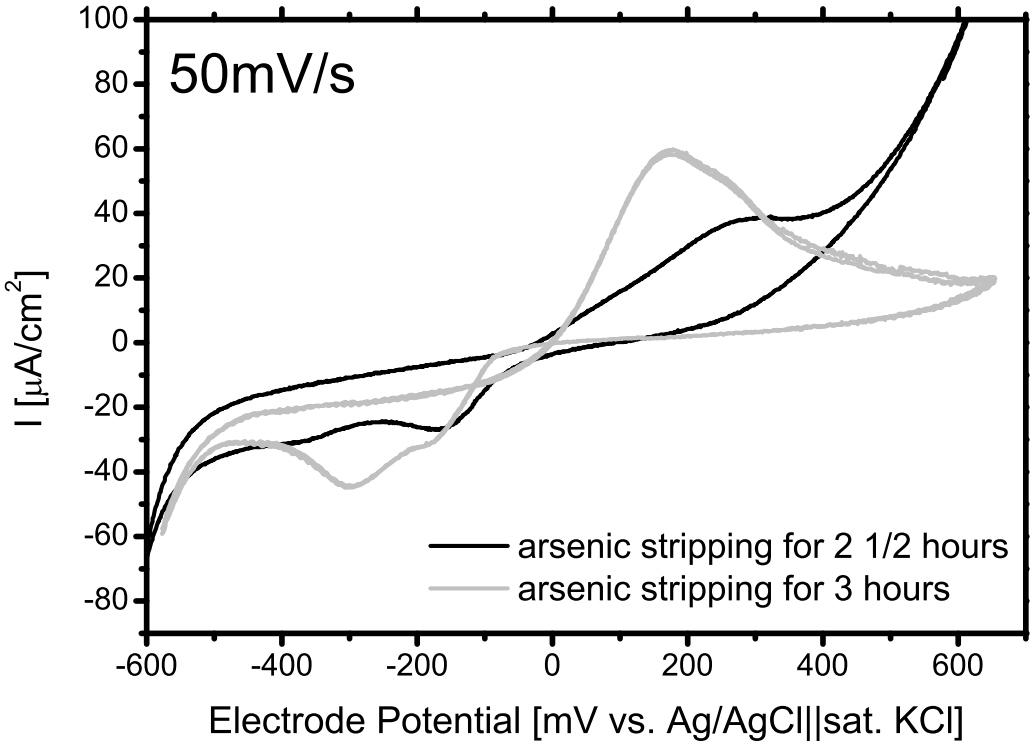

Fig. 7.3: *Cyclic voltammograms recorded in 1 mM $CuSO_4$ + 0.5 M H_2SO_4 on two GaAs(001) surfaces obtained by potential controlled stripping of the arsenic cap layer. One surface was stripped for 2 and a half hours, the other one for three hours.*

Two current increases in the reduction region were already observed in chloride containing electrolyte [77] on p-doped GaAs(001). In this case the first peak (at more positive potential) corresponds to a reduction from Cu^{2+} to Cu^{+} by forming a copper-chloride complexe. In sulfuric acid these two peaks are not always clearly observed.
The current reached in each reduction region and also their exact position depend clearly on the surface morphology. Interface states due to defects on the surface could be the origin of the change in the shape of the voltammograms. The first copper deposition, which occurs at the more positive potential, could be related to charge transfer from/to such defect states. Such a growth process is similar to the under potential deposition observed on metal surfaces. A field induced in-diffusion of the defects and the adsorbed copper may introduce new surface states. The formation of these states may be in addition facilitated by a rough surface. Also, the double reduction peaks may be associated with the preference of copper adsorption at the different sites available on the GaAs(001) surface. However, the copper deposition on GaAs is diffusion limited, to get a double peak due to two copper deposition processes the first process (giving rise to the reduction peak at more positive potentials) can not be limited by diffusion but by some other factors like the number of adsorption sites.

The electrochemical copper deposition on GaAs is so far not understood on atomic scale. However the surface morphology seems to be important. To gain more information about the copper

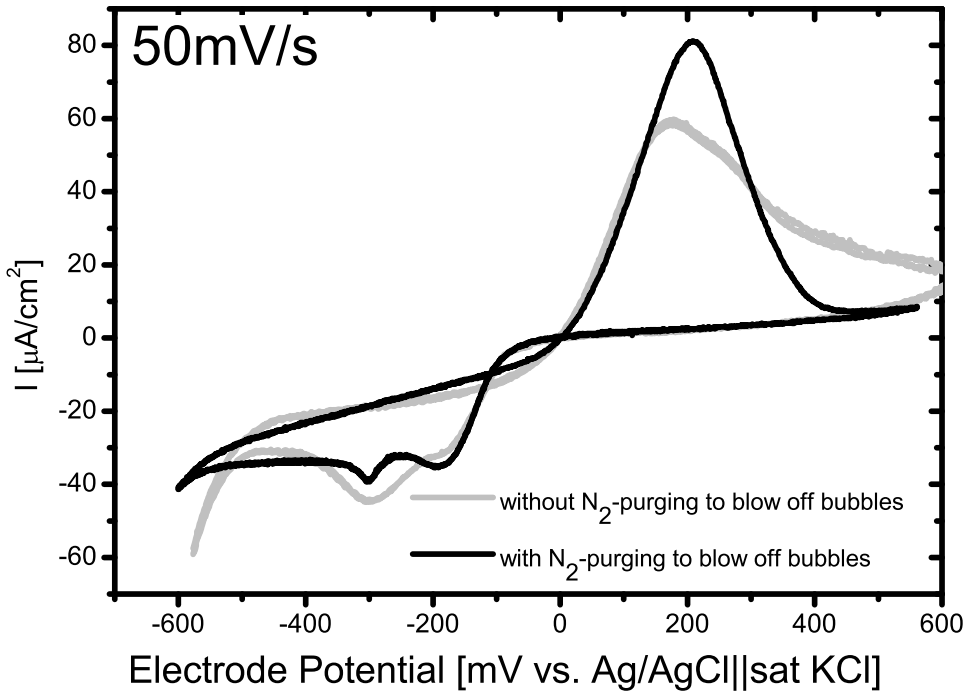

Fig. 7.4: *Cyclic voltammograms recorded in 1 mM $CuSO_4$ + 0.5 M H_2SO_4 on two GaAs(001) surfaces obtained by potential controlled stripping of the arsenic cap layer. For both surfaces the arsenic caps were dissolved by potential controlled stripping during three hours. One of the surfaces (black line) was mounted vertically and continuously purged with nitrogen during the stripping. The gray line is a reproduction of the gray line in Figure 7.3, which was recorded from a sample prepared without nitrogen purging.*

deposition and especially the processes leading to the two reduction peaks in the cyclic voltammogram, a more detailed study on the influence of the surface termination and morphology using smooth, mono-atomically terminated GaAs(001) surfaces prepared by UHV should be carried out. This has not been done so far.

Characterization by AFM

The copper deposited on the GaAs(001) surfaces prepared by stripping of the arsenic caps at -1160 mV was studied by AFM for two different deposition potentials and two different copper coverages. After three hours of stripping the applied potential was set to the open circuit potential. Copper was then added to the electrolyte and deposited by applying the deposition potential. Up to this point the sample surfaces were always in contact with the electrolyte. Afterwards, the samples were removed from the electrolyte and dried by blowing nitrogen over the surfaces. In Figure 7.5 the images of two different samples with a copper coverage of 20 ML are presented. The copper coverage was estimated from the transferred charge during the deposition.
Figure 7.5 (a) and (b) were recorded from a sample on which copper was deposited at -100 mV.

Figure 7.5 (a) shows a large scale image (5 μm $\times$ 5 μm) of this surface. The height profile along the white line is shown in Figure 7.5 (c). The surface is flat with some islands separated by about 300 nm. The islands are about 60 nm in height and 100 nm in width. An additional AFM image (200 nm $\times$ 200 nm) of the area between these islands is shown in Figure 7.5 (b) with the corresponding height profile in Figure 7.5 (d). The surface between the islands is flat. However, the height profile reveals a higher roughness than that of the GaAs(001) surface without copper deposition (Figure 7.2). The rms roughness deduced from this image is about 1.6 nm. Smaller islands with a height of about 4 nm and a width of about 20 nm can be identified. In comparison, in Figure 7.5 (e) and (f), AFM images of a sample with 20 ML of copper deposited at -400 mV are presented. Figure 7.5 (e) shows a 5 μm $\times$ 5 μm large section of the surface with the corresponding height profile in Figure 7.5 (g). Islands of 15 nm height and about 60 nm wide are now present on the surface. They are likely copper clusters. In Figure 7.5 (f) a closer view (1 μm $\times$ 1 μm) of the surface is shown and the corresponding height profile is given in 7.5 (h). Compared to the same copper coverage deposited at -100 mV the small islands between the large ones are much broader (the width is about 50 nm compared to 20 nm for copper deposited at -100 mV). It appears that copper deposited at a more negative potential grows into smaller clusters but more nucleation sites are present.
To compare with the above AFM images, two additional samples with the same surface preparation and deposition potentials but a higher coverage of 40 ML were studied. The thus obtained AFM images are presented in Figure 7.6. In Figure 7.6 (a) (5 μm $\times$ 5 μm) and (b) (1 μm $\times$ 1 μm) the surface after copper deposition at -100 mV is presented with the corresponding height profiles given in Figure 7.6 (c) and (d), respectively. In Figure (a) several large islands, most likely copper clusters, are clearly visible. They have a height of about 90 nm and a width of about 200 nm. Figure 7.6 (b) shows a smaller area (1 μm $\times$ 1 μm) between the copper islands. The height profile shown in Figure7.6 (d) does not look very different from Figure 7.5 (d). In comparison a sample with the same copper coverage (40 ML) deposited at -400 mV was also studied. A large scale image of such a surface is shown in Figure 7.6 (e). A clear difference to Figure 7.6 (a) is visible. Only small islands are present with a height of about 15 nm. Compared to the 20 ML surface [Figure 7.5 (e)] presumably copper clusters seem to exist. An image of 1 μm $\times$ 1 μm of this surface is shown in Figure 7.6 (f) with the corresponding height profile in Figure 7.6 (h).

Copper deposited at more negative potentials seems to grow more homogeneously. At a potential close to the copper deposition potential on GaAs, fewer but relatively large copper islands are obtained.

At both deposition potentials we studied the copper deposition seems to occur. This is an indication that both reduction peaks observed in the voltammogram on the stripped GaAs(001) surfaces can be associated with the copper deposition current. However, at the more positive deposition potential (-100 mV in this case) the surface has less nucleation sites and the copper forms larger islands, whereas a more negative deposition potential causes more nucleation sites and a more homogeneous film.

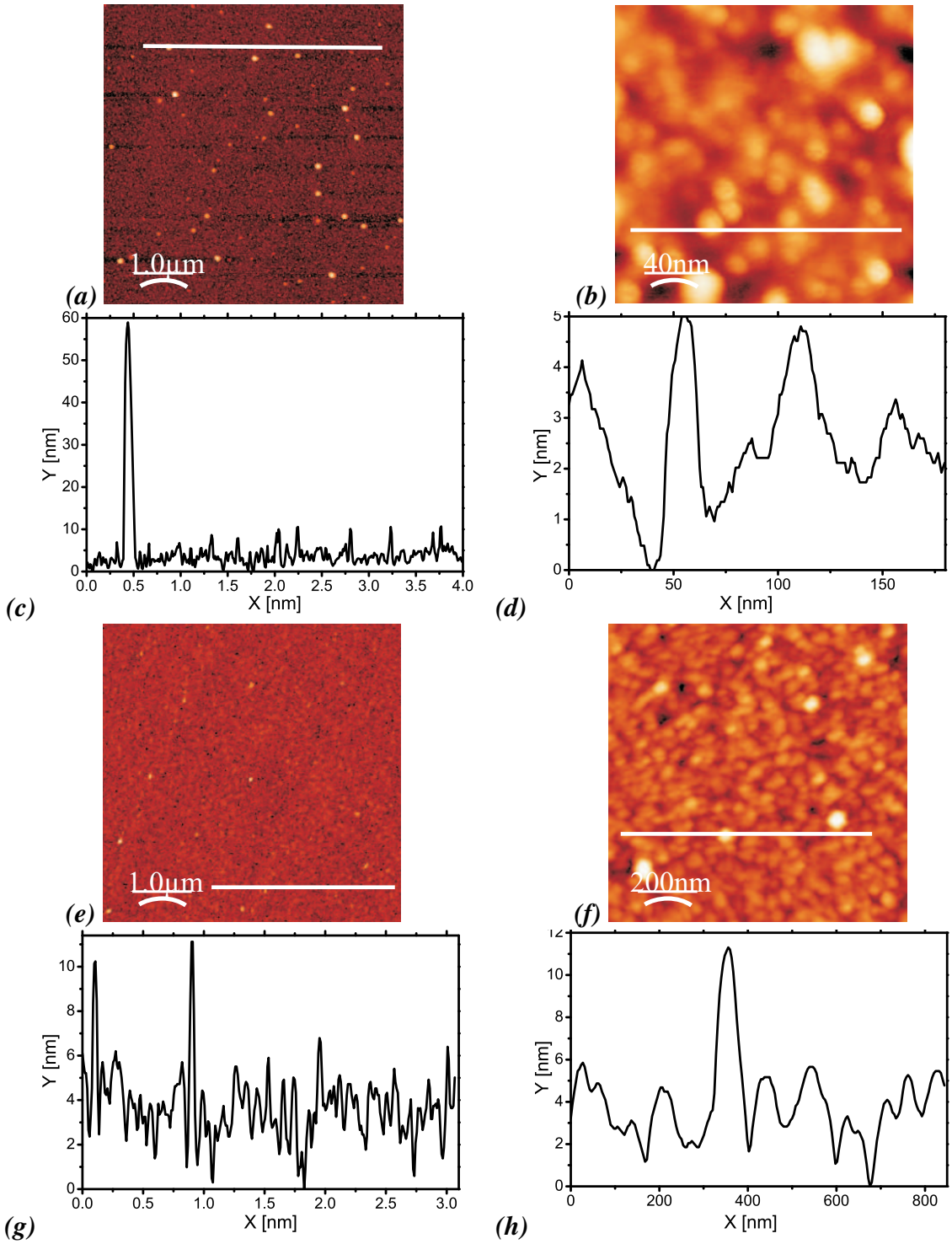

Fig. 7.5: *AFM images of GaAs(001) surfaces obtained from As/GaAs wafers by potential controlled stripping of the arsenic caps for 3 hours and subsequent deposition of 20 ML copper. (a) 5 µm × 5 µm and (b) 200 nm × 200 nm images showing the surface after copper deposition at -100 mV. (e) 5 µm × 5 µm and (f) 1 µm × 1 µm images showing the surface after copper deposition at -400 mV. The corresponding height profiles along the white lines are given below the images [(c), (d), (g) and (h)].*

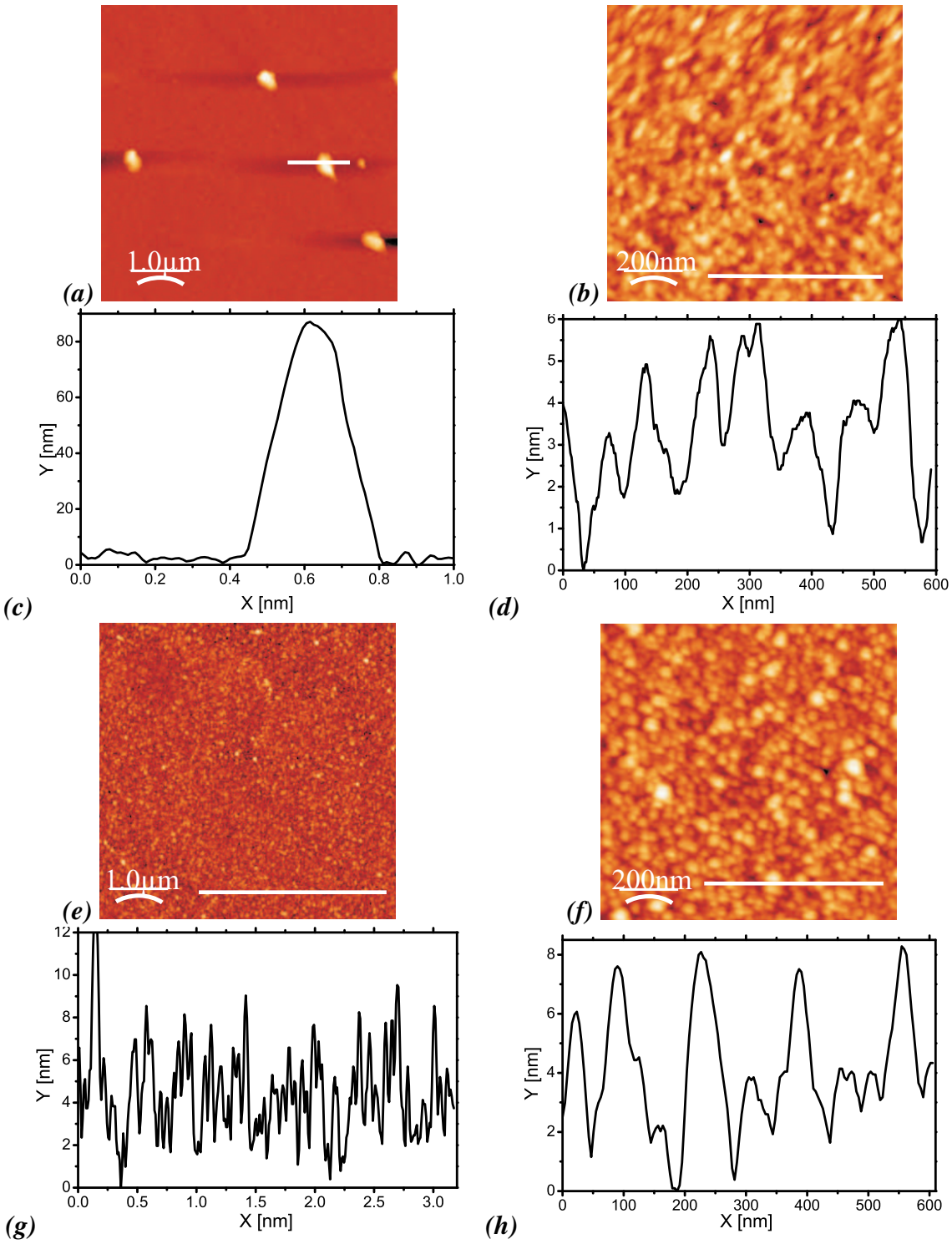

Fig. 7.6: *AFM images of GaAs(001) surfaces obtained from As/GaAs wafers by potential controlled stripping of the arsenic caps for 3 hours and subsequent deposition of 40 ML copper. (a) 5 µm × 5 µm and (b) 1 µm × 1 µm images showing the surface after copper deposition at -100 mV. (e) 5 µm × 5 µm and (f) 1 µm × 1 µm images showing the surface after copper deposition at -100 mV. The corresponding height profiles along the white lines are given below the images [(c), (d), (g) and (h)].*

7.2 Copper electrodeposition on a chemical etched surface

The arsenic cap of the GaAs(001) sample was removed by heating in air to 400°C on a hot plate. To make an ohmic contact, a wire was attached to the backside of the sample by an indium-zinc alloy. Afterwards, the sample was cleaned by the chemical etching process described in Section 4.1 and mounted in the thin layer cell presented in Section 4.3. The sample surface was contacted at a deposition potential of -500 mV in 0.5 M H_2SO_4 containing 1 mM $CuSO_4$ prior to the X-ray alignment to avoid beam damage to the bare GaAs surface. The X-ray data were taken using a beam energy of 22.5 keV and an incident angle of 0.2° with the sample surface.

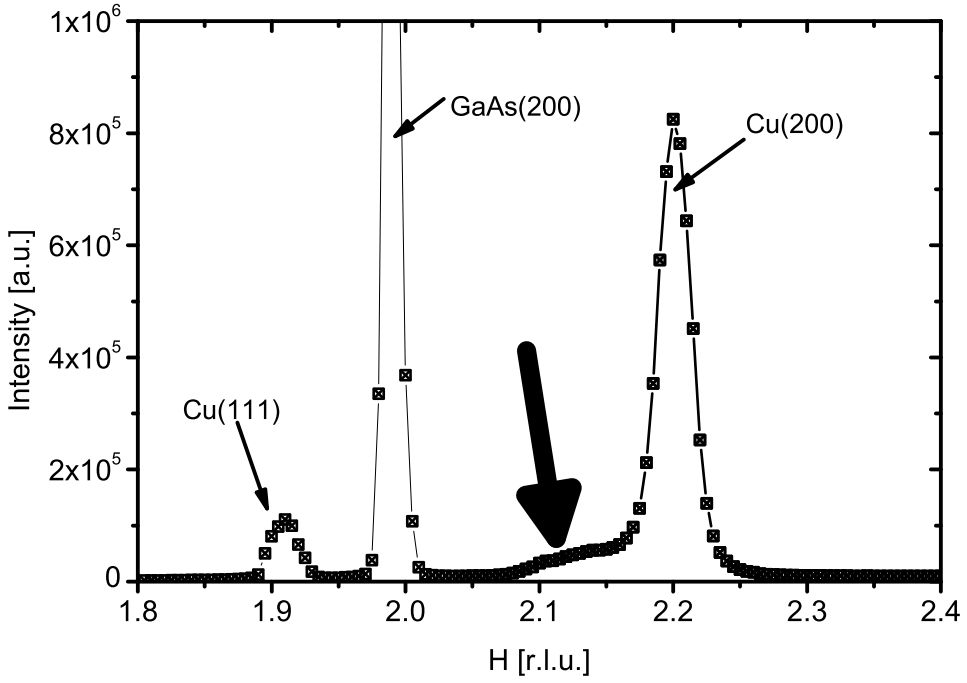

Fig. 7.7: *Radial in-plane scan around the GaAs(200) Bragg peak. The Cu(200) and Cu(111) peaks can be identified in addition to the GaAs(200) reflection. A shoulder close to the copper (200) peak is indicated by the large arrows.*

Figure 7.7 shows a radial in-plane scan (L=0.06 r.l.u.) around the GaAs(200) Bragg peak. Compared to the clean GaAs(001) surface, two additional peaks, which can be identified as the Cu(111) ($d_{(111)} = 2.087$ Å) and the Cu(200) ($d_{(200)} = 1.808$ Å) Bragg reflections, are observed.

The L-scan through the Cu(200) peak is presented in Figure 7.8 (a). The maximum of the Cu(200) peak is shifted from the in-plane position at $L = 0$ r.l.u. to L=0.25 r.l.u., which suggests that the Cu(100) planes are not exactly parallel to the GaAs(100) planes but tilted out-of-plane in the $[\bar{1}00]$-direction. The peak maximum at L=0.25 r.l.u. corresponds to a tilt angle of 4.6° of the Cu[001]-direction with respect to the GaAs[001]-direction. A rocking scan through the Cu(200) reflection is presented in Figure 7.8 (b). The peak has a FWHM of 1.8°, which reflects a large in-plane mosaicity.

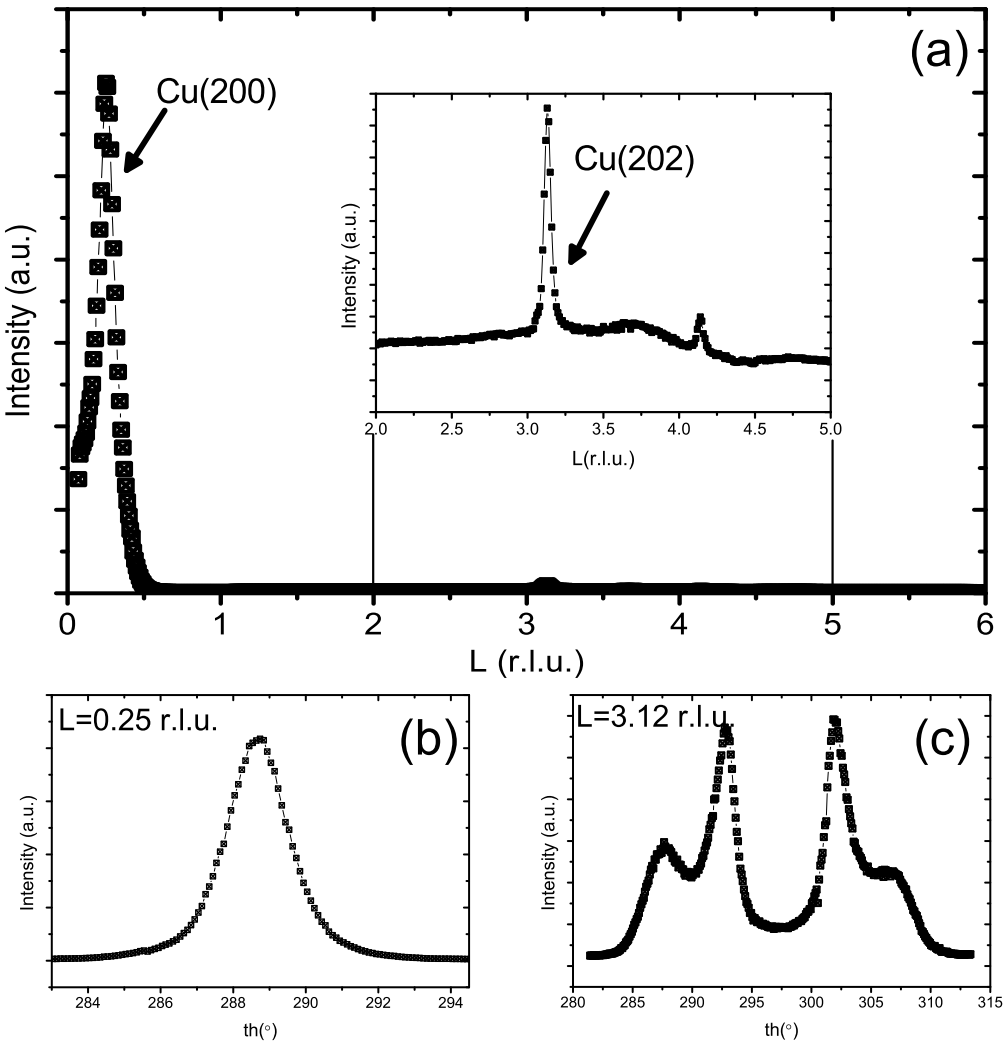

Fig. 7.8: *(a) L-scan through the Cu(200) Bragg peak. (b) and (c) show rocking scans through the Cu(200) and Cu(202) reflections respectively.*

The copper in-plane lattice constant determined from the Cu(200) position is $a_{Cu} = 3.622$ Å. The copper is thus within the error range totally relaxed. In addition, a shoulder extending to smaller $|\vec{Q}|$ is observed (Figure 7.7). By fitting this shoulder and the Cu(200) reflection with two Gaussians, the center of the shoulder (H=2.172 r.l.u) is found to correspond to an in-plane copper lattice constant of approximately $a_{shoulder} = 3.68$ Å, which is larger than that of natural copper (3.615 Å) and may represent the copper close to the interface.

The Cu(202) reflection appears at L=3.2 r.l.u. in terms of the used GaAs coordinates. A rocking scan through this reflection is shown in Figure 7.8 (c) and reveals an interesting splitting of the peak. Since the angular spread of the copper (202) peak is much larger than the width of the copper (200) peak in Figure 7.7, this splitting can not be explained by the in-plane mosaicity. Instead, an additional tilt of the copper [001]-axis in the GaAs [010]-direction may be responsible for the separation of the copper (202) peaks. The observation of four peaks in Figure 7.8 (c)

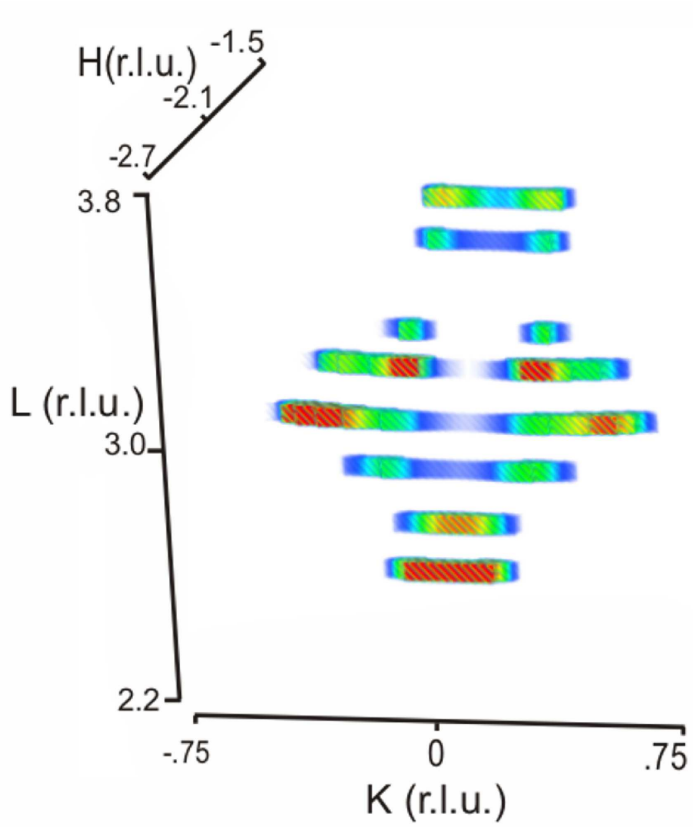

Fig. 7.9: *Intensity distribution around the expected Cu(-202) reflection. The scan was performed along the surface of a constant $|\vec{Q}|$. The color scale goes from blue (low intensity) over green and yellow to red (high intensity).*

also suggests that the tilt angle may not be uniquely defined. A tilt of the Cu[001]-axis in the GaAs[010]-direction produces two copper peaks, corresponding to the positive and negative tilt angles.
To investigate more the splitting of the copper (202) reflection, rocking scans were performed at a constant $|\vec{Q}|$ around the Cu($\bar{2}$02) peak position expected for an untilted copper lattice. A ring-like intensity distribution around the Cu($\bar{2}$02) is observed in Figure 7.9.

As discussed previously in Reference [14], this ring-like intensity distribution may be explained by a random tilt of the copper [001]-axes of the differently oriented copper clusters away from the GaAs[001]-axis in all directions by a constant angle of 6°. Such a random tilt distributes the copper [001]-axes on the surface of a cone around the GaAs[001]-axis. To compare the measured intensity with this model, a rotation matrix is needed to simulate the intensity distribution. The best way is to describe this rotation by three consecutive rotations:

- The first rotation is about the GaAs[001]-axis. It brings the selected tilt axis to one of the

coordinate axes of the system e.g. the x-axis, described by the rotation matrix

$$D = \begin{pmatrix} v_1 & v_2 & 0 \\ -v_2 & v_1 & 0 \\ 0 & 0 & 1 \end{pmatrix}, \tag{7.2}$$

with the normalized vector $\vec{v} = (v1, v2, 0)^T$ giving the tilt axis. v_1 and v_2 can be described by the angle θ between the tilt axis and the x-axis: $v_1 = \cos(\theta)$ and $v_2 = \sin(\theta)$.

- The second rotation applies the tilt by an angle β about the x-axis. It is described by the rotation matrix

$$R = \begin{pmatrix} 1 & 0 & 0 \\ 0 & \cos(\beta) & -\sin(\beta) \\ 0 & \sin(\beta) & \cos(\beta) \end{pmatrix}. \tag{7.3}$$

- The last rotation brings the tilt axis back by applying the inversion of the first rotation matrix.

The random tilt can then be expressed as

$$D^{-1}RD = \begin{pmatrix} 1+v_2^2 \cdot (\cos(\beta)-1) & v_1 \cdot v_2 \cdot (1-\cos(\beta)) & v_2 \cdot \sin(\beta) \\ v_1 \cdot v_2 \cdot (1-\cos(\beta)) & 1+v_1^2 \cdot (\cos(\beta)-1) & -v_1 \cdot \sin(\beta) \\ -v_2 \cdot \sin(\beta) & v_1 \sin(\beta) & \cos(\beta) \end{pmatrix}, \tag{7.4}$$

where the vector $\vec{v}$ has to take all possible in-plane directions, which can be described by letting the angle θ take all values between 0° and 360°. The such obtained distribution of the Cu(-202) peak position is shown in Figure 7.10 together with the measured intensity distribution. The measured intensity as well as the modeled peak positions all lie on a sphere with a constant $|\vec{Q}|$. Figure 7.10 shows their projection to the KL-plane. The blue circle is obtained for a tilt angle β of 4.6°, as determined by the position of the Cu(200) reflection in Figure 7.8 (b). The green circle corresponds to a β of 6°, as concluded in Ref. [14]. The model of the randomly tilted Cu[001]-axis reproduces some of the ringlike features of the measured intensity distribution. However, the correct shape of the intensity distribution and especially the four peaks observed in the rocking scan presented in Figure 7.8 (c) are not reproduced. The copper epitaxy seems more likely to be textured with preferable tilt directions.

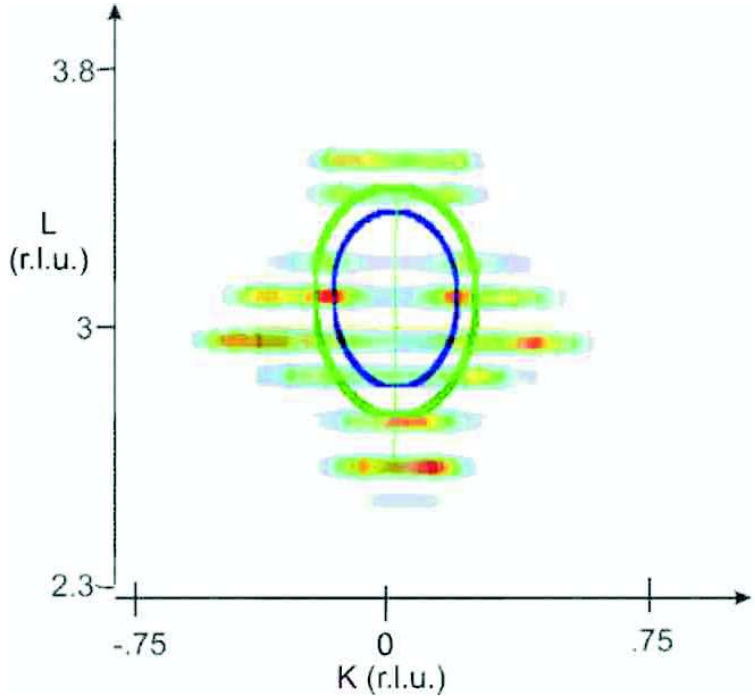

Fig. 7.10: *A projection in the KL-plane of the rocking scans at constant $|\vec{Q}|$ around the expected Cu(-202) reflection overlayed by its simulated peak distribution assuming that the Cu[001]-axis is randomly tilted by* 4.6° *(blue) and* 6° *(green). The color scale for the measured intensity goes from blue (low intensity) over green and yellow to red (high intensity).*

7.3 Copper electrodeposition on a UHV-prepared surface

The surfaces used for the electrodeposition of copper were prepared as described in section 4.5.3 and characterized in UHV and in inert gas at ambient pressure by surface X-ray diffraction (see Chapter 6). Afterwards, the samples were contacted with electrolyte using the electrochemical droplet cell described in Section 4.7.2. The copper was deposited from 0.5 M H_2SO_4 containing 1 mM $CuSO_4$. Several deposition conditions were studied and will be described in the following sections. To minimize roughening of the bare GaAs surface in contact with electrolyte due to beam damage, the surface was contacted with electrolyte directly at the copper deposition potential.

7.3.1 Epitaxy

A radial in-plane scan performed along the GaAs[100]-direction after the deposition of copper on an initially (4×2)-reconstructed surface at a potential of -350 mV is presented in Figure 7.11 (a). Some additional background arising from the scattering from the electrolyte droplet

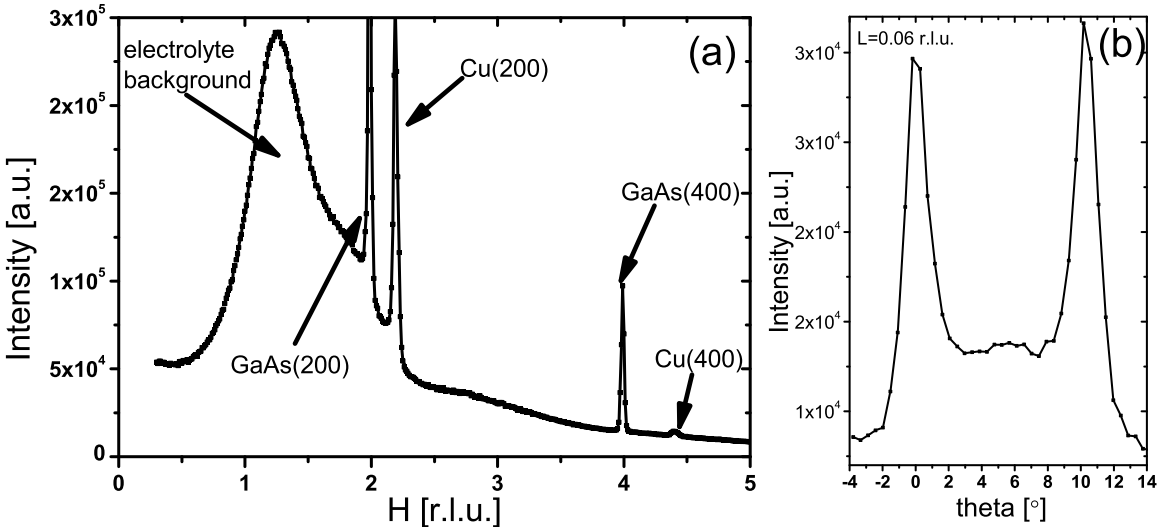

Fig. 7.11: *(a) Radial in-plane scan in the [100]-direction. (b) Rocking scan through the Cu(200) reflection reveals an in-plane rotation of the Cu lattice*

on the sample is observed at H=1.2 r.l.u..

The copper peaks at H=2.2 r.l.u. and H=4.4 r.l.u. can be assigned to the Cu(200) and the Cu(400) Bragg reflections respectively. A rocking scan of the theta angle through the Cu(200) reflection is presented in Figure 7.11 (b), which reveals a symmetric splitting of the Cu in-plane peak. The same splitting is observed for the Cu(400) reflection, which explains the low intensity of the Cu(400) peak in the radial in-plane scan in Figure 7.11 (a). The angular separation between the two split peaks is the same for the Cu(200) and the Cu(400) reflection, indicating an in-plane rotation of the copper lattice about the GaAs[001]-axis. Counter-clockwise and clockwise rotations are both possible, since the two peaks are symmetric to the GaAs[100]-axis.

H (r.l.u.)	K (r.l.u.)	L (r.l.u.)
2.18	0.16	0.46
2.18	-0.16	0.46
2.2	0.2	in-plane
2.2	-0.2	in-plane

Tab. 7.1: *The positions of the Cu(200) peaks for Cu deposited on a Ga-rich surface at -350 mV*

The positions of the Cu in-plane peaks at $H = 2.18$ r.l.u and $K = \pm 0.16$ r.l.u. correspond to a rotation angle of 4.2°.

A *L*-scan through one of the split Cu(200) peaks is shown in Figure 7.12 (a). A second Cu(200) reflection appears at *L*=0.46 r.l.u. indicating an additional tilt of the Cu[001]-axis towards the GaAs[100]-axis. A rocking scan through this peak also shows a symmetric splitting. The tilt angle can be determined from the peak positions ($\vec{Q} = 2.2, \pm 0.16, 0.46$) to be approximately 8.4°. In total four equivalent Cu(200) reflections are found at the positions given in Table 7.1.

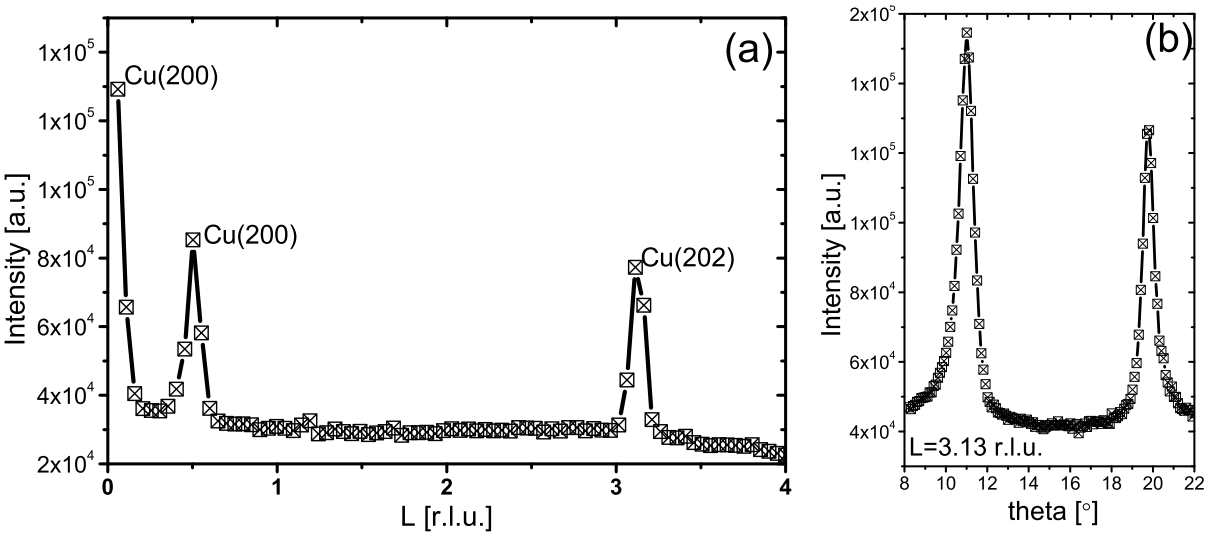

Fig. 7.12: *(a) L-scan through the copper in-plane reflection observed at $\vec{Q}$=(2.2, 0.18, 0.04). (b) Rocking through the Cu(202) reflection at L=3.13 r.l.u..*

In Figure 7.12 (a) the Cu(202) Bragg reflection can be identified at *L*=3.13 r.l.u.. This peak shows a symmetric splitting similar to the Cu(200) reflections, as demonstrated by the rocking scan in Figure 7.12 (b). In searching for the equivalent Cu(202) reflections resulting from the out-of plane tilt of the copper lattice, six additional Cu(202) reflections are identified at the positions given in Table 7.2. In total eight Cu domains are found, however only four of the Cu(200) reflections can be observed. This is because the Cu(200) peak is an in-plane reflection and can have negative *L*-compounds when the copper lattice undergoes an out-of-plane tilt.

The positions of the eight Cu(202) reflections are found to agree with an in-plane rotation of the copper lattice about the GaAs[001]-axis followed by an out-of-plane tilt of the Cu[001]-axis

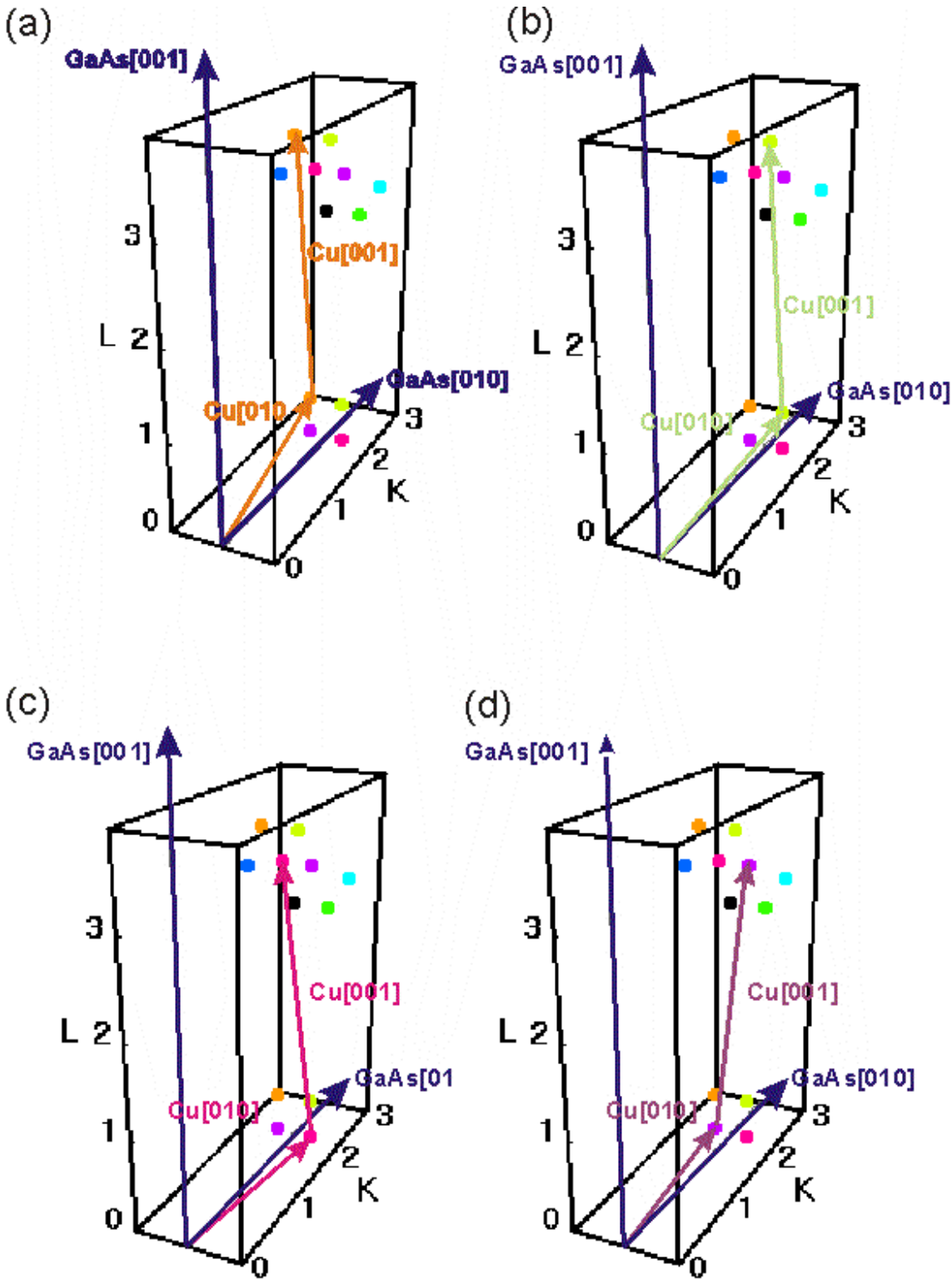

Fig. 7.13: *Four of the eight possible tilting and rotations of the copper lattice with respect to the GaAs-lattice.*

H [r.l.u.]	K [r.l.u.]	L [r.l.u.]
2.19	-0.168	3.13
2.19	0 .168	3.13
2.2	-0.51	3.04
2.2	0.51	3.04
1.81	-0.19	3.57
1.81	0.19	3.57
2.51	0.17	2.60
2.51	-0.17	2.60

Tab. 7.2: *The positions of the eight observed Cu(202) reflections for Cu deposited on a Ga-rich surface at -350 mV*

towards the GaAs [$\bar{1}$00]-, [100]-, [010]- or [0$\bar{1}$0]-direction. The combination of the in-plane rotation, clockwise or counterclockwise, with one of the four tilting possibilities leads to eight copper domains. The reciprocal space containing four of the Cu(020) and eight Cu(022) reflections is illustrated in Figure 7.13, together with the corresponding tilted Cu axes. In the figure only the tilt directions bringing the Cu(020) reflections to positive *L*-values are presented. They correspond to the following movement of the copper lattice:

- a counter-clockwise rotation about the GaAs[001]-axis combined with an inclination in the GaAs[0$\bar{1}$0]-direction [Figure 7.13 (a)]
- a clockwise rotation combined with an inclination in the [0$\bar{1}$0]-direction [Figure 7.13 (b)]
- a clockwise rotation combined with an inclination in the [$\bar{1}$00]-direction [Figure 7.13 (c)]
- and a counter-clockwise rotation combined with an inclination in the [100]-direction [Figure 7.13 (d)]

The tilting and rotation of the copper lattice with respect to the GaAs lattice are observed to occur always together. The Cu(202) reflection observed at $\vec{Q}$=(2.19, 0.17, 3.13), right above the Cu(200) reflection at $\vec{Q}$=(2.18, 0.16, 0.46), could be assigned to an untilted copper peak. However this reflection is the Cu(202) reflection corresponding to the Cu(200) peak at $\vec{Q}$=(2.2, -0.2, 0) with a tilting of the Cu[001]-axis in the GaAs[010]-direction as can be seen in Figure 7.13 (c) and 7.13 (d).
In Figure 7.14, a reciprocal space map around the Cu(022) peak at H=0.168 r.l.u., K=2.19 r.l.u and L=3.13 r.l.u. is presented with the *x*- and *y*-axes corresponding to the direction of the Cu[010]- and Cu[001]-directions respectively. The splitting of the peaks due to the tilting of the Cu[001]-axes in the GaAs[010]-direction is clearly visible.

As the tilt and rotation occur together, the simple estimations of the rotation and tilt angles from the Cu(200) peak positions made earlier without considering the motions simultaneously are not totally correct. A more precise way to determine the angles is to use a rotation matrix to describe the tilt and the rotation of the copper lattice and to reproduce the measured peak

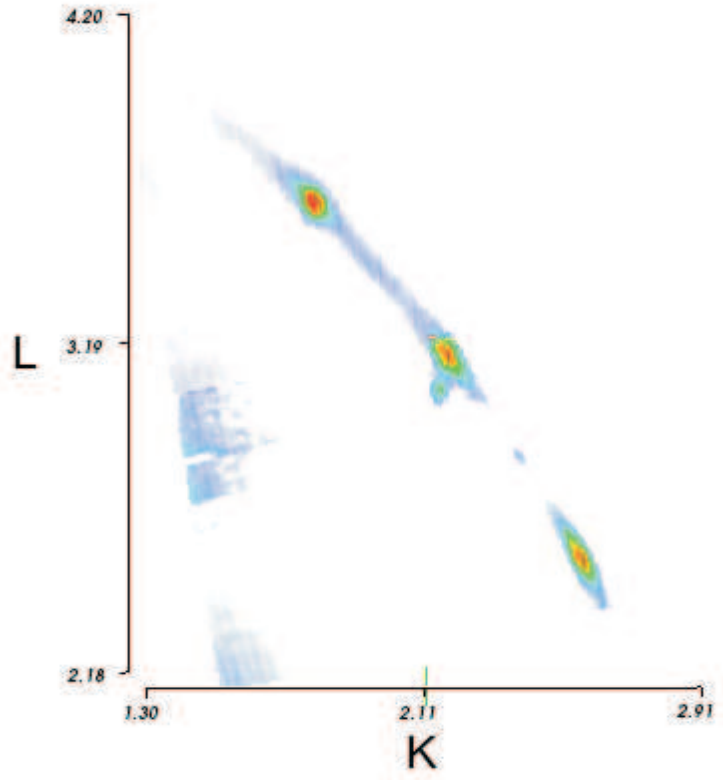

Fig. 7.14: *A reciprocal space map taken around the Cu(022) reflection. The Cu[010]-direction (for an in-plane rotation bringing the Cu(020) reflection to negative H) is taken as x-axis, the Cu[001]-direction (for an tilting of the Cu[001]-axis in the [010]-direction) is the y-axis*

positions.

A rotation matrix describing the rotation about the GaAs[001]-axis and an additional tilt about the GaAs[100]- or GaAs[010]-axis is required. Figure 7.15 shows the transformation of a cartesian coordinate system under a rotation about the z-axis by an angle θ followed by an additional rotation about the x-axis by an angle ϕ. The coordinates of the new base vectors $\vec{x}''$, $\vec{y}''$ and $\vec{z}''$ in Figure 7.15 can be deduced by projecting these vectors onto the old base vectors $\vec{x}$, $\vec{y}$ and $\vec{z}$. The prime and double prime denote the axes after the first and second rotation respectively. The final coordinates can be expressed as

$$\vec{x}'' = \begin{pmatrix} \cos\theta \\ \sin\theta \cdot \cos\phi \\ 0 \end{pmatrix}, \vec{y}'' = \begin{pmatrix} -\sin\theta \\ \cos\theta\cos\phi \\ \sin\phi \cdot \cos\theta \end{pmatrix} \text{ and } \vec{z}'' = \begin{pmatrix} 0 \\ -\sin\phi \\ \cos\phi \end{pmatrix}.$$

Knowing these vectors, one can construct the rotation matrix. The observed rotation and tilt of the copper lattice with respect to the GaAs lattice can be described by two rotation matrices:

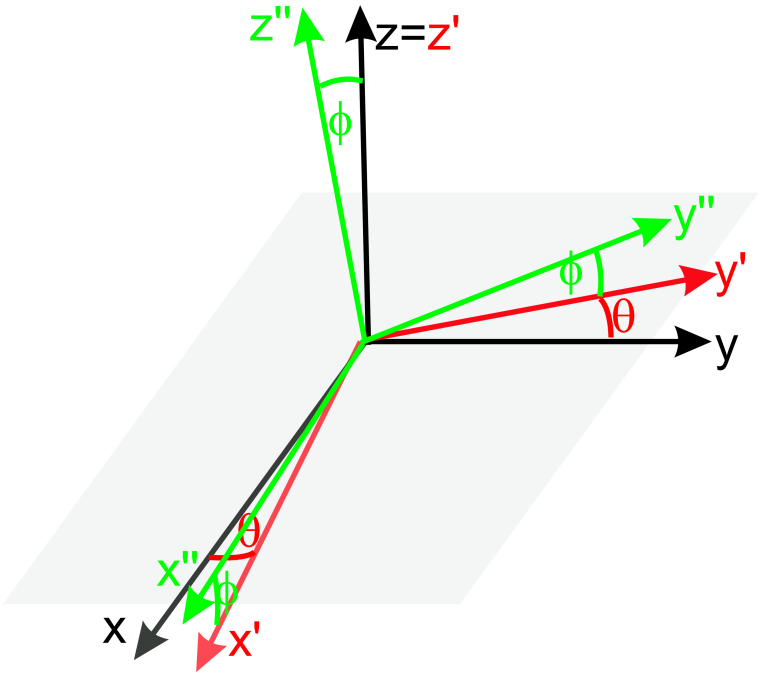

Fig. 7.15: *A schematic view of the rotation of the copper lattice with respect to the GaAs lattice. The copper lattice is rotated by an angle θ about the GaAs[001]-axis and tilted by an angle ϕ about the GaAs[010] or the GaAs[100]-axis.*

$$\text{M1} = \begin{pmatrix} \cos\theta\cos\phi & -\sin\theta\cos\phi & \sin\phi \\ \sin\theta & \cos\theta & 0 \\ -\cos\theta\sin\phi & \sin\theta\sin\phi & \cos\phi \end{pmatrix} \text{ and M2} = \begin{pmatrix} \cos\theta & -\sin\theta & 0 \\ \sin\theta\cos\phi & \cos\theta\cos\phi & -\sin\phi \\ \sin\theta\sin\phi & \cos\theta\sin\phi & \cos\phi \end{pmatrix}$$

Matrix M1 considers the tilt of the z-axis in the [100]-direction [as shown in Figure 7.13 (c) and 7.13 (d)] and matrix M2 the tilting of the z-axis in the [010]-direction [as demonstrated in Figure 7.13 (a) and 7.13 (b)]. Since positive and negative values for θ and ϕ are all possible, the two rotation matrices describe all eight equivalent domains. The tilt and rotation of the copper lattice with respect to the GaAs lattice is shown in real space for each domain in Figure 7.16. The domains obtained for the different tilt and rotation directions are labeled. Domains 1, 3, 5 and 7 (Domains 2, 4, 6 and 8) have a positive (negative) θ angle. Domains 1, 2, 5 and 6 (Domains 3, 4, 7 and 8) have a positive (negative) ϕ angle. In the following discussion the different domains will be referred to according to their labels in Figure 7.16.

The exact positions of several copper Bragg peaks were measured for a number of deposition conditions. After the domain and Bragg indices for each peak are assigned, the rotation and tilt angles as well as the copper in- and out-of-plane lattice constants can be determined by comparing the measured peak positions with the ones calculated from the rotation matrices. The results are summarized in Table 7.3. The rotation and tilt angles are similar for all deposition conditions. The angle of the in-plane rotation is about $4.7 \pm 0.4^\circ$ and the out-of-plane tilt angle is about $9.2 \pm .4^\circ$. In particular, no dependence of the tilt and rotation angles on deposition potential is observed. However, a slight dependence on the starting surface, arsenic-rich or gallium-rich, can be found. The tilt and rotation angles are smaller for the Ga-terminated than for the As-terminated surfaces. In addition, the lattice constants of the copper were determined

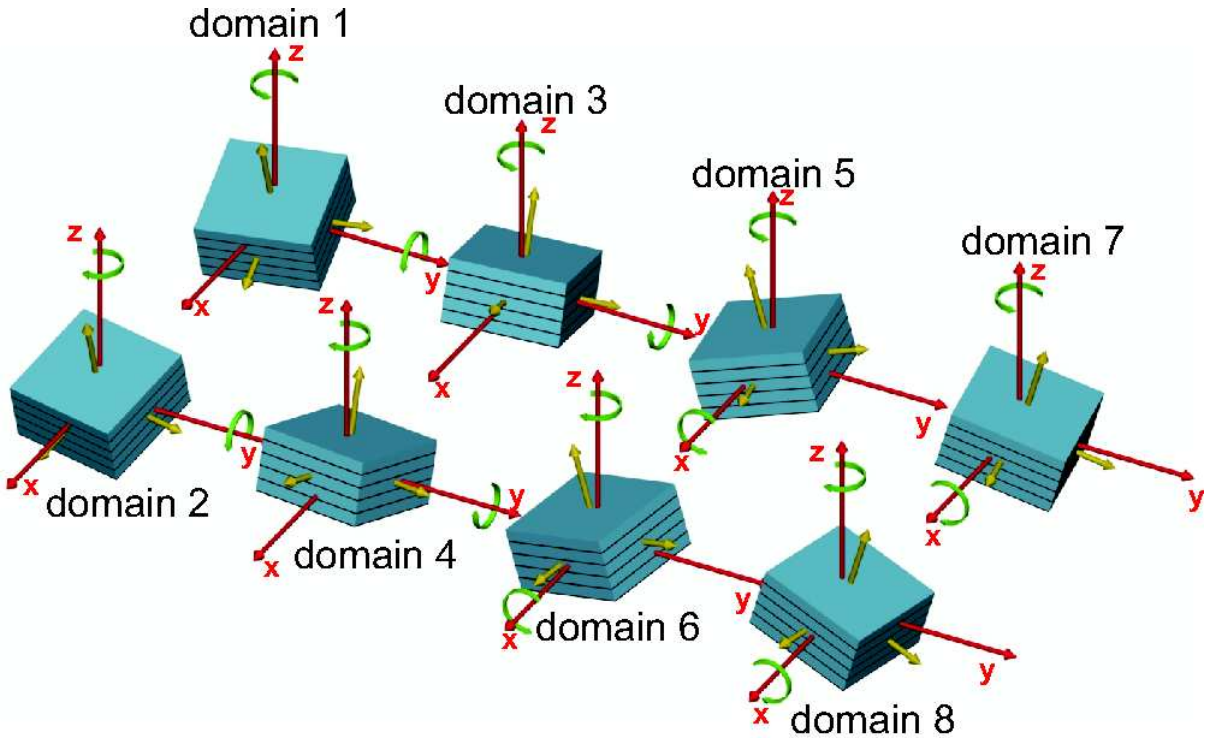

Fig. 7.16: *Eight copper domains resulting from the possible combinations of an out-of-plane tilt and an in-plane rotation. The x-, y- and z-axes (red arrows) represent the GaAs[100]-, [010]- and [001]-axes. The yellow arrows correspond to the copper [100]-, [010]- and [001]-axes. The direction of the in-plane rotation and of the out-of-plane tilt angles are represented as green arrows.*

for the different deposition conditions. The average in-plane lattice constant of the copper is about 3.622 Å and thus slightly larger than the one for natural copper (3.615 Å). The average out-of-plane copper lattice constant is 3.615 Å.

starting surface	deposition potential in mV	θ in $^\circ$	ϕ in $^\circ$	$d_{\parallel}$ in Å	$d_{\perp}$ in Å
2x4 As-rich	-350	5.05	9.53	3.629	3.614
	-500	4.77	9.16	3.626	3.624
	-900 $\rightarrow$ -350 [1]	5.09	9.55	3.618	3.613
	-1200$\rightarrow$ -350 [1]	4.92	9.26	3.616	3.612
4x2 Ga-rich	-350	4.43	8.78	3.62	3.612
	-600	4.31	8.75	3.62	3.616

[1] a step potential of -900 mV (-1200mV) has been applied for one second before jumping to -350 mV

Tab. 7.3: *The fitted rotation and tilt angles, as well as the Cu in-plane and out-of-plane lattice constants for different deposition conditions*

7.3.2 Line-shape analysis

The shape of several copper peaks was recorded by performing line-scans through the copper reflections. As eight possible copper domains with different tilts and rotations exist, it was more convenient to run the line-scans along the GaAs reciprocal lattice directions than along those of the copper.

Several factors can affect the width of a copper Bragg peak. Their contributions to the peak width projected to the GaAs H, K and L-directions depend differently on the peak position in the reciprocal space. These factors can be therefore quantified by analyzing the H, K and L dependence of the measured peak widths. To reduce the complications in separating the different contributions, only the Cu(HKL) reflections with H = 0 or K = 0 are included in the line-shape analysis. More specifically, the copper ($H0L$) reflections are used for the domains tilted about the GaAs[010]-axis (Domains 1-4 in Figure 7.16, described by the rotation matrix $M1$) and the copper ($0KL$) reflections for the domains tilted about the GaAs[100]-axis (Domains 5-8, described by the rotation matrix $M2$). For the purpose of clarity we derive the projected peak widths for only the Cu($H0L$) reflections associated with the Domains 1-4 in the following discussion. The same formulas can also be applied to the analysis of Domains 5-8 with the copper ($0KL$) reflections by simply replacing all H's by K's. Note that all the H, K and L appearing in the formulas below in this section refer to the indices of the copper reflections in the GaAs surface r.l.u.. The indices H, K and L referring to the copper reflections in copper r.l.u. are indicated by a subscript "Cu" in the formulas.

The contributions of the in- ($D_{\parallel}$) and out-of-plane ($D_{\perp}$) domain sizes to the broadening of a peak are

$$\Delta H_{domainsize}[r.l.u.] = \Delta K_{domainsize}[r.l.u.] = \frac{a}{D_{\parallel}} \tag{7.5}$$

$$\Delta L_{domainsize}[r.l.u.] = \frac{c}{D_{\perp}} \tag{7.6}$$

where a and c are the real-space in- and out-of-plane lattice constants defining the orientation matrix.

The broadening of the peaks due to the domain size does not depend on the indices of the Bragg reflection. The domain size in the [001]-direction affects the peak-width in the L-direction. Similarly the widths in the H- and K-directions can be affected by the domain size in the [100]- and [010]-directions, respectively.

Another source that can broaden a Bragg peak is a non-constant lattice parameter, which could arise from strain or a variation in the composition of the crystal (e.g. for an alloy). Variation of the in-plane lattice constant $\Delta d_{\parallel}$ causes the broadening of the peak in the in-plane radial direction and a change of the lattice spacing in the [001]-direction $\Delta d_{\perp}$ broadens the peak in the L-direction. For the variation of a lattice constant towards larger values, the peaks shift to smaller $\vec{Q}$ values. Such broadening of a peak (in r.l.u.) is proportional to the distance between the Bragg peak and the origin projected in the scan direction

$$\Delta H_{lattice}[r.l.u.] = \frac{\Delta d_{\parallel}}{d_{\parallel}} \cdot H_{Cu} \cdot \frac{d_{\parallel}}{a} \qquad \text{broadening in the radial in-plane direction}$$

$$\Delta L_{lattice}[r.l.u.] = \frac{\Delta d_{\perp}}{d_{\perp}} \cdot L_{Cu} \cdot \frac{d_{\perp}}{c} \qquad \text{broadening in the [001]-direction,}$$

where $d_{\parallel}$ and $d_{\perp}$ are the average in- and out-of-plane lattice constants of the copper clusters.
The third factor influencing the peak width is the mosaicity, which is due to variation in the orientation of the crystalline lattice between different crystalline grains. It does not affect the lattice constant, because mosaicity is related to the rotation of the crystalline lattice. The change in the intensity distribution of a reflection at $\vec{Q}$ due to mosaicity can therefore only be observed on a sphere centered at the origin with a radius of $|\vec{Q}|$.

In the case of the copper epitaxy one has to distinguish between the mosaicity $\Delta\phi$ of the tilt angle (defined by ϕ) and the mosaicity $\Delta\theta$ of the in-plane rotation (defined by θ about the [001]-axis). The mosaicity $\Delta\theta$ can be monitored by an in-plane rocking scan. For small $\Delta\theta$ this is equivalent to an in-plane line-scan perpendicular to the in-plane radial direction [e.g. a rocking scan is equivalent to a K-scan for an in-plane (H0) reflection and an H-scan for an in-plane (0K) reflection].

The in-plane mosaicity results from the variation of the in-plane rotation angle θ. For an (H0L) reflection such mosaicity broadens the peak in the K-direction. The angular width of the peak broadening, $\Delta\theta_{mosaicity}$, is a constant independent of the reflection. The width of this broadening in r.l.u., ΔK, is related to $\Delta\theta_{mosaicity}$ as

$$\Delta K_{mosaicity}[r.l.u.] = \Delta\theta_{mosaicity} \cdot H_{Cu} \cdot \frac{a}{d_{\parallel}} \tag{7.7}$$

assuming the mosaicity $\Delta\theta_{mosaicty}$ to be small.
Since the out-of-plane tilt is a rotation about the H- or K-axis, the mosaicity of the tilt angle broadens the peaks circularly in the copper KL- or HL-planes, depending on the tilt direction of each copper domain. The ID32 diffractometer does not permit an out-of-plane rocking scan about the H- or K-axis for determining this mosaicity. For this reason the out-of-plane mosaicity has to be deduced from H-, K- and L-scans.
The directions of the peak broadening due to the mosaicity $\Delta\phi$ of the tilt angle ϕ are shown in Figure 7.17 (green arrows) for the copper domain with the copper [001]-axis tilted in the GaAs[100]-direction (i.e. domain 1). The copper Bragg peaks lying in the copper HL-plane with K_{Cu}=0 are indicated. In Figure 7.17 the GaAs H- and L-axis are given as blue arrows for comparison. Due to the in-plane rotation of the copper lattice the GaAs H-axis does not lie in the copper HL-plane.

In Figure 7.17 the contribution of the mosaicity $\Delta\phi$ to the peak widths in the H- and L-directions depends on the peak positions in the HL-plane. For small L (and high H), the mosaicity basically broadens the peak in the L-direction without influencing the width in the H-direction. On the contrary for small H and large L, the mosaicity mostly affects the peak width in the H-direction. As the copper lattice is tilted, the influence of the mosaicity on the peak width of an H-scan or a L-scan will not be the same for the peak situated at $(H0L)_{Cu}$ and its counterpart at $(\overline{H}0L)_{Cu}$. In Figure 7.17, as the peak at $(\overline{H}0L)_{Cu}$ appears at a higher L in the GaAs reciprocal space than the $(H0L)_{Cu}$ peak does, the broadening due to mosaicity $\Delta\phi$ in an H-scan will be more pronounced for the $(\overline{H}0L)_{Cu}$ reflection than for the $(H0L)_{Cu}$ reflection (and vice versa for the L-scan).
When an H-, K- or L-scan is performed through a copper reflection, the mosaicity is projected

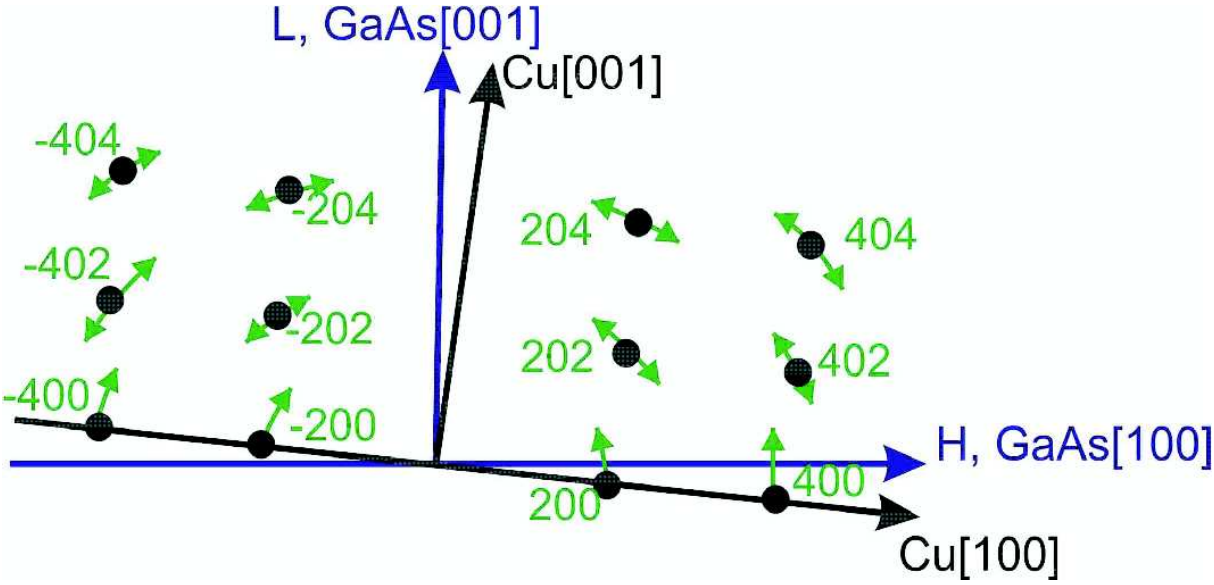

Fig. 7.17: *Projection of the plane defined by the Cu[100]- and the Cu[010]-direction in the HL-plane. The Cu(H0L)-Bragg reflections are indicated for the case of a tilt of the Cu[001]-axis in the GaAs[100]-direction. The peak broadening due to the mosaicity of the tilt is schematically shown by the green arrows.*

in the scan direction. In Figure 7.17 the projection of the out-of-plane mosaicity $\Delta\phi$ onto the H-axis is

$$\Delta H_{mosaicity}[r.l.u.] = \sin(\arctan(\frac{L}{H}\cdot\frac{a}{c}))\cdot\sqrt{L^2\cdot a^2/c^2+H^2}\cdot\Delta\phi[^\circ] \tag{7.8}$$

and the corresponding projection onto the L-axis is:

$$\Delta L_{mosaicity}[r.l.u.] = \cos(\arctan(\frac{L}{H}\cdot\frac{a}{c}))\cdot\sqrt{L^2+H^2c^2/a^2}\cdot\Delta\phi[^\circ] \tag{7.9}$$

The angle $\arctan\left(\frac{La}{Hc}\right)$ is the angle between the vector $(H0L)$ and its in-plane projection. a and c are the in- and out-of-plane lattice constants, respectively, defining the orientation matrix. A crucial point in determining the mosaicity from the basic line scans is to make sure that each scan covers the full range of a Cu Bragg peak in the HL-plane. Whether or not such a requirement can be fulfilled depends on the sizes of the detector slits. Consider the Cu($\bar{2}02$) reflection in Figure 7.17 as an example. The mosaicity $\Delta\phi$ about the K-axis causes the projection of the copper($\bar{2}02$) peak width to increase in both the H- and L-directions. Figure 7.18 shows the Laue condition satisfied for such a Cu reflection. The H- and L-resolutions, ΔH and ΔL, are determined by the sizes of the horizontal and vertical detector slits, respectively, with additional dependence on the angles γ and δ. When an H-scan is performed through the Cu($\bar{2}02$) reflection, in order to measure the peak width projected onto the H-axis, the horizontal detector slit should be set to a comparably small size to achieve a certain H-resolution, while the vertical detector slit should be opened wider than the L-projection of the peak width. If the vertical slit is too narrow, the H-scan does not measure the full projected width of the peak and no information on the mosaicity can be retrieved. By opening up the vertical slit until no further increase of the peak width is observed in the H-scans, one can be sure that the full projected peak width

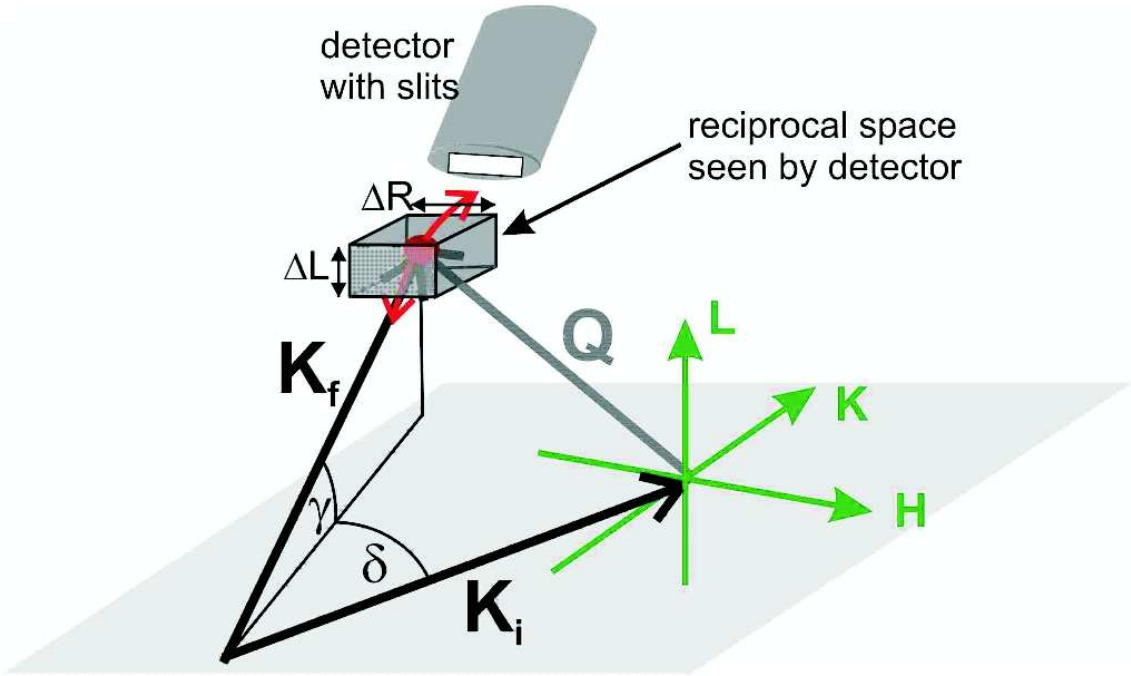

Fig. 7.18: *A schematic of the diffraction setup with the reciprocal space seen around a peak with high mosaicity of the tilt angle. If the total peak width in the radial in-plane or in the L-direction is recorded depends on the settings of the detector slits.*

is recorded.

Similarly, in an L-scan through the $(\bar{2}02)$ reflection, the vertical detector slit should be narrow enough to achieve the necessary L-resolution, while the horizontal detector slit should be wider than the H-projection of the peak width. The slit settings in Figure 7.18, for example, will allow the mosaicity to be properly measured by an L-scan, but not by an H-scan.

As the movement of the motors on the ID32 diffractometer for changing the detector slit sizes is quite slow, it was impractical to adjust the slit sizes for every scan. Therefore, only the horizontal detector slit size was optimized at the beginning of the measurement for the copper$(\bar{4}00)$ and the copper$(\bar{2}00)$ reflection such that the mosaicity $\Delta\phi$ can be deduced from the L-scans.

If we assume that the different effects causing peak broadening are uncorrelated, the final profile of a peak is the convolution of the individual line shapes arising from the different effects.

The peak width in the different directions can therefore be written as

$$\begin{aligned}
\Delta L[r.l.u.] &= \sqrt{\Delta L^2_{mosaicity} + \Delta L^2_{domainsize} + \Delta L^2_{lattice}} && (7.10)\\
&= \sqrt{(\cos(\arctan(\frac{L}{H}\cdot\frac{a}{c}))\cdot\sqrt{L^2+H^2c^2/a^2}\cdot\Delta\phi)^2 + (\frac{c}{D_\perp})^2 + (\frac{\Delta d_\perp}{d_\perp}\cdot L_{Cu}\cdot\frac{c}{d_\perp})^2}\\
\Delta H[r.l.u.] &= \sqrt{\Delta H^2_{mosaicity} + \Delta H^2_{domainsize} + \Delta H^2_{lattice}} && (7.11)\\
&= \sqrt{(\sin(\arctan(\frac{L}{H}\cdot\frac{a}{c}))\cdot\sqrt{L^2a^2/c^2+H^2}\cdot\Delta\phi)^2 + (\frac{a}{D_\parallel})^2 + (\frac{d_\parallel}{\Delta d_\parallel}\cdot H_{Cu}\cdot\frac{a}{d_\parallel})^2}\\
\Delta K[r.l.u.] &= \sqrt{(\Delta K_{mosaicity})^2 + (\Delta K_{domainsize})^2} && (7.12)\\
&= \sqrt{(\Delta\theta\cdot H_{Cu}\cdot\frac{a}{d_\parallel})^2 + (\frac{a}{D_\parallel})^2}.
\end{aligned}$$

Note that the broadening due to the in-plane lattice constant variation does not contribute to ΔK in Eq. 7.12 because K is close to zero for the copper reflections in Figure 7.17. With these equations the in- ($D_\parallel$) and out-of-plane ($D_\perp$) domain-sizes, the changes in the lattice constants ($\Delta d_\parallel/d_\parallel$ and $\Delta d_\perp/d_\perp$) and the mosaicity of the in-plane rotation ($\Delta\theta$) as well as the out-of-plane tilt ($\Delta\phi$) of a copper domain can be determined by comparing the measured and calculated ΔL, ΔH and ΔK as functions of the peak position.

To obtain reliable results, a large dataset is needed. Two large datasets have been collected, one from a Ga-rich starting surface and the other an As-rich one, both with copper deposited at a potential of -350 mV, where stable Cu-clusters and the sharpest Cu peaks could be obtained. Applying more negative potentials leads to broader and weaker copper reflections such that the peaks at higher $|\vec{Q}|$'s can not be resolved.
To analyze the data, each measured copper peak is assigned to one specific domain. Since for the initial surfaces, the [100]- and [010]-directions are not equivalent, the epitaxy of the copper and its properties could depend on the tilt direction of the copper [001]-axis. To detect the possible differences between the tilt in the [010]- and in the [100]-direction each domain was analyzed independently.
The recorded peaks are the copper($0KL$)- or ($H0L$) reflections. The GaAs base system was used to describe the peak positions. In this coordinate system the H of a copper($0KL$) peak and the K of a copper($H0L$) peak are non-zero because of the in-plane rotation and out-of-plane tilt of the copper clusters. To simplify the programming of the fitting routine such that the program does not have to distinguish between the copper($H0L$) and ($0KL$) reflections, $R = \sqrt{H^2+K^2}$ is used to replace H and K. Since the H and K values for the copper ($0KL$) and copper ($H0L$) reflection, respectively, are very small, replacing H and K by R will introduce an error less than 1%. Equations 7.10, 7.11 and 7.12 can then be rewritten as

Domain	$\Delta\phi_L$	$\Delta\phi_R$	$\Delta\theta$	$\Delta d_\perp/d_\perp$	$\Delta d_\parallel/d_\parallel$	$(D_\parallel)_R$	$(D_\parallel)_\theta$	$D_\perp$
1	0.68°	0.65°	0.78°	1.44%	0.84%	104 Å	117 Å	130 Å
3	0.68°	0.66°	0.70°	1.41%	0.85%	104 Å	271 Å	106 Å
6	0.60°	0.65°	0.65°	1.36%	0.72%	155 Å	131 Å	213 Å
8	0.61°	0.65°	0.65°	1.08%	0.71%	139 Å	117 Å	152 Å

Tab. 7.4: *The fitted values obtained from the scans in the H-, K- and L-directions are summarized for each domain. The mosaicity of the tilt obtained from the scans in the L-direction $\Delta\phi_L$ and the radial direction projected in the HK-plane $\Delta\phi_R$ are summarized. The mosaicity of the in-plane rotation $\Delta\theta$ as well as the variation of the out-of-plane copper lattice constant $\Delta d_\perp/d_\perp$ and the in-plane copper lattice constant $\Delta d_\parallel/d_\parallel$ could be fitted. Also the size of the copper clusters in the [001]-direction $D_\perp$ as well as in the-in-plane direction $(D_\parallel)_R$ and $(D_\parallel)_\theta$ could be deduced.*

$$\begin{aligned}
\Delta L[r.l.u.] &= \sqrt{(\cos(\arctan(\frac{L}{R}\cdot\frac{a}{c}))\cdot\sqrt{L^2+H^2c^2/a^2}\cdot\Delta\phi)^2+(\frac{c}{D_\perp})^2+(\frac{d_\perp}{\Delta d_\perp}\cdot L)^2} \\
\Delta R[r.l.u.] &= \sqrt{(\sin(\arctan(\frac{L}{R}\cdot\frac{a}{c}))\cdot\sqrt{L^2a^2/c^2+R^2}\cdot\Delta\phi)^2+(\frac{a}{D_\parallel})^2+(\frac{d_\parallel}{\Delta d_\parallel}\cdot R)^2} \\
\Delta\theta[^\circ] &= \sqrt{(\Delta\theta)^2+(\frac{a}{R\cdot D_\parallel})^2}.
\end{aligned}$$

In these equations ΔH was replaced by ΔR, which is the peak width in the scan-direction of an H- or K-scan for a copper($H0L$)- or a copper($0KL$) reflection respectively. ΔK was replaced by $\Delta\theta$, which is the peak width of the corresponding rocking scan. This notation will be used in the following discussion.
The above equations were used in the program to fit the different peak widths. Whether the mosaicity of the tilt angle was taken into account was based on the peak width (ΔP, ΔR or ΔL) perpendicular to the scan direction and the resolution in reciprocal space (ΔRS) in this direction. For $\Delta RS > \Delta P$ the mosaicity was included in the fit of the peak width. For $\Delta RS < \Delta P$ the tilt mosaicity could not be resolved and its contribution to the peak width was therefore omitted in the fit.

Line-shape analysis: copper deposition on an As-rich surface

In Figure 7.19 the measured ΔL (black squares) and its best fit (red circles) are plotted for copper deposited at -350 mV on a formerly (2×4)-reconstructed surface. All peaks arising from the same copper domains are plotted together. The peak widths of four different domains (Domain 1, 2, 3 and 8, see Figure 7.16) are shown. In Figure 7.19 (a) the peaks are labeled with the corresponding copper (HKL) values. As shown in Figure 7.17, the L-projection of the copper($\bar{2}02$) reflection is narrower than that of the copper(202) reflection when the peak-widths are dominated by the mosaicity $\Delta\phi$. In addition, because of the fixed size of the horizontal detector

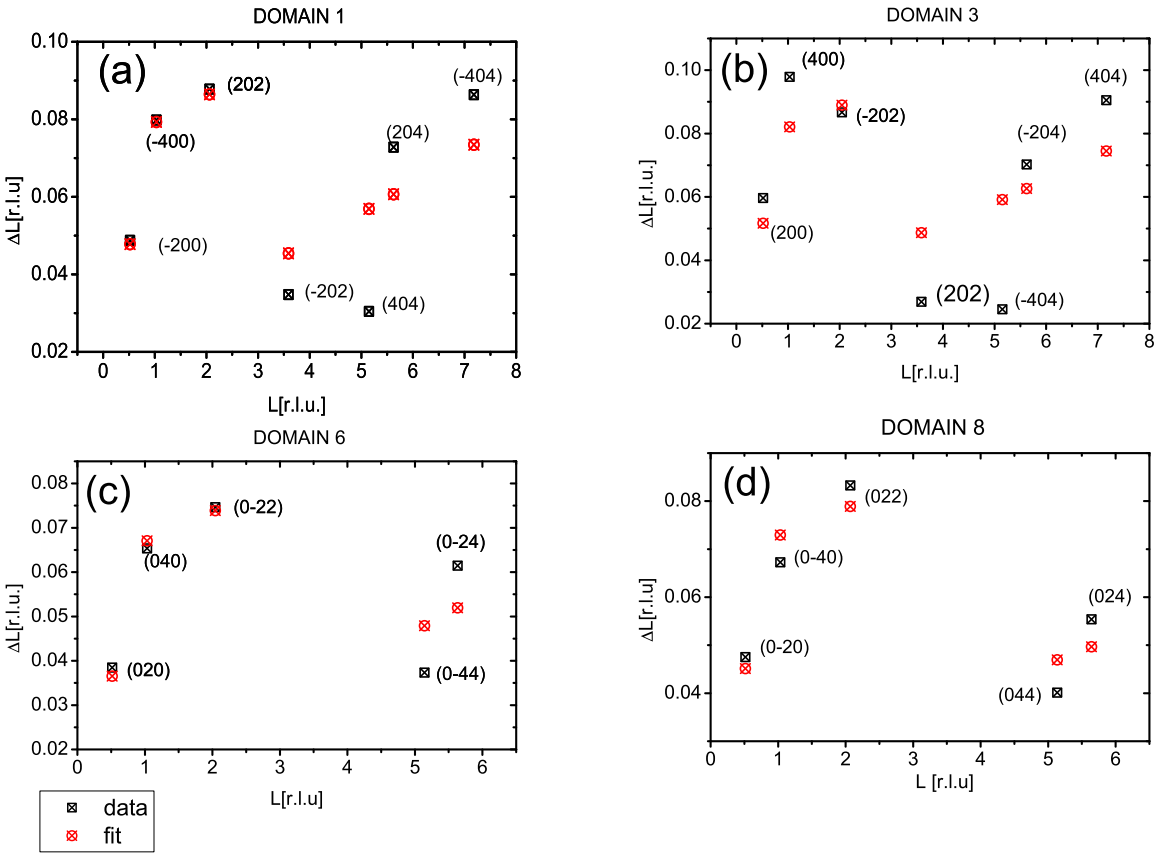

Fig. 7.19: *Measured (black squares) peak widths in the L-direction and their best fit (red circles)for the copper Bragg reflections of Domains 1, 3, 6 and 8. The copper was deposited at -350 mV on an arsenic rich surface. The peaks are indexed with the copper(HKL)-values.*

slits, as discussed previously, the out-of-plane mosaicity $\Delta\phi$ can be determined from the peak width only ΔL up to L=2.2 r.l.u.. As the copper (202)- and ($\bar{2}02$) peaks are observed below and above this limit, respectively, only the measured width of the copper (202) reflection has the full contribution from the mosaicity $\Delta\phi$. The ΔL of the ($\bar{2}02$) is thus much smaller than that of the copper(202) reflection. The $\Delta\phi_L$ obtained from the different domains are given in Table 7.4 and the average value is about $\Delta\phi_L = 0.64°$.
For $L > 2.2$ r.l.u. ΔL becomes dominated by the variation of the out-of-plane copper lattice constant $\Delta d_\perp/d_\perp$ and increases almost linearly with L. The values obtained for $\Delta d_\perp/d_\perp$ are given in Table 7.4. The ΔL's of Domains 1 and 3 were measured up to higher L than Domains 6 and 8, therefore $\Delta d_\perp/d_\perp$ could be determined more precisely with Domains 1 and 3. The mean value of $\Delta d_\perp/d_\perp$ is 1.4%. In addition, the domain-size $D_\perp$ in the [001]-direction contributes to ΔL with a constant offset. The values obtained for the different domains are given in Table 7.4. In Figure 7.19 (a) and (b) the measured ΔL's of the copper (404) peaks show the largest discrepancy with the calculated ones. This discrepancy could be due to misalignment of the peak, which can occur more easily at higher $|\vec{Q}|$.

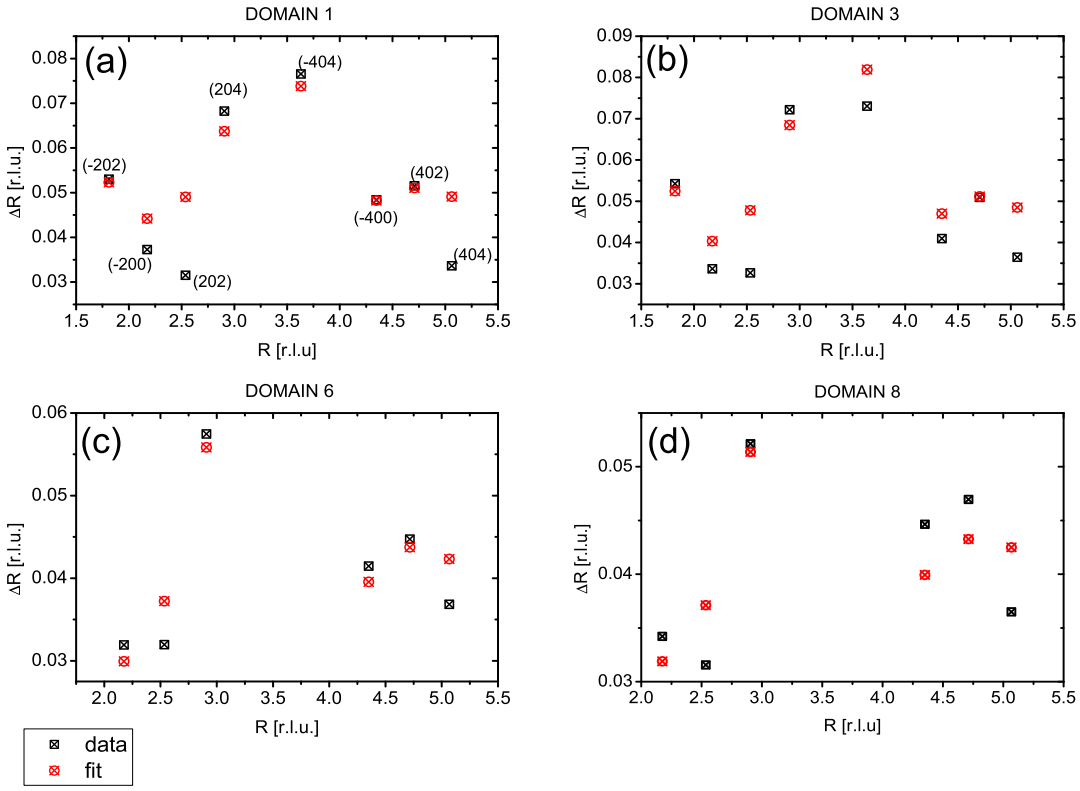

Fig. 7.20: *Measured (black squares) peak width ΔR and their best fit (red circles) for the copper reflections of Domains 1, 3, 6 and 8. The copper was deposited at -350 mV on an arsenic-rich GaAs(001)-surface. The peaks are indexed with the copper (HKL)-values.*

In Figure 7.20 the measured peak widths in the H- or K-direction, ΔR, and the corresponding best fits are plotted for the different domains. Compared to the analysis on ΔL, the different contributions to the ΔR are less easy to quantify. For the copper reflections with small R and large L, such as the $(\bar{2}02)$,(204) and $(\bar{4}04)$ copper peaks of Domain 1, the out-of-plane mosaicity $\Delta\phi$ contributes significantly to the peak broadening. The values of $\Delta\phi$ determined from ΔR, $\Delta\phi_R$, agree well with $\Delta\phi_L$ (Table 7.4).

The mean value of $\Delta d_{||}/d_{||}$ deduced from the analysis on ΔR is 0.84%. The last parameter determined by the fit of ΔR is the domain size $(D_{||})_R$. As it is the only value which does not depend on the peak position but contributes a constant offset to ΔR, it is also the least accurate one. The obtained values therefore fluctuate and the mean value of $(D_{||})_R$ is about 125 Å. Since the most accurate fits of ΔR are obtained for Domains 1 and 3 due to the larger numbers of reflections, the in-plane domain size is likely to be closer to $(D_{||})_R \approx 100$ Å (Table 7.4).
In Figure 7.21 the analysis of the peak widths $\Delta\theta$ in the direction of the rocking scans is shown for the copper deposited at -350 mV. The peak width $\Delta\theta$ decreases slowly with increasing R. The peak-width decreases slowly with increasing R, due to the fact that the main contribution to

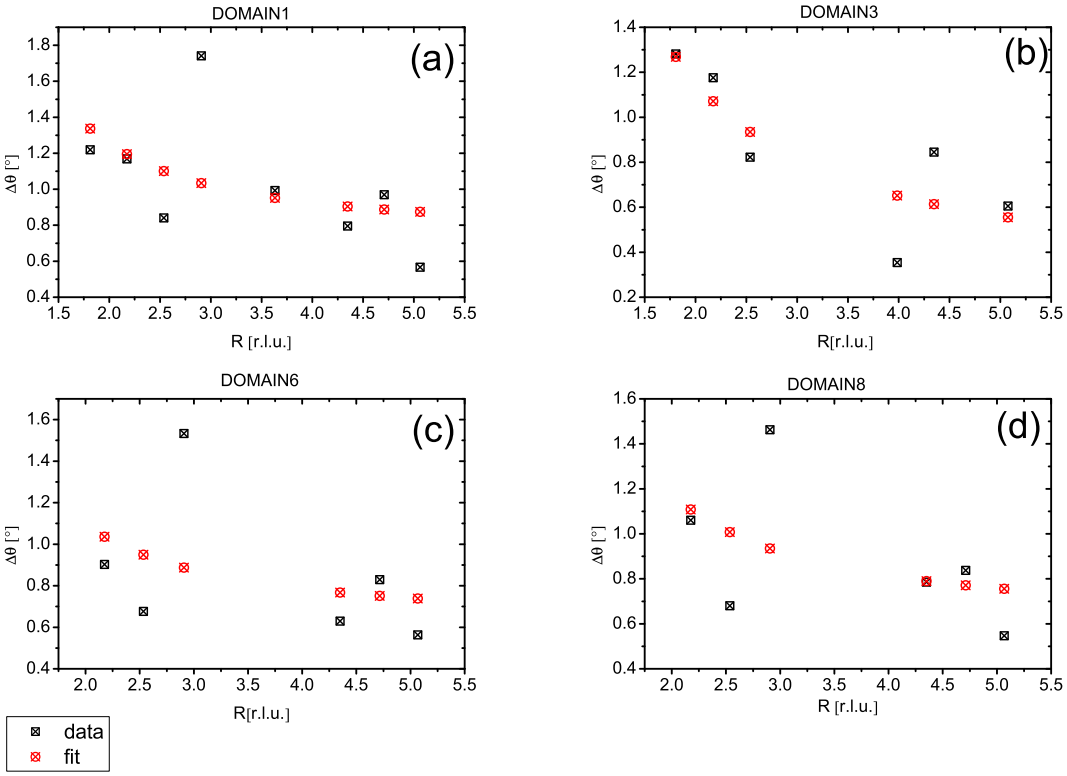

Fig. 7.21: *The measured peak widths $\Delta\theta$ (black squares) and their best fit (red circles) for the copper Bragg reflections of Domains 1,3, 6 and 8. The copper was deposited at -350 mV on an arsenic-rich GaAs(001)-surface.*

$\Delta\theta$ comes from the domain size $(D_{\|})_{\theta}$ and is constant in reciprocal lattice units and therefore decreases in angular units as R increases. The values of $\Delta\theta_{mosaicity}$ as well as $(D_{\|})_{\theta}$ are also given in Table 7.4. The averaged value of $\Delta\theta_{mosaicity}$ is 0.7°, comparable to the mosaicity $\Delta\phi$ of the tilt angle ϕ.

To study the influence of the nucleation potential on the copper growth, two samples were contacted with electrolyte at -900 mV and -1200 mV, respectively, and after one second the potential was set to -350 mV. The brief stays at the negative potential creates nucleation sites on the surface, however at such negative deposition potentials the copper peaks are broader, in particular the copper peaks at high $\vec{Q}$'s could not be resolved anymore. Therefore, only a small data set could be recorded for each domain at more negative potentials. To determine more reliably the mosaicities, domain sizes as well as the variation of the lattice constants all domains were analyzed together.
The results for the sample contacted at a potential of -900 mV are shown in Figure 7.22. Figure 7.22 (a) shows the peak width in the L-direction, ΔL. The mosaicity $\Delta\phi_L$ of the tilt angle mainly contributes to ΔL of the copper $(\bar{2}00)$ peak (at $L \approx 0.5$ r.l.u.) and the copper $(\bar{4}00)$ peak (at $L \approx 1$ r.l.u.). The best fit to the measured ΔL determines $\Delta\phi_L$ and $\Delta d_{\perp}/d_{\perp}$ and $D_{\perp}$ to be 0.81°, 1.4 %, 168 Å, respectively (Table 7.3).

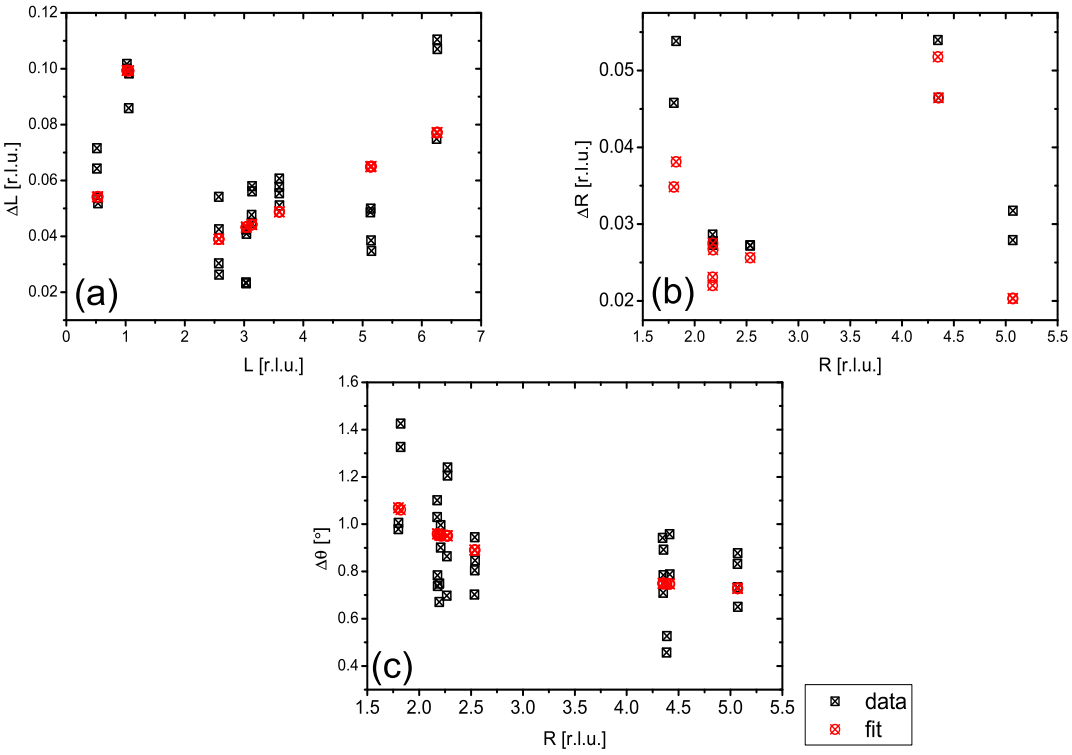

Fig. 7.22: *The peak widths of all eight domains fitted together for a sample contacted at a potential of -900 mV and set to -350 mV after one second. (a) The measured peak width in the L-direction as well as the corresponding values obtained from the fit are plotted. (b) The measured radial peak width and the values obtained from the fit are shown. (c) The fitted and measured peak widths of the linear scans perpendicular to the radial scans are combined. The peak width is determined by the mosaicity of the in-plane rotation as well as by the in-plane domain-size.*

In Figure 7.22 (b) the peak broadening in the radial direction, ΔR, is plotted. Unfortunately the peaks influenced the most by $\Delta\phi$ [e.g. the copper $(\bar{4}04)$ and the copper (204) reflections] were not recorded. The only measured peak that has the contribution $\Delta\phi$ to its broadening, is the copper $(\bar{2}02)$ reflection at $R = 1.7$ r.l.u., which determines $\Delta\phi_R$ to be $0.71°$. However the value $\Delta\phi$ obtained from fitting ΔL is more reliable.

The variation of the in-plane copper lattice constant is obtained by the fit: $\Delta d_{\parallel}/d_{\parallel}$ and $(D_{\parallel})_R$ from analyzing ΔR are 1.1% and 171 Å, respectively (Table 7.3).

Figure 7.23 shows the analysis of $\Delta\theta$ for the sample, which determines $\Delta D_{\parallel}$ to be 150 Å and $\Delta\theta_{mosaicity}$ to be $0.65°$ (Table 7.3).

The results of the sample contacted at -1200 mV are plotted in Figure 7.23. The best fit to the peak width ΔL [Figure 7.23 (a)], determines $\Delta\phi_L$, $\Delta d_{\perp}/d_{\perp}$ and $D_{\perp}$ to be $1.1°$, 1.8% and 140 Å, respectively (Table 7.3).

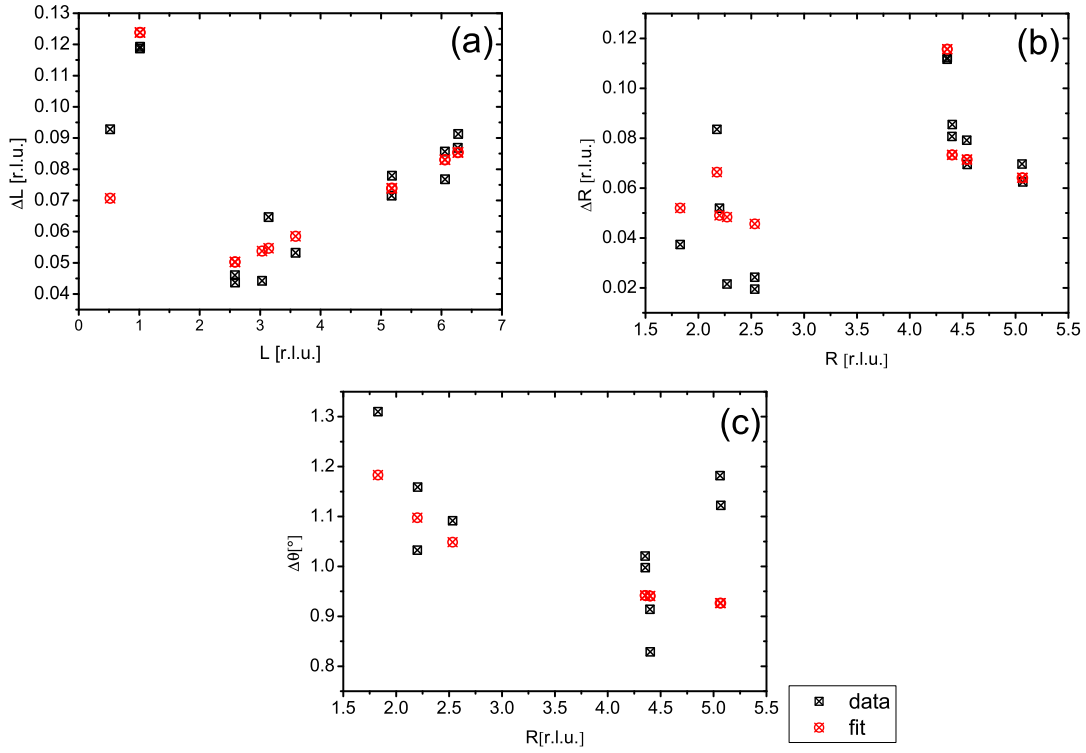

Fig. 7.23: *The peak widths of all eight domains fitted together for a sample contacted at a potential of -1200 mV and set to -350 mV after one second. (a) The measured peak widths obtained from an L-scan as well as the corresponding fitted values are shown. (b) The measured peak width in the radial direction and the values obtained from the fit are plotted. (c) The fitted and measured peak widths of the linear scans in the direction of the corresponding rocking scan are shown.*

The recorded peak widths ΔR [Figure 7.23 (b)] are not sensitive to the out-of-plane mosaicity, which could be due to the fact that no peaks at high L ($L_{Cu} = 4$) were recorded and the size of the vertical detector slit was too small to resolve the full width of the copper $(\bar{2}02)$ peak (the only copper peak recorded with $L > R$). The analysis on the peak width ΔR shows that $\Delta d_{\parallel}/d_{\parallel} = 0.86\%$ and $(D_{\parallel})_R = 140$ Å (Table 7.3).
The best fit of the peak width $\Delta\theta$ [Figure 7.23 (c)] reveals an in-plane mosaicity $\Delta\theta$ of 0.84° and an in-plane domain-size $(D_{\parallel})_\theta = 110$ Å.

In Table 7.3 $\Delta\phi$ and $\Delta d_{\perp}/d_{\perp}$ increase with more negative nucleation potential. The applied potential strongly influences the surface charge layer and the interface structure and therefore affects the surface mobility of the deposited atoms and their rearrangement, leading to copper epitaxy of different qualities.
Applying more negative nucleation potentials increases the number of nucleation sites and the growth rate of the copper. Consequently the quality of the epitaxy is expected to decrease with

Domain	$\Delta\phi_L$	$\Delta\phi_R$	$\Delta\theta$	$\Delta d_\perp/d_\perp$	$\Delta d_\parallel/d_\parallel$	$(D_\parallel)_R$	$(D_\parallel)_\theta$	$D_\perp$
2	1.16°	0.83°	1.22°	1.17%	1.16%	171 Å	114 Å	76 Å
4	1.24°	0.86°	0.85°	2.74%	1.26%	190 Å	67 Å	83 Å
5	0.95°	0.84°	1.07°	2.15%	0.64%	105 Å	119Å	176 Å
7	1.04°	0.72°	1.03°	1.79%	0.76%	99 Å	103 Å	101 Å

Tab. 7.5: *The fitted values obtained from the scans in the H-, K- and L-directions for copper deposited at a Ga-rich surface at -350 mV are summarized for each domain. The mosaicity of the tilt could be obtained from the scans in the L-direction $\Delta\phi_L$ as well as in the radial direction $\Delta\phi_R$. The mosaicity of the in-plane rotation $\Delta\theta$, the variation of the out-of-plane copper lattice constant $\Delta d_\perp/d_\perp$ and the in-plane copper lattice constant $\Delta d_\parallel/d_\parallel$ could be fitted. The size of the copper clusters in the in all three scan direction $D_\perp$, $(D_\parallel)_R$ and $(D_\parallel)_\theta$ could be deduced.*

more negative nucleation potentials. However no change of the $\Delta\theta_{mosaicity}$ can be observed. Also the $\Delta d_\parallel/d_\parallel$ and cluster-size $D_\parallel$ and $D_\perp$ of the copper do not show clear dependence on the nucleation potential.

Otherwise the variation of the in-plane lattice constant appears to be correlated to the in-plane cluster size. The smaller the $D_\parallel$ the less is the $\Delta d_\parallel/d_\parallel$. This could be due to the fact that the lattice constant needs a certain cluster size to fully relax, which could also explain why the copper in-plane lattice constants are larger (see Table 7.3) than the natural copper lattice constant.

Line-shape analysis: copper deposition on an Ga-rich surface

To detect any difference in the epitaxy for copper deposited on Ga- and As-rich surfaces, copper had been deposited at -350 mV on a formerly (4×2)-reconstructed surface. The same line-shape analysis described above was applied to the copper peaks measured from this surface. The energy of the X-ray beam used to take the data was 22.3 keV.
The measured and calculated peak widths are plotted in Figure 7.24. The mosaicity of the tilt influences the peak width ΔL for low L. The copper (202) peak at $L \approx 2$ r.l.u. is already half cut by the vertical detector slit and therefore the broadening due to the out-of-plane mosaicity could not be recorded. The best fit determining the average out-of-plane mosaicity $\Delta\phi_L$, $\Delta d_\perp/d_\perp$ and $D_\perp$ to be 1.08°, 1.96% and 100 Å. The values obtained for each domain are listed in Table 7.5.

In Figure 7.25 the measured peak widths in the radial direction ΔR as well as the corresponding calculated values are plotted. The peaks at high L [copper($\bar{4}04$) and copper(204)], which are broadened mostly by the tilt mosaicity were not recorded, these peaks were blocked by the top flange of the beryllium cylinder, because of the lower X-ray beam energy used for this measurement.
The out-of-plane mosaicity $(\Delta\phi)_R$ deduced from the radial scans is about 0.81°, which is less reliable than the one obtained from the L-scans. The variation in the copper in-plane lattice constant could be deduced to be $\Delta d_\parallel/d_\parallel = 1.1\%$ and the domain-size $(D_\parallel)_R = 140$ Å. The

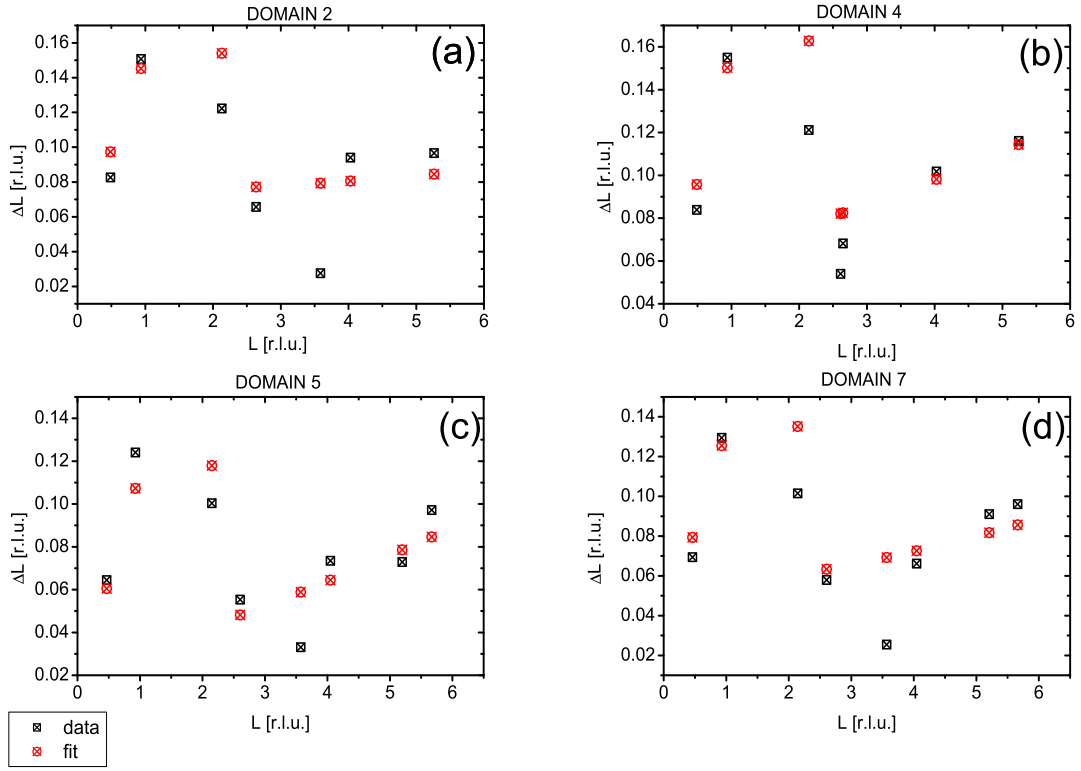

Fig. 7.24: *The measured (black squares) and fitted (red circles) peak widths of the copper Bragg reflections in the [001]-direction are plotted. The copper was deposited at -350 mV on a gallium-rich GaAs(001)-surface. At low L the mosaicity of the tilt has a major contribution to the peak broadening, at high L the peak width is basically determined by the variation in the out-of-plane lattice constant.*

detailed values for each domain are given in Table 7.5.
The fit of the $\Delta\theta$ and the measured data are plotted in Figure 7.26. The in-plane mosaicity and the domain-size in this direction could be determined. The detailed values for the domains are given in Table 7.5. The mosaicity of the in-plane rotation was obtained to be about $\Delta\theta = 1.04°$, comparable to the mosaicity of the tilt. The averaged domain-size is about $(D_{\parallel})_{\theta} = 100$ Å.
The results obtained from the As-rich starting surfaces as well as Ga-rich starting-surface are summarized in Table 7.6. In general the out-of-plane mosaicity of as well as the variation of the out-of-plane copper lattice constant are increasing with the nucleation potential. The $\Delta\phi$ and $\Delta\theta$ as well as $\Delta d_{\perp}/d_{\perp}$ and $\Delta d_{\parallel}/d_{\parallel}$ are larger for copper deposited on a Ga-rich surface than on an As-rich surface for the same deposition potential.

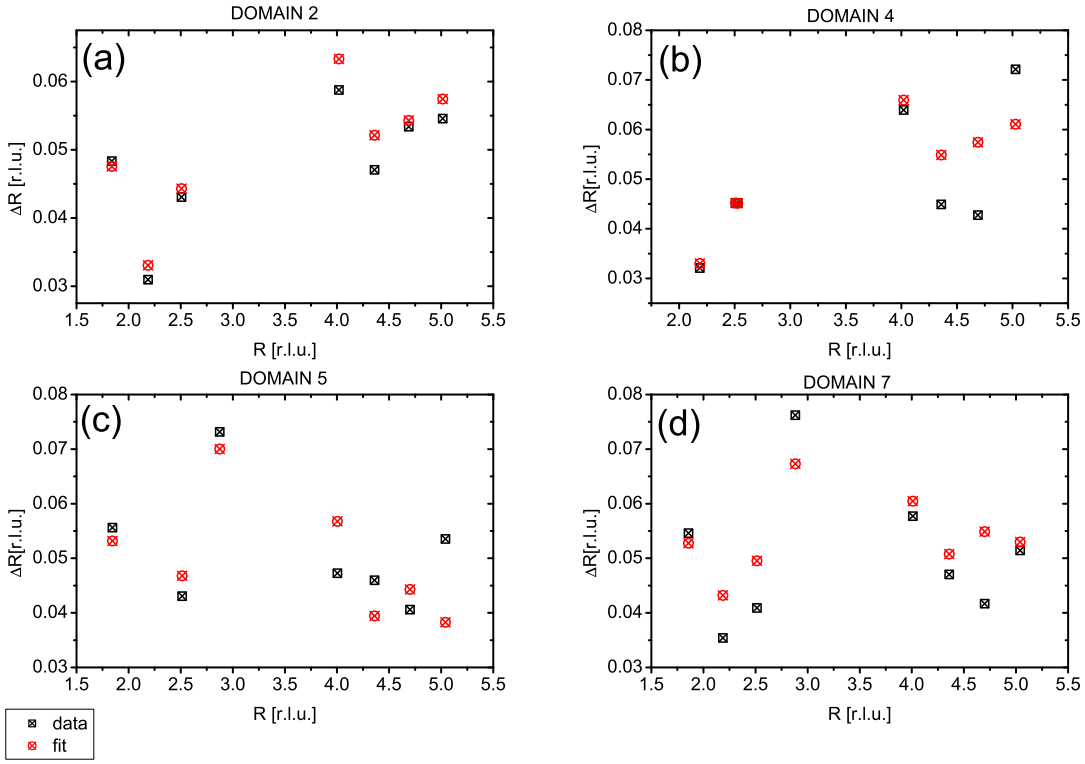

Fig. 7.25: *The peak widths of the copper Bragg reflections in the radial direction obtained for copper deposited at -350 mV on a Ga-rich surface are plotted. The measured data (black squares) as well as the corresponding values obtained from the fit (red circles) are shown.*

termination	deposition potential	$\Delta\phi$	$\Delta\theta$	$\Delta d_{\parallel}/d_{\parallel}$	$\Delta d_{\perp}/d_{\perp}$	$D_{\parallel}$	$D_{\perp}$
As-rich	-350mV	0.65°	0.7°	0.84%	1.4%	125Å	150Å
	-900 mV → -350 mV [1]	0.81°	0.7°	1.4%	1.7%	190Å	168Å
	-1200mV→ -350mV [1]	1.1°	0.84°	0.86%	1.8%	130Å	140Å
Ga-rich	-350mV	0.93°	1.0°	1.1%	1.8%	107Å	109Å

[1] a step potential of -900 mV (-1200 mV) has been applied for one second before jumping to -350 mV

Tab. 7.6: *In this table the mosaicity of the tilt and the in-plane rotation as well as the variation of the in-plane and out-of-plane copper lattice constants and the in-plane and out-of-plane copper cluster-sizes are summarized. The values were determined for different nucleation potentials and for an As-rich and a Ga-rich starting surface for copper deposited at -350 mV.*

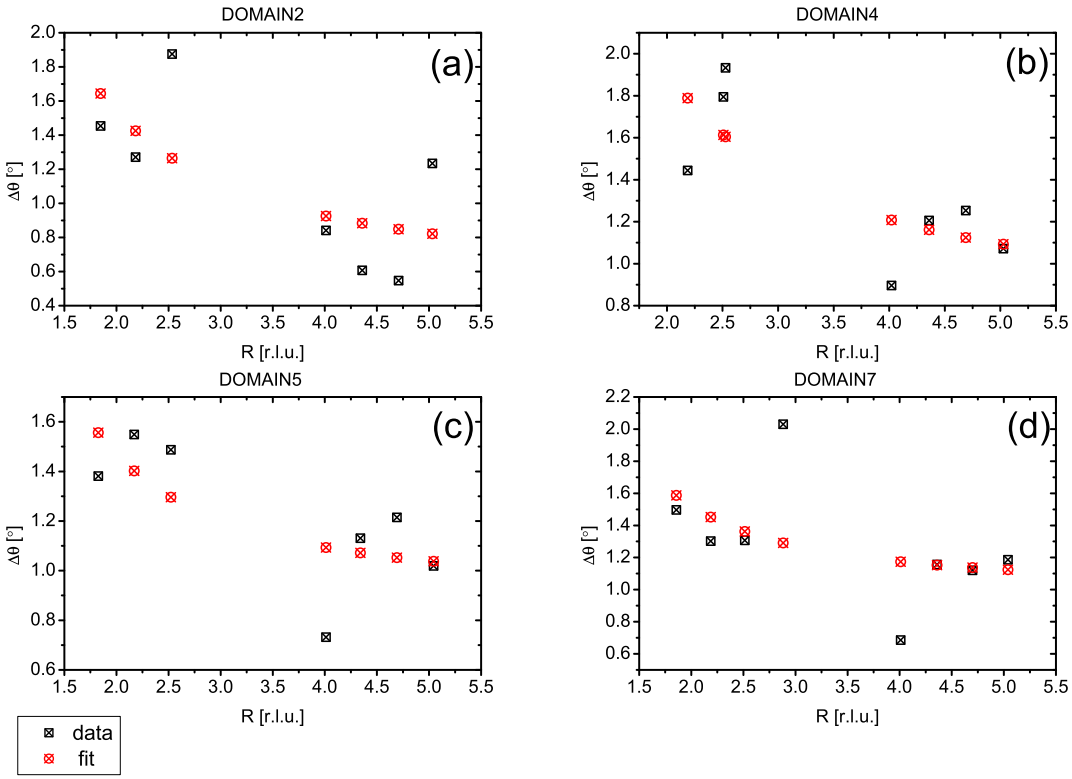

Fig. 7.26: *The peak widths of the copper Bragg reflections obtained in the in-plane direction perpendicular to the radial scan for copper deposited at -350 mV on a Ga-rich surface are plotted. The measured data (black squares and the values obtained from the fit (red circles) are shown together.)*

7.3.3 Facets

Smoothly terminated clusters give rise to diffuse intensity streaks perpendicular to the cluster surfaces, as modeled in Figure 7.27. The cluster in the figure has two inclined surfaces per-

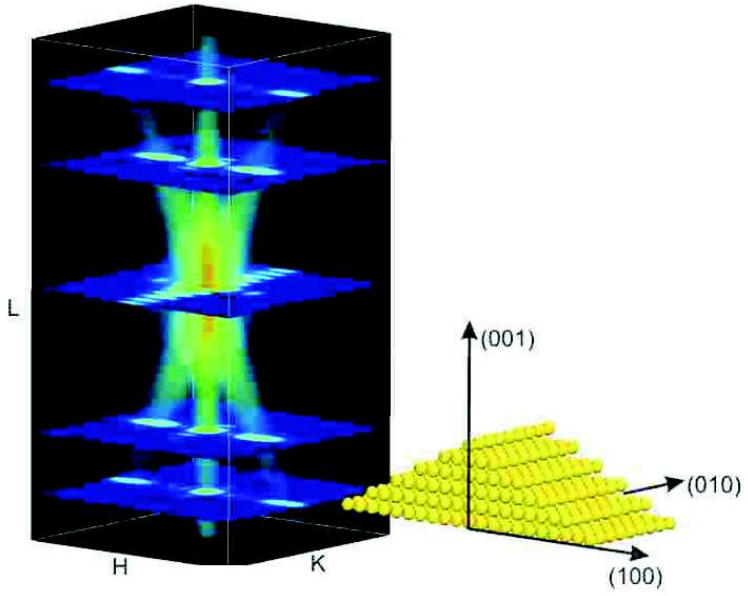

Fig. 7.27: *Simulation of the intensity streaks close to a Bragg peak arising from a smoothly terminated cluster. The cluster has two surfaces in the [*102*] and the [*$\bar{1}$02*]-directions and sharp terminations corresponding to the (*010*) planes. These planes give rise to diffuse intensity streaks in the direction perpendicular to the termination. Also a streak from the bottom (*001*)-plane can be observed. Modeled mesh-scans in the HK-plane at different L, cutting the streaks and the Bragg peak, are also shown.*

pendicular to the [102]- and the [$\bar{1}$02]-direction and two side walls corresponding to the $\{010\}$ planes. The electrochemically deposited copper forms eight different domains that tilt and rotate with respect to the GaAs lattice, which is ued as a coordinate system to define the orientation matrix. To find any intensity associated with the terminations of the clusters, mesh-scans in the HK-plane (parallel to the GaAs surface) at different L values in the region around the copper (020) reflections were performed. Such scans are illustrated in Figure 7.27. In the presence of smooth facets the scans cut through the intensity streaks at different L and therefore shifts of the intensity spots in the HK-planes towards or away from the copper peaks along the high symmetry directions can be observed with changing L.
A first set of mesh-scans was performed on a formerly As-rich GaAs(001) surface on which copper was deposited at -350 mV. As the best epitaxy (lowest mosaicity and variation of the copper lattice constants) was obtained at this potential, the sharpest streaks were expected for this deposition condition. The mesh scans recorded at L=0.06, 0.16, 0.26, 0.36, 0.46 and 0.56 r.l.u. in the region where 0 r.l.u.$< H <$0.6 r.l.u. and 1.8 r.l.u. $< K <$ 2.4 r.l.u. are shown in Figure 7.28 (a)-(f). This region covers the copper (020) reflections from two different domains, one at $\vec{Q} = (0.2, 2.2, 0.04)$ (Domain 4) and the other at $\vec{Q} = (0.2, 2.18, 0.48)$ (Domain 6). The for-

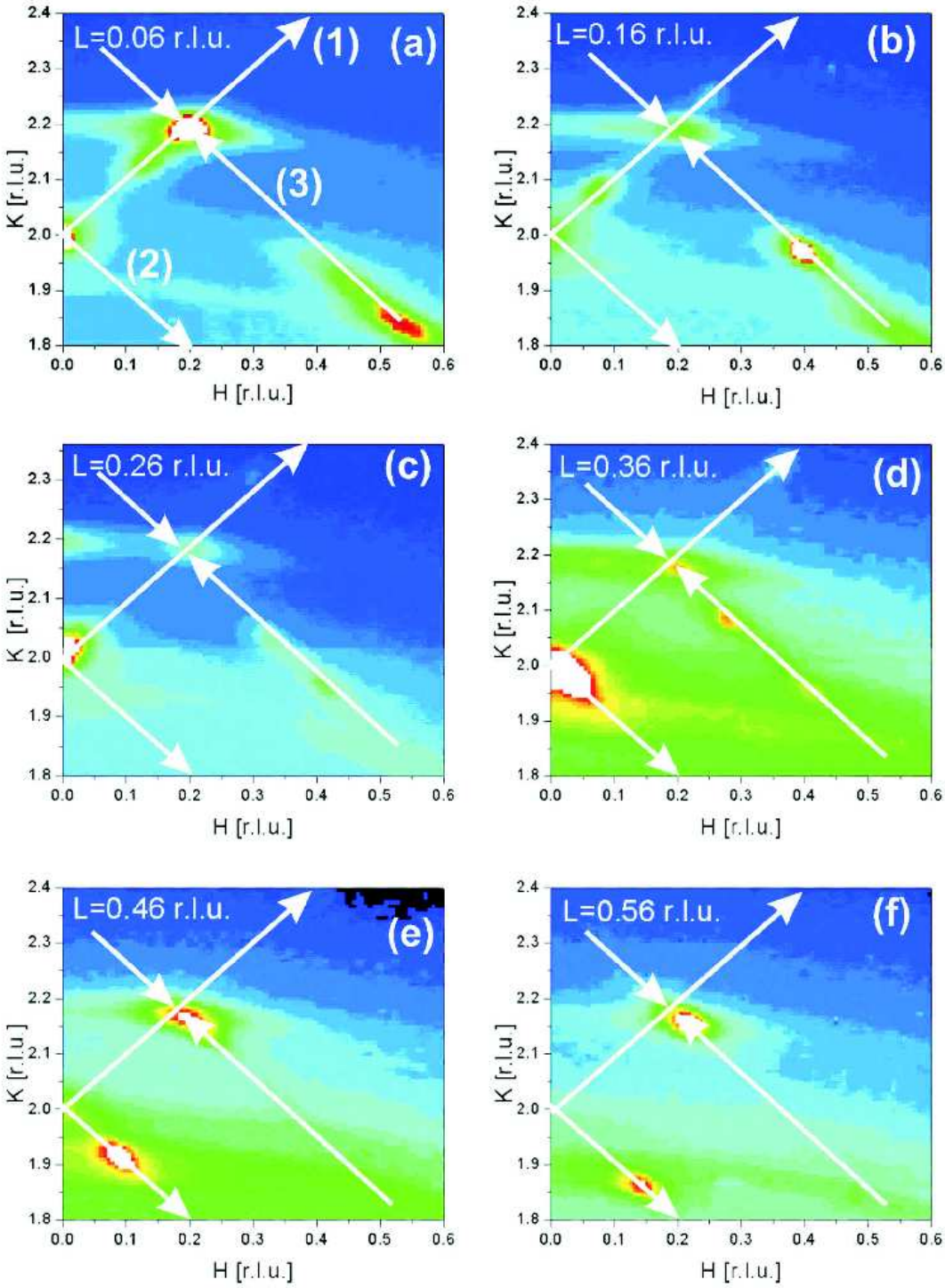

Fig. 7.28: *Mesh-scans in the HK reciprocal space plane at different L's are shown. Two copper* (020) *peaks are lying in the scanned region, one at* $\vec{Q} = (0.2, 2.2, 0.04)$ *and one at* $\vec{Q} = (0.2, 2.18, 0.48)$. *The arrows are indicating the direction of the intensity shift starting or ending at the copper* (020) *peaks.*

mer can be seen in Figure 7.28 (a). At higher L, a splitting of this peak into three weaker spots can be observed and is indicated by the arrow labeled (1). At L=0.16 r.l.u. [Figure 7.28 (b)] two peaks moving along Arrow (1) can be observed at $\vec{Q} = (0.28, 2.25, 0.16)$ and $\vec{Q} = (0.08, 2.08, 0.16)$. At even higher L, the maxima of the spots shift even further apart along this arrow. At L= 0.26 r.l.u. [Figure 7.28 (c)] the split peak moving towards lower H and K merges with the GaAs(0,2)-CTR lying on the edge of the image. At this point the higher intensity streak originating from the copper(020) peak at $\vec{Q} = (-0.2, 2.2, 0.04)$ (Domain 1), which is symmetric to the Cu(020) at $\vec{Q} = (0.2, 2.2, 0.04)$ (Domain 4) with respect to the H=0 plane, also intersects the GaAs(0,2) CTR and enters the scanned HK-range. It shifts along Arrow (2) and can be observed up to L=0.56 r.l.u..

Similarly, a third peak shift can be observed along the Arrow (3). At L=0.06 r.l.u. the peak of this intensity streak appears at H=0.55 r.l.u and K=1.85 r.l.u.. With increasing L the peak intensity decreases and its position moves towards the Cu(020) peak at $\vec{Q} = (0.2, 2.18, 0.48)$. Based on the reciprocal space maps in Figure 7.28, the three intensity streaks are identified to be oriented along the copper $\langle 111 \rangle$-directions of the corresponding copper domains. More specifically, streak (1) is oriented along the Cu[111]- and Cu[$\bar{1}\bar{1}$1]-direction of Domain 4, while streak (2) and (3) are parallel to the Cu[$\bar{1}$11]- and Cu[1$\bar{1}$1]-directions of Domains 1 and 6, respectively. Note that only two $\langle 111 \rangle$-streaks are observed for the Cu(020) peak of each domain.

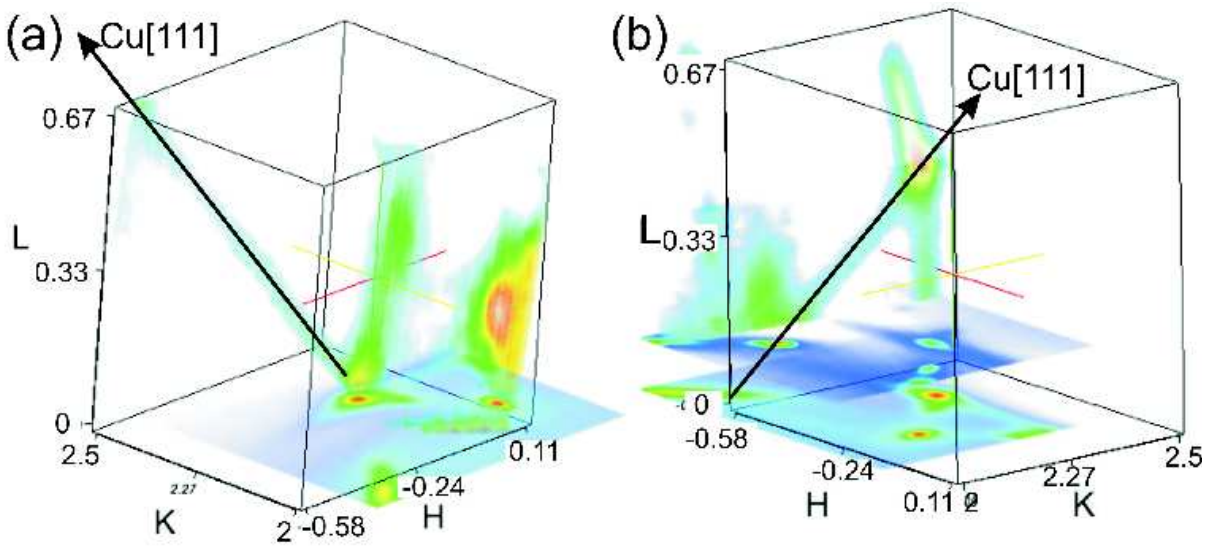

Fig. 7.29: *Two mesh-scans along copper ($\bar{1}$10) planes are shown. Figure (a) presents the diffuse intensity peak coming from the Cu(020) reflection at $\vec{Q} = (-0.2, 2.2, 0.04)$. Figure (b) shows the intensity profile around the Cu(020) peak at $\vec{Q} = (-0.2, 2.18, 0.48)$. The intensity due to the truncation of the copper clusters is clearly showing up. For both peaks the Cu[111]-direction is indicated.*

Additional mesh scans were performed to map the intensity streaks directly. Each scan lies in the plane spanned by the Cu$\langle 110 \rangle$- and the Cu[001]-directions and contains one of the Cu(020) peaks at $\vec{Q} = (-0.2, 2.2, 0.04)$ (Domain 1) and $\vec{Q} = (-0.2, 2.18, 0.48)$ (Domain 5). The thus ob-

tained intensity profiles are shown in Figure 7.29. The diffuse intensity streaks in the Cu⟨111⟩-directions can be clearly identified. No additional Cu⟨111⟩ streaks can be found in the mesh-scans perpendicular to those shown in Figure 7.29. In Figure 7.29 (a) the ⟨111⟩ streaks are oriented in the [$\bar{1}$11] and [1$\bar{1}$1]-directions of Domain 1. In Figure 7.29 (b) the ⟨111⟩ streaks are oriented in the [$\bar{1}\bar{1}$1] and [111]-directions of Domain 5.

In addition, for each two Cu⟨111⟩ streaks originating from the same copper peak, the one at smaller $|\vec{Q}|$ appears stronger and can be followed further. Also, neither Figure 7.28 nor Figure 7.29 show any copper diffuse streak through the copper peaks in the GaAs[001]- or the Cu[001]-direction, which can arise from a smooth Cu/GaAs interface. In Figure 7.29 the vertical streaks through the GaAs(020) reflection is the GaAs(0, 2)-CTR.

Additional mesh-scans were performed to map the intensity along the Cu⟨111⟩-directions

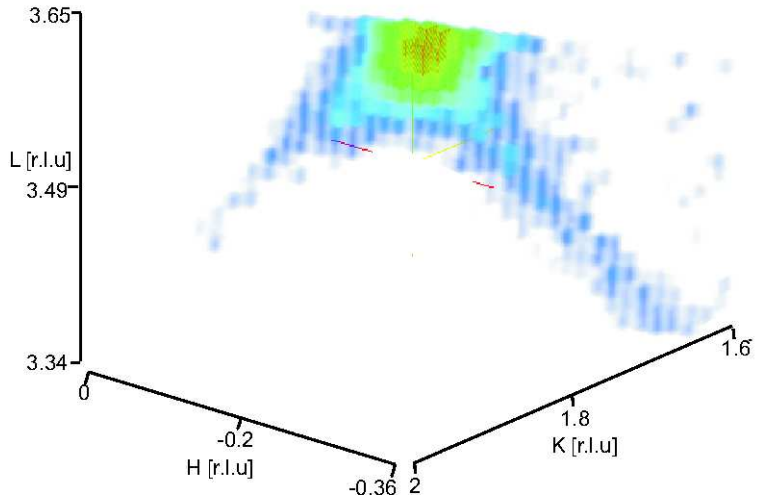

Fig. 7.30: *The intensity profile obtained in the copper ⟨$\bar{1}$10⟩-plane around the copper(*022*) reflection. Diffuse streaks in the copper[*111*] and copper[*$\bar{1}\bar{1}$0*]-directions are visible.*

around the Cu(022) reflection at $\vec{Q} = (-0.2, 1.8, 3.63)$ (Domain 5). Since this region is far away from any GaAs Bragg peak, it was chosen to verify if the ⟨111⟩ intensity streaks observed around the Cu(020) peaks were indeed caused by the facets of the copper clusters and to have lower background from the GaAs. The mapped areas were spanned by the Cu[110]- and Cu[001]-directions as well as the Cu[$\bar{1}$10]- and Cu[001]-directions. One of the obtained intensity profiles in the reciprocal space is shown in Figure 7.30. The intensity streaks are fairly sharp, but only two Cu⟨111⟩ streaks, oriented along the Cu[111] and Cu[$\bar{1}\bar{1}$1]-directions, can be observed. Also the two observed streaks do not have the same intensity: the streak appearing at smaller $|\vec{Q}|$ is more intense and can be followed further.

To study the influence of the nucleation potential on the termination of the deposited copper clusters, another set of mesh-scans was measured around the Cu(200) reflections from a sample prepared under a different growth condition. The sample surface was contacted at -1200 mV and after one second the potential was set to -350 mV.

The mesh-scans recorded in the *HK*-planes at different *L*'s (*L*=0.06, 0.16, 0.26, 0.36,0.46 and 0.56 r.l.u.) are shown in Figure 7.31. The intensity scales of the six images are not the same

but were chosen to best present qualitatively the various features emerging from each image. In total four copper (200) peaks at $\vec{Q} = (2.2, 0.2, 0.06)$ (Domain 5), $\vec{Q} = (2.2, -0.2, 0.06)$ (Domain 8), $\vec{Q} = (2.18, 0.18, 0.48)$ (Domain 3) and $\vec{Q} = (2.18, -0.18, 0.48)$ (Domain 4) are covered by the scanned region. The copper Bragg peaks are not as sharp as those measured from the copper deposited at -350 mV. They have particularly higher in-plane and tilt mosaicity, as described in section 7.3.2.
In Figure 7.31 the arrows are labeled in the same way as in Figure 7.28 [except for Arrow (4)]. Note that the region 0 r.l.u.$< H <$ 0.3 r.l.u. in Figure 7.28 is equivalent to the region -0.3 r.l.u.$< K <$0 r.l.u. in Figure 7.31 if the latter is rotated by 90° counterclockwise. Arrow (1) indicates the Cu$[\bar{1}11]$ or $[1\bar{1}1]$ intensity streak that is observed around $\vec{Q} = (2.1, -0.1, 0.06)$ and associated with the copper Bragg peak at $\vec{Q} = (2.2, -0.02, 0.04)$. Arrow (2) marks the intensity streak that is symmetric to the one marked by Arrow (1) with respect to K=0. Arrows (3) and (4) indicate the intensity streaks associated with the copper peaks at $\vec{Q} = (2.18, \pm 0.2, 0.48)$, which can be first observed at $\vec{Q} = (2.1, \pm 0.3, 0.26)$.
Figure 7.31 shows that the intensity streaks due to the facets of the copper clusters are also present at such a negative nucleation potential, although the copper peaks as well as the intensity streaks appear more diffuse with higher background around the GaAs(200) peak. Two additional streaks at L=0.06 r.l.u. can be observed, one running from $\vec{Q} = (2, 0.3, 0.06)$ to $\vec{Q} = (2.2, -0.2, 0.06)$ and the other one from $\vec{Q} = (2, -0.3, 0.06)$ to $\vec{Q} = (2.2, 0.2, 0.06)$. Another interesting point is the merging of all four copper(200) peaks at $\vec{Q} = (0, 2.2, 0.26)$, which could be due to the high mosaicities.

The copper clusters form facets in the Cu$\langle 111 \rangle$-directions. However, the intensity streaks could only be found in two of the four $\langle 111 \rangle$-directions for each copper domain. For each two streaks originating from the same copper reflection, the one closer to the origin appears stronger. All the mesh scans recorded around the copper Bragg reflections show that the intensity streaks of Domains 1, 3, 6 and 8 are oriented along the Cu$[\bar{1}11]$- and Cu$[1\bar{1}1]$-directions, and those of Domains 2, 4, 5 and 7 are parallel to the Cu[111]- and Cu$[\bar{1}\bar{1}1]$-directions. Such observed orientations of the streaks obey the rotational and mirror symmetries required by the eight domains due to the rotation and tilt of the copper clusters. It remains, however, an open question why for each domain the Cu$\{111\}$-facets do not form in the other two orientations.

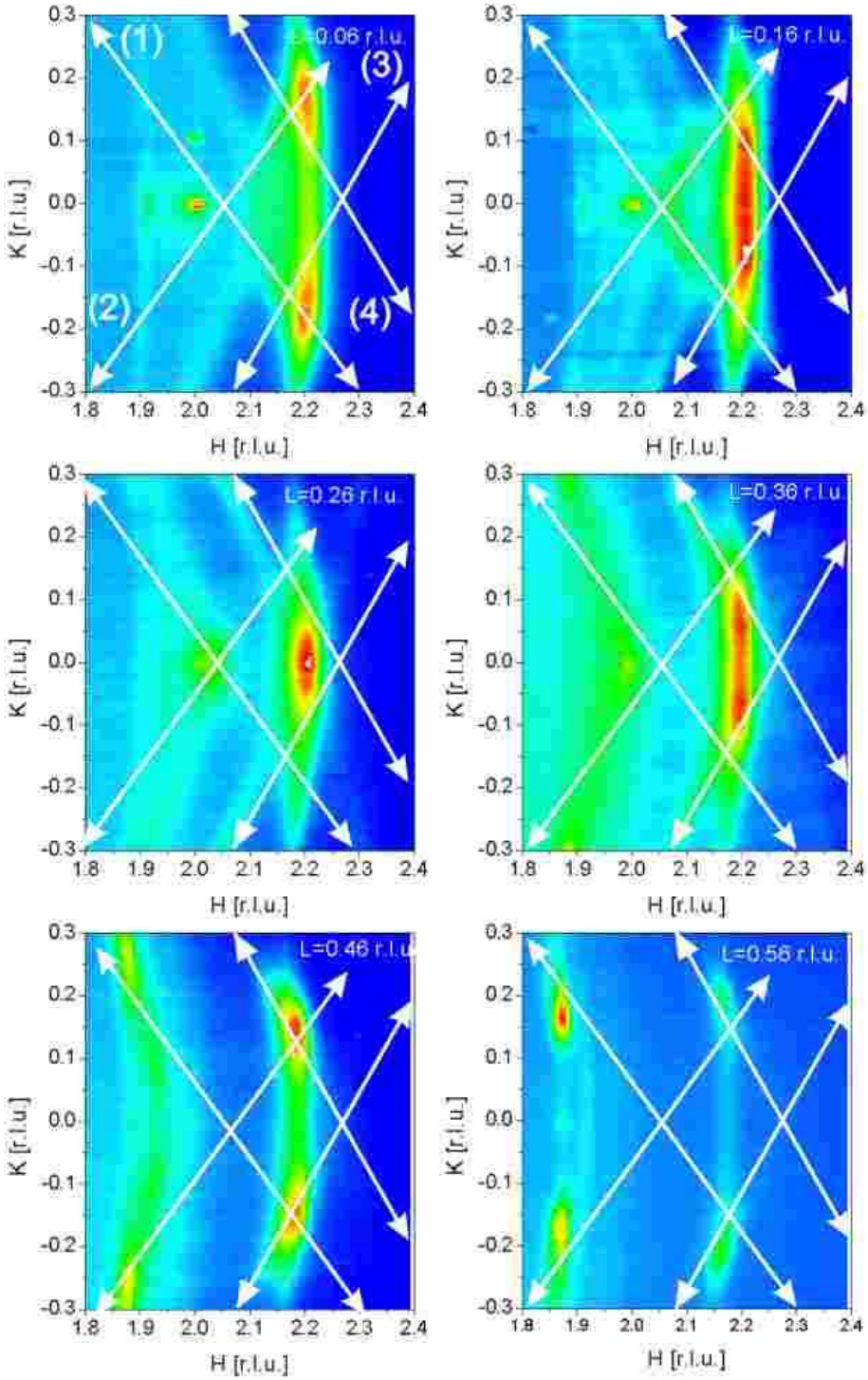

Fig. 7.31: *Mesh-scans in the HK reciprocal space plane at different L are shown around the copper(*200*) reflection. The copper has been deposited by contacting the sample with electrolyte at -1200 mV and changing the potential to -350 mV after one second. Four copper(*200*) peaks are lying in the scanned region, two at* $\vec{Q} = (\pm 0.2, 2.2, 0.04)$ *and at at* $\vec{Q} = (\pm 0.2, 1.8, 0.48)$*. The arrows are indicating the direction of the intensity shift starting or ending at the copper(*200*) peaks.*

7.3.4 Investigation of the Cu epitaxy close to the interface

As has been shown in the previous section, the copper clusters are terminated with copper{111}-planes. No intensity streaks originating from the Cu/GaAs interface are observed, which could be an indication for a rough interface. However, the copper peaks for the copper deposited at -350mV on a UHV prepared surface are sharp and the orientations of the copper lattices relative to the GaAs surface are well defined, indicating an epitaxial growth of the copper. In addition, the epitaxy obtained for copper deposited on a UHV prepared smooth surface was found to be slightly different from the copper deposited on a chemically etched and thus rough surface. To get more structural information about the interface and the first monolayers of the deposited copper, the relative intensity of X-rays diffracted from the copper close to the interface has to be enhanced. It is therefore essential to measure samples with thiner copper coverage.

However, the amount of the deposited copper is difficult to control with the used setup. The electrodeposition is diffusion limited, leading to a decreasing deposition current with time and therefore an almost constant copper coverage. However, each sample was typically measured over two days. During this timescale the copper coverage can still increase. In addition, the droplet evaporates with time and has to be replenished from time to time to keep a constant shape. By pumping new electrolyte into the droplet, more copper ions can reach the surface. Furthermore, beam damage can have strong effects on the local coverage of the copper layer.
To access the structure of the interface the copper was stripped. The outer layers of the copper are expected to dissolve first. Afterwards, copper was redeposited to assure that the same epitaxy as obtained after the first deposition can be restored and thus that the observed structure near the interface is not caused by the stripping. The thus obtained results are presented in this section. Despite the problem in controlling the copper coverage, another attempt to get more information about the interface was made by measuring ex-situ a sample with 20ML coverage.

Stripping and redeposition

The first measurement was conducted on a sample with copper deposited at -500 mV. For stripping the potential was slowly changed in steps of 50 mV to more positive values. During this procedure the copper($\bar{2}02$) reflection at $\vec{Q} = (-2.2, 0.52, 3.04)$ was scanned in the H-, K- and L-directions. The intensity as well as the change of the peak position were monitored. The scans measured in the H-, K- and L-directions during the stripping are shown in Figure 7.32. The intensity starts to decrease slowly at a potential of -200 mV. A strong reduction of the intensity is observed at a potential of -100 mV. The decreasing of the intensity is accompanied by a shift of the peak to lower $\vec{Q}$. One can see more clearly the shift of the peak in the scans in the H- and L-directions. The varying peak position and the corresponding lattice constant during the process are determined. The results are plotted versus the scan number in Figure 7.33. In Figure 7.33 (a) the applied potential is shown. Figure 7.33 (b) and (c) present the corresponding intensity and copper out-of-plane lattice constant, respectively. The copper in-plane and out-of-plane lattice constants are determined independently from the copper ($\bar{2}02$) peak position. Both of them are found to increase during the stripping. The changes of the lattice constants are therefore likely not due to strain.
After the copper was stripped, the potential was set again to -500 mV and later to -650 mV to redeposit the copper. An increase in the peak intensity indicates the regrowth of the copper. The

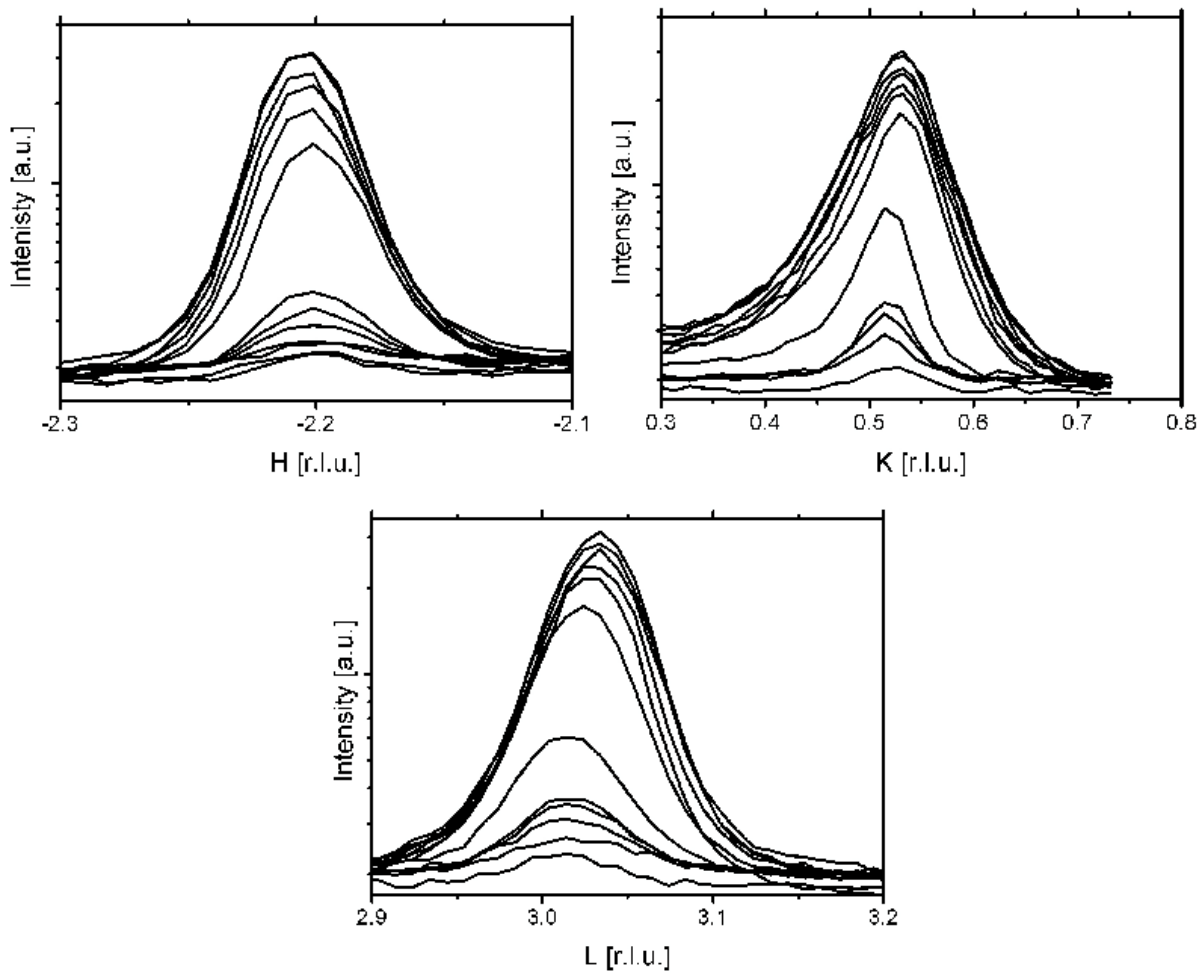

Fig. 7.32: *The peak profiles in the H-, K- and L-direction are shown during the stripping of copper deposited on a As-rich surface at -500 mV. The intensity is decreasing during the dissolution of the copper. Simultaneously a shift of the copper peak to smaller $|\vec{Q}|$ values is observed.*

copper lattice constant decreases immediately to the value of natural copper (3.615 Å) and then increases slowly but continuously to a larger value (3.618 Å).
During this stripping the peak position was not readjusted and a slight peak misalignment is expected. Therefore only a general conclusion about the change in the lattice constant can be drawn. To detect the possible changes of the rotation and tilt angles an additional measurement was done by stripping the copper and recording the copper(200) reflection at $\vec{Q} = (2.18, 0.15, 0.46)$. The *L*- and *K*-values of this peak are determined mainly by the tilt and the in-plane rotation of the copper lattice, respectively. This reflection is therefore most sensitive to any change of the tilt or rotation angle. However, it is totally insensitive to the out-of-plane lattice constant. The variation of the in-plane lattice constant affects mostly the *H*-value of this peak. During the copper dissolution the copper peak was readjusted to its maximum. This measurement was done on a formerly GaAs(001)-(4×2) surface, on which copper was deposited at -350 mV. For weaker peaks the readjustment became more difficult. The peak

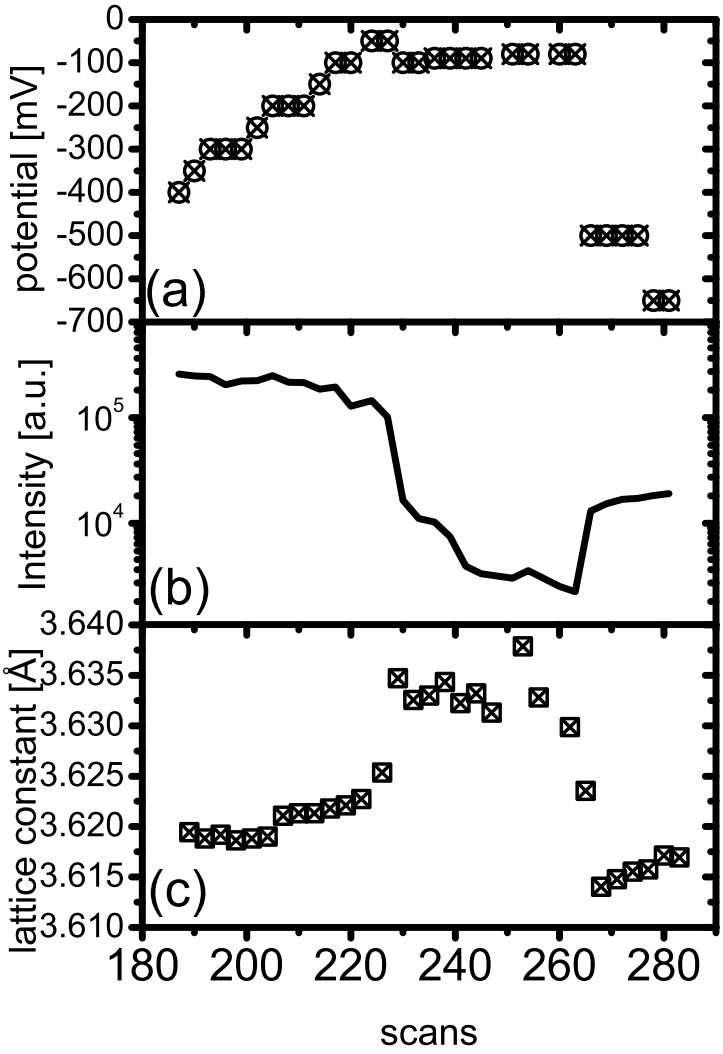

Fig. 7.33: *The copper ($\bar{2}$02) peak intensities (b) and the copper lattice constant (c) are plotted together with the applied potential (a) during the stripping and redeposition of copper. The copper lattice constant is deduced from the position of the copper ($\bar{2}$02) reflection.*

could therefore only be successfully realigned at the beginning of the stripping. The *H*-, *K*- and *L*-scans of this peak during the copper dissolution are shown in Figure 7.34. During the stripping the peak shifts to smaller *H*- and *K*-values, as observed for the copper (202) reflection. In the *L*-direction the peak shifts to a higher *L*-value, indicating an increasing tilt angle. The angles of the in-plane rotation and tilt as well as the copper in-plane lattice constant during the stripping can be determined from the peak positions.

The values obtained from this analysis are plotted in Figure 7.35. The data points corresponding to the scans shown in Figure 7.34 are given in red. The decrease in intensity is again accompanied by an increase of the copper in-plane lattice constant. Additionally, changes of the tilt and rotation angles are observed. The tilt angle increases, whereas the angle of the in-plane

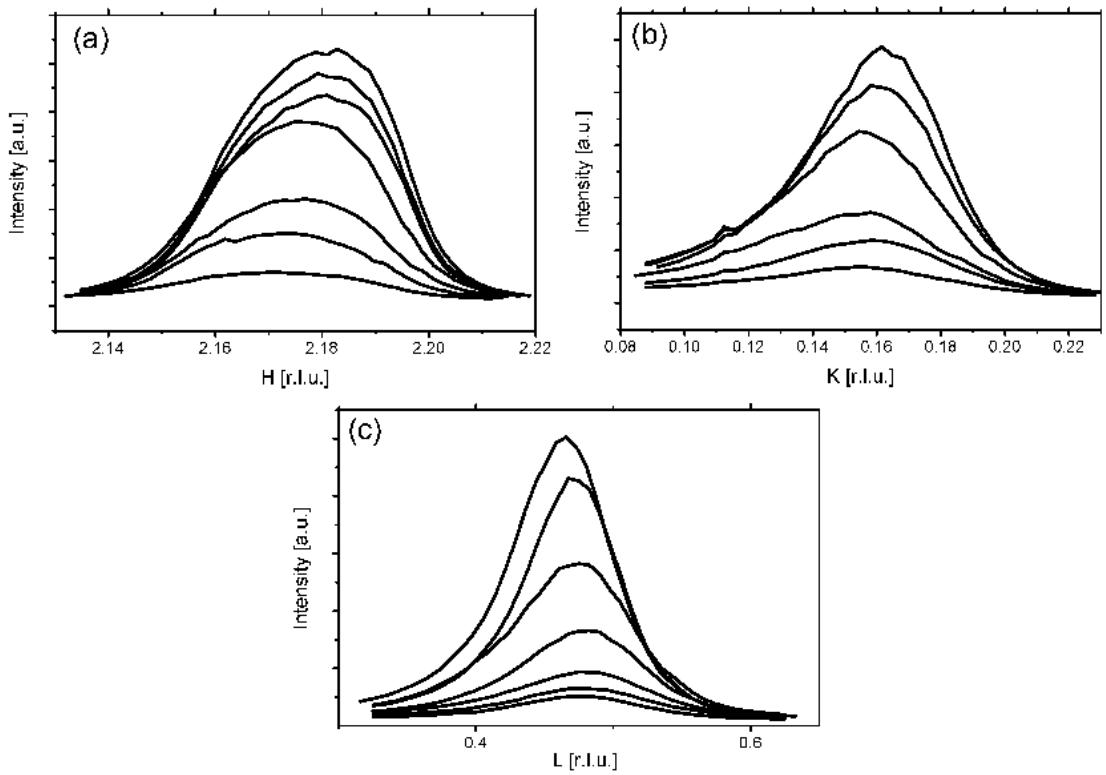

Fig. 7.34: *The H-, K- and L-scans through the copper (*200*) reflection during the stripping of the former electrodeposited copper. The peak is shifting to smaller H-values (a), to smaller K-values (b) and the L-value is increasing during stripping. Altogether the shifting of the peak is an indication, that the copper in-plane lattice constant is bigger for the copper closer to the GaAs-surface The in-plane rotation of the copper is smaller closer to the interface, whereas a larger tilt closer to the interface is indicated.*

rotation decreases.
Because of the decreasing intensity the peak could not be realigned reliably beyond a certain period of time after the stripping started. The peak shifted continuously afterwards, but the rotation and tilt angles could not be determined anymore and therefore the data points are not shown in Figure 7.35. The in-plane lattice constant increases up to $d_{\parallel}$=3.645 Å.

In Figure 7.36 (a) an in-plane (L=0.06 r.l.u.) mesh-scan around the GaAs($0\bar{2}0$) reflection is shown for the copper deposited at -650 mV on a clean (As-rich) surface. The same scan has been repeated after the copper has been totally dissolved and redeposited at -650 mV [Figure 7.36 (b)]. For the copper deposited on a clean surface the split copper ($0\bar{2}0$) peaks due to the in-plane rotation can be clearly observed at $\vec{Q} = (\pm 0.22, -2.2, 0.06)$. They are elongated in the direction of the GaAs($0\bar{2}0$) reflection due to the overlap of the copper and GaAs reflections, which causes higher intensity between the peaks. In addition the copper (111) reflection can be detected with a lower intensity at $\vec{Q} = (0, -1.9, 0.06)$. In Figure 7.36 (b), the previously split copper ($0\bar{2}0$) peaks seem to merge together to one broad peak at H=0. The copper (111) reflection becomes much stronger and is observed as a powder ring at $Q_{\parallel} = 1.9$ r.l.u.. Two ad-

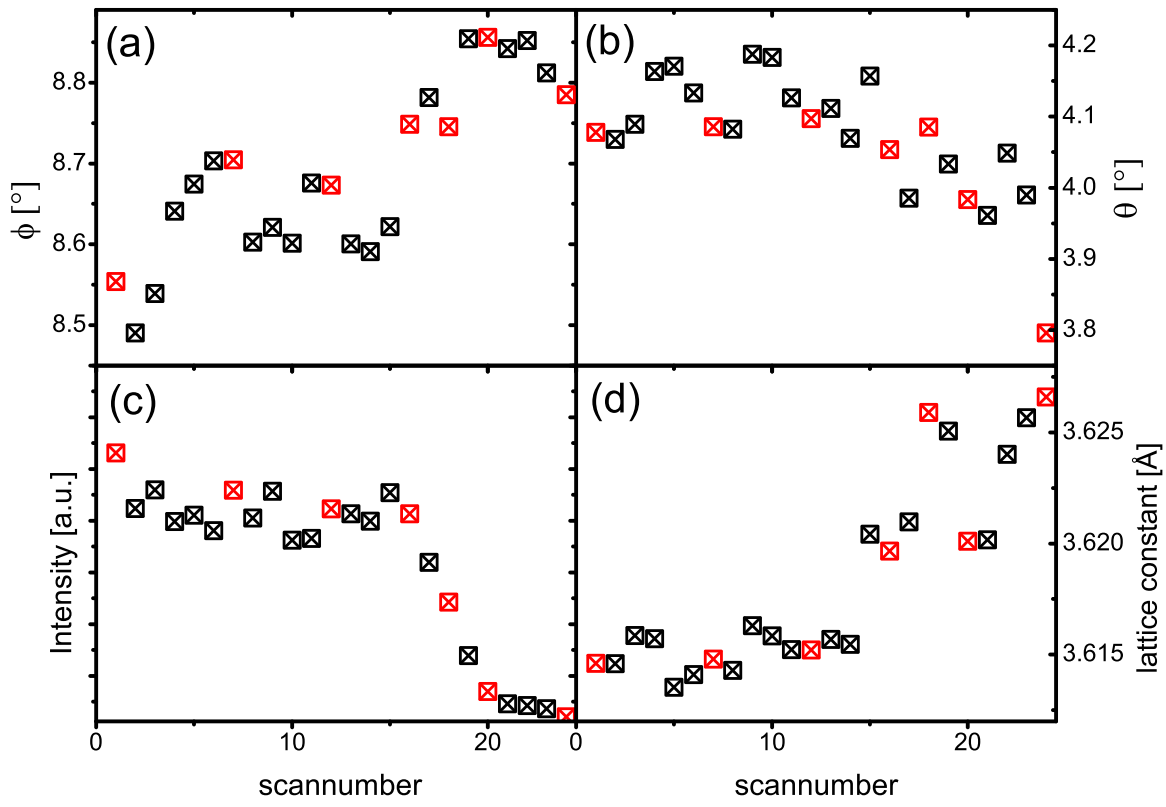

Fig. 7.35: *The fitting of the tilting angle ϕ (a), the angle of the in-plane rotation θ (b) and the intensity (c) are shown together with the copper in-plane lattice constant (d) during the stripping of copper deposited on a Ga-rich surface. During the copper dissolution the intensity of the copper peak is decreasing accompanied by an increase of the copper lattice constant. The tilting angle is shifting to higher values whereas the angle of the in-plane rotation is decreasing.*

ditional regions with higher intensities can be observed at H=±0.2 r.l.u. close to the GaAs(0$\bar{2}$0) reflection.

Ex-situ studied sample with low Cu coverage

The sample was prepared using the combined UHV-electrochemistry chamber in the surface characterization laboratory of ID32. A (2×4)-reconstructed GaAs(001) sample was transfered to the UHV-electrochemistry chamber. The chamber was then vented with nitrogen and the sample was contacted with electrolyte at -650 mV. After a charge transfer of 2.132 mC, corresponding to approximately acopper coverage of 20 ML, the electrochemical droplet cell was withdrawn and the remaining electrolyte was removed by blowing nitrogen through a glass tube onto the sample. Then the chamber was pumped down until the sample was allowed to be transferred to the big UHV chamber. LEED showed no indication of a crystalline structure but high background. With STM no stable conditions could be found for imaging the surface. The sample was then transfered in another UHV chamber with a beryllium dome to the diffractometer

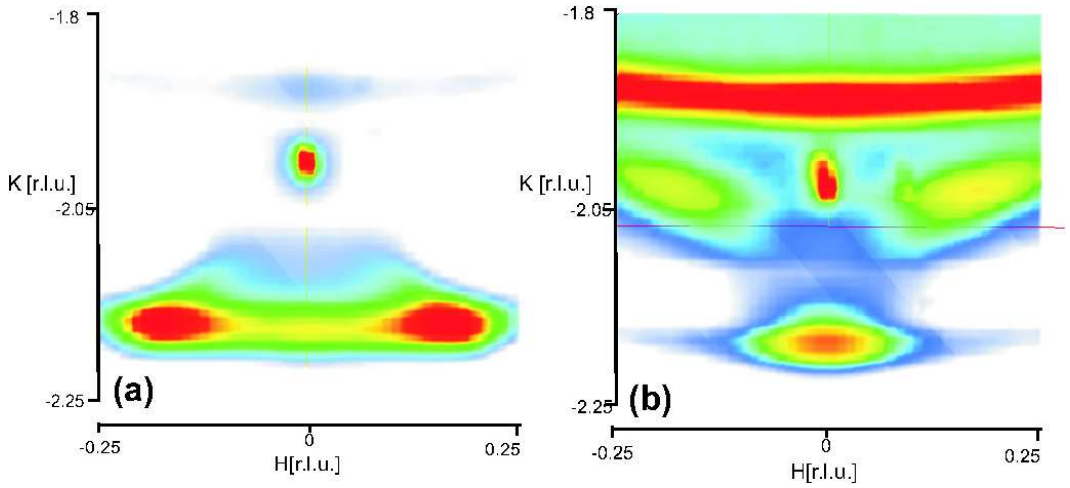

Fig. 7.36: *An in-plane map around the GaAs(0$\bar{2}$0) peak is presented for copper deposited on a former (2×4)-reconstructed GaAs(001) surface (a). The same scan has been repeated after the copper was stripped and redeposited again at the same potential(b). The intensity scale for (a) and (b) is not the same but was chosen to increase the contrast of the image.*

and characterized by X-rays.

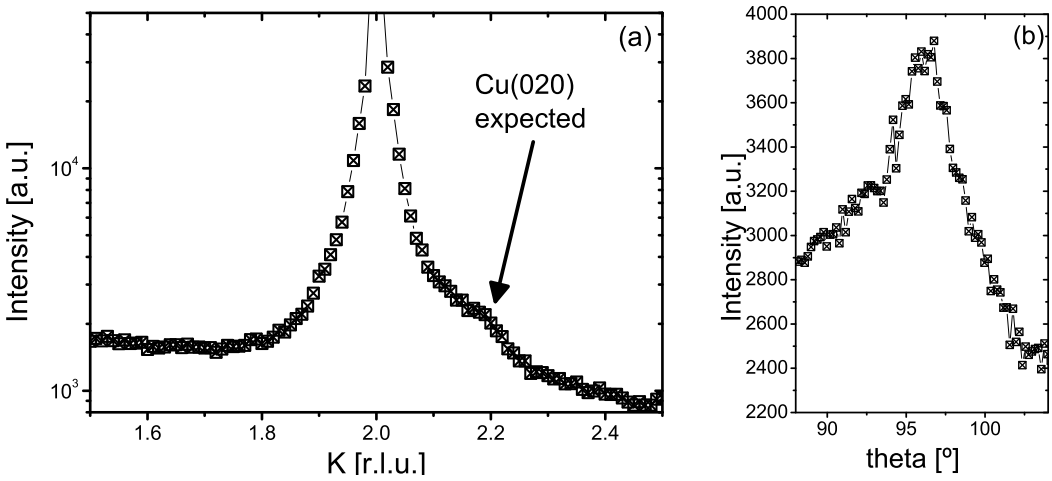

Fig. 7.37: *A radial in-plane scan of an ex-situ measured sample on which an equivalent charge of 20 ML was deposited (a). In (b) a rocking scan through the expected copper peak at K=2.2 r.l.u. is shown.*

An in-plane scan taken at L=0.06 r.l.u. around the GaAs(020) reflection is shown in Figure 7.37 (a). No clear copper peak appears at K=2.2 r.l.u. as observed for the in-situ samples with higher coverage. However, a shoulder of the GaAs(020) reflection extending up to the position of the expected copper (020) peak can be observed. A rocking scan through $\vec{Q} = (0, 2.2, 0.06)$ is shown in Figure 7.37 (b).

Looking for the copper peaks at the positions determined from the copper deposition on the UHV prepared GaAs(001) measured in-situ, we identified all the copper reflections for the ex-situ sample. The peak positions for the copper (200) reflection expected at L=0.48 r.l.u. is found at $\vec{Q} = (2.169, 0.16, 0.516)$. The peak position corresponds to an in-plane copper lattice constant of $d_{\parallel} = 3.624$ Å and an in-plane rotation of $\theta = 4.21°$. The angle of the tilt is $\phi = 9.56°$. Compared to the in-situ measured values in Table 7.3 for the copper deposited on the UHV prepared, arsenic-rich GaAs(001) surfaces, the ex-situ sample exhibits a comparable in-plane lattice constant, a smaller in-plane rotation angle and a tilt angle lying in the upper range of those measured in-situ.

7.4 Discussion and Conclusion

In this chapter the copper deposition on chemically and UHV prepared GaAs(001) surfaces was investigated. The GaAs(001) surface obtained by potential controlled stripping of the As-cap of an As/GaAs wafer was probed ex-situ by AFM. During the stripping process, the produced hydrogen sticks to and passivates the surface. To obtain a smooth surface a way to remove these bubbles has to be developed. The AFM images recorded after the electrochemical copper deposition on such a GaAs surface confirm the mechanism of progressive nucleation and growth of the copper.

The copper deposition on chemically etched and thus rough surfaces was investigated by surface X-ray diffraction. A broad, not well defined intensity distribution around the expected copper Bragg reflections was observed.
The cyclic voltammograms recorded for the differently prepared GaAs(001) surfaces as well as the results of the surface X-ray diffraction study point at the crucial dependence of the copper deposition process on the initial GaAs(001) surface morphology. Especially roughness and defect induced surface states seem to influence the exact process of nucleation and growth. To study the copper electrodeposition on GaAs(001), a smooth, well defined starting surface with a low defect density is pivotal.

A rotation and an additional tilt of the copper lattice with respect to the GaAs(001) surface were observed for electrodeposited copper on UHV prepared and therefore smooth GaAs(001) surfaces. This epitaxy is obtained on arsenic as well as on gallium rich surfaces and the rotation and tilt angles change little with the termination of the starting surface. No effect of the nucleation or deposition potential on the tilt and rotation angles is observed. For all studied potentials the tilt as well as the rotation angles were about the same for the same (arsenic or gallium) termination of the starting surface. The angle of the in-plane rotation is of the order of 5 degrees and the angle of the tilt is about 9 degrees (Table 7.3).

For epitaxial growth, the relationship between the in-plane lattice parameters of the substrate and the deposited material plays an important role in determining the epitaxy of the deposit. At the interface, to minimize the interfacial energy, a rotation of the lattice of the deposit with respect to the lattice of the substrate an be introduced [78].

The first layers of the deposit are often observed to be strained by the substrate and relax towards the bulk lattice spacing only further away from the interface. The incorporation of periodic misfit dislocations at the interface is known to decrease the strain energy of the epilayer [79, 80, 81]. As an alternative to the formation of misfit dislocation, strain relaxation by tilt was proposed [82, 83, 84]. This idea was applied to a 300 nm copper layer grown by MBE on GaAs(001) [85]. The copper was found to grow epitaxially with the Cu[100]-axis oriented in the GaAs[100]-direction (surface coordinates). The majority of the copper undergoes an out-of-plane tilt of the Cu[001]-axis by an angle of 10.3° in the GaAs[100]- or [010]-direction. Also a minor part of the copper was found to tilt in the GaAs[110]- or [$\bar{1}$10]-direction (surface coordinates) by 7.2°. This epitaxy was explained by introducing tilt dislocations at the interface with an average interval between two nearest dislocations of about 11.27 copper lattice constants. However, this conclusion was made mainly from geometric but not energetic considerations of the interface. In addition, the application of this model requires a rather smooth surface and it does not explain the in-plane rotation observed by the present work (which was not reported for the copper deposited in UHV).
Up to now no epitaxial system has been reported to my knowledge exhibiting both an in-plane rotation and an out-of-plane tilt. To obtain more information about the processes at the interface, the changes of the positions of the copper peaks during stripping and redeposition was monitored. In addition an ex-situ prepared sample with less than 20 ML copper was measured.

The measured average in-plane as well as the out-of-plane lattice constants increase during stripping (Figure 7.33 and 7.35). The copper lattice constant closer to the interface was determined to be at least 3.65 Å, which corresponds to a lattice constant variation of $\Delta d/d_{Cu} = 0.97\%$. This variation of the measured lattice constant observed during stripping of the copper with decreasing thickness of the clusters is consistent with the one determined from the analysis of the copper peak-width in section 7.3.2 (Tables 7.1, 7.2 and 7.3).

The expanding of the copper lattice constants can not be due to strain as both the in-plane and out-of-plane lattice constants increase towards the interface. Most likely the increase of the copper lattice constants is caused by interdiffusion at the interface. Diffusion of copper into the GaAs has already been observed [86] for UHV deposition of copper on GaAs as well as for electrochemical deposited copper on a chemically cleaned GaAs(001) surface [64]. Up to now diffusion of gallium or arsenic into the deposited copper has not been considered, although Cu-Ga- as well as Cu-As-alloys are known. These alloys were observed after high temperature treatment of copper with gallium or arsenic [87, 88, 89, 90].
The phase diagrams of the Cu-Ga-system [89] and the Cu-As-system [88] are shown in Figure 7.38 and 7.39, respectively. The α-phase of the gallium-copper system, which occurs at low gallium concentrations, represents a solid solution of gallium in copper that can form at low temperatures. The maximum solid solubility of Ga in copper was observed to be 24.5% [90] for the α-phase. The α-phase also exists for the arsenic-copper-system at low temperatures and low arsenic concentrations. The saturated α-phase corresponds to an arsenic concentration of 6.5% [88]. The α-phases of both Cu-As- and Cu-Ga-alloys exhibit a fcc structure. The lattice constants of these alloys increase linearly with the concentration of the dissolved arsenic or gallium, as shown in Figure 7.40. The lattice constant for the saturated α-phase copper-arsenic

is a=3.647 Å. The lattice constant for the gallium-copper is a=3.66 Å at 24.5% gallium.
The copper lattice constant determined for the copper grown on GaAs(001) is about a=3.65 Å close to the interface. This copper lattice constant is comparable to the ones of arsenic or gal-

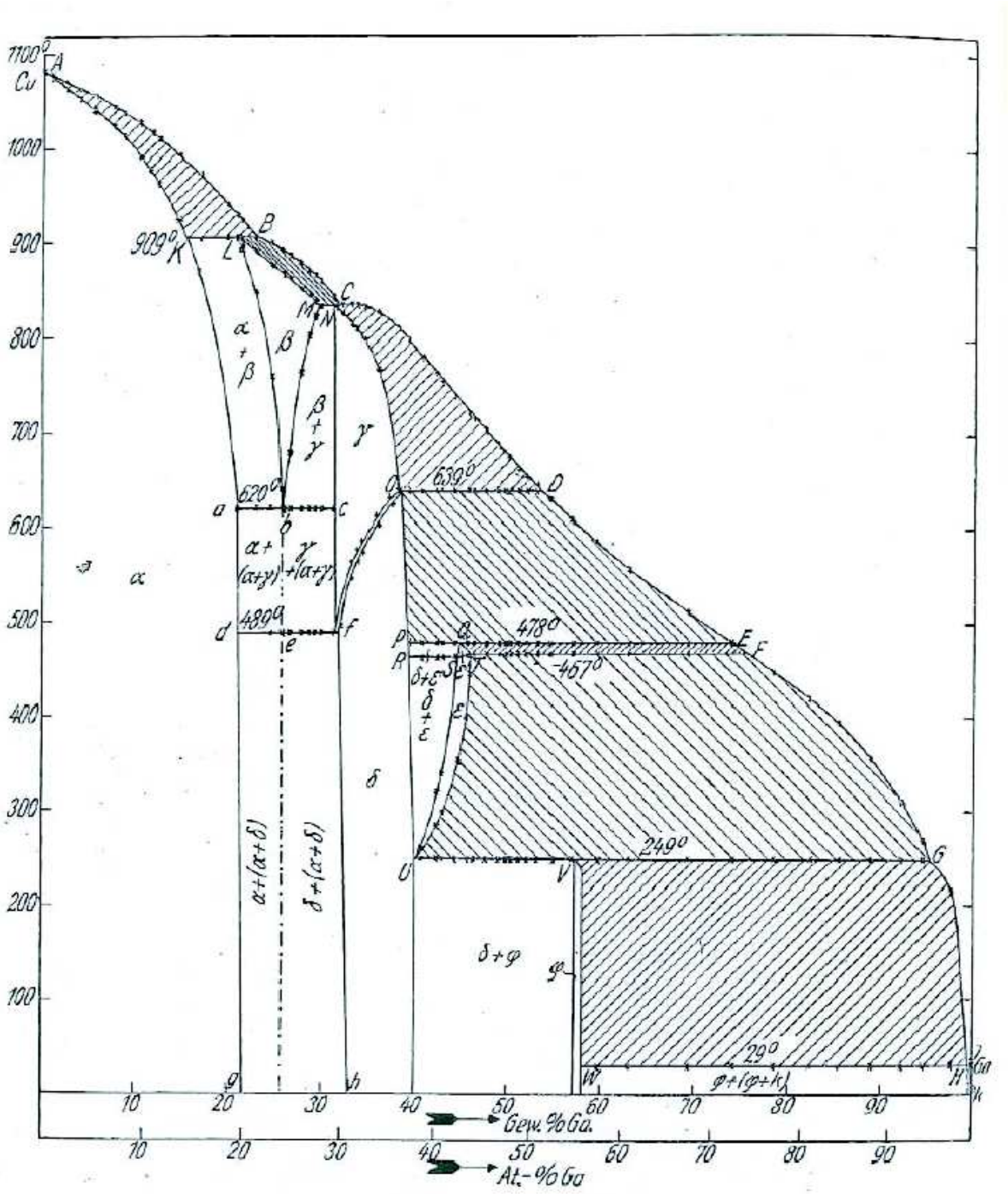

Fig. 7.38: *The phase diagram of the copper-gallium system. The α-phase corresponds to a solid solution of gallium in copper and is observed for a gallium concentration between 0 and 24.5%[90].*

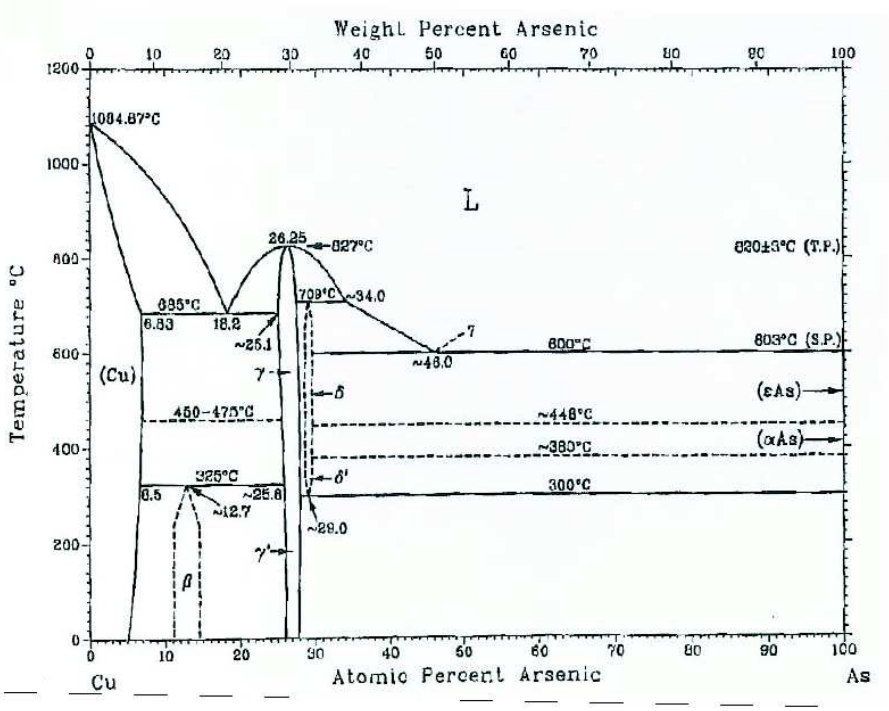

Fig. 7.39: *The phase diagram of the copper-arsenic system. The α-phase corresponding to a solid solution of arsenic into copper can be observed at an arsenic concentration between 0 and 6.5%.[88]*

lium dissolved in copper and could therefore be explained by the diffusion of gallium and/or arsenic from the interface into the deposited copper. This interdiffusion depends most likely on the applied potential influencing the band bending and the electric field close to the interface. The lattice constant of the copper deposited on the GaAs(001) surface was found to change smoothly during the stripping indicating a possible concentration gradient of the arsenic and the gallium in the copper.
The potential at which the copper is nucleated influences neither the in-plane rotation angle nor the tilt angle (Table 7.3). However, the rotation and tilt angles are larger for copper deposited on an arsenic rich ($\theta = 4.7°$, $\phi = 9.2°$) than on a gallium rich one ($\theta = 4.37°$, $\phi = 8.77°$). As the tilt and rotation angles depend not on the nucleation potential and weakly on the surface termination of the initial surface, the copper epitaxy appears to be mostly influenced by the strain relaxation and not by a potential driven interdiffusion. The origin of the tilt is still unsolved. Reducing strain energy in the Cu layer and at the interface is probably the main driving force for the tilt and rotation. For a better understanding of this process further studies of the nucleation and growth process are required.

Another interesting effect is the dependence of the mosaicity $\Delta\theta$ and $\Delta\phi$ as well as the variation of the copper lattice constants $\Delta d_{\parallel}/d_{\parallel}$ and $\Delta d_{\perp}/d_{\perp}$ on the nucleation potential and the initial surface termination (Table 7.6).
We observed that the mosaicity $\Delta\phi$ of the tilt angle increases with more negative nucleation potentials whereas the in-plane mosaicity $\Delta\theta$ does not change significantly with the nucleation

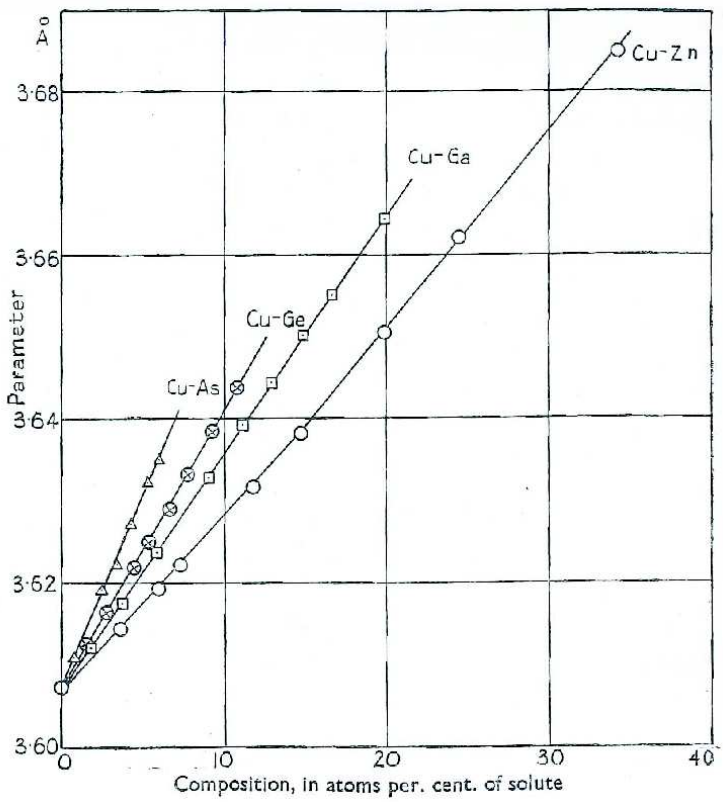

Fig. 7.40: *The lattice constants for the α-phase of some copper alloys are plotted (Cu-As, Cu-Ge. Cu-Ga, Cu-Zn). The lattice constants are linearly increasing with the amount of the second compound solved into the copper [87].*

potential. Also $\Delta d_{\parallel}/d_{\parallel}$ increases with more negative nucleation potential whereas $\Delta d_{\perp}/d_{\perp}$ is not affected. Both, $\Delta d_{\parallel}/d_{\parallel}$ and $\Delta d_{\perp}/d_{\perp}$ are higher for the copper deposited on a gallium-rich surface than for the copper deposited on an arsenic-rich surface. The dependence on the nucleation potential could be due to two effects. First, the number of nucleation sites and the nucleation rate increase with higher overpotentials [63]. A higher nucleation rate results in a less perfect epitaxy of the deposit. In this case a higher mosaicity of the in-plane rotation would be expected. The second effect influencing the epitaxy is the reduction of the arsenic by hydrogen evolution at the GaAs surface at negative potentials,

$$As + 3H^{+} + 3e^{-} \rightarrow AsH_3 \nearrow . \tag{7.13}$$

Due to this reaction the resulting GaAs(001) surface is roughened, introducing defects and kinks on the surface. As observed earlier [59] Cu predominantly grows on defect sites of the GaAs surface such as the kink sites. Copper growing on a more defect rich surface is likely to grow with a less perfect crystalline orientation.
However, no influence of the nucleation potential on the cluster sizes could be found, in contradiction to the earlier result for copper deposition on chemically etched GaAs(001) surfaces. The cluster sizes were extracted from the peak-width together with the lattice constant variation and the tilt and rotation mosaicity. The broadening due to the cluster size is the only value not

depending on the peak position and therefore probably the least accurate one. The dependence of the cluster size on the nucleation potential is perhaps just not detected. Another possibility is the lack of defects on the UHV prepared smooth surface. The potential for copper deposition on those defects acting as nucleation sites is less negative than the one for copper deposition on a perfect surface. The UHV prepared surfaces offer only very few of these defects and could therefore suppress the effect of the nucleation potential on the number of nucleation sites and therefore on the cluster size.

The interdiffusion rate may depend on the nucleation potential as $\Delta d_\perp / d_\perp$ increases with more negative nucleation potentials (Table 7.6). This could be due to the fact that a rougher GaAs(001) surface enhances the interdiffusion between Cu and GaAs. An influence of the initial surface structure was already observed earlier [59]. In addition, the mosaicity $\Delta\phi$ of the copper lattice is found to be larger for the copper deposited on a gallium-rich surface than for the copper deposited on an arsenic-rich surface (Table 7.6). A similar case was found for the variation of the out-of-plane lattice constant $\Delta d_\perp / d_\perp$. After dissolving of some arsenic from the surface at a more negative potential, the surface becomes more gallium-rich. The observed dependence of the copper epitaxy on the nucleation potential is therefore consistent with that on the initial termination.

The interdiffusion at the Cu/GaAs interface is also suggested by the X-ray diffraction data taken on an ex-situ sample with low copper coverage. The split copper peaks are observed at non-in-plane positions. Whereas in the radial in-plane scan no clear copper peak but a shoulder next to the GaAs(200) in-plane peak was observed. The copper epitaxy observed by in-situ X-ray diffraction measurements was mostly reproduced, but the $\Delta d_\parallel / d_\parallel$ is much larger for the ex-situ sample making it impossible to observe clear coper in-plane peaks. The interdiffusion of gallium and copper across the Cu/GaAs-interface seems energetically preferred to the one of arsenic and copper. This effect was already reported earlier [64]. The intensity streaks arising from the copper $\{111\}$-facets of the copper clusters also indicate a variation of the copper lattice constant in the z-direction, which introduces an asymmetry to the intensity of the streaks associated with each copper Bragg reflection. Such an effect was previously observed for germanium hut clusters on Si(001) [91]. No rod from the Cu/GaAs interface could be observed, which is an indication of a rough interface and consistent with an interdiffusion process taking place at the interface.

Comparison between copper deposition on UHV prepared and chemical etched GaAs(001) surfaces

As has been discussed in the previous section, the epitaxy of the copper is strongly influenced by the diffusion processes taking place at the Cu/GaAs-interface. The crystalline quality of the deposited copper depends on the morphology of the initial surface. An initial surface with more defects increases the mosaicity $\Delta\phi$ and facilitates the interdiffusion taking place at the Cu/GaAs interface. As described in section 7.2, copper deposited on a rough surface reveals a special epitaxy. The GaAs(001) surface prepared by chemical etching has a rather high rms roughness of 5 Å [13]. It is interesting to compare whether the copper peak intensity distribution obtained from the rough surface can be explained by the same copper epitaxy as observed for the copper

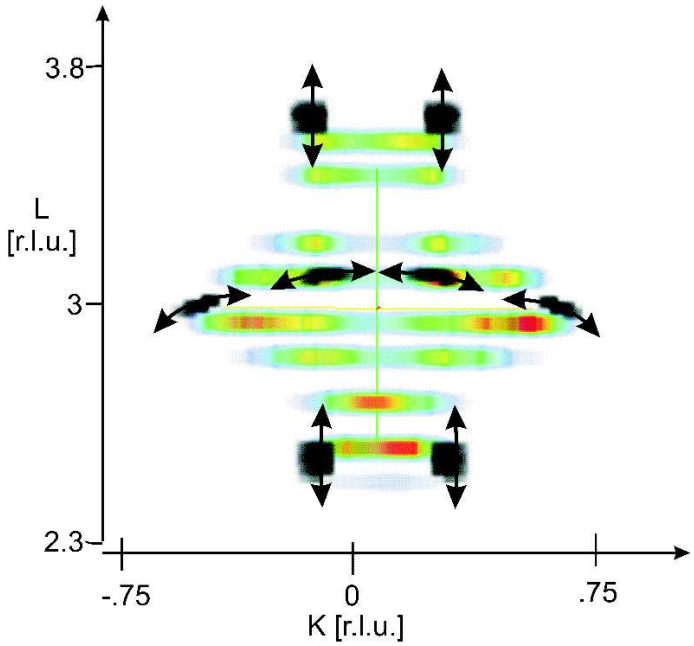

Fig. 7.41: *The intensity distribution measured around the Cu($\bar{2}$02) reflection by running rocking scans at constant $|\vec{Q}|$ is shown as a projection in the KL-plane. In addition the expected peak positions for all eight possible copper domains (black squares) for the copper deposited on a smooth UHV prepared arsenic rich surface are shown. The arrows are indicating the corresponding tilt direction of the copper lattice for each copper peak. The color scale goes from blue (low intensity) over green and yellow to red (high intensity).*

deposition on a UHV prepared GaAs(001) surface.The mosaicity of the tilt as well as the variation of the out-of-plane copper lattice constant are expected to be larger for a rough starting surface.

In Figure 7.41 the measured intensity distribution around the copper($\bar{2}$02) reflection at a constant $|\vec{Q}|$ for the copper deposition on chemically etched GaAs(001) surface is reproduced from Figure 7.9 as a projection in the *KL*-plane. For comparison, the copper($\bar{2}$02) peak positions of all eight possible copper domains (black squares) expected for the copper deposited on a UHV prepared, arsenic rich surface are also plotted. The direction of the tilt is indicated by an arrow for each peak.

The main features of the intensity distribution are reproduced by the copper epitaxy characterized by an in-plane rotation and an additional tilt of the copper lattice with respect to the GaAs lattice. A large mosaicity spread of the tilt angle is expected, resulting in a further extension of the copper peaks in the directions indicated by the black arrows in Figure 7.41. The in-plane rotation and tilt angles obtained for copper electrodeposited on a smooth arsenic rich surface were assumed in Figure 7.41. However, deviations from these values are probable. Such an epitaxy could also explain the four peaks observed in the rocking scan at *L*=3.12 r.l.u. in Figure

7.8 (c) as an extension of the two peaks observed at L=3.6 r.l.u overlapping with the two peaks observed at L=3.13 r.l.u. (black squares in Figure 7.41).

In summary, the copper epitaxy depends clearly on the surface termination and morphology of the starting GaAs(001) surface. We found the indications of interdiffusion processes, taking place at the Cu/GaAs-interface, which influence the mosaicity and the crystalline quality of the deposited copper clusters. The interdiffusion at the interface may be enhanced by the roughness of the surface. Also a gallium-rich interface appears to facilitate the interdiffusion. Such an enhancement can be observed by a larger variation of the copper lattice constant and an increasing tilt mosaicity.
The deposition potential controls the number of nucleation sites and thus the cluster size. At more negative deposition potentials, more nucleation sites exist, resulting in smaller copper clusters. These are difficult to study by X-ray diffraction, as the corresponding copper Bragg peaks are broader and less intense due to the size effects. In addition, the smaller clusters have less parts with a lattice constant relaxed to the one of natural copper. The lattice constant can therefore vary over the entire clusters, introducing an additional broadening of the copper Bragg peaks.

Chapter 8

Conclusion and Outlook

The aim of this work was to enhance our knowledge on the structure on the atomic scale of the electrochemical processes on semiconductor electrodes in contact with electrolyte. Especially the metalization of an electrode was studied, which is fundamental e.g. for the improvement of nano-scale devices and the global understanding of the mechanisms of chemical processes on surfaces.

With the realization of the first in-situ X-ray diffraction experiments for copper electrodeposition on smooth UHV prepared GaAs surfaces the crucial dependence of the epitaxial quality of the deposited copper on the starting surface (morphology and termination) was revealed. The surfaces were prepared in UHV from arsenic capped GaAs(001) wafers, which were first characterized by STM and LEED. The surface structure and morphology was monitored by SXRD during each step, from UHV over exposure to ambient pressure in inert gas to the contact with electrolyte under potential control. The electrochemical copper deposition on GaAs(001) surfaces was studied for different nucleation potentials and surface terminations (As-rich and Ga-rich).

The arsenic capped GaAs(001) wafer were characterized by AFM and SXRD. During several days of transport through ambient, the surface slowly oxidizes as proven by the observation of powder rings arising from As_2O_3 crystallites. The oxide layer can be thermally desorbed at about 160° C in UHV. The sample shows no sign of As_2O_3 crystallites afterwards. A still unresolved question is the structure of the buried GaAs(001) surface. No reconstruction peaks were observed with radial in-plane scans along the high symmetry directions of the surfaces. However, the CTR's recorded from the buried interface reveal a non bulk-like termination. Their shape could be reproduced in the best way by assuming a GaAs(001)-(2×4) structure. For a more detailed analysis a larger data set is needed. It is plausible that the reconstruction at the buried interface is not identical to the UHV exposed surface.

From such an arsenic capped GaAs(001), the GaAs(001) surfaces for copper electrodeposition were prepared by thermal annealing of the arsenic cap and different reconstructions with different arsenic-gallium ratio can be obtained depending on the annealing temperature. In this work we concentrated on the arsenic rich GaAs(001)-(2×4) structure which is the technologically most important surface as it is used for growing high quality epi-layers for opto-electronic

devices. In addition also the gallium-rich GaAs(001)-(4×2) surface was investigated in order to analyze the influence of the surface termination on the copper electrodeposition. The reconstructions of the GaAs(001) surface were first characterized by LEED and STM.
The used MBE grown and "decapped" GaAs(001)-(2×4) surfaces are terminated by about 100nm large terraces. A typical surface exhibits three different high levels, separated by the thickness of one GaAs by-layer. The coexistence of the (2×4) and the c(2×8) structure could be confirmed by STM and LEED. In addition a disorder in the [010] direction could be observed due to the shifts of the reconstruction unit cells in this direction by one half or one quarter of the unit cell. This disorder could be analyzed more quantitatively by SXRD as it is introducing an additional broadening of the fractional order in-plane peaks. The shift of the unit cells by one quarter is observed with a probability of 7.4% and the shift by one half with a probability of 2.4%. Analysis of the data confirms the $\beta 2$-model for the GaAs(001)-(2×4)/c(2×8) structure. The coexistence of more or less arsenic rich domains (γ or $\alpha 2$ phases, respectively) can not be excluded. The surface has larger terraces but also a higher degree of disorder than the MBE prepared GaAs(001)-(2×4) which can be explained by the lower mobility of the surface atoms due to the lower preparation temperature. However, higher temperatures could lead to a loss of arsenic from the surface.
The GaAs(001)-(4×2) is also terminated by about 100nm large terraces. The coexistence of the (4×2) and c(8×2) structure could be confirmed by STM, LEED and SXRD. No disorder in the [100]-direction is observed.

In order to contact the surfaces with electrolyte, the samples have to be exposed to ambient pressure. With the setup used for this work, the samples could be exposed to inert gas (nitrogen) without passing through air thus avoiding significant oxidation of the sample. Both surface terminations were characterized by SXRD in nitrogen at ambient pressure. The surface reconstructions are lifted (no fractional order peak could be observed). However the CTR's reveal a non bulk-like termination for both surfaces. The surfaces are most probably relaxed, also a adsorption of the nitrogen on the surface is probable. No increase in rougheness is observed. The different surface terminations appear to be quite stable under ambient pressure since only a slight difference between the surface truncation rods on a former (2×4) and a former (4 × 2) reconstructed surface is observed.

The epitaxy of the copper electrodeposited from 0.5 M H_2SO_4 + 1mM $CuSO_4$ on such prepared GaAs(001) surfaces was investigated. The UHV preparation and SXRD characterization of each surface allowed a better control and led to a better knowledge of the starting surface. The copper is observed to grow epitaxially in islands. The lattice of the copper clusters is rotated with respect to all three axes of the GaAs unit cell, giving rise to eight symmetry equivalent domains. The copper epitaxy can be described by an in-plane rotation about the GaAs [001] axis and an additional tilt about the GaAs[100] or [010] axis. The in-plane epitaxial rotation is about $\theta = 5^\circ$ and the out-of-plane tilt angle is about $\phi = 9^\circ$. A dependence of the rotation angles on the surface termination has been found. Both angles are slightly smaller for the copper deposited on a gallium-rich surface ($\theta \approx 4.4^\circ$ and $\phi \approx 8.8^\circ$) than for copper deposited on a arsenic-rich surface ($\theta \approx 5.0^\circ$ and $\phi \approx 9.2^\circ$). No influence of the deposition or nucleation potential on the rotation angles could be found.
In a more detailed line-shape analysis of the copper peaks, the mosaicities of the tilt and rotation

angles as well the variation of the copper lattice constants and the cluster sizes were determined for the different deposition conditions (on the arsenic-rich surface) and surface terminations. No influence of the cluster sizes on the nucleation potential could be found in contradiction to earlier result for copper deposition on chemical etched GaAs(001). This could be an artifact of treatment of data since several effects introduce a broadening of the peak. The cluster sizes, the lattice constant variations and mosaicity of the tilt and rotation were extracted from the peak widths all together. The value for the cluster size deduced from the line-shape analysis is therefore expected to be the less accurate. A small effect of the cluster size on the nucleation potential is perhaps just not detected.
The fact that no dependence of the number of nucleation sites and the cluster size on the deposition potential could be detected, could also be the lack of defects on the UHV prepared smooth surface. On chemical cleaned GaAs(001) surfaces these defects act as copper nucleation sites at more positive deposition potentials introducing larger copper clusters on less nucleation sites at more positive potentials. Without surface defects nucleation centers at positive potential are missing and this effect would not be observed.

The in-plane mosaicity does not seem to depend on the nucleation potential and reveals a value of about $\Delta\theta \approx 0.75^\circ$. The mosaicity of the tilt angle is increasing with more negative nucleation potential. At a deposition potential of -350 mV the mosaicity of the tilt is about $\Delta\phi = 0.6^\circ$, whereas for a copper nucleation at -1200 mV the mosaicity of the tilt angle is about $\Delta\phi = 1.1^\circ$. This effect could be induced by a roughening of the GaAs surface at the applied nucleation potentials leading to a less perfect copper epitaxy. The mosaicity of the tilt angle and the mosaicity of the in-plane rotation are slightly larger on gallium terminated ($\Delta\theta = 0.93^\circ$ and $\Delta\phi = 1.1^\circ$) than on arsenic terminated GaAs(001) surfaces ($\Delta\theta = 0.65^\circ$ and $\Delta\phi = 0.7^\circ$). Also the variation of the copper out-of-plane lattice constant depends on the deposition conditions and the termination of the starting surface. A higher variation ($\Delta d/d_\perp$=1.8%) was found for gallium terminated surfaces and for more negative nucleation potentials than for an arsenic terminated surface and less negative nucleation potentials ($\Delta d/d_\perp$=1.4%).

The stripping of the copper revealed a larger lattice constant of the copper closer to the Cu/GaAs interface (a_{Cu} ≈3.64 Å compared to a_{Cu} ≈3.615 Å for the relaxed copper). This effect can be explained by interdiffusion and thus the formation of Cu/Ga, Cu/As and/or Cu/Ga/As-alloys. Arsenic and gallium are known to dissolve in Cu resulting in an enlargement of the copper lattice constant.
The copper clusters are found to be terminated by facets perpendicular to the copper (111)-plane. These facets give rise to a diffuse scattering streak (rod) through the copper Bragg peak in the [111]-direction. These rods are found to be asymmetric with higher intensity at lower $|\vec{Q}|$. Such an effect is known [91] for clusters with a non constant lattice parameter, shifting the intensity away from the bulk like position.

The results obtained on the UHV prepared GaAs(001) surfaces for copper electrodeposition finally allow a better understanding of the obtained results on chemical etched GaAs(001) surfaces. These rough surfaces lead to a larger mosaicity of the tilt angle and to a larger variation of the copper lattice constant. In addition, gallium as well as arsenic surface atoms are present, leading to a less clearly defined rotation and tilt angle. A quite complicated intensity distrib-

ution around the expected Cu Bragg peaks is observed. Its basic features can be reproduced assuming the same epitaxy as obtained on the smooth surface with a larger mosaicity of the tilt angle.

While this work revealed the epitaxy of the electrodeposited copper on GaAs(001) and its crucial dependence on the surface termination and surface morphology, the atomic processes at the Cu/GaAs interface are still not understood in detail. For a better understanding, the use of direct imaging methods would be very helpful. An in-situ UHV-EC STM would aid to achieve a better knowledge about the nucleation processes and the nucleation sites as well as the interdiffusion process. An open question is e.g. the influence of defects on the interdiffusion which could be answered by direct imaging. For the understanding of the interdiffusion layer, TEM as well as anomalous scattering measurements might reveal important information about its structure and morphology. An anomalous scattering study would be possible but is quiet demanding as the K-edges for Cu, As and Ga are in the energy range of 10 keV for the X-ray beam. In this energy range the transmission of the X-rays through 7 mm of electrolyte is about 0.03 (compared to 0.7 at 23 keV). For such a study, also an ex-situ sample with low copper coverage might be considered.

The used setup with one point detector imposed serious limitations. An improvement for the SXRD experiments would be a 2D detector assuring faster measurements and covering a larger area in reciprocal space. The change of the shape of at least two copper peaks during this process has to be monitored in an adequate time-scale, which would lead to a better understanding of the epitaxy of the first copper monolayers especially its mosaicity and lattice constant variation during the growth or stripping.

Chapter 9

Acknowledgements

This work has been carried out within the Surface and Interface Science Group of the European Synchrotron Radiation Facility (E.S.R.F.) in Grenoble and would not have peen possible without the help, support and encouragement of my colleagues and friends.

I would like to thank Privat Dozent Dr. Jörg Zegenhagen, who suggested the subject, for providing the opportunity to work at an excellent facility, for suggesting a challenging and very interesting topic. He always showed interest in the progress and outcome of the work.

I want to thank Professor Dr. Christian Thomsen for having accepted the duties of the advisor and referee. I hope he got an insight into a interesting research field.

I acknowledge Professor Dr. Dieter M. Kolb for welcoming me at his Institute in Ulm. From the discussions with the members of his group I received a nice impressions about modern electrochemistry.

I am thankful to Dr. Frank Renner for having me introduced to electrochemistry and SXRD (and the combination of both). I learned how to prepare and carry out good experiments. Thank you for having constantly supported this work and never having been too far away for discussion and advice!

I am grateful to Dr. Tien-Lin Lee for having supported this work with a lot of scientific (but not only) discussions and help. I learned how to take good data and carry out nice experiments. Thank you for all your help (by discussion, good advices but also the chocolate supply) before, during and after experiments and especially during writing!

I acknowledge B.O. Fimland and the member of his group for having provided the samples and any information about them.

I especially want to thank Lionel Andre and Manuel Perez for the technical support, having me facilitated a lot this work. Thank you for some good moments we spent together!

I am thankful to Dr. Helena Isern for her support in the laboratory and at the beamline and for

some enjoyable months of office co-habitation.

I am grateful to the ID32 staff for the good atmosphere and the help and support!

I want to thank Dr. Till-Hartmut Metzger for his constant interest in the work (beyond the duties of a tutor). Thank you for your support!

I especially want to thank all the members of ID01 and ID03 for some nice collaboration, an enjoyable atmosphere and the cordially accommodation in their offices.

I am grateful to the OGG-INFM staff for the nice laboratory co-habitation and some helpful hands.

I want to thank Frederik Golks for his help, friendship and motivation during some long beamtimes and beyond!

I am thankful to Dr. Sebastian Schöder for his help with some experiments and for having corrected this work. Thank you for some relaxing coffee breaks!

I want to thank all the friends from the ESRF and from Grenoble with whom I spent some enjoyable years in France!

I am thankful to all the people from the Karate Club Grenoble (especially Nadir and Rolland!) who contributed to the motivation and physical balance.

I especially want to thank my family for always having supported me during my studies, this work and all decisions I took.

Appendix

Appendix A

Correction Factors

In this chapter the correction factors as used for the measurements presented in this work are documented. The motor names are corresponding to the notation normally used for the ID32 diffractometer. The out of-plane angle described by the incident and the diffracted beam is called *gam* (γ). The in-plane angle described by the incident and the diffracted beam is called *del* (δ) and the angle of the incident beam with the sample surface is called *mu* (μ). The rotation about the surface normal is called *theta* (θ.)

A.1 Correction of integrated intensities

Usually the measured variable used for structure analysis is the integrated intensity of a reflection, not its maximal intensity. This way, influences due to the sample properties or the beam profile and its divergence, which could affect the FWHM of a peak in a non uniform way are eliminated [27]. The integrated intensity is measured by rotating the sample about the surface normal in 30 to 40 steps around the optimized Bragg peak. The range of this so-called "rocking scan" has to be sufficiently large to cover the constant intensity (the background) of each side of the Bragg reflection. The thus obtained peak profile can be integrated numerically or by assuming a theoretical line-profile fit to the measured line shape. The background is subtracted.

The Lorentz-factor The integrated intensity is proportional to the structure factor when integrated in units of the reciprocal space (r.l.u. or 1/Å). The rocking scan is measured in units of angle. Therefore, a correction factor, the so-called Lorentz-Factor, is introduced to convert reciprocal units to angular units:

$$L = \frac{1}{\cos(\mu) \cdot \cos(\gamma) \cdot \sin(\delta)} \tag{A.1}$$

The rod-intersection factor The resolution in L and therefore the measured area of a rod is determined by the angle γ of the detector with the sample surface. For in-plane measurements with small γ, the rod and the detected diffracted beam are almost perpendicular, the acceptance

of the detector ΔL parallel to the rods is only determined by the detector slits. For measurements of a complete rod (at higher L) the reflected beam is no longer perpendicular to the rod.

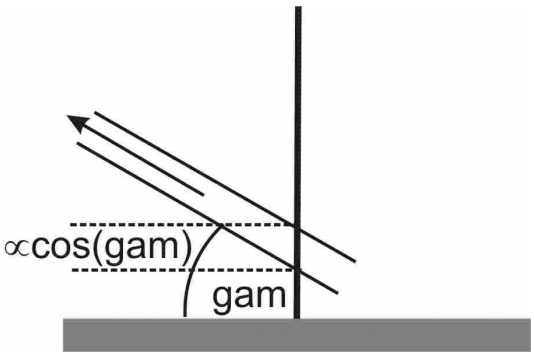

Fig. A.1: *Schematic of the rod interception in a side-view of the sample. The projection of rod to the detected area in reciprocal space defined by detector slit is proportional to* $\cos(\gamma)$.

The acceptance of the detector in L is determined by the angle γ of the diffractometer, as shown in Figure A.1. Therefore a rod interception correction factor R is introduced:

$$R = \cos(\gamma) \tag{A.2}$$

The polarization factor Due to the vertical magnetic field of the undulator, the electrons are deflected horizontally. The thus emitted radiation is polarized horizontally. The detected intensity depends on the sinus of the angle between the polarization direction and the detector (the detector does not „see“ the compound of the radiation corresponding to the oscillation of the electromagnetic vector $\vec{E}$ in the direction of the detector). The position of the detector is determined by the incident angle μ, the out-of-plane angle γ and the in-plane-angle δ with the incident beam. The polarization factor is:

$$P = 1 - [\sin(\mu) \cdot \cos(\delta) \cdot \cos(\gamma) + \cos(\mu) \cdot (\sin(\gamma))^2] \tag{A.3}$$

The area correction Only the part of the surface which is illuminated by the incident beam and seen by the detector is contributing to the measured intensity. This active sample area depends on the rotation of the detector in the surface plane described by the angle δ, as shown in Figure A.2 (a). The so-called area correction is:

$$A = \frac{1}{\sin(\delta)} \tag{A.4}$$

This factor is correct when the area of the surface contributing to the intensity has the form of a parallelogram. For high energies and small $|\vec{Q}|$ this is often not the case. The area contributing to the scattered intensity is defined by the edges of the sample and the in-plane detector angle “gam “, as shown in Figure A.2 (b). For a surface not having the shape of a circle in addition also the angle of the sample edges with the incident beam has an influence on the area contributing to the scattered intensity. This was the case for the GaAs samples. The active sample

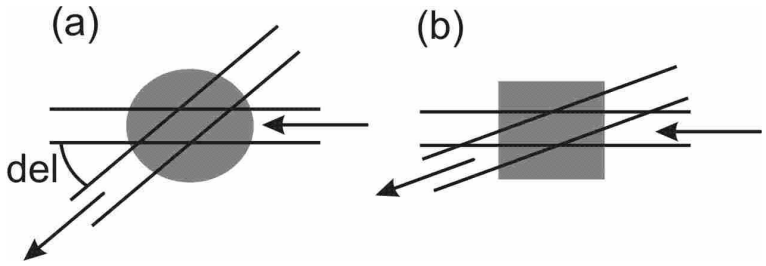

Fig. A.2: *Top-view of the sample surface with the active sample area indicated. The incident and diffracted beams are indicated. Two different cases have to be distinguished. (a) In the ideal case the active sample area can be calculated as the area of an parallelogram described by the sizes of incident and diffracted beam (determined by the entrance slits and the detector slits). (b) For small in-plane angles, described by the detector with the diffracted beam, the active sample area depends also on the shape of the sample surface. For non circular surfaces it also depends on the surface orientation orientation with the incident beam.*

area was determined numerically.

The measured corrected intensity (which is proportional to the square of the structure factor) is then:

$$I_{corrected}(\vec{Q}) = \frac{I_{measured}(\vec{Q})}{LRPA} \tag{A.5}$$

A.2 Correction of peak-widths

The vertical and horizontal detector slits ($\Delta_{slit\_horizontal}$ and $\Delta_{slit\_vertical}$, respectively) determine the part of the reciprocal space seen by the detector and therefore the resolution in reciprocal space. The detector slits have to be adjusted carefully before each measurement to assure that the desired information can be extracted from the data and to achieve a low background.
The resolution in the out-of-plane direction L, δL, in the radial in-plane direction, ΔR, and for a rocking scan $\Delta\theta$ will be derived in this section for the (001)-surface of a cubic crystal described in surface coordinates. The reciprocal lattice vectors $\vec{v}$ and $\vec{u}$ with $|\vec{u}|=|\vec{v}|$ are describing the plane parallel to the sample surface. $\vec{w}$ is the lattice vector perpendicular to the surface. $\vec{a}$ and $\vec{b}$ are the in-plane lattice vectors in real space and $\vec{c}$ is th out-of-plane lattice vector in real space.
The geometry of a diffraction experiment is shown in Figure A.3. The incident $\vec{k}_i$ and diffracted $\vec{k}_f$ wave vector and the momentum transfer $\vec{Q}$ are indicated in Figure A.3 (a). In Figure A.3 (b) the projection of the diffraction geometry onto the plane parallel to the sample surface is shown. The part of this plane seen by the detector is indicated by a gray rectangle and the resolutions in the direction of a rocking scan $\Delta\theta$ and a radial in-plane scan ΔR are indicated.
The resolution in L is obtained similar to equation A.2:

$$\Delta L[r.l.u.] = \Delta L_0 \cdot \cos(\gamma). \tag{A.6}$$

ΔL_0 is the resolution in the L-direction for an in-plane position in reciprocal space ($\gamma \approx 0$):

$$\Delta L_0 = \Delta\gamma \cdot \frac{k}{|\vec{w}|} \tag{A.7}$$

with the angular resolution $\Delta\gamma$ defined by the vertical detector slit $\Delta_{slit\_vertical}$, $k = \frac{2\pi}{\lambda}$ is the wave number. The detector-sample distance for the ID32 diffractometer is about 1 m. The resolution in L is therefore given by

$$\Delta L[r.l.u.] = \frac{\Delta_{slit\_vertical}[m]}{1\ \mathrm{m} \cdot \lambda} |\vec{c}| \cdot \cos(\gamma) \tag{A.8}$$

with the wavelength λ of the X-ray beam used.

For the resolutions on the scan directions parallel to the sample surface $\Delta\theta$ and ΔR the in-plane (the plane described by $\vec{Q}_{\parallel}$ and $\vec{k}_i$) projection of $\vec{k}_f$ has to be considered. A schematic of this plane is shown in Figure A.3 with $\vec{k}_i$, $\vec{Q}_{\parallel}$ and the in plane projection of $\vec{k}_f$ indicated. The section seen by the detector is indicated by a gray rectangle. From this $\Delta\theta$ (the resolution of a rocking scan) and ΔR (the resolution of a scan parallel to $\vec{Q}_{\parallel}$) can be deduced;

$$\Delta\theta[^\circ] = \frac{\Delta\gamma \cdot k \cdot \sin(\gamma)}{|\vec{Q}_{\parallel}| \cdot \cos(\phi)} \tag{A.9}$$

$$\Delta R[r.l.u.] = \frac{\Delta\delta \cdot k}{|\vec{u}| \cdot \cos(\phi)} \tag{A.10}$$

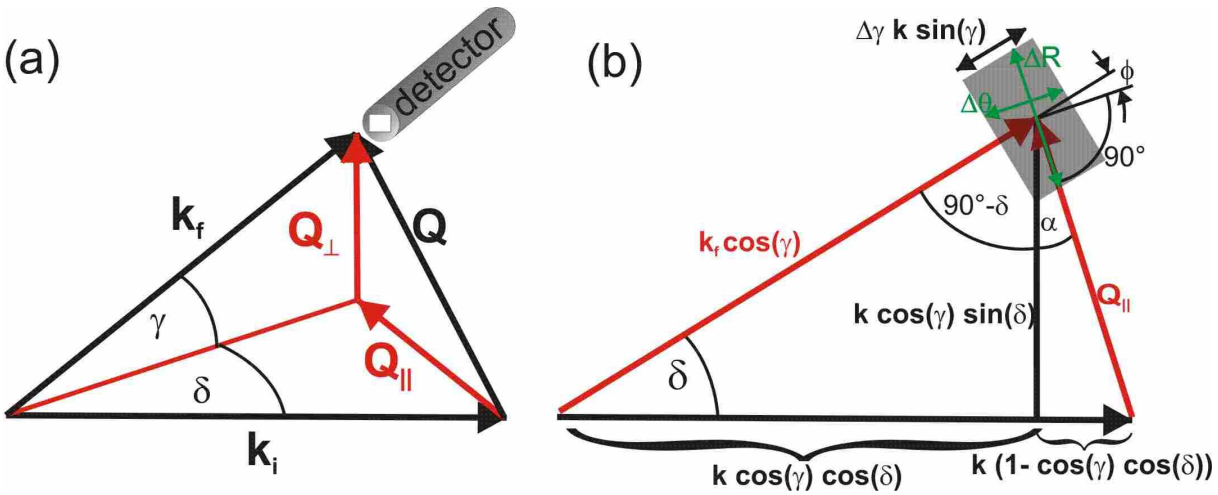

Fig. A.3: *The geometry of a grazing incidence scattering experiment (a). The wave vectors of the incident $\vec{k}_i$ and scattered $\vec{k}_f$ beam and the scattering vector $\vec{Q}$ and its in-plane $\vec{Q}_{\parallel}$ and out-of-plane $\vec{Q}_{\perp}$ components are indicated. In (b) the in-plane projection of the scattering geometry is shown together with the active area of the reciprocal space defined by the detector slits.*

The angle $\phi = 90 - (90 - \delta) - \alpha = \delta - \alpha$ is indicated in Figure A.3. $|\vec{Q}_{\parallel}| \cdot \cos(\phi)$ can be rewritten as:

$$\begin{aligned} |\vec{Q}_{\parallel}| \cdot \cos(\phi) &= |\vec{Q}_{\parallel}| \cdot \cos(\delta - \alpha) \\ &= |\vec{Q}_{\parallel}| \cdot (\cos(\delta)\cos(\alpha) + \sin(\delta)\sin(\alpha)) \\ &= \cos(\delta)(|\vec{Q}_{\parallel}| \cdot \cos(\alpha)) + \sin(\delta)(|\vec{Q}_{\parallel}| \cdot \sin(\alpha)) \\ &= \cos(\delta) \cdot k \cdot \cos(\gamma) \cdot \sin(\delta) + \sin(\delta) \cdot k(1 - \cos(\delta) \cdot \cos(\gamma)) \\ &= k \cdot \sin(\delta) \end{aligned} \tag{A.11}$$

The resolution $\Delta\theta$ and ΔR can then be rewritten as:

$$\Delta\theta[^{\circ}] = \frac{\Delta\gamma \cdot \sin(\gamma)}{\sin(\delta)} \tag{A.12}$$

$$= \frac{\Delta_{slit\_vertical}[m]}{1\ \mathrm{m}} \cdot \frac{\sin(\gamma)}{\sin(\delta)} \tag{A.13}$$

$$\Delta R[r.l.u.] = \frac{\Delta\delta \cdot |\vec{Q}_{\parallel}|}{|\vec{u}| \cdot \sin(\delta)} \tag{A.14}$$

$$= \frac{\Delta_{slit\_horizontal}[m]}{1\ \mathrm{m}} \cdot \frac{|\vec{Q}_{\parallel}|}{|\vec{u}| \cdot \sin(\delta)} \tag{A.15}$$

$|\vec{Q}_{\parallel}|$ can be expressed as a function of the position of the recorded peak in H (in r.l.u.) and in K (in r.l.u.):

$$|\vec{Q}_{\parallel}| = \sqrt{H^2 + K^2} \cdot |\vec{u}| \tag{A.16}$$

or as a function of the motors δ and γ [as deduced from Figure A.3 (b)]:

$$|\vec{Q}_{\parallel}| = k \cdot \sqrt{(\cos(\gamma) \cdot \sin(\delta))^2 + (1 - \cos(\gamma)\cos(\delta))^2} \tag{A.17}$$

$$= k \cdot \sqrt{(\cos(\gamma))^2 - 2 \cdot \cos(\gamma) \cdot \cos(\delta) + 1} \tag{A.18}$$

Appendix B

Electrochemical setup

B.1 Using the potentiostat with *spec*

The potentiostat is controlled via a GPIB interface. If the potentiostat was used with another program before, it has to be initialized. This is done by pressing the CELL ON/OFF button and switching the potentiostat on at the same time.

After Starting SPEC, following message should appear:
–Setting up VERSASTAT potentiostat
PAR263 > Using controller at address <2>

The GPIB address could change. In this caseit has to be replaced in the following commands by the new GPIB address.

Commands

Calibration

The potentiostat can be calibrated using its internal dummy cell:

gpib_put(02,"CAL")

Potentiostatic or Galvanostatic Mode

The potentiostat can be used in galvanostatic or in potentiostatic control. The galvanostatic control corresponds to mode 1:

gpib_put(02,"MODE 1")

The potentiostatic control corresponds to mode 2:

gpib_put(02,"MODE 2")

The used mode is shown by:

gpib_put(02,"MODE"); p gpib_get(02)

Potentiostat on/off

To switch on the potential control on the cell:

gpib_put(02,"CELL 1")

To switch off the potential control on the cell:

gpib_put(02,"CELL 0")

Potential and Current Control

BIAS n

gpib_put(02,"BIAS n")

sets an additional potential n to be applied as soon as the cell is on. The potential has to be given in mV (-8000 < n < 8000) .

SETE n

gpib_put(02,"SETE n")

sets the number of millivolts to be applied (-10000 < n <10000). This command only works in potentiostatic mode.

SETI n

gpib_put(02,"SETI n1 n2")

This command only works in the galvanostatic mode and sets the current to be applied.

READE

gpib_put(02,"READE"); p gpib_get(02)

reports the potential (in mV) applied on the working electrode.

READI

gpib_put(02,"READI"); p gpib_get(02)

reports the measured current. The current is given in two parts, $n1$ is the mantissa and $n2$ the exponent. *1000 -6* would indicate $1000 \cdot 10^{-6}$ A, that is , 1 mA.

I/E n

gpib_put(02,"I/E n");

sets the full scale current range. If *n* is omitted, I/E reports the selected current range. The codes are:

n	Current Range
-1	100mA
-2	10mA
-3	1mA
-4	100μA
-5	10 μA
-6	1 μA

COUL

gpib_put(02,"COUL");p gpib_get(02)

reports the accumulated charge in coulombs. The charge is in two parts $n1$ is the mantissa and $n2$ the exponent. $1000\ -6$ would indicate $1000 \cdot 10^{-6}$ Q ($0 < n1 < 9999$; $-16 < n2 < 3$).

gpib_put(02,"Q");p gpib_get(02)

is an alias for the *COUL* command.

gpib_put(02,"QRST")

resets the accumulated charge to zero.

Recording voltammograms

For performing cyclic voltammograms a macro called "par263voltammogram" is available. Before it can be used in a spec session it has to be initialized by typing

qdo par263voltammogram.

The basic command to run it is

par263voltammogram init_pot up_potential dow_pot slope ppsec

with
init_pot: the initial (starting and ending) potential (in mV)
up_pot: the upper limit (in mV)
dow_pot: the lower limit (in mV)

slope: the speed (in mV/s)
pps: sample per point (NO AVERAGING)
The current and voltage resolution is given directly in the macro *par263voltammogram*, they can be changed in the file. The modulation resolution is defined in the beginning and can be changed by choosing another command line *mr* and *mr_cmd*, with the corresponding modulation resolution given in the line above.
The current resolution is defined in the file by the command

_par263_write("I/E n").

and can be changed.

B.2 Commands for the Hamilton PSD3

Initialization

When starting SPEC with the Hamilton PSD syringes connected you shoud get this message:
–Setting up PDS syringe controller.
If SPEC was already running while you connected the syringes, type:

resetup

to get this message.
To get the right syringe position the pumps have to be initialised. Both syringes have to be at position zero (empty). If not they have to be emptied by turning the screw on the bottom of the syringes downward so that the can be pushed by hand.
The syringes can now be initialized by

psd_init

After the warning:
WARNING: the syringe and the valve may move, continue (NO)?
and answering *yes* the syringes will move to position zero. The screws on the bottom of the syringes can now be fixed again. When asking for the position of syringe 1:

psd_pos 1

one should get:

Current position of seringe "1" is: 0
Current speed of seringe "1" is: 4
Current return steps "1" is: 8
Current backoff steps "1" is: 0
Current mode of seringe "1" is: 0x04
resolution: half
operation: normal
steps range: 0-15000

and the same for syringe 2.

Basic commands

psd_push n1 n2 n3

This is the command to fill on of the two syringes by a certain amount of electrolyte. With $n1$ the syringe which would be addressed is indicated ($n1$=1 for Syringe 1 with the fresh electrolyte and $n1$=2 for Syringe 2 with the used electrolyte). $n2$ gives the number of steps the syringe should move. The full number of steps is 15000. $n3$ indicates the time per step. A good number for fast moving is 50. For lower numbers (faster moving) the syringe could get stuck.

psd_pull n1 n2 n3

This command is similar to *psd_push n1 n2 n3*, but the syringe addressed is emptied, not filled.

psd_valve n1 n2

This is the command to change the position of the valve. $n1$ is the syringe to be addresses and $n2$ to the position to which the valve should move (see Figure 4.11). With *psd_valve n1* the position of the valve of syringe $n1$ is reported.

psd_pos n

This is the command to get the position of syringe 1. The values given back is the number of steps the syringe is moved from its empty position (the full range is 15000).

Using the Hamilton PSD for the droplet control

Filling syringe 1

To fill Syringe 1 the valve has to be moved to position one:

psd_valve 1 1

You need to know the current position *c1* of the syringe, given by the command:

psd_pos 1

Now the syringe can be filled by moving it *n=15000-c1* steps:

psd_push 1 n 50

Afterwards, the valve has to be moved back Position 4 to use the droplet cell:

psd_valve 1 4

Draining syringe 2

To empty the syringe 2, it has to be moved to position one:

psd_valve 2 1

The current position *c2* of the syringe has to be known and is the given by:

psd_pos 2

The syringe is emtied by by moving it *c2* steps :

psd_pull 2 c2 50

Afterwards the valve has to be moved back to position 4 to use the droplet cell:

psd_valve 2 4

Appendix C

List of Acronyms

AFM	Atomic Force Microscope
CB	Conducion Band
CE	Counter Electrode
CF	Conflat (trade name)
CRL	compound refractive lenses
CTR	Crystal Truncation Rod
ESRF	European Synchrotron Radiation Facility
FWHM	Full Width Half Maximum
LEED	Low Energy Electron Diffraction
l.u.	lattice units
MBE	Molecular Beam Epitaxy
ML	Monolayer
RE	Reference Electrode
r.l.u.	reciprocal lattice units
RHEED	Reflection High Energy Electron Diffraction
SC	Semiconductor
SCL	Surface Characterization Laboratory
SHE	Standard Hydrogen Electrode
SPM	Scanning Probe Microscope
STM	Scanning Tunneling Microscope
SXRD	X-Ray Diffraction
SXS	Surface X-ray Scattering
UHV	Ultra High Vacuum
VB	Valence Bande
WE	Working Electrode
XBPM	X-Ray Beam Position Monitor
XRD	X-Ray Diffraction

Bibliography

[1] J. Rusling and S. Suib, *Characterizing materials with cyclic voltammetry*, Advanced Materials **6**, 922 (1994).

[2] J. Li and E. W. EK, *Scanning tunneling microscopy characterization of electrode materials in electrochemistry*, Electroanalysis **8**, 107 (1996).

[3] P. Bindra, H. Gerischer, and D. Kolb, *Electrolytic Deposition of Thin Metal Films on Semiconductor Substrates*, Journal of the Electrochemical Society **124**, 1012 (1977).

[4] P. Allongue and E.Souteyrand, *Metal electrodeposition on semiconductors, Part I. Comparison with glassy carbon in the case of platinum deposition*, Journal of Electroanalytical Chemistry **286**, 217 (1990).

[5] P. Allongue and E.Souteyrand, *Metal electrodeposition on semiconductors, Part II. Description of the nucleation process*, Journal of Electroanalytical Chemistry **362**, 79 (1993).

[6] P. Allongue, E.Souteyrand, and L. Allemand, *Metal electrodeposition on semiconductors, Part III. Description of charge transfer and implication for the formation of Schottky diodes*, Journal of Electroanalytical Chemistry **362**, 89 (1993).

[7] G. Oskam, J. Long, A. Natarajan, and P. Searson, *Electrochemical deposition of metals onto silicon*, J. Phys. D: Appl. Phys. **31**, 1927 (1998).

[8] P. Allongue and E. Souteyrand, *Schottky barrier formation of various metals on n-GaAs (100) by electrochemical deposition*, Journal of Vacuum Science Technology B **5**, 1644 (1987).

[9] R. Reineke and R. Memming, *High barrier GAAS metal schottky junctions produced by electrochemical metal-deposition*, Surface Science **192**, 66 (1987).

[10] K. Robinson, I. Robinson, and W. Ogrady, *Structure Au(100) and Au(111) single-crystals surfaces prepared by flame annealing*, Surface Science **262**, 387 (1992).

[11] H. Gerischer, *Über den Mechanismus der anodischen Auflösung von Galliumarsenid*, Berichte der Bunsengesellschaft **69**, 578 (1965).

[12] Y. Huang, J. Luo, and D. Ivey, *Steady-state and impedance study of n-GaAs in H_2SO_4 solution: Mechanism analysis*, Thin Solid Films **496**, 724 (2006).

[13] J. Zegenhagen, A. Kazimirov, G.Scherb, D. Kolb, D.-M. Smilgies, and R. Feidenhans'l, *X-ray diffraction study of a semiconductor/electrolyte interface: n-GaAs(001/H_2SO_4(:Cu))*, Surface Science **352-354**, 346 (1996).

[14] D.-M. Smilgies, R. Feidenhans'l, G. Scherb, D. Kolb, A. Kazimirov, and J. Zegenhagen, *Formation of tilted clusters in the electrochemical deposition of copper on n-GaAs(001)*, Surface Science **367**, 40 (10 November 1996).

[15] C. Hamann and W. Vielstich, *Electrochemistry*, Wiley-VCH, 2005.

[16] V. Myamlin and Y. Pleskov, *Electrochemistry of semiconductors*, Plenum Press New York, 1967.

[17] S. Morrison, *Electrochemistry of semiconductor and oxidized metal electrodes*, Plenum Prss New York and London, 1980.

[18] N. Sato, *Electrochemistry of metal and semiconductor electrodes*, Elsevier, 1998.

[19] M. Paunovic and M. Schlesinger, *Fundamentals of electrochemical deposition*, John Wiley & Sons, 1998.

[20] E. Budevski, G. Staikov, and W. Lorenz, *Electrochemical Phase Formation and Growth*, Wiley-VCH, 1997.

[21] H. Helmholtz, *Studien über elektrische Grenzschichten*, Wiedemanns Annalen **7**, 337 (1879).

[22] G. Gouy, *Constitution of the Electric Charge at the Surface of an Electrolyte*, Journal of Physics **9**, 457 (1910).

[23] D. Chapman, *A Contribution to the Theory of Electrocapillarity*, Philosophical Magazine **25**, 475 (1913).

[24] B. Warren, *X-Ray Diffraction*, Dover Publications, Inc., New York, 1990.

[25] A. Guinier, *X-Ray Diffraction*, W.H. Freeman & Co., 1956.

[26] C. Giacovazzo, H. Monaco, and B. Viterbo, *Fundamentals of Crystallography*, International Union of Crystallography Texts on Crystallocraphy, Oxford, 1992.

[27] R. Feidenhans'l, *Surface structure determination by X-ray diffraction*, Surface Science Reports **10**, 105 (1989).

[28] I. Robinson and D. Tweet, *Surface X-ray diffraction*, Reports on Progress in Physics **55**, 599 (1992).

[29] I. Robinson, *Handbook of Synchrotron Radiation*, chapter 7, North-Holland, 1991.

[30] I. Robinson, *Crystal Truncation Rods and Surface Roughness*, Physical Review B **33**, 3830 (1986).

[31] A. Patterson, *A Fourier Series method for the Determination of the components of interatomic distances*, Physical Review B **46**, 372 (1934).

[32] A. Patterson, *A direct method for the Determination of the components of interatomic distances in crystals*, Zeitschrift für Kristallographie A **90**, 517 (1935).

[33] G. Srivastava, *The electron counting rule and passivation of compound semiconductor surfaces*, Applied Surface Science **252**, 7600 (2006).

[34] C. Duke, *Semiconductor Surface Reconstruction: The structural Chemistry of Two-Dimensional Surface Compounds*, Chemical Review **96**, 1237 (1996).

[35] M. Pashley, *Electron counting model and its application to island structures on molecular-beam epitaxy grown GaAs(001) and ZnSe(001)*, Physical Review B **40**, 10481 (1989).

[36] V. P. LaBella, M. Krause, Z. Ding, and P. Thibado, *Arsenic-rich GaAs(001) surface structure*, Surface Science Reports **60**, 1 (2005).

[37] A. Ohtake and N. Koguchi, *Two types of structures for the GaAs(001)-c(4×4) surface*, Applied Physics Letters **83**, 5193 (2003).

[38] O. Romanyuk, P. Jiricek, M. Cukr, and I. Bartos, *LEED structural analysis of GaAs(001)-c(4×4) surface*, Surface Science Reports **60**, 89 (2004).

[39] A. Nagashima, A. Nishimura, T. Kawakami, and J. Yoshino, *Surface structure of GaAs(001)-c(4×4) studied by LEED intensity analysis*, Surface Science **564**, 218 (2004).

[40] M. Takahasi, , and J. Mizuki, *Element specific X-Ray diffraction study of GaAs-c(4×4)*, Physical Review Letters **96**, 055506 (2006).

[41] V. P. LaBella, H. Yang, D. Bullock, P. Thibado, P. Kratzer, and M. Scheffler, *Atomic Structure of the GaAs(001)-(2×4) Surface Resolving Using Scanning Tunneling Microscopy and First-Principles Theory*, Physical Review Letters **83**, 2989 (1999).

[42] T. Hashizume, Q. Xue, J. Zhou, A. Ichimiya, and T. Sakurai, *Structures of As-Rich GaAs-(2×4) Reconstructions*, Physical Review Letters **73**, 2208 (1994).

[43] A. Ohtake, *Structures of the As-deficient phase on GaAs(001)-(2×4)*, Physical Review B **74**, 165 (2006).

[44] S.-H. Lee, W. Moritz, and M. Scheffler, *GaAs(001) Surface under conditions of Low pressure: Evidence for a novel surface geometry*, Physical Review Letters **85**, 3890 (2000).

[45] M. Takahasi, Y. Yoneda, and J. Mizuki, *X-ray diffraction study on GaAs(001)-2×4 surfaces under molecular-beam epitaxy conditions*, Applied Surface Science **237**, 219 (2004).

[46] A. Ohtake, M. Ozeki, T. Yasuda, and T. Hanada, *Atomic structure of the GaAs(001)-(2×4) surface under As flux*, Physical Review B **65**, 165315 (2002).

[47] Y. Garreau, M. Sauvage-Simkin, N. Jedrecy, R. Pinchaux, and M. Veron, *Atomic structure and faulted boundaries in the GaAs(001) β(2x4) surface as derived from X-ray diffraction and line-shape analysis*, Physical Review B **54**, 17638 (1996).

[48] W. Schmidt and F. Bechstedt, *Atomic structures of GaAs(100)-(2×4) reconstructions*, Surface Science **360**, L473 (1996).

[49] A. Avery, C. Goringe, D. Holmes, J. L. Sudijo, and T. Jones, *Mechanisms for Disorder on GaAs(100)-(2×4) surfaces*, Surface Science **76**, 3344 (1996).

[50] D. Biegelsen, R. Bringans, J. Northrup, and L.-E.Swartz, *Surface reconstructions of GaAs(100) observed by scanning tunneling microscopy*, Physical Review B **41**, 5701 (1990).

[51] D. Frankel, C. Yu, J. Harbison, and H. Farrel, *High-resolution electron-energy-loss spectroscopy studies of GaAs (100) surfaces*, Journal of Vacuum science Technology B **5**, 1113 (1987).

[52] S. Skala, J. Hubacek, J. Tucker, J. Lyding, S. Chou, and K. Cheng, *Structure of GaAs(100)-c(8×2) determined by scanning tunneling microscopy*, Physical Review B **48**, 9138 (1993).

[53] C. Kumpf, D. Smilgies, E. Landemark, M. Nielsen, R. Feidenhans'l, O. Bunk, J. Zeysing, Y. Su, R. Johnson, L. Cao, J. Zegenhagen, B. Fimland, L. Marks, and D.Ellis, *Structure of metal rich (001) surfaces of III-V compound semiconductors*, Physical Review B **64**, 075307 (2001).

[54] C. Kumpf, L. D. Marks, D. Ellis, E. Landemark, M. Nielsen, R. Feidenhans'l, J. Zegenhagen, O. Bunk, J. Zeysing, Y. Su, and R. Johnson, *Subsurface Dimerization in III-V Semiconductor (001) surfaces*, Physical Review Letters **86**, 3586 (2001).

[55] F. Lukes, *Oxidation of Si and GaAs in air at room temperature*, Surface Science **30**, 91 (1972).

[56] U. Resch, N. Esser, Y. Raptis, W. Richter, J. Wasserfall, A. F"orster, and D. I. Westwood, *Arsenic passivation of MBE grown GaAs(100): structural and electronic properties of the decapped surfaces*, Surface Science **269/270**, 797 (1992).

[57] U. Resch-Esser, N. Esser, D. Wang, M. Kuball, K. Zegenhagen, B. Fimland, and W. Richter, *Surface quality and atomic structure of MBE-grown GaAs(100) prepared by the desorption of a protective layer*, Surface Science **352**, 71 (1996).

[58] K. Uosaki, T. Kondo, M. Koinuma, K. Tamura, and H. Oyanagi, *Structural study of electrochemically deposited copper on p-GaAs by atomic force microscopy ans surface X-ray absorption fine structure measurement*, Applied Surface Science **121/122**, 102 (1997).

[59] M. Koinuma and K. Uosaki, *An electrochemical AFM study on electrodeposition of copper on p-GaAs(100) surface in HCl*, Electrochimica Acta **40**, 1245 (1995).

[60] K. Tamura, H. Oyanagi, T. Kondo, M. Koinuma, and K. Uosaki, *Structural study of electrochemically deposited Cu on p-GaAs in H_2SO_4 Solution by in-situ surface-sensitive X-ray Absorption fine structure measurements*, Journal of Physical Chemistry B **104**, 9017 (2000).

[61] K. Tamura, T. Kondo, H. Oyanagi, M. Koinuma, and K. Uosaki, *Copper nanoclusters electrochemically deposited on p-GaAs in H_2SO_4 Solution probed by surface sensitive XAFS*, Journal of Surface Analysis **3**, 498 (1997).

[62] P. Vereecken, G. M. Vanalme, R. van Meirhaegge, F. Cardon, and W. Gomes, *Electrochemical reduction vs. vapour deposition for n-GaAs/Cu Schottky-barrier formation: A comparative study*, Journal of the Chemical Society **92**, 4069 (1996).

[63] G. Scherb and D. Kolb, *Cu-deposition onto n-GaAs(001): optical transient studies*, Journal of Electroanalytical Chemistry **396**, 151 (1995).

[64] G. Scherb, A. Kazimirov, J. Zegenhagen, T. Lee, M. Bedzyk, H. Noguchi, and K. Uosaki, *In-situ X-ray standing wave analysis of electrodeposited Cu monolayers on GaAs(001)*, Physical Review B **58**, 10800 (1998).

[65] J. Zegenhagen, F. Renner, A. Reitzle, T. Lee, S. Warren, A. Stierle, H. Dosch, G. Scherb, B. Fimland, and D. Kolb, *In sity X-ray analysis of solid/electrolyte interfaces: electrodeposition of Cu and Co on Si(111):H and GaAs(001) and corrosion of $Cu_3Au(111)$*, Surface Science **573**, 67 (2004).

[66] S. Warren, J. Zegenhagen, A. Reitzle, D. Kolb, J. Ziegler, F. Maroun, P. Allongue, A. Kazimirov, and G. Scherb, *X-Ray structural analysis of semiconductor-electrolyte interfaces*, in *Physics at Surfaces and Interfaces*, edited by B. N. Dev, pages 22–38, World Scientific, 2003.

[67] F. Renner, Y. Gründer, and J. Zegenhagen, *Portable Chamber for the Study of UHV prepared electrochemical Interfaces by hard X-Ray Diffraction*, Review of Scientific Instruments **78**, 033903 (2007).

[68] J. Zegenhagen, private communication.

[69] E. Maslen, A. Fox, and M. O'Keefe, *International tables of Crystallography*, volume C, chapter 6.1, Union of Crystallography, 2004.

[70] T. Head-Gordon and G. Hura, *Water Structure from Scattering Experiments and Simulation*, Chemical Review **102**, 2651 (2002).

[71] G. Hura, D. Russo, R. Glaeser, T. Head-Gordon, M. Krack, and M. Parrinello, *Water Structure as a function of temperature from from X-Scattering Experiments and ab initio molecular dynamics*, Physical Chemistry and Chemical Physics **5**, 1981 (2003).

[72] B. Fimland, private communication.

[73] E. Vlieg, J. van der Veen, S. Gurman, C. Norris, and MacDonald, *X-ray diffraction from rough, relaxed and reconstructed surfaces*, Surface Science **210**, 301 (1989).

[74] K. Shiraishi and T. Ito, *Atomic and electronic structures of surface kinks on GaAs(001) surfaces*, Applied Surface Science **121/122**, 98 (1997).

[75] R. Duszak, C. J. Palstrøm, L. Florez, Y.-N. Yang, and J. Weaver, *Dramatic work function variations of molecular -beam epitaxially grown GaAs(100) surfaces*, Journal of Vacuum Science Technology B **10**, 1891 (1992).

[76] G.Scherb, A. Kazimirov, J. Zegenhagen, T. Schultz, , R. Feidenhans'l, and B. Fimland, *Potential controlled stripping of an amorphous As layer on GaAs(001) in an electrolyte: An in situ X-ray scattering study*, Applied Physics Letters **71**, 2990 (1997).

[77] P. Vereecken, F. V. Kerchove, and W. Gomes, *Electrochemical behavior of (100) GaAs in copper(II)-containing solutions*, Electrochimica Acta **41**, 95 (1996).

[78] D. Doering, *Rotational epitaxy of periodic overlayers*, Journal of Vacuum Science & Technology A-Vacuum Surfaces and Films **3**, 8093 (1985).

[79] R. Hull and J. Bean, *Misfit dislocations in lattice-mismatched epitaxial-films*, Critical Reviews in Solid State and Material Science **17**, 507 (1992).

[80] D. Dunstan, *Strain and strain relaxation in semiconductors*, Journal of Material-Science in Electronics **8**, 337 (1997).

[81] S. Jain, A. Harker, and R. Cowley, *Misfit strain and misfit dislocations in lattice mismatched epitaxial layers and other systems*, Philosophical Magazine A **75**, 1461 (1997).

[82] B. Dodson, D. Myers, A. Datye, V. Kaushik, D. Kendall, and B. Martinez-Tovar, *Asymmetric Tilt Boundaries and Generalized Heteroepitaxy*, Physical Review Letters **61**, 2681 (1988).

[83] F. Riesz, *Crystallographic tilting in high-misfit (100) semiconductor heteroepitaxial systems*, Journal of Vacuum Science Technology A **14**, 425 (1995).

[84] F. Riesz, *Can epilayer tilt relieve misfit strain in lattice-mismatched heterostructures?*, Vacuum **46**, 1021 (1995).

[85] A. Yamada, P. Fons, R.Hunger, K. Iwata, K. Matsubara, and S. Niji, *Static analysis of off-axis crystal growth onto a lattice-mismatched substrate*, Applied Physics Letters **79**, 608 (2001).

[86] D. MacQuistan and F. Weinberg, *The behavior of copper on gallium arsenide*, Journal of Crystal Growth **110**, 745 (1991).

[87] E. Owen and E. Roberts, *Factors affecting the Limit of Solubility of Elements in Copper and Silver*, Philosophical Magazine **27**, 294 (1939).

[88] P. Subramanian and D. Laughlin, *The As-Cu (Arsenic-Copper) System*, Bulletin of Alloy Phase Diagrams **9**, 605 (1988).

[89] P. Subramanian and D. Laughlin, *Cu-Ga (Copper-Gallium)*, Bulletin of Alloy Phase Diagrams **9**, 174 (1988).

[90] F. Weibke, *Das Zustandsdiagramm des Systems Kupfer-Gallium*, Zeitschrift für anorganische und allgemeine Chemie **220**, 293 (1934).

[91] A. Steinfort, P. Scholte, A.Ettema, F. Tuinstra, M. Nielsen, E. Landemark, D.-M. Smilgies, R. Feidenhans'l, G.Falkenberg, L. Seehofer, and R. Johnson, *Strain in nanoscale germanium hut clusters on Si(001) studied by X-ray diffraction*, Physical Review Letters **77**, 2009 (1996).

Index